University of Alberta

Numerical Simulation of the SAGD Process Coupled with Geomechanical Behavior

By

Pingke Li ©

A thesis submitted to the Faculty of Graduate Studies and Research in partial fulfillment
of the requirements for the degree of **Doctor of Philosophy**

In

Geotechnical Engineering

Department of Civil and Environmental Engineering

Edmonton, Alberta

Fall 2006

Library and
Archives Canada

Published Heritage
Branch

395 Wellington Street
Ottawa ON K1A 0N4
Canada

Bibliothèque et
Archives Canada

Direction du
Patrimoine de l'édition

395, rue Wellington
Ottawa ON K1A 0N4
Canada

Your file Votre référence
ISBN: 978-0-494-23065-7
Our file Notre référence
ISBN: 978-0-494-23065-7

NOTICE:
The author has granted a non-exclusive license allowing Library and Archives Canada to reproduce, publish, archive, preserve, conserve, communicate to the public by telecommunication or on the Internet, loan, distribute and sell theses worldwide, for commercial or non-commercial purposes, in microform, paper, electronic and/or any other formats.

The author retains copyright ownership and moral rights in this thesis. Neither the thesis nor substantial extracts from it may be printed or otherwise reproduced without the author's permission.

AVIS:
L'auteur a accordé une licence non exclusive permettant à la Bibliothèque et Archives Canada de reproduire, publier, archiver, sauvegarder, conserver, transmettre au public par télécommunication ou par l'Internet, prêter, distribuer et vendre des thèses partout dans le monde, à des fins commerciales ou autres, sur support microforme, papier, électronique et/ou autres formats.

L'auteur conserve la propriété du droit d'auteur et des droits moraux qui protège cette thèse. Ni la thèse ni des extraits substantiels de celle-ci ne doivent être imprimés ou autrement reproduits sans son autorisation.

In compliance with the Canadian Privacy Act some supporting forms may have been removed from this thesis.

While these forms may be included in the document page count, their removal does not represent any loss of content from the thesis.

Conformément à la loi canadienne sur la protection de la vie privée, quelques formulaires secondaires ont été enlevés de cette thèse.

Bien que ces formulaires aient inclus dans la pagination, il n'y aura aucun contenu manquant.

Canada

ABSTRACT

Canada has vast oil sand resources. While a large portion of this resource can be recovered by surface mining techniques, a majority is located at depths requiring the application of in situ recovery technologies. Although a number of in situ recovery technologies exist, the steam assisted gravity drainage (SAGD) process has emerged as one of the most promising technologies to develop the in situ oil sands resources. During the SAGD operations, saturated steam is continuously injected into the oil sands reservoir, which induces pore pressure and stress variations. As a result, reservoir parameters and processes may also vary, particularly when tensile and shear failure occur. This geomechanical effect is obvious for oil sands material because oil sands have the in situ interlocked fabric. The conventional reservoir simulation generally does not take this coupled mechanism into consideration. Therefore, this research is to improve the reservoir simulation techniques of the SAGD process applied in the development of oil sands and heavy oil reservoirs.

The analyses of the decoupled reservoir geomechanical simulation results show that the geomechanical behavior in SAGD has obvious impact on reservoir parameters, such as absolute permeability. The issues with the coupled reservoir geomechanical simulations of the SAGD process have been clarified and the permeability variations due to geomechanical behaviors in the SAGD process investigated. A methodology of sequentially coupled reservoir geomechanical simulation technique was developed based on the reservoir simulator, EXOTHERM, and the geomechanical simulator, FLAC. In addition, a representative geomechanical model of oil sands material was summarized in

this research. Finally, this reservoir geomechanical simulation methodology was verified with the UTF Phase A SAGD project and applied in a SAGD operation with gas-over-bitumen geometry. Based on this methodology, the geomechanical effect on the SAGD production performance can be quantified. This research program involves the analyses of laboratory testing results obtained from literatures. However, no laboratory testing was conducted in the process of this research.

ACKNOWLEDGMENTS

I wish to express my sincere and grateful thanks to my supervisor, Dr. Rick J. Chalaturnyk. His guidance and support, both personally and professionally, during these years of research have been invaluable. I greatly appreciate his exceptional patience and encouragement. His directions, advice, and expertise were instrumental in accomplishing this research.

I am also grateful to my co-supervisors, Drs. Marcel Polikar and Dave H. Chan, for their valuable discussions, suggestions, and review of the text. Drs. Luciane B. Cunha and Douglas R. Schmitt proposed good suggestions to improve the research work. In addition, Drs. Ron Wong and Tony Settari sent me a few of their publications for me to refer to. Their assistance and enthusiasm are very much appreciated.

Numerical simulation is a large component of this research. The successful completion of this proposed methodology was due in part to the assistance of Dr. Thomas B. Tan. He provided me a research version of the reservoir simulator, EXOTHERM, as I requested. I would like to express my appreciation to him for his tireless support.

I acknowledge Mr. Kazimierz Oldakowski for "re-finding" his original laboratory testing data.

I acknowledge Mr. Mike McCormack and Mr. Patrick Collins for their review and suggestions that lead to improvements of Chapter 3.

I appreciate the financial support from the NSERC research grant to Dr. Rick J. Chalaturnyk.

I would like to thank numerous friends and colleagues, in particular Xiteng Liu, Xueqing Su, Fagang Gu, Xiaobo Wang, and Namkak Cho, for their help and discussions.

The love and support of my parents, my parents-in-law, and my family, Xiaoli Dong and Jiaqi Li, have always been a source of strength in my work. I am deeply grateful to them.

TABLE OF CONTENTS

Chapter Page

1 INTRODUCTION 1

1.1 Oil Sand Reserves in Canada 1

1.2 Recovery Technologies 1

1.3 Concept of the SAGD Process 3

1.4 Geomechanics Related to SAGD 4

1.5 Necessity of Coupled Reservoir Geomechanical Simulations 5

1.6 Objective, Scope, and Methodology 7

1.7 Organization of Thesis 7

2 DEVELOPMENT OF THE SAGD PROCESS AND THE RESERVOIR GEOMECHANICAL SIMULATION 13

2.1 Development of the SAGD Process 13

2.1.1 Background 13

2.1.2 Theoretical development of the SAGD process 15

2.1.3 Evolution of the SAGD process 18

2.1.4 Current applications of the SAGD process 22

2.2 Geotechnical Properties of Oil Sands 25

2.3 Review of the Coupled Reservoir Geomechanical Simulation 26

2.3.1 Lewis and Sukirman's model (1993) 26

2.3.2 Chen, Teufel, and Lee's model (1995) 26

2.3.3 Osorio, Chen, and Teufel's model (1999) 27

2.3.4 Chin and Thomas's model (1999) 27

2.3.5 Tortike and Farouq Ali's model (1991) 27

2.3.6 Fung, Buchanan, and Wan's model (1994) 28

2.3.7 Settari, Walters, and Behie's Model (2001) 28

2.3.8 Summary 29

3 DECOUPLED RESERVOIR GEOMECHANICAL SIMULATIONS 32

3.1 Introduction 32

3.2 Geomechanical Parameters for SAGD 34

3.2.1 Thermal Volume Change 34

3.2.2 Bulk Compressibility 35

3.2.3 Compressibility in Reservoir Geomechanics 36

3.2.4 Strength and Stress-Strain Behavior 38

3.2.5 Stress-Induced Permeability Changes 40

3.3 Numerical Models 41

3.4 Reservoir Simulations 42

3.5 Geomechanical Simulations 42

3.6 Results and Discussion 43

3.6.1 Shallow Reservoir – Zone in Middle of Reservoir 43

3.6.2 Shallow Reservoir – Zone at Top of Reservoir 45

3.6.3 Medium Reservoir – Zone in Middle of Reservoir 46

3.6.4 Medium Reservoir – Zone at Top of Reservoir 46

3.6.5 Deep Reservoir 46

3.7 Conclusions 47

4 ISSUES WITH RESERVOIR GEOMECHANICAL SIMULATIONS 61

4.1 Introduction 61

4.2 Geomechanical Behavior in SAGD Process 63

4.3 Geomechanical Zones around A Steam Chamber 64

4.3.1 Drained zone 65

4.3.2 Partially drained zone 66

4.3.3 Undrained zone 66

4.4 Reservoir Properties/Processes Modified by Geomechanics 67

4.4.1 Pore Pressure Transmission vs. Fluid Flow 68

4.4.2 Gas evolution 70

4.4.3 Porosity 71

4.4.4 Absolute permeability, k_a 72

4.4.5 Relative permeability, k_{rw}, k_{ro}, and k_{rg} 74

4.4.6 Compressibility 75

4.4.7 Thermal expansion effect 76

4.4.8 Saturation, S_o, S_w, and S_g 77

4.4.9 Capillary Pressure, p_c 77

4.4.10 Enthalpy transmissibility, T_H 78

4.5 Summary 78

5 **DEVELOPMENT OF THE METHODOLOGY OF THE COUPLED RESERVOIR GEOMECHANICAL SIMULATIONS FOR THE SAGD PROCESS** 91

5.1 Introduction 91

5.2 Mathematical Formulation in EXOTHERM 92

5.3 Mathematical Formulation in FLAC 93

5.4 Windows Automation Software AUTOMATE 95

5.5 Methodology of Coupling between EXOTHERM and FLAC 95

5.5.1 Coupling Categories 95

5.5.2 EXOTHERM-FLAC coupling 96

5.5.3 EXOTHERM-FLAC coupling modules 96

5.5.4 Operation Procedure of the Methodology 97

5.5.5 Coupling Relationships for EXOTHERM and FLAC 98

5.6 Testing of the Methodology 98

5.7 Application Cases of the Coupling Procedure 99

5.7.1 Effect of Steam Injection Pressure 101

5.7.2 Effect of Initial Reservoir Permeability 101

5.7.3 Effect of Geomechanical Behavior 102

5.8 Characteristics of the Methodology 103

5.9 Concluding Remarks and Suggestions 104

6 PERMEABILITY VARIATIONS ASSOCIATED WITH GEOMECHANICAL BEHAVIORS IN SAGD 116

6.1 Introduction 116

6.2 Geomechanical Behaviour During SAGD 116

6.2.1 Isotropic Unloading Process 117

6.2.2 Shearing Process 117

6.3 Absolute Permeability Variations in Response to Isotropic Unloading 119

6.4 Absolute Permeability Variations in Response to Shearing 120

6.5 Effective Permeability to Water 122

6.6 Discussions 124

6.6.1 Comparison of Permeability Changes due to Different Geomechanical Behavior 124

6.6.2 Tortike's Equation and Kozeny-Carman Model 125

6.6.3 Permeability of Horizontal and Vertical Specimens 127

6.6.4 Calculation of Absolute Permeability due to Shearing 128

6.6.5 Water Relative Permeability 129

6.6.6 Field Applications 131

6.7 Conclusions 132

7 GEOMECHANICAL MODEL OF OIL SANDS 158

7.1 Introduction 158

7.2 Laboratory Testing On Oil Sands 158

7.2.1 Oldakowski's Lab Tests 158

7.2.2 Samieh and Wong's Lab Tests 159

7.2.3 Touhidi-Baghini's Lab Tests 159

7.3 FLAC Numerical Experiments Matching Laboratory Tests 159

7.4 Geomechanical Model of Oil Sands 161

7.5 Concluding Remarks 162

8 HISTORY MATCH OF THE UTF PHASE A SAGD PROJECT WITH COUPLED RESERVOIR GEOMECHANICAL SIMULATION 176

8.1 Introduction 176

8.2 Project And Reservoir Description 177

8.3 Geotechnical Instrumentation 179

8.4 Operation History of UTF Phase A Project 179

8.4.1 Al Well Pair 180

8.4.2 A2 Well Pair 180

8.4.3 A3 Well Pair 181

8.5 Base Case Reservoir Model and Geomechanical Model 184

8.6 History Match with Reservoir Geomechanical Simulation 184

8.6.1 Oil Production, Steam Oil Ratio, and Oil Recovery Factor 184

8.6.2 Injection and Production Pressures 185

8.6.3 Reservoir Pressure Field 186

8.6.4 Reservoir Temperature Field 187

8.6.5 Vertical Strain 187

8.6.6 Vertical Strain in the Geotechnical Cross Section 191

8.6.7 Horizontal Displacement 192

8.6.8 Horizontal Strain within the Geotechnical Cross Section 194

8.6.9 Volumetric Strain within the Geotechnical Cross Section 194

8.6.10 Surface Heave and Vertical Displacement of the Reservoir Top 194

8.7 Conclusions 195

9 GAS-OVER-BITUMEN GEOMETRY AND ITS SAGD PERFORMANCE ANALYSIS WITH COUPLED RESERVOIR GEOMECHANICAL SIMULATION 222

9.1 Introduction 222

9.2 Geomechanical Properties of Oil Sands 223

9.3 Geomechanical Properties of Mudstones 224

9.4 Linking Parameters of Reservoir and Geomechanical Simulators 226

9.4.1 Oil Sands Reservoir 226

9.4.2 Mudstone Layer 227

9.5 Numerical Simulation 228

9.5.1 Reservoir Model and Geomechanical Model 228

9.5.2 Base Case: Mudstone Permeability = .001 md 228

9.5.3 Evolution of Failure within Mudstone Layer 229

9.5.4 Effect of Mudstone Permeability 230

9.5.5 Effect of Steam injection Pressures 232

9.6 Summary 233

10 CONCLUSIONS AND RECOMMENDATIONS 256

10.1 Summary 256

10.2 Conclusions 256

10.2.1 Decoupled Reservoir Geomechanical Simulations 256

10.2.2 Reservoir Geomechanical Zones and Reservoir Processes/Parameters Affected by Geomechanics 257

10.2.3 Methodology of Sequentially Coupled Reservoir Geomechanical Simulation 258

10.2.4 Permeability Variations due to Reservoir Geomechanical Behaviors in SAGD Operations 258

10.2.5 Geomechanical Model of Oil Sands 259

10.2.6 Verification of the Coupled Reservoir Geomechanical Simulation Methodology with UTF Phase A Project 260

10.2.7 Application of the Coupled Reservoir Geomechanical Simulation Methodology in SAGD with Gas over Bitumen Geometry 261

10.3 Recommendations 262

REFERENCE 264

APPENDIX A Numerical Experiments Matching Lab Testing 277

APPENDIX B UTF Phase A History Match Figures 308

LIST OF TABLES

Table 1-1	Initial in-place volumes of crude bitumen	9
Table 1-2	In-place volumes and established reserves of crude bitumen	10
Table 3-1	Physical properties of the three model reservoirs	49
Table 3-2	Properties required for the geomechanical analyses	49
Table 4-1	Impact of absolute permeability variation due to geomechanics on SAGD production performance	81
Table 5-1	Reservoir and geomechanical parameters	106
Table 6-1	Specimen conditions after consolidation for isotropic unloading tests	134
Table 6-2	Specimen properties from block oil sand sample	134
Table 6-3	Isotropic unloading after consolidation under 5.6 to 6.0 MPa	135
Table 6-4	Specimen conditions at the beginning of shear tests	135
Table 8-1	Reservoir properties in the coupled reservoir geomechanical simulation	196
Table 8-2	Reservoir geomechanical properties in the coupled reservoir geomechanical simulation	197
Table 8-3	Extensometer modules and their elevations in wells AGE2, AGE3, and AGE4 within the geotechnical cross section	198
Table 9-1	Reservoir Properties in EXOTHERM Simulation	234
Table 9-2	Geomechanical Properties in FLAC Simulation	235

LIST OF FIGURES

Figure 1-1	Oil sand reserves in Alberta, Canada	11
Figure 1-2	SAGD concept	12
Figure 2-1	Fabric of Athabasca oil sands	31
Figure 3-1	Interaction between Fluid Flow and Geomechanics in a Deformable Reservoir	50
Figure 3-2	Schematic showing possible increase in horizontal stresses due to steam chamber growth	50
Figure 3-3	Possible stress paths within reservoir during SAGD process	51
Figure 3-4	Change in effective permeability to water	52
Figure 3-5	Schematic reservoir models and numerical grid systems	53
Figure 3-6	Schematic geometry of the grid systems for the geomechanical analyses	54
Figure 3-7	Shallow reservoir model: stress path for element adjacent to wellpair	55
Figure 3-8	Change in absolute permeability for shallow reservoir model	56
Figure 3-9	Shallow reservoir model: stress path for element at top of reservoir – $K_0 = 1.6$	56
Figure 3-10	Medium depth reservoir model: stress path for element adjacent to wellpairs	57
Figure 3-11	Medium depth reservoir model: stress path for element at top of reservoir	58
Figure 3-12	Deep reservoir model: stress path for element - (a) adjacent to wellpairs and (b) top of reservoir	59
Figure 3-13	Change in absolute permeability for deep reservoir model	60
Figure 4-1	Sketch of three geomechanical zones	82
Figure 4-2	Pore pressure generation in the drained zone	83
Figure 4-3	Pore pressure generation in the partially drained and undrained zone	83

Figure 4-4 Plan view and geotechnical cross-section of UTF Phase A site 84
Figure 4-5 Schematic distance of the outside boundary of three geomechanical zones from edge of steam chamber 85
Figure 4-6 The three geomechanical zones in UTF Phase A Project 85
Figure 4-7 Injection pressure front tracks 86
Figure 4-8 Undrained triaxial compression test 87
Figure 4-9 Bubble plugging effect 88
Figure 4-10 Compressibility versus effective stress 89
Figure 4-11 Effect of geomechanical behavior on relative permeability 90
Figure 5-1 Flow chart of the coupled reservoir geomechanical simulation procedure with EXOTHERM and FLAC 107
Figure 5-2 Grid system in reservoir simulator 108
Figure 5-3 Grid system in geomechanical simulation 108
Figure 5-4 Comparison of steam rates and cumulative steam injections between conventional simulation and the coupled simulation 109
Figure 5-5 Comparison of oil rates and cumulative oil productions between conventional simulation and the coupled simulation 109
Figure 5-6 Comparison of oil recoveries between conventional simulation and the coupled simulation 110
Figure 5-7 Oil recovery and SOR versus time for k_i = 5000 md 111
Figure 5-8 Oil recovery and SOR versus time for k_i = 2500 md 112
Figure 5-9 Comparison of oil production rates for different simulation techniques 113
Figure 5-10 Porosity, vertical effective stresses, and displacement fields after the SAGD operation (k_i=5000 md) 114
Figure 5-11 Porosity, vertical effective stresses, and displacement fields after the SAGD operation (k_i=2500md) 114
Figure 5-12 Permeability variation due to steam injection pressure (k_i=5000 md) 115
Figure 5-13 Permeability variation due to steam injection pressures (k_i=2500 md) 115

Figure 6-1 Thermal expansion of oil sands 136

Figure 6-2 Shearing in the SAGD process 136

Figure 6-3 Shear failure of top element 137

Figure 6-4 Shear failure of side element 137

Figure 6-5 Volume change vs. confining effective stress 138

Figure 6-6 Regression curve through all the data shown in Figure 6-5 138

Figure 6-7 Volumetric strain vs. isotropic confining effective stress 139

Figure 6-8 Absolute permeability ratio vs. volumetric strain from isotropic unloading test 139

Figure 6-9 Absolute permeability ratio vs. isotropic effective stress 140

Figure 6-10 Stress paths for absolute permeability test during shearing 140

Figure 6-11 Volume change vs. axial strain for horizontal specimens 141

Figure 6-12 Volume change vs. axial strain for vertical specimens 141

Figure 6-13 Absolute permeability change during shearing for horizontal specimens 142

Figure 6-14 Absolute permeability change during shearing for vertical specimens 142

Figure 6-15 Absolute permeability ratio vs. volume change for horizontal specimens 143

Figure 6-16 Absolute permeability ratio vs. volume change for vertical specimens 143

Figure 6-17 Volume change vs. effective confining stress 144

Figure 6-18 Regression curve through all the data shown in Figure 6-17 144

Figure 6-19 Effective permeability to water vs. volume change 145

Figure 2-20 Effective permeability ratio vs. volume change including the curve with Tortike's equation 145

Figure 6-21 Volume change vs. axial strain during shearing 146

Figure 6-22 Derivative of volume change to axial strain for specimen S19 146

Figure 6-23 Derivative of volume change to axial strain for specimen S20 147

Figure 6-24 Derivative of volume change to axial strain for specimen S21 147

Figure 6-25 Derivative of volume change to axial strain for specimen S22 148

Figure 6-26 Derivative of volume change to axial strain for specimen S23 148

Figure 6-27 Variation of effective permeability to water vs. volume change during shearing 149

Figure 6-28 Derivative of water effective permeability to axial strain for specimen S19 149

Figure 6-29 Derivative of water effective permeability to axial strain for specimen S20 150

Figure 6-30 Derivative of water effective permeability to axial strain for specimen S21 150

Figure 6-31 Derivative of water effective permeability to axial strain for specimen S22 151

Figure 6-32 Derivative of water effective permeability to axial strain for specimen S23 151

Figure 6-33 Comparison of water effective permeability ratio due to isotropic unloading and shearing 152

Figure 6-34 Impact of confining effective stress on change in permeability 152

Figure 6-35 Comparison of effective permeability to water due to isotropic unloading and shearing 153

Figure 6-36 Absolute permeability ratios from isotropic unloading test and Tortike's equation 153

Figure 6-37 Absolute permeability ratios from shearing test of horizontal specimens and Tortike's equation 154

Figure 6-38 Absolute permeability ratios from shearing test of vertical specimens and Tortike's equation 154

Figure 6-39 Tortuosity change for vertical (left) and horizontal (right) specimens 155

Figure 6-40 Determination of absolute permeability due to shearing for horizontal specimens 155

Figure 6-41 Determination of absolute permeability due to shearing for vertical specimens 156

Figure 6-42	Determination of absolute permeability due to the isotropic unloading process	156
Figure 6-43	Determination of effective permeability to water due to the pure shearing process	157
Figure 6-44	Impact of isotropic unloading and shearing on water relative permeability	157
Figure 7-1	Stress paths (Oldakowski, 1994)	164
Figure 7-2	Typical stress strain relationships (Oldakowski, 1994)	165
Figure 7-3	Volume change versus axial strain of oil sands (Oldakowski, 1994)	165
Figure 7-4	Deviatoric stress and volumetric strain versus axial strain (Samieh and Wong , 1997)	166
Figure 7-5	Typical stress strain relationship (Stress path 1) (Touhidi-Baghini, 1998)	167
Figure 7-6	Volumetric strain versus axial strain (Stress path 1) (Touhidi-Baghini, 1998)	167
Figure 7-7	Typical drained triaxial test results on dense sands (After Touhidi-Baghini, 1998)	168
Figure 7-8	Oil sands model in FLAC	169
Figure 7-9	Deviatoric stress versus axial strain, Stress Path 2 (Initial σ_3' = 1390 kPa), Lab tests simulated by FLAC (Oldakowski's sample S23)	169
Figure 7-10	Volumetric strain versus axial strain, Stress Path 2 (Initial σ_3' = 1390 kPa), Lab tests simulated by FLAC (Oldakowski's sample S23)	170
Figure 7-11	Deviatoric stress versus axial strain, Lab tests simulated by FLAC (Samieh and Wong's sample, σ_3' = 750 kPa)	170
Figure 7-12	Volumetric strain versus axial strain, Lab tests simulated by FLAC (Samieh and Wong's sample, σ_3' = 750 kPa)	171
Figure 7-13	Deviatoric stress versus mean effective stress, Stress Path 3 (Initial σ_3' = 250 kPa), (Touhidi-Baghini's Vertical Core, T36)	171
Figure 7-14	Deviatoric stress versus axial strain, Stress path 3 (Initial σ_3' = 250 kPa) (Touhidi-Baghini's Vertical Core, T36)	172
Figure 7-15	Volumetric strain versus axial strain, Stress path 3 (Initial σ_3' = 250 kPa) (Touhidi-Baghini's Vertical Core, T36)	172

Figure 7-16	Summarized modulus of elasticity for oil sands	173
Figure 7-17	Summarized maximum friction angle for oil sands	173
Figure 7-18	Summarized maximum dilation angle for oil sands	174
Figure 7-19	Summarized post peak friction angle for oil sands	174
Figure 7-20	Summarized post peak dilation angle for oil sands	175
Figure 8-1	Vertical stratigraphic Column	199
Figure 8-2	Plan view of instrument well locations	200
Figure 8-3	Temperature measurement points in the geotechnical cross section	200
Figure 8-4	Location of inclinometer wells within the geotechnical cross section	201
Figure 8-5	Extensometers modules within the geotechnical cross section	202
Figure 8-6	Piezometer locations within the geotechnical cross section	202
Figure 8-7	Grid systems in reservoir geomechanical simulations	203
Figure 8-8	Assumptions for Unit F permeability change	203
Figure 8-9	Cumulative oil production and steam Injection	204
Figure 8-10	Oil production rate and steam injection rate	204
Figure 8-11	CSOR and ISOR	205
Figure 8-12	Oil recovery	205
Figure 8-13	Temperature distribution (699 days)	206
Figure 8-14	Temperature distribution (1035 days)	206
Figure 8-15	Permeability distribution (coupled simulation time 699 days)	207
Figure 8-16	Permeability distribution (coupled simulation time 1035 days)	207
Figure 8-17	History match of AI1 well pressures	208

Figure 8-18 History match of AP1 well pressures 208
Figure 8-19 History match of AI2 well pressures 209
Figure 8-20 History match of AP2 well pressures 209
Figure 8-21 History match of AI3 well pressures 210
Figure 8-22 History match of AP3 well pressures 210
Figure 8-23 History match of pore pressure field (500 days) 211
Figure 8-24 History match of pore pressure field (700 days) 211
Figure 8-25 Field steam chamber evolution 212
Figure 8-26 History match of reservoir temperature field (500 days) 212
Figure 8-27 History match of reservoir temperature field (700 days) 213
Figure 8-28 Vertical strain for AGE2 (Elevation 280.5 m) 213
Figure 8-29 Vertical strain for AGE2 (Elevation 283.5 m) 214
Figure 8-30 Vertical strain for AGE2 (Elevation 286.5 m) 214
Figure 8-31 Vertical strain for AGE2 (Elevation 289.5 m) 215
Figure 8-32 Vertical strain in the geotechnical cross section (550 days) 215
Figure 8-33 Vertical strain in the geotechnical cross section (679 days) 216
Figure 8-34 Horizontal displacement at AGI1 (375 days) 216
Figure 8-35 Horizontal displacement at AGI1 (550 days) 217
Figure 8-36 Horizontal displacement at AGI1 (679 days) 217
Figure 8-37 Horizontal displacement at AGI1 (sensitivity study) (375 days) 218
Figure 8-38 Horizontal displacement at AGI1 (sensitivity study) (550 days) 218
Figure 8-39 Horizontal displacement at AGI1 (sensitivity study) (679 days) 219

Figure 8-40 Horizontal strain in the geotechnical cross section (550 days) 219

Figure 8-41 Horizontal strain in the geotechnical cross section (679 days) 220

Figure 8-42 Volumetric strain in the geotechnical cross section (550 days) 220

Figure 8-43 Volumetric strain in the geotechnical cross section (679 days) 221

Figure 8-44 Vertical displacement and surface heave 221

Figure 9-1 Athabasca oil sands reserves and gas production area 236

Figure 9-2 Numerical experiment match of deviatoric stress versus axial strain 237

Figure 9-3 Numerical experiment match of volumetric strain versus axial strain 237

Figure 9-4 Assumed permeability improvements due to shear failure (a) and tensile failure (b) 238

Figure 9-5 Definition of failure index (modified from Chalaturnyk, 1997) 239

Figure 9-6 Top gas and top water overlying bitumen bearing formation with A2 mudstone in between 239

Figure 9-7 Stratigraphical scheme of the reservoir model 240

Figure 9-8 Grid system used in EXOTHERM (middle) and FLAC (right) 240

Figure 9-9 Oil rates and steam rates for conventional simulation and coupled simulation 241

Figure 9-10 Cumulative steam injection and oil production for conventional simulation and coupled simulation 241

Figure 9-11 Oil recovery and OSR for conventional simulation and coupled simulation 242

Figure 9-12 Pore pressure distribution in the mudstone layer (Initial k_MS = 0.00001 md, P_inj = 2500 kPa, time =1399 days) 242

Figure 9-13 Failure index (EX_17) in the mudstone layer (Initial k_MS = 0.00001 md, P_inj = 2500 kPa, Time =1399 days) 243

Figure 9-14 Permeability distribution in the mudstone layer (Initial k_MS = 0.00001 md, P_inj = 2500 kPa, Time =1399 days) 243

Figure 9-15 Pore pressure distribution in the mudstone (Initial k_MS = 0.00001 md, P_inj = 2500 kPa, Time = 1639 days) 244

Figure 9-16 Minimum effective principal stress (EX_11, unit: Pa) in the mudstone layer (Initial k_MS = 0.00001 md, P_inj = 2500 kPa, Time = 1639 days) 244

Figure 9-17 Failure index (EX_17) in the mudstone layer (Initial k_MS = 0.00001 md, P_inj = 2500 kPa, Time = 1639 days) 245

Figure 9-18 The modified permeability distribution (Initial k_MS = 0.00001 md, P_inj = 2500 kPa, Time = 1639 days) 245

Figure 9-19 The modified permeability distribution (Initial k_MS = 0.00001 md, P_inj = 2500 kPa, Time = 2369 days) 246

Figure 9-20 Failure index (EX_17) in the mudstone layer (Initial k_MS = 0.00001 md, P_inj = 2500 kPa, Time = 2369 days) 246

Figure 9-21 The modified permeability distribution (Initial k_MS = 0.00001 md, P_inj = 2500 kPa, Time = 7305 days) 247

Figure 9-22 Failure index (EX_17) in the mudstone layer (Initial k_MS = 0.00001 md, P_inj = 2500 kPa, Time = 7305 days) 247

Figure 9-23 The modified permeability in the mudstone layer (Initial k_MS = 0.0001 md, P_inj = 2500 kPa, Time = 7305 days) 248

Figure 9-24 Oil and steam rate comparison for mudstone permeability of 0.1 md and 0.00001 md 248

Figure 9-25 Cumulative oil production and steam injection for mudstone permeability of 0.1 md and 0.00001 md 249

Figure 9-26 Oil recovery and OSR for mudstone permeability of 0.1 md and 0.00001 md 249

Figure 9-27 The modified permeability distribution (Initial k_MS = 0.000001 md, P_inj = 2500 kPa, and Time = 7305) 250

Figure 9-28 The modified permeability distribution (Initial k_MS = 0 md, P_inj = 2500 kPa, and Time = 7305) 250

Figure 9-29 Oil rate and steam rate for mudstone permeability of 0.00001 md and 0.000001 md (Mudstone failure occurs at time 1719 days for k_MS = 0.000001 md) 251

Figure 9-30 Cumulative oil production and steam injection for mudstone permeability of 0.00001 md and 0.000001 md (Mudstone failure occurs at time 1719 days for k_MS = 0.000001 md) 251

Figure 9-31 Oil recovery and OSR for mudstone permeability of 0.00001 md and 0.000001 md 252

Figure 9-32 The modified permeability distribution (Initial k_MS = 0.001 md, P_inj = 5000 kPa, and Time = 7305 days) 252

Figure 9-33 Failure index (EX_17) distribution (Initial k_MS = 0.0001 md, P_inj = 5000 kPa, and Time = 4519 days) 253

Figure 9-34 The modified permeability distribution (Initial k_MS = 0.0001 md, P_inj = 5000 kPa, and Time = 4519 days) 253

Figure 9-35 Oil rate and steam rate for injection pressures of 2500 kPa and 5000 kPa (Mudstone failure occurs at time 4519 days for P_inj = 5000 days) 254

Figure 9-36 Cumulative oil production and steam injection for injection pressures of 2500 kPa and 5000 kPa (Mudstone failure occurs at time 4519 days for P_inj = 5000 days) 254

Figure 9-37 Oil recovery and OSR for injection pressures of 2500 kPa and 5000 kPa (Mudstone failure occurs at time 4519 days for P_inj = 5000 days) 255

Figure A1 Deviatoric stress versus mean effective stress 278
Stress Path 1 (σ_3' = 250 kPa), Horizontal Core, T40

Figure A2 Deviatoric stress versus axial strain 278
Stress Path 1 (σ_3' = 250 kPa), Horizontal Core, T40

Figure A3 Volumetric strain versus axial strain 279
Stress Path 1 (σ_3' = 250 kPa), Horizontal Core, T40

Figure A4 Deviatoric stress versus mean effective stress 279
Stress Path 2 (Initial σ_3' = 250 kPa), Horizontal Core, T41

Figure A5 Deviatoric stress versus axial strain 280
Stress Path 2 (Initial σ_3' = 250 kPa), Horizontal Core, T41

Figure A6 Volumetric strain versus axial strain 280
Stress Path 2 (Initial σ_3' = 250 kPa), Horizontal Core, T41

Figure A7 Deviatoric stress versus mean effective stress 281
Stress Path 3 (Initial σ_3' = 250 kPa), Horizontal Core, T42

Figure A8 Deviatoric stress versus axial strain 281
Stress Path 3 (Initial σ_3' = 250 kPa), Horizontal Core, T42

Figure A9 Volumetric strain versus axial strain 282
Stress Path 3 (Initial σ_3' = 250 kPa), Horizontal Core, T42

Figure A10 Deviatoric stress versus mean effective stress 282
Stress path 4 (Initial σ_3' = 250 kPa), Horizontal Core, T43

Figure A11 Deviatoric stress versus axial strain 283
Stress Path 4 (Initial σ_3' = 250 kPa), Horizontal Core, T43

Figure A12 Volumetric strain versus axial strain 283
Stress Path 4 (Initial σ_3' = 250 kPa), Horizontal Core, T43

Figure A13 Deviatoric stress versus mean effective stress 284
Stress path 1 (σ_3' = 250 kPa), Vertical Core, T29

Figure A14 Deviatoric stress versus axial strain 284
Stress path 1 (σ_3' = 250 kPa), Vertical Core, T29

Figure A15 Volumetric strain versus axial strain 285
Stress path 1 (σ_3' = 250 kPa), Vertical Core, T29

Figure A16 Deviatoric stress versus mean effective stress 285
Stress Path 3 (Initial σ_3' = 250 kPa), Vertical Core, T36

Figure A17 Deviatoric stress versus axial strain 286
Stress path 3 (Initial σ_3' = 250 kPa), Vertical Core, T36

Figure A18 Volumetric strain versus axial strain 286
Stress path 3 (Initial σ_3' = 250 kPa), Vertical Core, T36

Figure A19 Deviatoric stress versus mean effective stress 287
Stress path 2 (Initial σ_3' = 250 kPa), Vertical Core, T38

Figure A20 Deviatoric stress versus axial strain 287
Stress path 2 (Initial σ_3' = 250 kPa), Vertical Core, T38

Figure A21 Volumetric strain versus axial strain 288
Stress path 2 (Initial σ_3' = 250 kPa), Vertical Core, T38

Figure A22 Deviatoric stress versus mean effective stress 288
Stress Path 4 (Initial σ_3' = 250 kPa), Vertical Core, T39

Figure A23 Deviatoric stress versus axial strain 289
Stress Path 4 (Initial σ_3' = 250 kPa), Vertical Core, T39

Figure A24 Volumetric strain versus axial strain 289
Stress Path 4 (Initial σ_3' = 250 kPa), Vertical Core, T39

Figure A25 Deviatoric stress versus axial strain 290
(σ_3' = 50 kPa)

Figure A26 Volumetric strain versus axial strain 290
(σ_3' = 50 kPa)

Figure A27 Deviatoric stress versus axial strain 291
(σ_3' = 100 kPa)

Figure A28 Volumetric strain versus axial strain (σ_3' = 100 kPa) 291

Figure A29 Deviatoric stress versus axial strain (σ_3' = 300 kPa) 292

Figure A30 Volumetric strain versus axial strain (σ_3' = 300 kPa) 292

Figure A31 Deviatoric stress versus axial strain (σ_3' = 450 kPa) 293

Figure A32 Volumetric strain versus axial strain (σ_3' = 450 kPa) 293

Figure A33 Deviatoric stress versus axial strain (σ_3' = 600 kPa) 294

Figure A34 Volumetric strain versus axial strain (σ_3' = 600 kPa) 294

Figure A35 Deviatoric stress versus axial strain (σ_3' = 750 kPa) 295

Figure A36 Volumetric strain versus axial strain (σ_3' = 750 kPa) 295

Figure A37 Deviatoric stress versus axial strain Stress Path 1 (σ_3' = 1300 kPa), Specimen S3 296

Figure A38 Volumetric strain versus axial strain Stress Path 1 (σ_3' = 1300 kPa), Specimen S3 296

Figure A39 Deviatoric stress versus axial strain Stress Path 1 (σ_3' = 480 kPa), Specimen S4 297

Figure A40 Volumetric strain versus axial strain Stress Path 1 (σ_3' = 480 kPa), Specimen S4 297

Figure A41 Deviatoric stress versus axial strain Stress Path 1 (σ_3' = 970 kPa), Specimen S5 298

Figure A42 Volumetric strain versus axial strain Stress Path 1 (σ_3' = 970 kPa), Specimen S5 298

Figure A43 Deviatoric stress versus axial strain Stress Path 1 (σ_3' = 2030 kPa), Specimen S6 299

Figure A44 Volumetric strain versus axial strain Stress Path 1 (σ_3' = 2030 kPa), Specimen S6 299

Figure A45 Deviatoric stress versus axial strain Stress Path 1 (σ_3' = 240 kPa), Specimen S7 300

Figure A46 Volumetric strain versus axial strain Stress Path 1 (σ_3' = 240 kPa), Specimen S7 300

Figure A47 Deviatoric stress versus axial strain Stress Path 1 (σ_3' = 1970 kPa), Specimen S8 301

Figure A48 Volumetric strain versus axial strain Stress Path 1 (σ_3' = 1970 kPa), Specimen S8 301

Figure A49 Deviatoric stress versus axial strain Stress Path 1 (σ_3' = 2960 kPa), Specimen S10 302

Figure A50 Volumetric strain versus axial strain Stress Path 1 (σ_3' = 2960 kPa), Specimen S10 302

Figure A51 Deviatoric stress versus axial strain Stress Path 2 (Initial σ_3' = 3000 kPa), Specimen S19 303

Figure A52 Volumetric strain versus axial strain Stress Path 2 (Initial σ_3' = 3000 kPa), Specimen S19 303

Figure A53 Deviatoric stress versus axial strain Stress Path 2 (Initial σ_3' = 890 kPa), Specimen S20 304

Figure A54 Volumetric strain versus axial strain Stress Path 2 (Initial σ_3' = 890 kPa), Specimen S20 304

Figure A55 Deviatoric stress versus axial strain Stress Path 2 (Initial σ_3' = 1950 kPa), Specimen S21 305

Figure A56 Volumetric strain versus axial strain Stress Path 2 (Initial σ_3' = 1950 kPa), Specimen S21 305

Figure A57 Deviatoric stress versus axial strain Stress Path 2 (Initial σ_3' = 570 kPa), Specimen S22 306

Figure A58 Volumetric strain versus axial strain Stress Path 2 (Initial σ_3' = 570 kPa), Specimen S22 306

Figure A59 Deviatoric stress versus axial strain Stress Path 2 (Initial σ_3' = 1390 kPa), Specimen S23 307

Figure A60 Volumetric strain versus axial strain 307
Stress Path 2 (Initial σ_3' = 1390 kPa), Specimen S23

Figure B1 Comparison of simulated vertical strain and the field survey at elevation 280.5 in well AGE2 309

Figure B2 Comparison of simulated vertical strain and the field survey at elevation 283.5 in well AGE2 309

Figure B3 Comparison of simulated vertical strain and the field survey at elevation 286.5 in well AGE2 310

Figure B4 Comparison of simulated vertical strain and the field survey at elevation 289.5 in well AGE2 310

Figure B5 Comparison of simulated vertical strain and the field survey at elevation 270.6 in well AGE3 311

Figure B6 Comparison of simulated vertical strain and the field survey at elevation 275.6 in well AGE3 311

Figure B7 Comparison of simulated vertical strain and the field survey at elevation 280.6 in well AGE3 312

Figure B8 Comparison of simulated vertical strain and the field survey at elevation 285.6 in well AGE3 312

Figure B9 Comparison of simulated vertical strain and the field survey at elevation 290.6 in well AGE3 313

Figure B10 Comparison of simulated vertical strain and the field survey at elevation 295.6 in well AGE3 313

Figure B11 Comparison of simulated vertical strain and the field survey at elevation 271 in well AGE4 314

Figure B12 Comparison of simulated vertical strain and the field survey at elevation 276 in well AGE4 314

Figure B13 Comparison of simulated vertical strain and the field survey at elevation 281 in well AGE4 315

Figure B14 Comparison of simulated vertical strain and the field survey at elevation 286 in well AGE4 315

Figure B15 Comparison of simulated vertical strain and the field survey at elevation 291 in well AGE4 316

Figure B16 Comparison of simulated horizontal displacement and the field survey at 375 days in well AGI1 316

Figure B17 Comparison of simulated horizontal displacement and the field survey at 550 days in well AGI1 317

Figure B18 Comparison of simulated horizontal displacement and the field survey at 679 days in well AGI1 317

Figure B19 Comparison of simulated horizontal displacement and the field survey at 375 days in well AT1 318

Figure B20 Comparison of simulated horizontal displacement and the field survey at 550 days in well AT1 318

Figure B21 Comparison of simulated horizontal displacement and the field survey at 679 days in well AT1 319

Figure B22 Comparison of simulated horizontal displacement and the field survey at 375 days in well AGI2 319

Figure B23 Comparison of simulated horizontal displacement and the field survey at 550 days in well AGI2 320

Figure B24 Comparison of simulated horizontal displacement and the field survey at 679 days in well AGI2 320

Figure B25 Comparison of simulated horizontal displacement and the field survey at 375 days in well AT7 321

Figure B26 Comparison of simulated horizontal displacement and the field survey at 550 days in well AT7 321

Figure B27 Comparison of simulated horizontal displacement and the field survey at 679 days in well AT7 322

Figure B28 Comparison of simulated horizontal displacement and the field survey at 375 days in well AGI3 322

Figure B29 Comparison of simulated horizontal displacement and the field survey at 550 days in well AGI3 323

Figure B30 Comparison of simulated horizontal displacement and the field survey at 679 days in well AGI3 323

LIST OF SYMBOLS

a_v	specific internal surface area of the medium (ratio of exposed surface area to solid volume)
a, b	constants determined by experiment
A, B	pore pressure parameters
B	constant in Equation (6-10)
B_T	parameter relating thermally generated pore pressure with undrained temperature change
c_b	rock compressibility
C	shape factor in Kozeny-Carman equation
C_{nl}	constant in equation (6-8)
C_c	isotropic compressibility
C_u	undrained isotropic compressibility
C_b	bulk compressibility
C_{cb}	constrained bulk compressibility
C_R	rock compressibility
C_s	solid compressibility
C_ϕ	pore compressibility
C_s	heat capacity of rock
D_s	mean size of solid particles
d	uniform diameter of spherical particles
e	void ratio
E	Young's modulus
F	free surface energy per unit interfacial area
g	acceleration due to gravity
h	steam chamber height
H	specific enthalpy
I	identity tensor (dimensionless)
I_D	relative density
k	(modified) permeability

k_0	initial absolute permeability
k_{ew}	effective permeability to water
k_{ew0}	initial effective permeability to water
k_h	thermal conductivity of reservoir material
k_{rw}, k_{ro}, k_{rg}	relative permeability of water, oil, and water
$[k]$	permeability tensor
K	bulk modulus; thermal conductivity
K_0	ratio of horizontal to vertical effective stresses
L	length of horizontal well
m	dimensionless parameter
m_v	volumetric compressibility
n	exponent in equation (6-12)
p_c	capillary pressure
p'	mean effective stress
Δp	pore pressure change or pressure difference between the bubble ends
p_i	initial reservoir pressure
p_{inj}	steam injection pressure
P_a	atmospheric pressure
q	oil flow rate
q, q'	deviatoric stress
q_ν, q_w, q_h	rate of injection or production of component ν, water, and enthalpy
r_1	bubble radius within pore space
r_2	bubble radius within pore throat
S	specific volume; specific surface area; saturation
S_{wi}	initial water saturation
S_α	phase saturation
ΔS_o	oil saturation change
S_0	particle surface area per unit solid volume
S_o, S_g, S_w	oil, gas, and water saturation

t	Time
T	Temperature
T_H	enthalpy transmissibility = $T_wH_w+T_oH_o+T_gH_g$
T_w, T_o, T_g	transmissibility of water, oil and gas
∇T	temperature gradient
u	displacement (vector)
U	specific internal energy
V	Volume
V_b	bulk volume
x_v	mole fraction of component v in liquid phase
y_v	mole fraction of component v in vapor phase
y_w	mole fraction of water in vapor phase
α	coefficient of volumetric thermal expansion; thermal diffusivity; Biot's constant for a porous media (dimensionless)
α_s	thermal expansion coefficient of solids
β	coefficient of linear thermal expansion
β_s	solid grain thermal expansion coefficient
β_T	linear thermal expansion coefficient of the medium
β_u	undrained thermal expansion coefficient
β_{DR}	drained thermal expansion coefficient
γ_p	plastic shear strain
ε_v	volumetric strain
ε^e, ε^p, ε^T	elastic, plastic, and thermal volumetric strain
λ_o, λ_g, λ_w	phase mobility = kk_r/μ
μ	viscosity
ν	poisson's ratio
ν_o	kinematic viscosity of oil
ν_s	kinematic viscosity of oil at steam temperature in Equation (2-1)
ρ_o, ρ_g, ρ_w, ρ_s, ρ_m	density of oil, gas, water, solid, and mass, respectively

ρ_a	Phase density in Equation (3-1)
Σ	two-fluid interfacial area per unit pore volume
σ_{12}	interfacial tension; total stress
σ_t, σ	total stress
σ'	effective stress
σ_1', σ_3'	major and minor principal effective stress
σ_h'	horizontal effective stress
σ_v'	vertical effective stress
σ_m'	mean effective stress
$\Delta\sigma'$	effective stress change
σ_{ij}	components of stress tensor
$\Delta\sigma_1$	changes in the major principal total stresses
$\Delta\sigma_3$	changes in the minor principal total stresses
τ	tortuosity
ϕ	porosity; friction angle
ϕ_0	initial fractional porosity
ϕ'	friction angle based on effective stress
ϕ_p	peak friction angle
ϕ_r	post-peak friction angle
ϕ_w	water porosity
$\nabla\Phi_o, \nabla\Phi_g, \nabla\Phi_w$	oil, gas, water phase potential gradient
ψ'	dilation angle based on effective stress
ψ_p	peak dilation angle
ψ_r	post-peak dilation angle

CHAPTER 1 INTRODUCTION

1.1 Oil Sand Reserves in Canada

Canada has vast oil sand resources. The total volume of oil sand resource is $259{,}200\times10^6$ m^3, which is distributed in three major areas in Alberta: Athabasca ($206{,}740\times10^6$ m^3), Cold Lake ($31{,}947\times10^6$ m^3), and Peace River ($20{,}518\times10^6$ m^3) (Figure 1-1 and Table 1-1) (AEUB, 2002). The Athabasca oil sands deposit, located in northeastern Alberta, is the largest of Alberta's oil sands deposits and is one of the world's largest and best known resources of bitumen. It covers some 46,800 km^2. The bitumen is located primarily in the Lower Cretaceous McMurray Formation. These sands have an average thickness of 38 m. In the southwest regions of the deposit it reaches depths of up to 750 m (AOSTRA, 1990).

The total ultimate potential reserve (recoverable) is $50{,}000\times10^6$ m^3, in which $39{,}000\times10^6$ m^3 is suitable for in situ recovery methods and nearly $11{,}000\times10^6$ m^3 are expected to be recovered by surface mining technology (AEUB, 2002). The initial established reserves are $28{,}330\times10^6$ m^3 and up to December 31 of 2001, only two per cent of the initial established crude bitumen reserves had been produced (560×10^6 m^3). Consequently, the total in situ and mineable remaining established reserves are $27{,}700\times10^6$ m^3, in which 77% is expected to be recovered by in situ technologies (Table 1-2).

1.2 Recovery Technologies

It is well known that two categories of recovery technologies for oil sand reserves exist. One is surface mining and the other is in situ recovery. Roughly 10% of the oil sand deposit, which has less than 45 m of overburden, may be recovered using surface mining methods. The well-known Suncor and Syncrude operations, which are located on the Athabasca River approximately 30 km north of Fort McMurray, utilize surface mining methods. Surface mining technology has potentially serious environmental problems and is inconceivable in deep deposits or in formations with a too high overburden/thickness ratio. Therefore, in situ recovery technology is important for deeper deposits. Presently, in situ development technologies mainly include hot-water injection, in-situ combustion (ISC), vapor extraction (VAPEX), cyclic steam stimulation (CSS), steam flooding, and steam assisted gravity drainage (SAGD).

Hot water lowers its temperature so rapidly that it is insufficient to mobilize the bitumen in oil sand reservoirs. In-situ combustion involves air injection into the reservoir. After ignition, a heat wave propagates within the formation due to the combustion of part of the in-place oil with oxygen of the injected air (Wilson et al., 1963). It includes forward combustion, fire-water flooding, and reverse combustion. A cold oil bank occurs ahead of the combustion zone for forward combustion. For reverse combustion, fracturing of the formation is necessary to attain an adequate air injectivity. Also, the risk of spontaneous ignition near the injection well exists. Overall, the in situ combustion process is difficult to manage (Chilingarian and Yen, 1978). In addition, an unconventional ISC process, THAI - Toe to Heel Air Injection, has been studied extensively over the past 10 years by the Improved Oil Recovery (IOR) group at the University of Bath. THAI is an integrated horizontal well process for in situ recovery and upgrading of heavy oil and bitumen. It uses a vertical injection well and a horizontal production well in a direct line drive or staggered line drive configuration. The injection well is placed at the top of the oil layer, and the horizontal production well at the bottom. Oil which is cracked and displaced ahead of the combustion front flows into the horizontal production well. However, the answer to the question: "Why does oxygen breakthrough into the toe of the horizontal well not occur?" has not been fully developed (Xia et al., 2003).

In the vapor extraction (VAPEX) process, hydrocarbon (low molecular weight) vapors at a pressure close to their dew points are injected into the reservoir using a horizontal injection well (Butler and Mokrys, 1991). Hydrocarbon vapor dissolves in the bitumen or heavy oil and reduces the viscosity; the diluted oil drains by gravity to a horizontal production well. If the injection pressure is close to the vapor pressure of the hydrocarbon at the operating temperature, de-asphalting can take place and this can cause additional reduction in viscosity (Singhal et al., 1996).

Cyclic steam stimulation (CSS) involves steam injection into a well for a limited period of time, followed by a shut-in period (soak time) and by production of the same well until a new injection phase is initiated. In another words, successive cycles are necessary to heat the reservoir that is more and more remote from the production well. For this near-well bore stimulation mechanism, the effect of subsequent cycles deteriorates as the reservoir pressure (or other driving mechanism) becomes dissipated (Butler, 1997). The CSS process is fast to recoup capital investment, but its oil recovery is low (in general, recovery < 25%). Steam flooding involves a pattern distribution of separate injection and production wells. It is effective for certain heavy oil reservoirs, but it is not suitable for very viscous bitumen in oil sand reservoirs (oil viscosity must be less than 5000 cp) (Li et al., 2002).

The steam assisted gravity drainage (SAGD) process has become the most promising technology for the development of oil sand reserves. The SAGD concept will be discussed in detail below. It has been proven in the field and its oil recovery can be as high as 60-70% and steam oil ratio (SOR) as low as 2.5 (Komery et al., 1995).

1.3 Concept of the SAGD Process

The steam assisted gravity drainage (SAGD) process was introduced by Butler and his former colleagues at Imperial Oil in early 1980s (Butler, 1980; Butler et al., 1981; Butler and Stephens, 1981). Conventional SAGD consists of two horizontal wells, which are approximately five meters apart in vertical direction. The upper well is a steam injector and the lower well is a producer. In the SAGD process, the injected steam moves upward and sideways due to the lower density of steam. Gradually, it forms a steam-saturated zone known as the steam chamber. The movement of oil to the producer is caused by gravity force and it flows parallel to the surface of the steam chamber (Figure 1-2). The upwardly moving interface, the ceiling of the steam chamber, tends to be in the form of steam fingers with oil flowing between them in a meandering or rather erratic manner (Butler, 1987). In contrast, the lateral interface moves sideways and downwards in a very stable manner because it is stabilized by gravity. The nature of the process is such that there is a systematic heating and displacement of the cold oil by the steam and the oil remains hot as it flows to the lower production well. At later stages in the process, the steam chamber will reach the top of the reservoir and spread sideways beneath the overburden, as shown in Figure 1-2 (Butler, 1994).

The SAGD process is a combined conduction-convection mechanism more similar to ablation than displacement. Cold bitumen cannot be displaced at any practical rate, and fills the pore space so completely that it also prevents entry of steam or other hot fluids into the sand matrix. However, when a steam zone is established, SAGD will cause it to rise and spread through the sand. Conduction heats a thin layer of oil sand adjacent to the steam chamber, mobilizing the bitumen. The difference in density between steam and bitumen causes the latter to drain to the bottom of the chamber, along with the steam condensate. The steam gains access to new unheated surfaces in the formation as the bitumen drains, and so the front advances upward and outward. This process will continue as long as more steam is available, and as long as the draining bitumen and condensate are removed from the bottom of the chamber (Edmunds et al., 1991).

1.4 Geomechanics Related to SAGD

The SAGD process described above results in a complex interaction of geomechanics and multiphase thermal flow in uncemented oil sand material. The geomechanical response of an oil sand reservoir to fluid pressure change and temperature change induces variations of in situ stress and strain. Temperature increases cause thermal expansion of sand grains, pore fluids, and reservoir matrix, which results in an increase of total stress. Pore pressure increase due to steam injection lowers the effective confining stress. Based on these temperature and pore pressure variations, three geomechanical processes occur in the reservoir. The first one is isotropic unloading due to the decrease of effective stress. The second one is shear dilation when the stress variations are anisotropic and the failure criteria of reservoir material is satisfied. The third one is compaction. These geomechanical behaviors affect reservoir parameters and processes, such as absolute permeability, relative permeability, porosity, pore pressure transmission, and gas evolution.

1.5 Necessity of Coupled Reservoir Geomechanical Simulations

SAGD production performance is predicted by numerical simulation. Its reasonable prediction is an integral component in the design and management of a SAGD project. Most reservoir models used in simulating the steam assisted gravity drainage process do not account for the geomechanical responses described above. However, a series of reservoir parameters and processes which affect the SAGD performance are directly affected by the geomechanical behavior of the reservoir.

Firstly, conventional reservoir simulation emphasizes multiphase flow in the porous media but generally does not take the interactions between fluid and solid into account. It applies elastic rock compressibility to characterize the coupling mechanism of multiphase flow and rock skeleton. The assumption of this treatment is that the boundary loads and temperature are constant, $\Delta p = \Delta\sigma'$ (Dusseault, 1999). All analytical flow equations in petroleum engineering are based on this assumption. It is clear that the recovery process of conventional oil from cemented sandstones can roughly satisfy this assumption. For the SAGD process, however, volumetric deformations within the reservoir due to pore pressure and temperature changes result in variations of both in situ stress and strain. These stress and strain variations are functions of the in situ boundary conditions. Due to deformations in response to in situ heating, the total stresses in the vertical and horizontal directions may also vary. Under these conditions, the assumption used in conventional reservoir simulation is no longer validated.

Secondly, field measurements during SAGD operations of the UTF Phase A project showed that both vertical displacement and horizontal displacement were induced in the reservoir. Within an instrumented cross-section of the reservoir, a maximum vertical extensional strain of 2.5% and a horizontal extensional strain of -0.3% were measured. Based on full strain field analyses, a maximum shear strain of 3.0% and a volumetric strain of 2.6% were predicted to have occurred between two horizontal well pairs. Based on an empirical correlation linking absolute permeability change to volumetric strains, the absolute permeability within this region was predicted to have increased approximately 30%, increasing from 7.5 darcies to 9.8 darcies (Chalaturnyk, 1996).

Thirdly, experimental results also support the geomechanical processes occurring under SAGD conditions. Based on reconstituted Athabasca oil sands specimens, Scott et al. (1991) obtained increases in absolute permeability of approximately 30% and 70% by unloading from initial effective confining stresses of 1000 kPa and 4360 kPa, respectively. They also obtained a 30% increase of permeability for an increase in volume of 3% during shear. Effective permeability to water can increase by three orders of magnitude as a result of a 17% increase in pore volume or a 6% increase in total volume brought about by shear dilation. Wong et al. (1991) indicated that during triaxial compression, a 50-fold increase in effective permeability to water was measured when the specimen volume had increased by 1%. Oldakowski (1994) and Touhidi-Baghini (1998) also indicated the influence of volumetric strains for several test types on permeability and effective permeability to water.

Fourthly, oil recovery from the SAGD process is sensitive to reservoir porosity. However, the porosity variation due to geomechanical behavior occurring in the SAGD process is not taken into account in the conventional reservoir simulation. Porosity variation can influence a number of reservoir parameters and processes. For example, a number of reservoir parameters, such as pore pressure transmission, gas evolution, permeability, relative permeability, compressibility, capillary pressure, and thermal expansion effect, are all related to reservoir porosity.

Finally, current gas-over-bitumen debate has involved the discussions of the effect of gas pool depressurization on the SAGD production performance (Bachu et al., 2002). Gas pool depressurization increases the effective stress within the gas pool that may initiate the process of consolidation in the overburden. This may result in significant horizontal movements if the surrounding formation is unable to provide restraint.

So, it is necessary to apply coupled reservoir geomechanical simulations, rather than the conventional reservoir simulation, to predict the SAGD production performance.

1.6 Objective, Scope, and Methodology

The objective of this research is to quantify the effect of geomechanical behavior on the oil recovery by the SAGD process. This research objective will be achieved through seven interrelated phases: (1) analyze the decoupled simulation results; (2) clarify the issues with the coupled reservoir geomechanical simulations of the SAGD process; (3) develop a methodology of sequentially coupled reservoir geomechanical simulations; (4) investigate the permeability change due to SAGD; (5) establish a representative geomechanical model of oil sands; (6) verify the methodology by history matching the UTF Phase A Project; and (7) apply the methodology to simulate the SAGD production performance of a reservoir model with gas over bitumen geometry.

This research program involves the analyses of lab testing results obtained by previous researchers. No lab testing was conducted in the process of this research.

The methodology of sequentially coupled reservoir geomechanical simulations will be developed based on two commercial simulators. One is the reservoir simulator, EXOTHERM, developed by T.T. & Associates Inc, and the other is the geomechanical simulator, FLAC, developed by Itasca Consulting Group Inc (2000). The properties of oil sands material obtained in this research will be incorporated into the developed simulation technology.

The results of this research are expected to improve the prediction of SAGD production performance and provide reasonable evaluations for candidate reservoirs.

1.7 Organization of Thesis

Chapter 2 summarizes the research work on the development of the SAGD process and the coupled reservoir geomechanical simulations based on previous publications. The concept of coupling between fluid flow and solid deformation and the methodology of coupled reservoir geomechanical simulations in both the conventional oil recovery and the thermal recovery are also discussed.

Chapter 3 presents the decoupled reservoir geomechanical simulation results. It mainly shows the effect of geomechanical behavior on the reservoir parameters (such as permeability). However, geomechanical effects on the SAGD production performance were not studied in this chapter.

Chapter 4 introduces the concept of geomechanical zones surrounding the steam chamber and their specific geomechanical responses relative to the SAGD process. It also discusses a number of reservoir processes and parameters affected by geomechanics due to SAGD, including pore pressure transmission and fluid flow, gas evolution from the bitumen, variations of compressibility, porosity, absolute permeability, relative permeability, and phase saturations. Other issues, such as thermal expansion, heat transfer, and capillary pressure change, are also included.

Chapter 5 is the development of the sequentially coupled reservoir geomechanical simulation methodology and verification analyses of the methodology.

Chapter 6 compares the permeability variation characteristics due to isotropic unloading process and the shearing process occurring in SAGD.

Chapter 7 establishes an appropriate geomechanical model for oil sands material based on lab testing results and corresponding numerical experiments that verify the model parameters.

Chapter 8 verifies the coupled reservoir geomechanical simulation methodology based on the history match of the UTF Phase A SAGD project.

Chapter 9 is the application of the coupled reservoir geomechanical simulation methodology to a gas-over-bitumen geometry and presents the effect of geomechanical effect on the SAGD production performance.

Chapter 10 summarizes the conclusions obtained in the previous chapters and provides a set of recommendations and suggestions for further research in this field.

Table 1-1 Initial in-place volumes of crude bitumen

(AEUB, 2002)

Oil sands area Oil sands deposit	Initial volume in place (10^6 m^3)	Area (10^6ha)	Average pay thickness (m)	Average bitumen saturation Mass (%)	Average bitumen saturation Pore volume (%)	Average porosity (%)
Athabasca						
Grand Rapids	8 678	689	7.2	6.3	56	30
Wabiskaw-McMurray (mineable)	17 998	286	30.5	9.7	69	30
Wabiskaw-McMurray (in situ)	119 234	4 329	19.0	7.9	62	28
Nisku	10 330	499	8.0	5.7	63	21
Grosmont	50 500	4 167	10.4	4.7	68	16
Subtotal	206 740					
Cold Lake						
Grand Rapids	17 304	1 709	5.8	9.5	61	31
Clearwater	11 051	589	15.0	8.9	64	30
Wabiskaw-McMurray	3 592	658	5.8	6.3	54	26
Subtotal	31 947					
Peace River						
Bluesky-Gething	9 926	1 254	8.7	6.4	60	23
Belloy	282	26	8.0	7.8	64	27
Debolt	7 800	328	22.5	5.3	65	19
Shunda	2 510	143	14.0	5.3	52	23
Subtotal	20 518					
Total	259 205					

Table 1-2 In-place volumes and established reserves of crude bitumen (10^6 m^3)

(AEUB, 2002)

Recovery method	Initial volume in-place	Initial established reserves	Cumulative production	Remaining established reserves	Remaining established reserves under active development
Mineable	18 000	5 590	400	5 200	1 350
In situ	241 200	22 740	170	22 570	490
Total	259 200	28 330	560	27 770	1 830

Note: Differences are due to rounding.

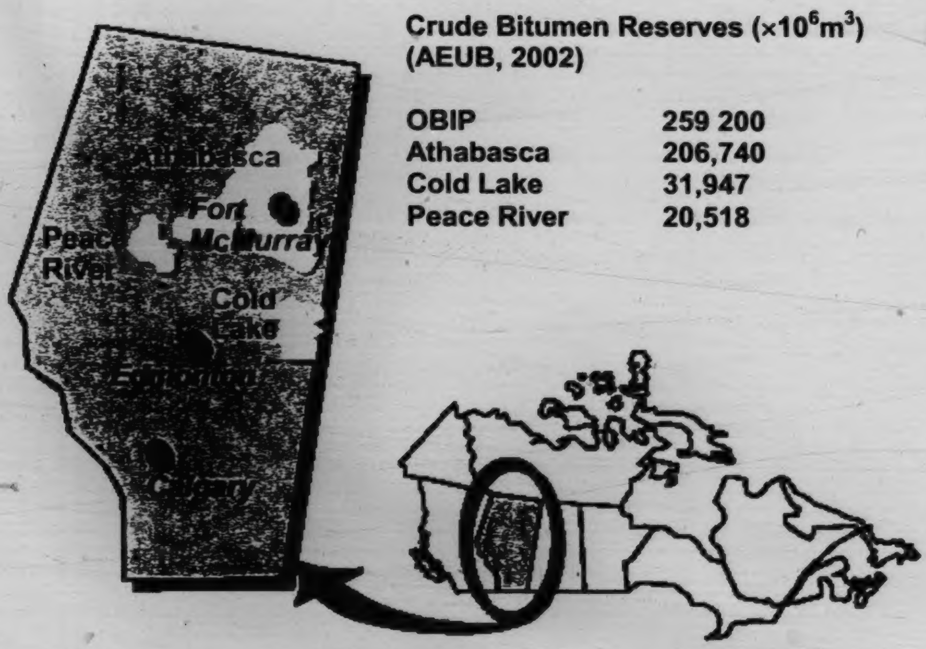
Athabasca
Fort McMurray
Peace River
Cold Lake
Edmonton
Calgary

Crude Bitumen Reserves ($\times 10^6 m^3$)
(AEUB, 2002)

OBIP	259 200
Athabasca	206,740
Cold Lake	31,947
Peace River	20,518

Figure 1-1 Oil sand reserves in Alberta, Canada (Modified after AEUB, 2002)

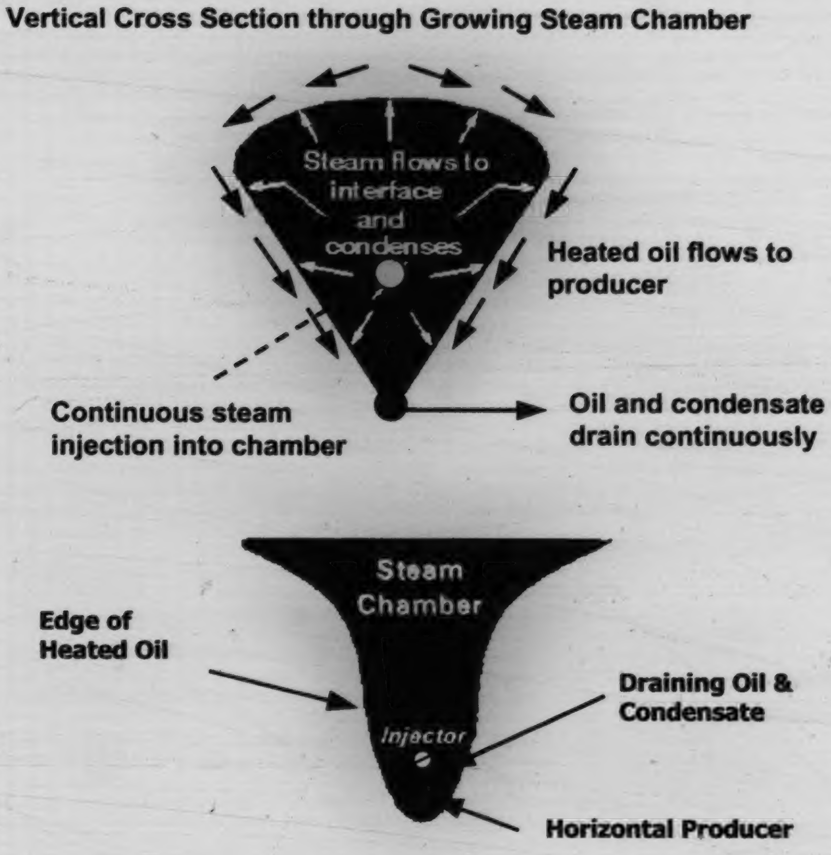
Vertical Cross Section through Growing Steam Chamber
Steam flows to interface and condenses
Heated oil flows to producer
Continuous steam injection into chamber
Oil and condensate drain continuously
Steam Chamber
Edge of Heated Oil
Draining Oil & Condensate
Injector
Horizontal Producer

Figure 1-2 SAGD concept (Modified after Butler, 1980)

CHAPTER 2 DEVELOPMENT OF THE SAGD PROCESS AND THE RESERVOIR GEOMECHANICAL SIMULATION

2.1 Development of the SAGD Process

2.1.1 Background

Of the major oil sands deposits in Alberta, Athabasca is the largest. About 10 percent of the reserves lie in an area with less than 50 m of overburden and surface mining technology is a viable technique to develop these reserves. Away from the mineable area, the oil sands are progressively more deeply buried. Oil sands deposits in these areas, together with that in Cold Lake area and Peace River area, are too deep to develop by surface mining technology. So, appropriate in situ recovery technologies must be sought in order to develop these vast oil resources. The brief history of the in situ recovery development technology is summarized below based on AOSTRA (1990).

A wide variety of in situ recovery methods have been investigated, starting with the first steam test by the bituminous Sand Extraction Co. Limited in 1926. Since that time, a number of field pilots have been conducted based on different recovery technologies (AOSTRA, 1990). From 1957 to 1962, Shell Canada Resources Ltd. attempted to recover bitumen from a shallow Athabasca oil sands deposit at their Muskeg River Pilot. They applied hydraulic fracturing near the base of the deposit using caustic solution followed by steam from the injection wells. The problem is that repeated production well stimulations with hot caustic and steam were required to maintain the output of bitumen, which adversely affected the economics of the operation.

From 1957 to 1976, Amoco Canada Petroleum Company Ltd. conducted experiments and field trials of the COFCAW (combination of forward combustion and water) process at Gregoire Lake in the Athabasca. Over the period 1963 to 1965, Atlantic Richfield tested fracture assisted steam drive to recover bitumen from the deeply buried Athabasca deposits at their Pony Creek Pilot. This test was not successful due to very limited production yields. In the same 1963 to 1965 period, Mobil Oil Canada conducted an inverted nine-spot combustion test in a propped horizontal fracture. It terminated due to well damage and corrosion of surface facilities.

From 1966 to 1969, Fina Oil Company also applied fracture assisted steam drive process based on five-spot pattern and encountered problems in maintaining communication paths as the injection of steam commenced. In 1969, Suncor conducted a small inverted five-spot pattern combustion pilot in a shallow oil sand deposit. During the period 1973 to 1985, Texaco Exploration Co. Ltd. operated a series of three pilots at their Fort McMurray lease. The first pilot was a nine-spot well pattern with central injection. The second pilot was a seven-spot with central and peripheral steam injection. The second pilot attained a total recovery of 50 percent of the oil-in-place, which was better than the first pilot because of good communication throughout the pattern. The third pilot consisted of parallel horizontal wells drilled near the base of the McMurray deposit.

From 1977 to 1981, Gregorie Lake Block I project was conducted based on the COFCAW process by Amoco with AOSTRA, Shell, Suncor, and Petro-Canada as partners. It was proven that the COFCAW process was not viable in this project. Over the period 1979 to 1983, the Stony Mountain pilot was conducted based on electrical heating approach followed by steamflooding. This project was tested by Petro-Canada with partners Cities Service, Esso Resources, and Japan Canada. The production was disappointing.

The largest and most successful in situ pilot in the Athabasca deposit is located at Kearl Lake. The project was operated by Canterra Energy (now Husky) with Tenneco (now Esso) and AOSTRA as partners involving the use of a modified steamflood. The recovery process, which consists of developing horizontal fractures to establish interwell communication, steamflooding from a central injection well, and steam stimulating production wells to obtain and maintain production, was initially tested in 1981. Inverted seven-spot, inverted-nine spot, and five-spot well patterns were tested sequentially.

The recovery procedure used in the Cold Lake area for commercial production is cyclic steaming or the "huff and puff" method. The ultimate recovery of oil in place using this method in the best parts of the Clearwater formation is about 20 percent.

The Peace River oil sands deposit, located in the northwestern region of Alberta, has an important feature, which is the extensive area of thick rich oil sands, underlain by a thin water-sand layer. This water layer permits very effective steam injection without fracturing the reservoir. Thus, the zone at the base of the reservoir is heated and overlying bitumen mobilized. Based on this specific feature, pressure cycle steam drive process was applied in PRISP (Peace River In Situ Pilot) operated by Shell and AOSTRA. The pressure cycle steam drive has several steps. Initially each well undergoes cyclic stimulation in special sequences to create hot communication paths between wells, and to create tar banks surrounding the project to prevent the influx of cold water from the water-sand outside the project boundary. Continuous steam injection is then begun with the injection and production rates so controlled as to alternately pressure-up and blow-down the reservoir. The PRISP pilot has particularly excelled in recovery efficiency, already achieving close to the expected recovery of 55 percent of the oil-in-place. From the success of the PRISP pilot, Shell proceeded directly into commercial operations with the PREP (Peace River Expansion Project) facility, which began operations in 1986. The performance of PREP has obtained good response and followed predictions very well.

Although a large number of in situ pilot tests and research have been conducted in the last 60 years since the first steam test, the key to unlock the Alberta oil sands reserves is still under investigation. The invention of the steam assisted gravity drainage (SAGD) process by Butler (1980) may be that key based on the number of pilots and commercial projects with this technology.

2.1.2 Theoretical Development of the SAGD Process

A great number of in situ pilot tests discussed in §2.1.1 indicated that in situ recovery of oil sands reserves is basically dependent upon the reduction of viscosity. The steam injection technology, including cyclic steam stimulation and steam drive, is effective to reduce the viscosity of bitumen. However, both approaches may have some inherent difficulties that limit displacement efficiency. First, the fluid flow is relatively rapid and can break up the oil phase into droplets, leaving a significant amount behind. Secondly, oil and other fluids flow simultaneously through the same section of the bed, thereby reducing the oil relative permeability (Butler et al., 1981).

Although the cyclic steam stimulation has a fast return on investment, it only obtains 15 to 20 percent of oil recovery (AOSTRA, 1990), which is not efficient. The steam drive process has problems in that the steam and condensed water are much less viscous than the oil and hence fingering and poor sweep efficiency can occur (Butler et al., 1981). In addition, the oil sands reservoir parameters cannot satisfy the screen criteria of the steam drive process (Farouq Ali and Meldau, 1979). The high viscosity of bitumen can significantly lower the recovery of the steam drive process (Li et al, 2002). Also, in order to obtain high heat efficiency, the steam drive process requires a lower steam injection pressure (less than 5 MPa) (Li et al., 2001). Because of the extremely high viscosity of bitumen, however, lower steam injection pressure may not even initiate the process.

The basic concept of the SAGD process has been described in Chapter 1. It can be looked upon as a special form of steamflooding, called reverse steam flooding, where horizontal wells are employed. The intention in developing SAGD was to devise a process whereby heavy oil/bitumen could be removed in a systematic manner in order to give a more complete recovery. By using gravity, which obviously is present throughout the reservoir, it is possible to avoid the steam overriding which occurs when viscous oil is flooded by a less viscous fluid. As such, it can overcome the drawbacks of the CSS process and the steam drive process (Butler et al., 1981).

A field pilot at Kearl Lake discussed in §2.1.1, which applied the steam drive process, provided interesting information about bitumen saturation change. When the project was terminated, it was found that the layers with reduced bitumen saturations were located at the top of the main oil sands that have created a steam override condition. Steam override at Athabasca has in the past been considered undesirable. The very good bitumen rates and steam-oil ratio performance at Kearl Lake, however, were a significant achievement and demonstrated that bitumen recovery with steam override may have commercial application at Athabasca (AOSTRA, 1990). It was not difficult to conclude following this pilot that the favorable production performance was due to the effect of gravity drainage.

The rate of flow was analyzed based on a group of assumptions, which are listed as follows. Heat transfer into the cold reservoir is by thermal conduction normal to the interface; temperature distribution ahead of the front corresponds to a steady state; the drainage in each element of the reservoir is parallel to the interface; effective permeability is constant; and oil viscosity depends upon the temperature of the element (Butler, 1994). The rate is calculated from Darcy's law, using the gravity gradient resolved along the angle of the interface, and the density difference between the flowing oil and the steam to determine the potential gradient. There is a coupling of the equations because the temperature distribution depends upon the front velocity, the oil flow depends upon the temperature distribution and the front velocity is determined from the oil flow gradient by means of a material balance. Based on these assumptions and mechanisms, the rate of drainage originally obtained (Butler et al., 1981) is expressed by Equation (2-1).

$$q = 2L\sqrt{\frac{2k_0 g\alpha\phi\Delta S_o h}{m\nu_s}} \tag{2-1}$$

This equation is dimensionally correct and any consistent set of units can be employed. Equation (2-1) shows that each of the variables under the square root sign is equally important. This equation tends to overestimate the drainage rate because it assumes that the temperature corresponds to steady state conditions everywhere along the interface. In practice, this is nearly true in the central part of the interface, but it cannot be true at the ends. TANDRAIN and LINDRAIN are two modifications to the original theory (Butler, 1981). TANDRAIN assumes that the lower parts of the interface curves can be replaced by tangents drawn from the wells to the curves. LINDRAIN assumes that the interface remains straight right up to the top of the reservoir and as the steam chamber grows in size, this straight interface becomes more inclined and longer. The LINDRAIN assumptions may give the most realistic answer. TANDRAIN and LINDRAIN change the factor 2 underneath the square root sign to 1.5 and 1.3, respectively. As a result, they reduce the predicted flow rate to about 87 percent and 80 percent, respectively, of that predicted by the original equation.

The detailed description of the theoretical issues on SAGD, such as the rising of steam chamber, finger rising phenomenon, effect of reservoir properties, can be found from Butler (1997).

2.1.3 Evolution of the SAGD Process

Conventional SAGD utilizes two parallel horizontal wells as shown in Figure 1-2. Initial heat communication between steam injector and oil/steam condensate producer is a significant operational challenge. To establish this communication, an injection well is above but close to the production well. The intervening bitumen can be mobilized by heating both wells and by applying a pressure difference between them. The vertical separation between the producer and injector should be defined based on reservoir properties and oil viscosities. The higher the oil viscosity is, the smaller the separation between the two horizontal wells (Butler, 1994).

Vertical steam injection wells have also been used. A possible advantage of such an arrangement is that a vertical injector is cheaper than a horizontal injector. Also, it may be practical to employ existing vertical wells instead of drilling new ones. In addition, it allows the point of steam injection to be raised as the project matures. When this is done, the pressure gradient required to move the steam to the interface tends to promote rather than restrict oil drainage. However, it also has the disadvantages that steam is not supplied along the length of the production well and some time is required for the steam chamber to grow transversely along the axis of the horizontal producer. Thus, the effective length of the production well, particularly in the early stages, may be less than its physical length. Many vertical injection wells are required to give the same performance as a single horizontal injector if a long horizontal production well is to be used.

Esso Resources first horizontal well pilot in the bitumen reservoir at Cold Lake was constructed in 1978. It has a single, near-horizontal producer with a vertical injection well located directly above it. The effective horizontal length of the producer is about 150 m. The reservoir is quite heterogeneous and contains numerous tight streaks and layers of varying permeability (Sawhney et al., 1995). Field production was significantly higher than that predicted with analytical simulations (Butler, 1994). This resulted from the fact that the well had been steamed for most of a year before the start of the SAGD operation. This preheating of reservoir would be expected to accelerate the growth of the chamber. A second horizontal well was drilled at Cold Lake by Esso in 1984. This well had a horizontal length of over 1000 m and was produced using vertical wells for steam injection. Over the period 1993 to 1994, Esso drilled four further horizontal wells at Cold Lake. These wells were placed underneath rows of existing cyclic steam stimulated wells that were intended to be used as steam injectors. The wells were each 500 m in horizontal length. Production performance results from these wells remain proprietary.

A field pilot with four vertical injectors and a horizontal producer was operated by Sceptre Resources in the Tangleflags field. The horizontal well had a length of 420 m placed at the bottom of the reservoir. The oil viscosity of the crude oil is about 6000 mPa.s. Very high production rates have been achieved and the project is encouraging. They also drilled a second horizontal well in this field, which has been operating since 1990. The performance is similar to that of the first well. So, with lower oil viscosity, this well configuration can obtain a good production response.

Based on theoretical calculations, Sawhney et al. (1995) found that it requires over seven years for five vertical injection wells to match the productivity of a single 500 m horizontal injection well at Cold Lake. They concluded that with long horizontal producers, it seems likely that horizontal injectors rather than vertical injectors will be more economical for the production of oil by SAGD.

In thinner reservoirs, it is nearly impossible to drill two vertically separated horizontals in order to conduct the conventional SAGD process. So, single well SAGD (SW-SAGD) was investigated, in which steam is injected from the toe of the horizontal well and oil produced at the heel of the well (Elliott and Kovscek, 1999). Not only is the SW-SAGD process advantageous over conventional SAGD in thinner reservoirs, but also provides a substantial cost saving associated with drilling one horizontal well rather than two.

The key to apply SW-SAGD is to heat the near-wellbore region rapidly and uniformly so as to reduce the oil viscosity and promote gravity drainage. This can be performed by steam circulation within the wellbore or cyclic steam stimulation (CSS) with the horizontal well. The CSS process is the most thermally efficient early-time heating method (Elliott and Kovscek, 2001).

Based on Falk et al. (1996), a roughly 850 m long well was installed in a region with 12 to 16 m of net pay to produce 12 °API gravity oil in the Cactus Lake Field, Alberta, Canada. The reservoir is clean and unconsolidated sands with the permeability of 3400 md. Before initiation of SW-SAGD, no attempts were made to preheat the reservoir. Steam was injected into the cold reservoir at the toe of the well and oil produced at the heel. Oil production response was slow and gradually increased to more than 100 m^3/d. The cumulative steam-oil ratio was between 1 and 1.5 for the roughly one-half year of reported data.

Another operating experience with nineteen SW-SAGD installations was reported by McCormack et al. (1997). Positive results were seen in fields with relatively high reservoir pressure, relatively low oil viscosity, significant primary production by heavy-oil solution gas drive, and/or insignificant bottom-water drive. Poor results were seen in fields with high initial oil viscosity, strong bottom-water drive, and/or sand production problems. They suspect that the production performance was a mixture of gravity drainage, increased primary recovery with near-wellbore heat conduction, and hot water induced drive/drainage.

Based on sensitivity studies, Elliott and Kovscek (2001) indicated that SW-SAGD is most applicable to heavy oils with initial viscosity of less than 10,000 mPa.s. Although SW-SAGD is advantageous over conventional SAGD in thinner reservoirs, they suggested that the reservoir be sufficiently thick to allow significant vertical steam chamber growth.

The Fast-SAGD process was proposed by Polikar et al. (2000). It is a combination of horizontal well cyclic steaming and conventional SAGD. When the conventional SAGD is started in operation, a set of equidistant horizontal wells are applied to accelerate the propagation of the steam chamber down to the bottom of the reservoir. These horizontal wells, the so-called offset wells, are parallel to but 50 m away from the producer of the SAGD well pair. Also, they are located at the base of the pay zone with the same length and depth as the SAGD producer. The offset wells will act as both injectors and producers for the CSS process during early period of SAGD operations.

As initially discussed by Butler (1981), the upward rate of growth of the steam chamber is faster than its lateral growth. Once the upward growth is constrained by the overburden, the lateral growth rate becomes faster. The Fast-SAGD process can accelerate the lateral growth of the steam chamber and the interface velocity toward the base of the reservoir. With the movement of the lateral interface, the offset wells begin the CSS process sequentially. If heat communication of the steam chamber and the heated zone due to the CSS operation are established, the offset wells are placed on production. Thus, the Fast-SAGD process not only saves the cost of drilling and completing more SAGD injectors, but reduces steam consumption as well.

The concept of steam and gas push (SAGP) process was proposed by Butler (1999). In the SAGD process, a fraction of non-condensable gas (typically methane) is injected together with steam so that the non-condensible gas accumulates in the steam chamber, particularly near the top of the reservoir. The concentration of the non-condensible gas is maintained intentionally at a level well over 90 mole percent. Its maintenance is achieved by addition of natural gas to the injected steam. The gas addition must be sufficient to supply the fill of steam chamber and production losses. Although a high concentration of non-condensible gas must be maintained near the top of the reservoir, its concentration in the combined injection stream should be quite small. The reason is that when the injected steam condenses, it leaves a higher concentration of non-condensible gas. "Molar concentration of non-condensible gas in the injection stream of the order of a few percent is adequate; in some cases even less is required" (Butler, 1999). Jiang et al. (2000) obtained similar conclusion. They indicated that the amount of gas required is usually in the order of less than one percent volume of the injected steam in the typical field conditions. Meanwhile, based on lab tests, it is reported that steam injection rate in SAGP is approximately 25% lower than SAGD to produce the same amount of oil. Compared to the conventional SAGD, the interface of SAGP is steeper, so SAGP reduces the heat loss to the overburden because of the small heated area and the lower temperature near the overburden. In addition, the total heat required is smaller because the average temperature of the steam chamber is lowered and water cut in the total production reduced.

In the SAGP process, the major heat transfer mechanism is thermal conduction (Butler et al., 2000). Heat transfer by diffusive steam flow and convection is significant in the region at the saturated steam temperature around the injection and production wells and becomes less important as temperature falls (Butler et al., 2000; Butler et al., 2001). SAGP has lower temperatures in the region where gas fingers rise and oil drains above the steam condensation zone. This is also a source of steam saving. Based on their test results, Butler et al. (2001) indicated that for both uniform and layered models, SAGP produced similar oil rates as SAGD but lower steam consumption.

Although derivations of the SAGD process exist, the fundamental principles are the same. In addition, most field applications are focused on the conventional SAGD process.

2.1.4 Current Applications of the SAGD Process

Based on Butler (2001), four advanced commercial SAGD projects are being operated in Athabasca area. Each of them is expected to have a recovery of more than 50 percent. These projects involve

- Alberta Energy Company (AEC) Foster Creek (T70 R4 W4M)
- PanCanadian Petroleum Christina Lake (T76 R6 W4M)
- Suncor Firebag (T95 R6 W4M)
- Petro-Canada MacKay River (T93 R12 W4M).

Two further large SAGD projects are under construction, i.e.

- CNRL Mic Mac (T96 R12 W4M)
- OPTI Canada Long Lake (T85 R6 W4M)

In addition, there are 17 SAGD pilots and smaller commercial operations from north to south. They are listed as follows.

- Northstar Dover (T93 R12 W4M)
- Shell Canada Peace River (T85 R18 W5M)
- Jacos Hangingstone (T84 R11 W4M)
- Gulf Canada Surmont (T83 R7 W4M)
- CNRL Burnt Lake (T67 R3 W4M)
- CNRL Wolf Lake (T66 R5 W4M)
- Blackrock Ventures Hilda Lake (T64 R3 W4M)
- Murphy Oil Lindbergh (T57 R5 W4M)
- Marathon Oil Canada Bolney (T52 R23 W3M)
- CNRL Tangleflags (T52 R25 W3M)
- Exxon Mobil Canada Celtic (T52 R23 W3M)
- Probe Exploration Kitscoty (T51 R02 W4M)
- Husky Energy Pikes Peak (T50 R24 W3M)
- Marathon Oil Canada Edam Sparky (T48 R19 W3M)
- PanCanadian Senlac East (T39 R26 W3M)

- Nexen Plover Lake (T35 R26 W3M)
- Gulf Canada Kerrobert (T32 R24 W3M)

Up to March 2006, totally 15 commercial SAGD projects have been operated in the field or approved by AEUB (AEUB, 2006). These projects are listed below.

- Encana Christina Lake (11 to 16, E17, 24-76W4M; 1, 2-20-76-6W4M; 1 to 4-21-76-6W4M; 1 to 4-22-76-6W4M; 1 to 4-23-76-6W4M)
- Encana Foster Creek (7 to 10, 15 to 22, 27 to 29, 32 to 34-70-3W4M; 7 to 10, 15 to 22, 27 to 29, 32 to 34-70-3W4M; 7 to 24, W27, 28 to 33, W34-70-4W4M; 10 to 15, 22 to 27-70-5W4M; 3 to 5-71-3W4M; 3 to 5, 8 to 10-71-4W4M)
- Petro-Canada Athabasca (32 to 34-92-12W4M; 8 to 16-9-93-12W4M; SW3, 4, 5, 8, 9, 16, 17, 20, 21-93-12W4M)
- Japan Canada Hangingstone (NW26, N27, N28, 33, 34, W35-84-11W4M)
- Suncor Firebag (19, 20, 29 to 32-94-5W4M; 22 to 36-94-6W4M; W25, 36-94-7W4M; 6 to 8, 17 to 20, 29 to 32-95-5W4M; 95-6W4M; 4 to 6-96-6W4M)
- Nexen Athabasca (NW29, NE30, SE31, W32-85-6W4M)
- Deer Creek Joslyn Creek (28, 29, 32, 33, 34-95-12W4M; 4, 5-96-12W4M)
- Petro-Canada Meadow Creek (NW84-8W4M; 6, 7, 13 to 36-84-9W4M; E1, E12, E13, E24, E25-84-10W4M; 2 to 5, E6, SE7, S8 to S10, 14, 23, 26, 35-85-9W4M)
- ConocoPhillips Athabasca (81-6W4M; 1, 2, 11 to 14, 23 to 29, 32 to 36-81-7W4M; NW 82-5W4M; 82-6W4M, 82-7W4M; SW 83-5W4M; 83-6W4M, 83-7W4M; 82-22W4M)
- Opti/Nexen Long Lake (W 85-6-W4M; 13, 24, 25, 36-85-7W4M; 5 to 8, 17-86-6W4M; 1, 11 to 14, 22 to 27, 34 to 36-86-7W4M; 2, 3, 10, 11-87-7W4M)

- Devon Jackfish (19 to 21, 28 to 33-75-6W4M; 4 to 6-76-6W4M)
- MEG Energy Christina Lake (7 to 9, 16 to 18, N19 to N21-77-5W4; E12, E13, E24-77-6W4)
- Husky (1 to 4, 10 to 13-96-5W4; 1 to 5, 7 to 30, 32 to 36-95-5W4; 1, 12, 13, 20 to 29, 32 to 35-94-5W4; 5 to 8, 17 to 21-94-6W4)
- Husky Tucker Lake (N21, 28, 29, 32-64-4W4M)
- BlackRock Cold Lake (N9, N10, 15 to 17-64-3W4)

For both the commercial SAGD projects and the SAGD pilots in the field, reservoir simulation is an integral component in the design and management of these projects.

2.2 Geotechnical Properties of Oil Sands

Dusseault and Morgenstern (1978) concluded that the oil sands had frictional shear strength in the order of 60° or greater which arose from the interlocked fabric of the sand. They called this class of materials locked sands (Dusseault and Morgenstern, 1979). Unconsolidated (or uncemented) sands can be divided into three categories, i.e., loose sands, dense sands, and locked sands. Locked sands are much different from the other two sands in geotechnical properties. It is dense but not limited to the characteristics of dense sands. Owing to the grain-to-grain contacts observed in locked oil sands (Figure 2-1), it shows the following characteristics: absence of cohesion, highly quartzose mineralogy, high strength, steeply curved failure envelopes, low porosities, lack of interstitial cement, brittle behavior, and exceptionally large dilation rates at failure (Chalaturnyk, 1996). These properties are the basis of large variations of reservoir parameters and processes in the SAGD process.

In addition, the geotechnical properties of oil sands have been studied extensively since 1970s (Dusseault, 1977; Agar, 1984; Kosar, 1989; Oldakowski, 1994; Chalaturnyk, 1996; Samieh and Wong, 1997; Touhidi-Baghini, 1998). With increasing experience in sampling and testing, good quality data can be obtained from lab testing. The stress-strain relationships, volume change as a function of stress change, permeability change due to volumetric strain, and thermal properties of oil sands material are all available based on the previous research.

The necessity of the coupled reservoir geomechanical simulation methodology to simulate the production performance of the SAGD process has been explained in Chapter 1. An extensive study of oil sands geomechanical properties has shown that sufficient data is available to support numerical simulations of the SAGD process. Consequently, the development of an applicable reservoir geomechanical simulation methodology is warranted and the following sections describe reservoir geomechanical simulation research.

2.3 Review of the Coupled Reservoir Geomechanical Simulation

Since Biot (1941) proposed the theory of coupled problems in 1941, many research papers on the numerical simulation of these problems have been published. The following was related to coupled reservoir and geomechanical modeling, including single-phase fluid and isothermal cases.

2.3.1 Lewis and Sukirman's model (1993)

This is a fully coupled finite element model, which can be used to simulate three immiscible and compressible fluids flowing in a deforming saturated oil reservoir. It applies the equilibrium equation and the continuity of the fluid flow in the model. The effects of capillarity, relative permeability variation, and the compressibility factors of rock and fluids are taken into account. The Mohr-Coulomb yield surface is used for elastoplastic soil materials. This model is used to investigate the compaction and subsidence problems of a saturated oil reservoir.

2.3.2 Chen, Teufel, and Lee's model (1995)

This model is an introduction of theory and governing equations for the coupled fluid flow and geomechanical modeling. It applies Biot's two-phase (fluid and solid), isothermal, linear poroelastic theory to the conventional porous fluid-flow modeling point of view to derive the simple coupling equations between fluid flow and solid deformation. So, this model helps understand the complex procedure of reservoir geomechanical simulations.

2.3.3 Osorio, Chen, and Teufel's model (1999)

This model is a 3D finite-difference, fully implicit model simulating the coupled fluid-flow and geomechanical behavior of reservoirs with stress-sensitive mechanical and fluid-flow properties. It considers two physical domains: (1) inner porous domain representing the reservoir, where fluid-flow and rock deformation occurs; (2) a surrounding domain representing the extended stress-disturbed region caused by the reservoir depletion. This model assumes that reservoir fluid is an isothermal single-phase fluid. Also, it treats the reservoir as a nonlinear elastic system with small strains.

2.3.4 Chin and Thomas's model (1999)

This model is an iterative, fully coupled procedure that integrates geomechanical and reservoir simulation through volume coupling (reservoir model) and coupling of pressure and water saturation (geomechanical model). The reservoir model and geomechanical model are linked together through an interface code. The iterative process of performing reservoir simulation and geomechanical computation by the two separate models and passing the needed state variable values between the two models continues until a convergence criterion is satisfied. It is capable of simulating both the elasto-plastic compaction behavior and the water weakening effect for a water-sensitive weak reservoir rock. Its nonlinear constitutive model developed is based on a hypoelastic/hypoplastic 3-D formulation.

Over the last decade, the oil sand recovery process, particularly the CSS process, were simulated and coupled with geomechanics. Major research work is summarized below.

2.3.5 Tortike and Farouq Ali's model (1991)

Tortike and Farouq Ali developed a comprehensive numerical model of oil sands, consisting of steam/water-oil-gas flow in 3-D with geomechanical behavior of oil sands. This model consists of two parts: 3-phase 3-D finite element thermal flow simulator, FESPS-F3, incorporating the fluid and heat flow equations for bitumen, water, gas, and steam and finite element solid model, PLAST-PT3, incorporating the formation displacement. It assumes that the solid grains are incompressible and neglects the change in surface area of a grain undergoing thermal expansion. Based on Kozeny-Carmon model, the effect of volumetric strains on permeability was proposed (Equation (2-2))

$$\frac{k}{k_0} = \frac{\left(1 + \frac{\varepsilon_v}{\phi_0}\right)^3}{\left(1 + \varepsilon_v\right)} \tag{2-2}$$

2.3.6 Fung, Buchanan, and Wan's model (1994)

This model calculates the elasto-plastic deformations of oil sand reservoirs using a finite element incremental plasticity model with Mohr-Coulomb and Drucker-Prager as the yield criteria. It is coupled with CMG's thermal simulator, STARS, which is capable of handling many advanced thermal recovery processes. The coupling process is conducted by the volume change and the associated permeability increase. The volume change is calculated by the plasticity model, whereas the permeability increase is related to the volume change via tabular data.

2.3.7 Settari, Walters, and Behie's Model (2001)

The GEOSIM system consists of a conventional thermal reservoir simulator, a thermo- and poroelasto-plastic stress-strain finite element simulator, a hydraulic fracturing simulator, and interfaces that couple the modules together. The coupling is achieved by communication between simulators on a time step (or iteration within time step) basis. The pressure and temperature changes occurring in the reservoir simulator are passed to the geomechanical simulator. The updated strains and stresses are passed back to the reservoir simulator and are used to compute coupled parameters in the reservoir formulation (i.e. porosity and permeability). The reservoir solution is based on finite difference model and the stress solution is based on finite element model.

2.4 Summary

The SAGD process was developed as a requirement of the in situ recovery of the oil sands resources in Alberta. A great number of the SAGD projects are under construction and operation in the field. Since the oil sands material is locked sands with specific geotechnical properties, coupled reservoir geomechanical simulation methodology needs to be applied in the simulation of the SAGD production performance.

All the coupled reservoir geomechanical simulation methods discussed in this chapter take the coupling effect of fluid flow and solid deformation into account. Unfortunately, Lewis's model, Chen's model, Osorio's model, and Chin's model are all isothermal models. These models are not suitable for the simulation of the SAGD process with geomechanical characteristics.

Tortike's model, Fung's model, and Settari's model apply the elastoplastic stress-strain relationships. This treatment is consistent with the oil sand behavior during the SAGD operations. However, Tortike's model apply finite element method to do the reservoir simulation, which still needs further investigations and more tests to validate and prove that it is as good as a commercial reservoir simulator based on finite difference method. Fung's model is a simple treatment of the geomechanical effects, which does not consider the total stress variations beyond the steam chamber. Moreover, its updated permeability value is based on a set of tabular data, which is not enough to incorporate the effect of geomechanical behavior. Settari's model introduced the theory of different degrees of coupling, formulation of the constitutive models, running efficiency of the software. It accounted for the theoretical and modeling aspects of thermal compaction phenomenon. For all the three models, however, further investigations on oil sands geomechanical behavior and permeability variations associated with different geomechanical effects are still necessary.

It is suggested to develop a realistic reservoir geomechanical simulation methodology to overcome the shortcomings in the current models. Further studies on the geomechanical issues associated with the coupled reservoir geomechanical simulations, geomechanical models of oil sands, and permeability variations due to different geomechanical behaviors should be taken into account.

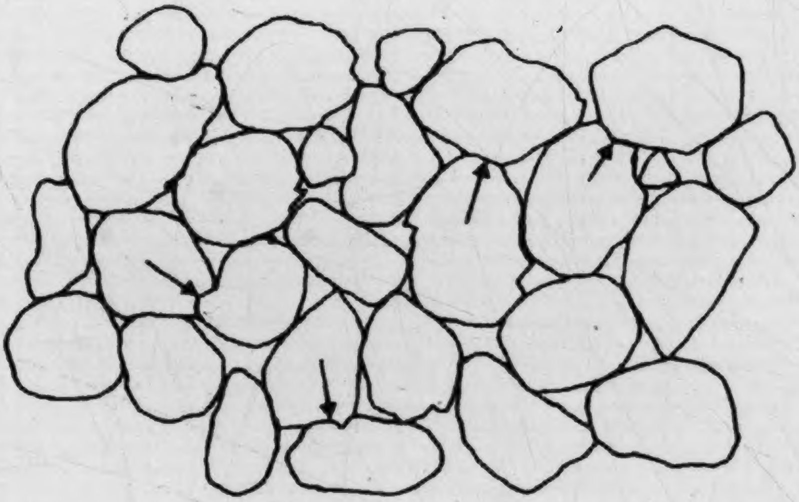

Figure 2-1 Fabric of Athabasca oil sands (arrows indicate the interlocked contacts of oil sands grains) (Modified from Dusseault and Morgenstern, 1978)

CHAPTER 3 DECOUPLED RESERVOIR GEOMECHANICAL SIMULATIONS[*]

3.1 Introduction

The geomechanical response of an oil sands/heavy oil reservoir is complex, reacting to both near and far field temperatures and pore pressures. To aid in elucidating fundamental geomechanical principles affecting the steam assisted gravity drainage (SAGD) process and to gain insight into a reservoir's response to thermal loading and pore pressure change, a parametric analysis of the SAGD process within three separate but similar reservoir settings was completed. To support the objective of this research which is to examine how the geomechanical response of the formations affects the SAGD process, two-dimensional analyses of reservoir cross sections with basic treatment of the inherent complex geology have been conducted. The analysis results presented herein are not intended to portray a history match of any particular SAGD operation.

Fully coupled thermal-stress-fluid flow analyses are extremely difficult to conduct. While fully coupled mathematical formulations exist (Beattie et al., 1991; Hart and St. John, 1981; Tortike and Farouq Ali, 1991), the computational effort in their solution is onerous and continues to be an area of active research. Coupled solutions that consider single phase flow only have become common (Chin et al, 1998; Khan and Teufel, 2000) and are routinely utilized in both advanced reservoir simulations and geotechnical/hydrogeological simulations. Consequently, a decoupled approach was adopted for the analyses presented herein. The decoupled approach consisted of conducting a reservoir simulation of SAGD using STARS (an advanced process and thermal reservoir simulator developed by CMG in Calgary) and utilizing the temperatures and pore pressures as input to a geomechanical simulation of the formation response to SAGD. In agreement with Tortike (1991), that while the removal of "feedback" to the fluid flow model would not allow conclusions to be drawn regarding the fluid solution, this decoupled approach would permit conclusions to be drawn and inferences to be made concerning the likely response of the formation to the SAGD process.

---

[*] Part of this chapter entitled *When Is It Important to Consider Geomechanics in SAGD Operations?* (Chalaturnyk, R.J. and Li, P.) has been published by the Journal of Canadian Petroleum Technology (JCPT), Volume 43, No. 4, 2004. pp. 53-61. It was first presented at the 2nd Canadian International Petroleum Conference (the 52nd Annual Technical Meeting of the Petroleum Society), June 12-14, 2001, Calgary, Alberta.

In what can now be considered conventional practice, geomechanics is applied routinely in problems such as borehole stability, hydraulic fracturing, and subsidence. Gutierrez and Lewis (1998) provided a summary of the role of geomechanics in reservoir behavior. As they correctly pointed out, rock deformations due to pore pressure and temperature changes can affect the permeability and pore compressibility of the rock. In turn, the pore pressure will vary due to changes in the pore volume and drainage conditions (i.e. drained, partially drained, and undrained). Geomechanics is also required in order to account for the effect of the non-pay rock surrounding the reservoir on the overall reservoir compressibility and the loads transmitted to the reservoir by the weight of the overburden rock.

Recently, there has been a growing recognition of the importance of incorporating geomechanics in reservoir simulation studies. For conventional, primary production processes, fluid production of a hydrocarbon reservoir generally results in a decrease in fluid pressure and an increase in effective confining stress. Figure 3-1 illustrates the basic interactions between geomechanics and fluid flow in a deformable reservoir. For the SAGD process, the reservoir fluid pressure commonly increases leading to a decrease in the effective confining stress of the reservoir rock. Heating of the reservoir rock also produces a thermal expansion induced increase in confining stress. The combination of these pore pressure and temperature effects creates a complex set of interactions between geomechanics and fluid flow.

But if reservoir simulation models (Edmunds and Suggett, 1995; Kisman and Yeung, 1995; Law et al., 2000) appear to adequately model the production rates for SAGD processes, why pursue the inclusion of geomechanical phenomena within thermal reservoir simulation programs? As far back as 1984, the concept of sand deformation (Ito,

1984) was used to explain the behavior of injection and production wells during steam injection and allowed some success in history matching the performance of several field projects. However, even as recently as 1996, in a simulation of the SAGD process in the Hangingstone Oil Sands reservoir (Ito and Suzuki, 1996), Ito and Suzuki concluded, "geomechanical change of the formation during the SAGD process in the oil sand reservoir seems to be very important". For most of these analyses, the sand deformation concept was implemented in the geomechanics module of STARS where adjustments are made to porosity, absolute permeability, and relative permeability as a function of pressure to simulate shear failure. The analyses based on this approach did not take into account the geomechanical effects both inside and outside the steam chamber.

Clearly, the leading work of Ito and his colleagues to incorporate in some fashions of the geomechanical formation responses within SAGD reservoir simulations has shown that the deformational response of the reservoir can affect drainage patterns and steam chamber development. The study results presented subsequently provide additional data to support this hypothesis while attempting to elucidate the complexity of the dilation or volume change process within the reservoir.

As a preface to the numerical results of the modeling part of the study, the following sections describe the geomechanical role of thermal volume change, bulk compressibility, shear strength and stress induced permeability changes within the context of the SAGD process. It is important to review these concepts prior to discussing what impact, if any, geomechanical processes may have on the SAGD process.

3.2 Geomechanical Parameters for SAGD

3.2.1 Thermal Volume Change

Volumetric deformations within the reservoir resulting from temperature changes influence both stress and strain fields in situ. The extent of these deformations is a function of the "restraint" boundary conditions existing within the reservoir. For relatively shallow depth reservoirs, such as at the Dover UTF Project, there is a limited restraint for vertical deformations. Owing to the horizontal continuity of the reservoir, horizontal deformations in response to in situ heating are highly restrained in comparison to vertical deformations. Consequently, horizontal stresses increase more than vertical stresses and thermally induced vertical deformations are larger than horizontal deformations. This is particularly true for a multiple well pair geometry where the formation between opposing well pairs may be subjected to large increases in horizontal stress. This is conceptually illustrated in Figure 3-2. In order to predict the magnitude of these thermally induced stresses and deformations, the thermal volume change behavior of the reservoir materials must be understood.

In most cases, these total stress induced changes due to thermal expansion of the reservoir have not been incorporated in pseudo-coupled simulations of the SAGD process. These total stresses can be significant and play a dominant role in the shear deformations and resulting shear induced volume changes within the reservoir.

The coefficient of thermal expansion is an important variable for both reservoir and geomechanical analyses of the SAGD process. Interpretation issues, however, do arise for what a "thermal expansion coefficient" means to a reservoir simulator and what it means geomechanically. The definition of "thermal expansion coefficient" suffers from the same inherent problem as compressibility; geomechanical tests generally provide "bulk" values while reservoir simulators (not modified to incorporate geomechanics) generally require "pore" values. For coupled, sequentially coupled, or decoupled reservoir geomechanical simulations, the coefficient of thermal expansion should be chosen with great care.

3.2.2 Bulk Compressibility

The reservoir mechanics of SAGD are not dominated by the displacement mechanisms typically associated with steam injection processes such as cyclic steam stimulation. Reservoirs undergoing cyclic steam stimulation typically have high oil viscosity and low native water mobility resulting in negligible initial injectivity at pressures well below fracture pressures (Butler, 1986). Steam injection at commercial rates requires injection pressures high enough to cause both localized fracturing and widespread pore volume increases in the formation. In these cases, pore volume compressibility is a critical reservoir parameter for understanding reservoir production.

In the SAGD process, the major drive mechanism at work is gravity. Consequently, compressibility of the formation will only have a minor effect on long-term production. Compressibility may have an effect on the startup or initial communication phase of the SAGD process. In start-up, hot water or steam is circulated under pressure in both wells, with a small pressure differential applied between the wells. Variations in pore volume, as a function of effective confining stress during this stage of SAGD, will influence the rate of initial bitumen production (Siu et al., 1991).

3.2.3 Compressibility in Reservoir Geomechanics

In the dual jargon world of reservoir engineering (e.g. porosity) and geotechnical engineering (e.g. void ratio), compressibility is perhaps the most difficult material property to assimilate in both disciplines. Fundamentally, compressibility is based on the same concept in both sciences: a pore volume change resulting from a change in stress. The nature of the pore volume change and the definition of a change in stress constitute the divergence in the concept of compressibility for both sciences. Previous work (Tortike, 1991; Settari, 1989) has examined the relationships between geotechnical compressibility and reservoir compressibility. Because of the importance in understanding the treatment of compressibility when discussing geomechanical processes, these relationships are summarized below.

The various measures of compressibility (Settari, 1989) are derived by examining the mass accumulation term in a set of fluid flow equations. The numerical treatment of the mass accumulation terms will influence the form of the compressibility equations. For example, the general accumulation equation (Tortike, 1991) is given by:

$$\frac{\partial}{\partial t}(\phi \rho_{\alpha} S_{\alpha}) = \phi \frac{\partial}{\partial t}(\rho_{\alpha} S_{\alpha}) + \rho_{\alpha} S_{\alpha} \frac{\partial \phi}{\partial t} \qquad (3\text{-}1)$$

and will be assumed valid for the subsequent derivations. The second term on the right side of Equation (3-1) relates to the physical change in porosity and is conventionally handled through a pore compressibility term. Pore compressibility is sometimes confused with rock compressibility (Settari, 1989); the differences are discussed below.

The typical reservoir engineering formulation for rock compressibility assumes it is measured at constant total stress. Therefore, rock compressibility is explicitly defined as

$$C_R = \frac{1}{\phi}\frac{\partial \phi}{\partial p} \tag{3-2}$$

Equation (3-2) is typically simplified and restated as:

$$\phi = \phi_o\left[1 + C_R \Delta p\right] \tag{3-3}$$

In geotechnical engineering, however, it is the drained bulk compressibility of a specimen that is measured and defined as a function of effective stress. Classically, the drained bulk compressibility is represented by a parameter m_v, the coefficient of volume compressibility. The parameter, m_v, is defined in terms of void ratio, e, but knowing:

$$e = \frac{\phi}{1-\phi} \tag{3-4}$$

So, m_v can be expressed in the following form:

$$m_v = \frac{1}{1-\phi_o}\left(\frac{\Delta\phi}{\Delta\sigma'}\right) \tag{3-5}$$

Equation (3-5) inherently assumes the solid grains are incompressible. Replacing m_v with the symbol C_b (to represent coefficient of bulk compressibility) and recasting Equation (3-3) to include C_s, the solid compressibility, the following relationship is obtained:

$$\phi = \phi_o + \left[(1-\phi_o)C_b - C_s\right]\Delta\sigma' \tag{3-6}$$

For the conventional reservoir engineering assumption of no change in total stress, $\Delta\sigma' = \Delta p$ (since $\sigma' = \sigma_t - p$), therefore equating Equation (3-3) and (3-6) provides the following relationship between C_R and C_b and C_s:

$$\phi_o C_R = (1-\phi_o)C_b - C_s = C_\phi \tag{3-7}$$

It is important to note that the correct definition of pore volume compressibility, expressed as a function of effective stress, is by Equation (3-6). Compressibility tests based on changes in effective stress can be conducted in two ways in order to obtain equal increments of effective stress:

1) Holding σ_t constant and decreasing p, or

2) Holding p constant and increasing σ_t

In general, drained compressibility of a specimen is measured by maintaining a constant fluid pressure, p, (drained conditions) and varying the total stress σ_t, applied to the specimen (Method 2 above). Geomechanical testing typically employs Method 2 since the interpretation of bulk compressibility from this type of test does not require knowledge of fluid compressibility.

As Equation (3-7) reveals, several definitions of compressibility exist and their corresponding values depend on the type of test used to derive these parameters. For example, if the bulk compressibility is obtained from a geomechanical test (oedometer or triaxial) and rock compressibility is required, then C_R will be given by:

$$C_R = \frac{C_b(1-\phi_o)-C_s}{\phi_o} \tag{3-8}$$

As well, compressibility can be measured either by isotropic compression in the triaxial cell or constrained compression in the oedometer. The term "constrained" is used to reflect the lateral confinement on specimen during an oedometer test.

3.2.4 Strength and Stress-Strain Behavior

In geotechnical practice, it is accepted that the stress-strain response of sands are stress path dependent and previous testing (Chalaturnyk and Scott, 1992; Agar, 1984; Dusseault, 1977; Kosar, 1989; Oldakowski, 1994) has confirmed this to be true for McMurray Formation oil sands. In general, two predominant stress paths are followed within the reservoir during the SAGD process:

1) Assuming total stress does not vary, a pore pressure increase will result in equal reductions in σ'_1 and σ'_3. To assess the changes in σ'_1 and σ'_3, two main parameters are of interest:

- The shear or deviatoric stress defined as $(\sigma'_1 - \sigma'_3)/2$ and commonly given the symbol q; and
- The mean stress defined as $(\sigma'_1 + 2\sigma'_3)/3$ and commonly given the symbol p'.

A plot of q versus p' provides a graphical representation of the "effective stress path" followed by any particular point within the reservoir. So, for a pore pressure increase that results in equal increments of both σ'_1 and σ'_3, this path in p'-q space is horizontal because q is unchanged along this path; and

2) Horizontal total stresses will increase due to thermal expansion of the reservoir within the developing steam chamber. However, vertical total stress remains relatively constant due to the shallow depth of the reservoir. Assuming no pore pressure changes, these effects result in the development of shear stresses and a stress path where the shear stress and mean effective stress increase together.

These individual stress paths are schematically illustrated in Figure 3-3. Both pore pressures and thermal expansion stresses occur simultaneously resulting in the curved stress path shown in Figure 3-3.

For the SAGD process, it is the volumetric strain response along this stress path that is of primary importance. If, under the actions of shear stress or changes in mean effective stress, reservoir deformations result in volumetric dilation or contraction, the porosity and hence k_a will be altered. Absolute permeability, k_a, which is inherently linked to porosity, imparts a substantial influence on the drainage of fluids from the reservoir. Related to absolute permeability is the effective permeability to water, k_{ew} ($k_{ew} = k_{rw}k_a$). At a reservoir temperature of 8°C, bitumen is essentially immobile ($\mu \geq$ 5,000,000 mPa·s). If the SAGD processes create shear-induced volume changes within the ambient temperature zones of the reservoir, the effective permeability to water in this zone will increase dramatically. The reason is that the pore volume increase causes an influx of the mobile fluid, water. An increase in k_{ew} will increase the hydraulic conductivity and will permit injection pore pressures to migrate further into the reservoir. This leads to a reduction in effective confining stress, a reduction in strength, and an increased propensity for volumetric deformations. These concurrent phenomena act to alter the reservoir conditions in advance of the steam chamber. It should be noted that conventional reservoir simulators, including STARS pseudo-geomechanical model, cannot capture these shear induced permeability changes ahead of the steam chamber.

Correctly identifying the magnitude of the strength-deformation behavior and its resulting effect on reservoir processes is important for understanding the effectiveness of the SAGD process. To this end, laboratory experiments examining the stress-induced permeability changes of oil sands have been conducted (Oldakowski, 1994; Touhidi-Baghini, 1998). Figure 3-4 shows triaxial test results (Oldakowski, 1994) demonstrating the effect of shear induced changes on the effective permeability to water in Athabasca oil sands; an important aspect of the pore pressure development within the UTF Phase A reservoir.

The stress-strain behavior of oil sands, both Athabasca McMurray Formation oil sands (Dusseault, 1977; Agar, 1984; Plewes, 1987; Kosar, 1989; Oldakowski, 1994) and Cold Lake Clearwater Formation oil sands (Kosar, 1989; Wong et al., 1993; Zhang, 1994), have been studied extensively with the goal of determining the constitutive behavior of oil sands. The majority of the testing has focused on stress-strain-strength properties of oil sands and related strata.

3.2.5 Stress-Induced Permeability Changes

The geomechanical phenomena of volumetric straining under the combined effect of pore pressure changes (i.e. effective confining stress changes) and shear stress constitutes the primary factor influencing SAGD processes. Scott et al. (1991) outlined the effects of steam stimulation on oil sands pore volume changes. A temperature increase causes thermal expansion of sand grains and matrix and results in shear stresses. Pore pressure increase during steam injection decreases the effective confining stress and causes an unloading of the reservoir matrix. For an anisotropic in situ stress state, pore pressure injection will possibly generate shear strains in the reservoir. These processes can combine to result in a net change in the reservoir pore volume and permeability. To examine these porosity/permeability variations, Oldakowski (1994) conducted a laboratory testing program to investigate changes in absolute permeability and effective permeability to water in response to deformations induced by different stress paths. The tests were performed on Athabasca McMurray Formation oil sands from the UTF Phase A site at the in situ temperature of 8 °C. While the evolution of geomechanical testing on oil sands is mature, almost all of these laboratory programs were conducted at 20 °C or ambient laboratory temperatures. At 20 °C, the bitumen viscosity is approximately 400,000 mPa.s. Decreasing the temperature to 8 °C, the initial in situ temperature at the UTF, increases the viscosity to approximately 5,000,000 mPa.s; an increase of 1,150%. At 8 °C, the bitumen acts like a solid phase in the pore spaces and may even contribute to the mechanical behavior of oil sands. While several field cases of oil sands exhibiting tensile properties have been reported, Plewes (1987) concluded that these tensile properties do not originate from the interlocking structure of the sand grains and postulates that bitumen viscosity at lower temperatures (his testing was also conducted at 20°C) may be the source of the apparent tensile strength.

Consequently, the testing program of Oldakowski (1994) represents the first data set available of hydraulic and geomechanical properties of oil sands obtained for an in situ temperature of 8 °C, the ambient temperature of the UTF Phase A reservoir.

3.3 Numerical Models

For the SAGD simulations, the thermal reservoir model, STARS, developed by the Computer Modelling Group (CMG) Ltd. in Calgary, Alberta was used. For the geomechanical simulations, the two dimensional explicit finite difference program, FLAC (Fast Langrangian Analysis of Continua), developed by Itasca (2000) was used. FLAC is used to simulate the behavior of structures built of soil, rock, or other materials that undergo plastic flow when their yield limits are reached. This capability allows the process of dilation or shear induced volume changes to be modeled for the temperature and pressure conditions of the SAGD process.

3.4 Reservoir Simulations

Numerical simulation of the SAGD process was done based on the three different kinds of heavy oil reservoirs for which SAGD projects are underway (Butler, 2001). While not meant to be complete representations of the reservoir geometry, the three models are SHALLOW (modeled after the Dover Project site), MEDIUM (modeled after the Surmont site), and DEEP (modeled after the Senlac Project site). The major differences between these models are reservoir depth, initial reservoir pressure, and oil viscosity under reservoir conditions. The detailed reservoir properties and SAGD process parameters used in the numerical simulation are shown in Table 3-1. The grid systems for the three heavy oil reservoirs are illustrated in Figure 3-5.

In order to study the effect of the magnitude of the steam injection pressure relative to the in situ stress state of the reservoir, SAGD simulations for each of the three models were conducted for three different steam injection pressures. The values selected were:

Shallow: $p_{inj}/p_i = 1, 2.5$, and 5;

Medium: $p_{inj}/p_i =1, 2$ and 3; and

Deep: $p_{inj}/p_i =1, 2$ and 3.

Nine numerical simulations of the SAGD process were conducted and for each case, the reservoir pressure distribution and temperature distribution data were extracted at times of 182 days, 365 days, 547 days and 730 days, respectively. These data serve as the input conditions for the geomechanical simulations. It should be noted that the geomechanical simulation results are only used to show the geomechanical behavior occurring in the SAGD process and not input into the reservoir simulator.

3.5 Geomechanical Simulations

Geomechanical analysis during the SAGD process is conducted with FLAC based on the pressure distribution and temperature distribution data obtained from the output file of STARS, as described above. Table 3-2 shows the basic parameters required for the geomechanical analysis. It is important to note the major differences in the initial total and effective confining stresses for each case. The shallow, medium, and deep reservoirs are at low, medium, and high confining stresses, respectively. Figure 3-6 illustrates the dimensions and grid systems used in FLAC for the three heavy oil reservoirs. As mentioned above the pore pressures and temperatures obtained from the reservoir simulations are interpolated from the STARS grid to match the nodal positions in the FLAC grid. Based on the numerical simulation of the three heavy oil reservoirs with three different values of p_{inj}/p_i and four time period extraction of pore pressures and temperatures, a total of 72 sets of data were interpolated. After the pore pressure and temperature distributions in the FLAC grid system were determined, they were used directly in numerical simulations with FLAC. As listed in Table 3-2, different values of p_{inj}/p_i and K_0 $(K_0 = \sigma_h'/\sigma_v')$ are considered in the analysis.

Each of the figures that follow provides the stress path for selected zones (elements) within the reservoir. The particular element for which the stress path is drawn is shown as a square with a cross in each inset contour diagram. The inset contour diagrams show the distribution of temperature (line contours) and pore pressure (shaded contours) at 365 days. Each stress path plot contains three contour diagram plots corresponding to a particular steam injection pressure, which is shown in each diagram. For the stress path plots, the p' axis represents the mean (or average) effective confining stress and the q axis represents the deviatoric or shear stress. A stress path is shown for each particular steam injection pressure and each initial stress ratio condition. On each stress path plot, the position of the failure envelope, which defines the relationship between p' and q for which shear failure will occur for the strength parameters listed in Table 3-2, is shown.

3.6 Results and Discussion

3.6.1 Shallow Reservoir – Zone in Middle of Reservoir

The stress paths for an element adjacent to the injection/production well pair (10 m horizontally away from the injector) are shown in Figure 3-7 for $K_0 = 1$ and $K_0 = 1.6$. Initially, the injection pressure front has not progressed to the element in question, and the start points (Day 0) of the stress paths for three different injection pressures are the same. Clearly, if the initial state of stress is anisotropic (i.e. $K_0 = 1.6$), the zone adjacent to the SAGD wells reaches the failure envelope much more rapidly. For the case of $K_0 = 1$, it is only the case of the highest injection pressure that eventually reaches the failure envelope at 730 days. For $K_0 = 1.6$, however, the moderate injection pressure, $p_{inj} = 1375$ kPa, results in formation yield or failure after 6 months of injection. For $K_0 = 1.6$ and $p_{inj} = 2750$ kPa, the adjacent reservoir zone yields within 6 months and remains in a failed or yielded state over the full 2 year injection period.

The shape of the stress paths is indicative of the loading induced by pore pressure and temperature. Initially, when the steam chamber size is small, the advancing pore pressure front dominates the behavior of the formation. As pore pressure increases, the mean effective stress, p', will decrease and hence, the stress path will move to the left. In reference to the discussion on geomechanical parameters for SAGD, a volume increase will occur due to the bulk compressibility increase with decreasing effective stress in the oil sands formation. These processes lead to an increase in the absolute permeability. This volume increase is not due to shearing, and it is strictly a bulk compressibility effect. For McMurray Formation oil sands, bulk compressibility can increase by almost one order of magnitude when p' is decreased from 2.8 MPa to 1.4 MPa. Shear induced volume change does not become a significant component of the total volume change until the stress path is close to or reaches the failure envelope. For the case of the shallow reservoir, the shear induced dilation or volume change becomes important only at 730 days for $K_0 = 1$ and high injection pressure. For $K_0 = 1.6$ and high injection pressure, shear failure occurs within the first 180 days of steaming.

The resulting impacts of these particular stress paths are shown in Figure 3-8. To establish the increase in k attributed to volumetric strain, the following expression (Tortike, 1991) was employed:

$$k / k_0 = \frac{\left(1 + {}^{\varepsilon_v}\!/_{\phi_o}\right)^3}{\left(1 + \varepsilon_v\right)} \tag{2-2}$$

The initial porosity chosen for each reservoir is listed in Table 3-2. For the low injection pressure case (which corresponds to injection pressure equal to reservoir pressure), the stress path followed by an element adjacent to the well pairs indicated no shear failure would occur. Consequently, no shear induced volume change occurs and the only volume change that should occur will be due to bulk compressibility effects. Figure 3-8 clearly shows essentially identical k/k_0 curves for K_0 = 1 and K_0 =1.6 with approximately 3% increases in absolute permeability. For the high injection pressure case, however, the impact or contribution of shear induced volume change to the total volumetric strain is clear when comparing the curves for K_0 =1 and K_0 =1.6. As noted in Figure 3-7, for K_0 =1.6, this element reaches shear failure near 180 days and remained in a failed state from that point on. This is reflected in the much larger (13% compared to 8%) increase in k_a for K_0 =1.6.

3.6.2 Shallow Reservoir – Zone at Top of Reservoir

Figure 3-9 shows the stress path followed by an element at the top of the reservoir, roughly in the midpoint of the grid (13 m above and 22 m away from the injector). This zone within the reservoir responds quite differently than the element adjacent to the well pairs and serves to highlight the powerful interrelationship between steam chamber growth (temperature) and pore pressure distribution.

For both the low and middle injection pressures, there is almost no change in mean effective confining stress beyond one year of steaming. The reason is that as pore pressures are evolving, the total stresses applied by the expanding steam chamber compensate for the rise in pore pressure and consequently, no change in p'. Shear stresses develop at this point in the reservoir and increase continuously during steaming.

For the high injection pressure, the response is dramatically different. The high injection pressure causes p' to decrease faster than the thermal expansion induced total stresses can increase p'. As p' decreases, it takes less shear stress to fail the oil sands and consequently, shear failure conditions are reached rather quickly with the final stress condition after two years; even approaching $p' = 0$ conditions.

3.6.3 Medium Reservoir – Zone in Middle of Reservoir

Figure 3-10 illustrates the stress paths for an element adjacent to the well pairs for K_0 =1 and K_0 =1.6. The stress paths for each injection pressure are similar and in general, do not reach a shear failure condition. The stress conditions approach the failure envelope for K_0 =1.6 indicating that reservoirs at this depth could experience shear failure within the reservoir if K_0 was slightly higher than K_0 =1.6, which is the case for many oil sands reservoirs. The converse to this statement is that operating at a low injection pressure for these assumptions would not gain the advantage of shear induced volume changes and the increases in absolute permeability associated with these volume changes.

3.6.4 Medium Reservoir – Zone at Top of Reservoir

Figure 3-11 illustrates the stress paths for an element at the top of the reservoir. For the medium depth reservoir geometry, the distance to the element, while visually similar to the shallow case, is actually farther away from the well pairs (30 m above and 29 m away from the injector). Consequently, the rapid pore pressure response seen in the shallow case is not significant for this reservoir geometry. Conversely, what controls the stress path is the thermal expansion induced total stress changes induced by the steam chamber growth. As a result, all the stress paths show an increasing p' path with the corresponding increase in shear stress. As shown in Figure 3-11, for K_0 =1.6, this zone at the top of the reservoir actually exhibits shear failure after 540 days for the high injection pressure case and approaches failure conditions at 730 days for the medium injection pressure case.

3.6.5 Deep Reservoir

The stress paths for K_0 =1.7 for elements in the middle (27 m horizontally away from the injector) and top (9 m above and 46 m away from the injector) of the reservoir are shown in Figures 3-12a and 3-12b, respectively. Again, the strong interrelationship between the rate at which pore pressure develops within the reservoir and the rate at which total stresses increase due to thermal expansion (rate and geometry of steam chamber growth) is clearly illustrated in this figure. For low injection pressures, the total stress increases the mean stress, p', but for the high injection pressure case, the pore pressure can increase significantly in this zone and under the developing shear stresses induced by steam chamber growth, reaches shear failure quite rapidly.

Because of the reservoir geometry and the position of the element chosen for the stress path plots, the response for an element at the top of the reservoir, shown in Figure 3-12b, is almost identical to the middle zone element. This is primarily due to the fact that the direction of steam chamber growth is almost horizontal by the time it approaches these two elements. The plots for K_0 =1 are not shown but illustrate the same phenomena.

Figure 3-13 illustrates the change in absolute permeability experienced by an element adjacent to the well pairs. As for the case of the shallow reservoir, the injection pressure is sufficient to cause a zone within the reservoir to approach failure, the oil sands will dilate under the shear stresses. For the deep reservoir case, an injection pressure of 15,000 kPa results in a 26% increase in absolute permeability for K_0 =1.7. Note that if the operating pressures are at reservoir pressure, in this case an injection pressure of 5,000 kPa, the SAGD process will not be affected by any volumetric strains induced by shear failure. But it is clear that at a low injection pressure (relative to reservoir pressure), the thermal induced total stresses can increase the mean effective confining stress quite substantially. For the case of an element adjacent to the wellpairs, p' increased by 50% from 15 MPa to 22.5 MPa. This may be of interest to those concerned with the design of liners in thermal applications.

3.7 Conclusions

These decoupled simulations generalize the typical reservoir conditions for which SAGD is being implemented or considered in order to parametrically analyze the influence of geomechanical factors on the startup and production phases of SAGD projects.

From the range of reservoir geometries studied in this initial phase, it is difficult to be conclusive about specific geomechanical processes relative to the multiphase characteristics of SAGD. General observations derived from this study are:

- The evolution of zones of shear induced volume changes is sensitive to the initial stress state and injection pressure.

- The magnitude of shear stress developed at the top of the reservoir depends on the relative size of the steam chamber to the reservoir dimensions.

- The interrelationship between pore pressure (reduction in effective stress) and temperature (increase in total stress) is complex.

- For injection pressures close to the initial mean effective confining stress within the reservoir, significant zones of shear failure can occur which correspond to regions of enhanced absolute permeability.

- These decoupled simulations illustrate the strong influence geomechanical processes may have on the SAGD process and provide clear support for more realistically coupled reservoir geomechanical simulations applied in the SAGD process, such as the sequentially coupled or fully coupled simulations.

Table 3-1: Physical properties of the three model reservoirs

Reservoir	Shallow (Dover UTF Phase B)	Medium (Surmont)	Deep (Senlac East)
Depth (m)	160	285	750
Pay thickness (m)	20	40	15
Porosity (%)	35	35	33
Horizontal permeability (μm^2)	10	2.2	10
Vertical permeability (μm^2)	5	2	5
Oil saturation (%)	85	85	85
Oil viscosity (mPa.s)	5E+6 (7 °C)	2E+6 (11 °C)	1.5E+4 (20 °C)
Initial reservoir pressure (kPa)	550	1,200	5,000
Initial reservoir temperature (°C)	8	11	20
Compressibility (1/kPa)	5E-6	5E-6	5E-6
Thermal expansion coefficient (1/K)	6E-5	6E-5	6E-5
Horizontal well length (m)	500	550	550
Well pair spacing (m)	75	80	135
Injector producer spacing (m)	5	5	5
Steam quality (%)	98	100	98
Steam injection pressure (kPa)	550	1,200	5,000
	1,375	2,400	10,000
	2,750	3,600	15,000

Note: 1 $\mu m^2 \approx 1$ D.
Thermal expansion coefficient is volumetric (bulk) value.
Horizontal well length means the real completion length.

Table 3-2: Properties required for the geomechanical analyses

Model Input Parameter	Shallow	Medium	Deep
Thermal expansion coefficient (1/°C)	2E-5	2E-5	2E-5
Overburden dry density (E+3kg/m^3)	1.7	1.7	1.7
Wet density (E+3kg/m^3)	3.053	3.600	2.650
Bulk modulus (E+5 kPa)	2.86	2.86	2.86
Shear modulus (E+5 kPa)	1.32	1.32	1.32
Shear Failure Model	Mohr-Coulomb	Mohr-Coulomb	Mohr-Coulomb
Cohesion (kPa)	0	0	0
Dilation angle (°)	20	20	20
Friction angle (°)	45	45	45
Overburden bulk modulus (E+5 kPa)	2.08	2.08	2.08
Overburden shear modulus (E+5 kPa)	0.96	0.96	0.96
K_0	1.0	1.0	1.0
σ_x' (kPa)	2,995	6,336	12,324
σ_y' (kPa)	2,995	6,336	12,324
σ_z' (kPa)	2,995	6,336	12,324
K_0	1.6	1.6	1.7
σ_x' (kPa)	4,768	10,104	20,986
σ_y' (kPa)	2,995	6,336	12,324
σ_z' (kPa)	4,768	10,104	20,986

Note: Vertical stress is σ_y which is consistent with that used in FLAC.

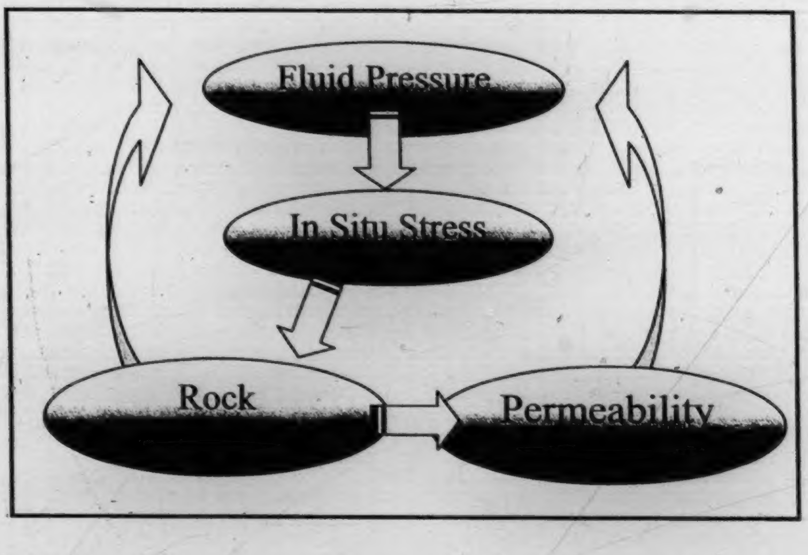
Fluid Pressure
In Situ Stress
Rock
Permeability

Figure 3-1 Interaction between fluid flow and geomechanics in a deformable reservoir (after Gutierrez and Lewis, 1996)

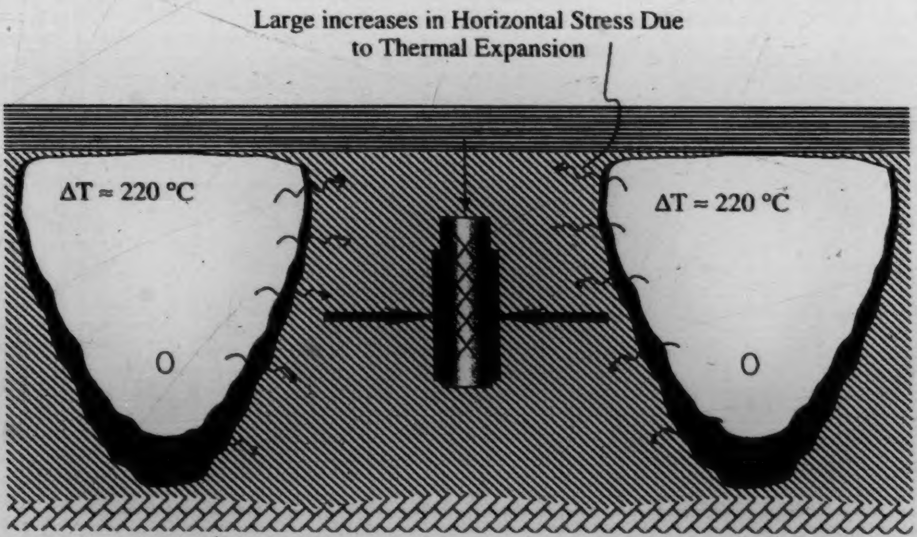
Large increases in Horizontal Stress Due to Thermal Expansion
ΔT ≈ 220 °C
ΔT ≈ 220 °C
O
O

Figure 3-2 Schematic showing possible increase in horizontal stresses due to steam chamber growth

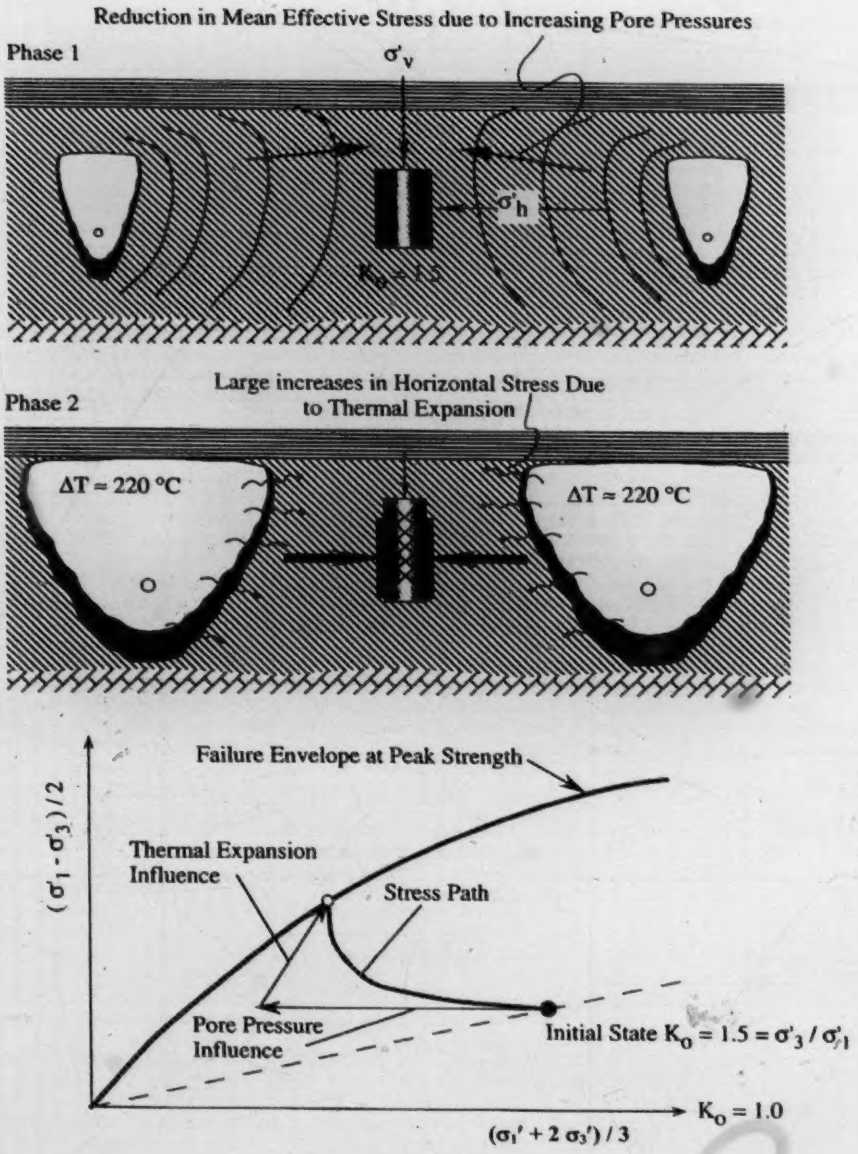
Reduction in Mean Effective Stress due to Increasing Pore Pressures
Phase 1
σ'v
σ'h
Ko = 1.5
Phase 2
Large increases in Horizontal Stress Due to Thermal Expansion
ΔT = 220 °C
ΔT ≈ 220 °C
Failure Envelope at Peak Strength
(σ'1 - σ'3) / 2
Thermal Expansion Influence
Stress Path
Pore Pressure Influence
Initial State Ko = 1.5 = σ'3 / σ'1
Ko = 1.0
(σ1' + 2 σ3') / 3

Figure 3-3 Possible stress paths within reservoir during SAGD process

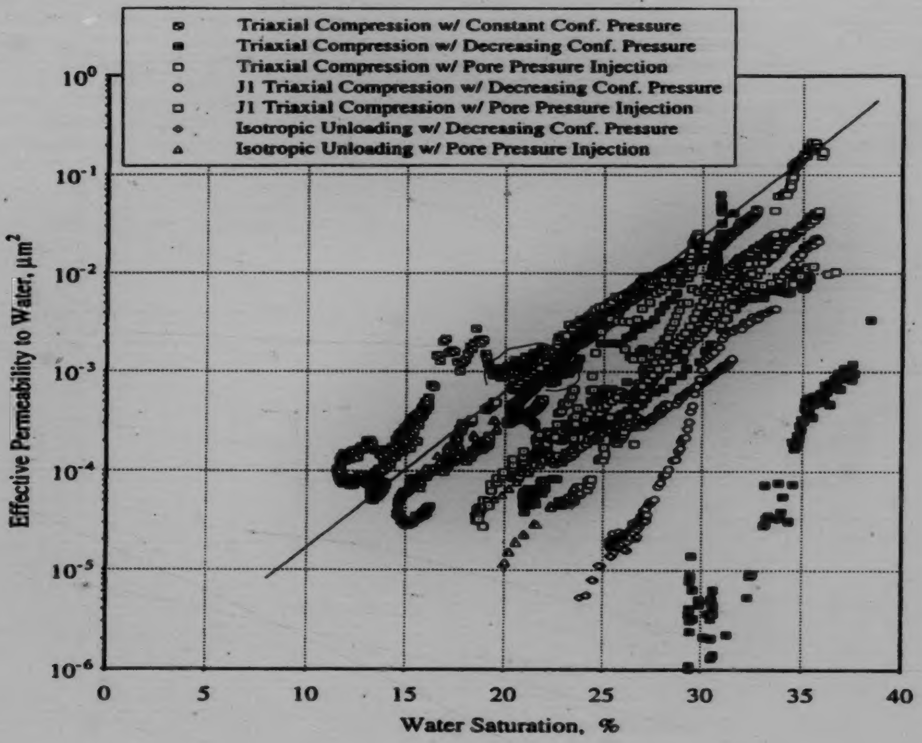

Figure 3-4 Change in effective permeability to water (After Oldakowski, 1994)

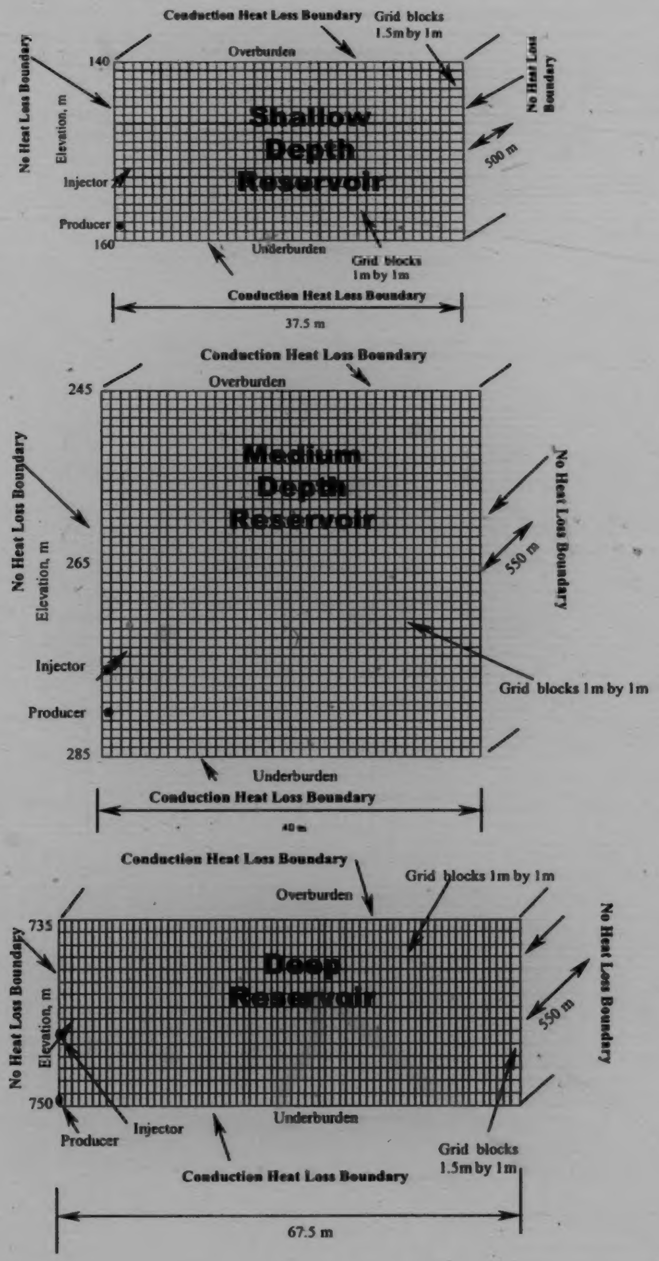
Conduction Heat Loss Boundary
Grid blocks 1.5m by 1m
Overburden
140
No Heat Loss Boundary
Elevation, m
Shallow Depth Reservoir
No Heat Loss Boundary
500 m
Injector
Producer
160
Underburden
Grid blocks 1m by 1m
Conduction Heat Loss Boundary
37.5 m
Conduction Heat Loss Boundary
245
Overburden
Medium Depth Reservoir
No Heat Loss Boundary
Elevation, m
265
No Heat Loss Boundary
550 m
Injector
Producer
Grid blocks 1m by 1m
285
Underburden
Conduction Heat Loss Boundary
40 m
Conduction Heat Loss Boundary
Grid blocks 1m by 1m
Overburden
735
No Heat Loss Boundary
Elevation, m
Deep Reservoir
No Heat Loss Boundary
550 m
750
Producer
Injector
Underburden
Grid blocks 1.5m by 1m
Conduction Heat Loss Boundary
67.5 m

Figure 3-5 Schematic reservoir models and numerical grid systems

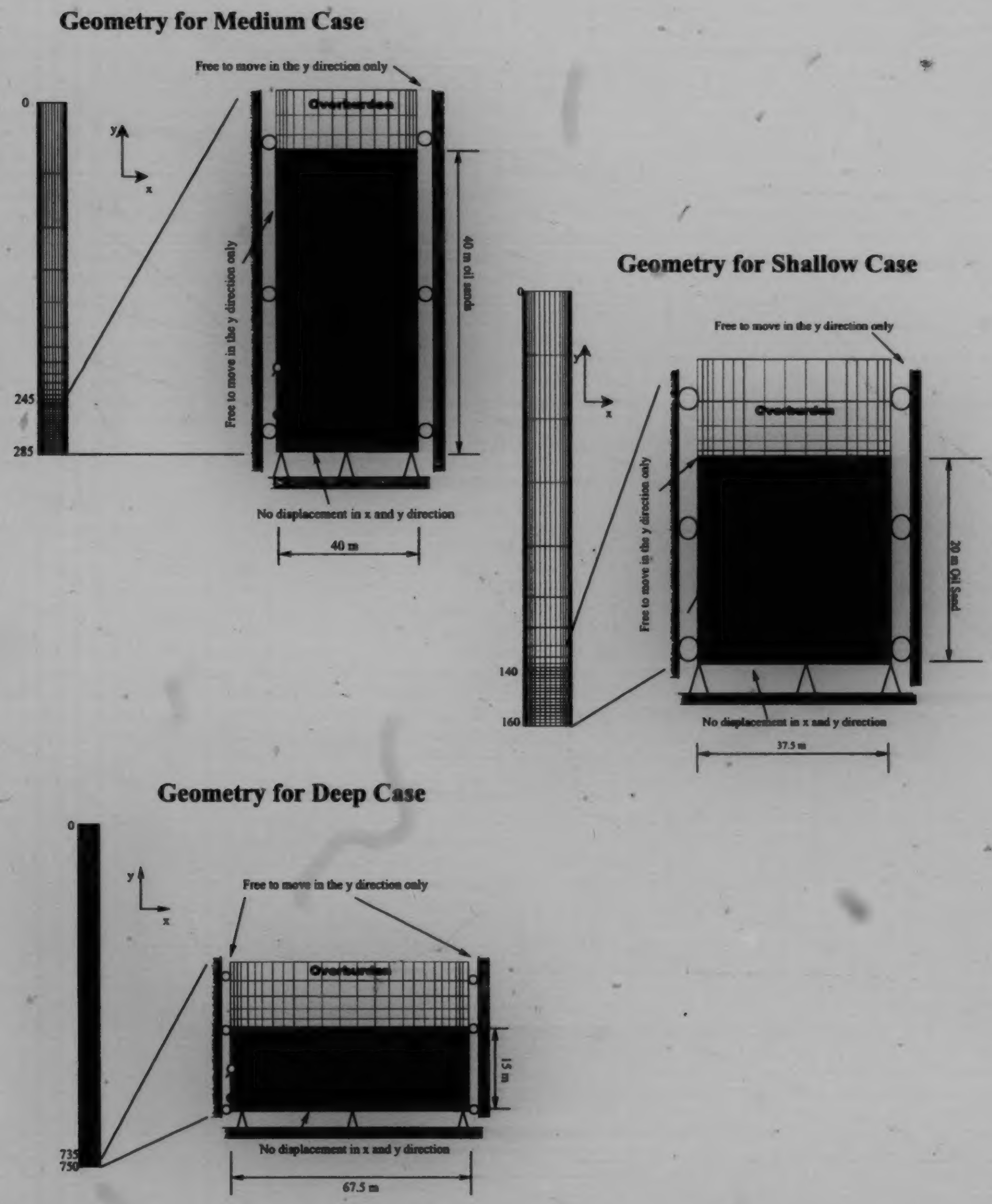
Geometry for Medium Case
Free to move in the y direction only
Overburden
0
245
285
y
x
Free to move in the y direction only
40 m oil sands
No displacement in x and y direction
40 m
Geometry for Shallow Case
Free to move in the y direction only
Overburden
0
140
160
y
x
Free to move in the y direction only
20 m Oil Sand
No displacement in x and y direction
37.5 m
Geometry for Deep Case
Free to move in the y direction only
Overburden
0
735
750
y
x
15 m
No displacement in x and y direction
67.5 m

Figure 3-6 Schematic geometry of the grid systems for the geomechanical analyses

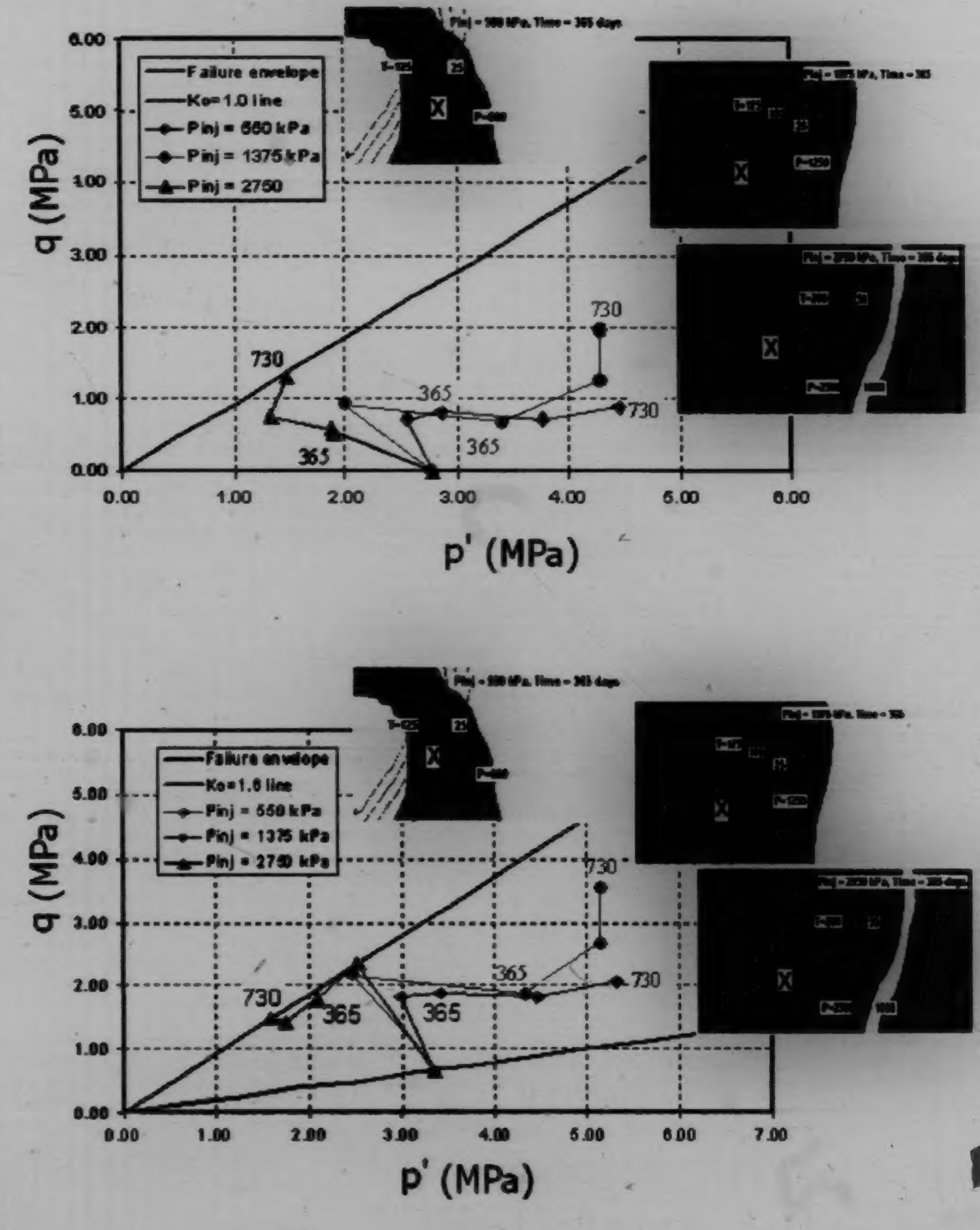

Figure 3-7 Shallow Reservoir Model: Stress path for element adjacent to wellpair

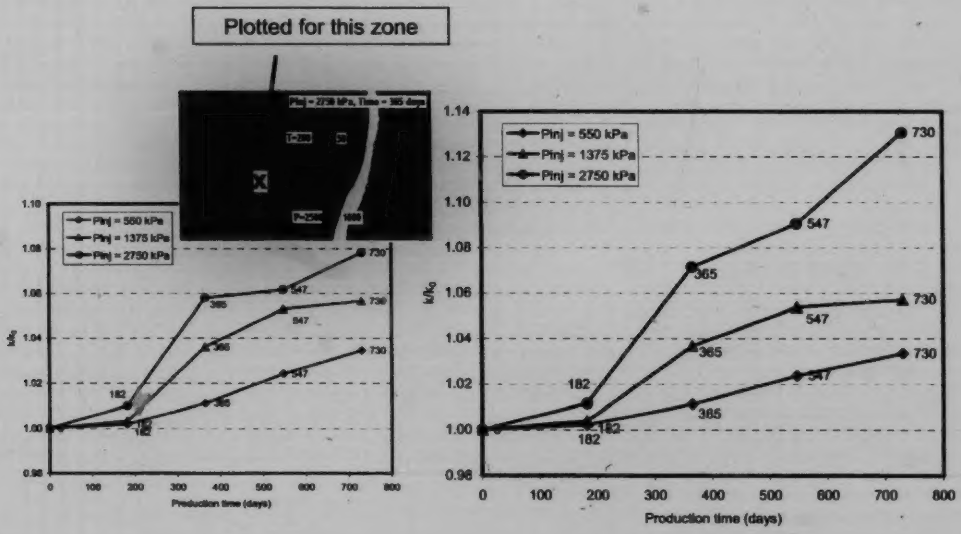

Figure 3-8 Change in absolute permeability for shallow reservoir model

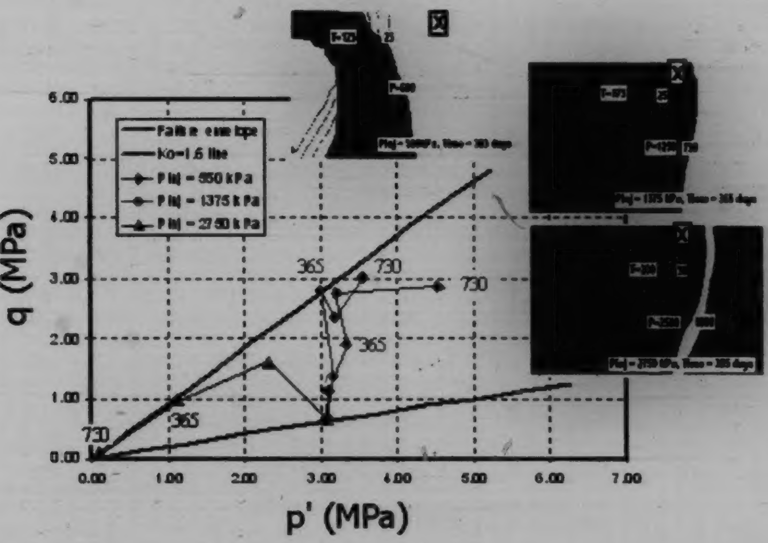

Figure 3-9 Shallow reservoir model: stress path for element at top of reservoir – $K_0 = 1.6$

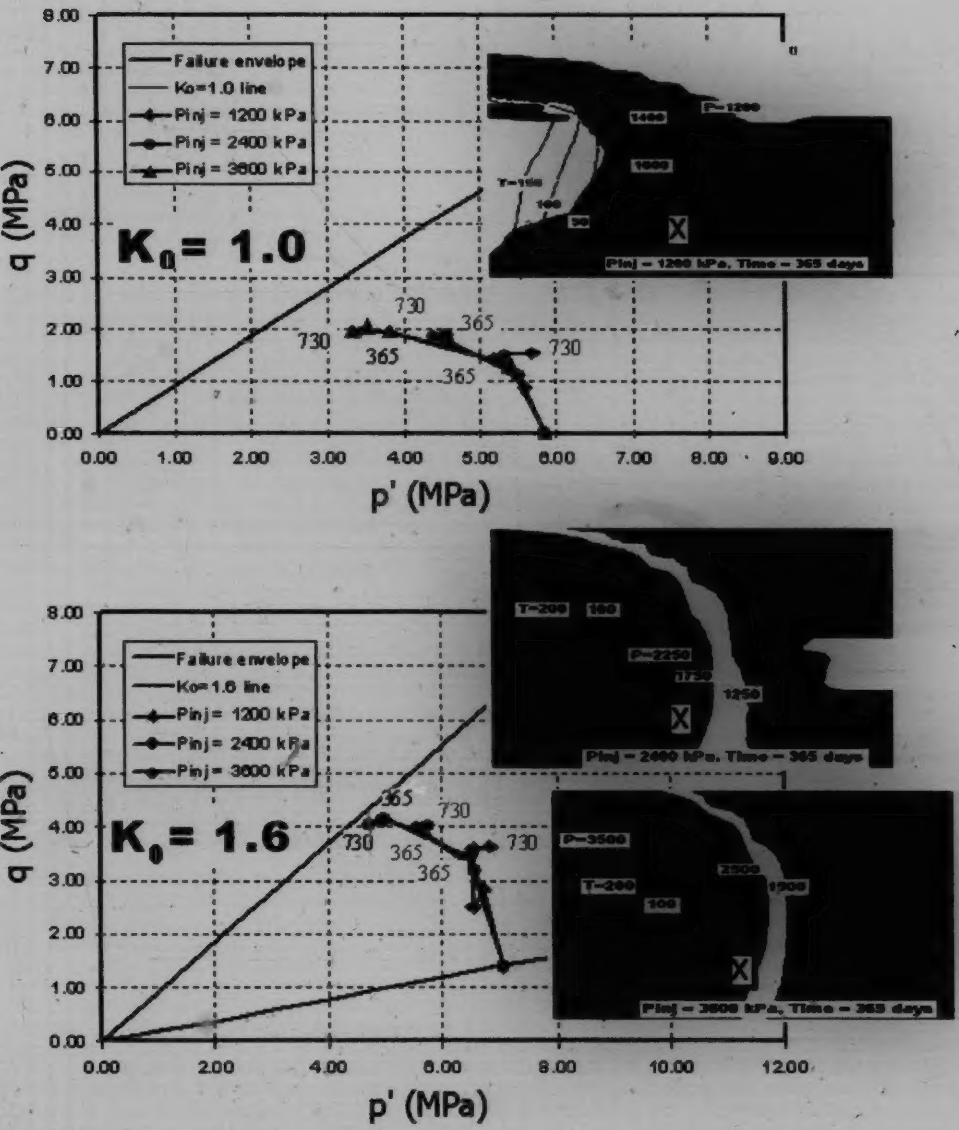

Figure 3-10 Medium depth reservoir model: stress path for element adjacent to wellpairs

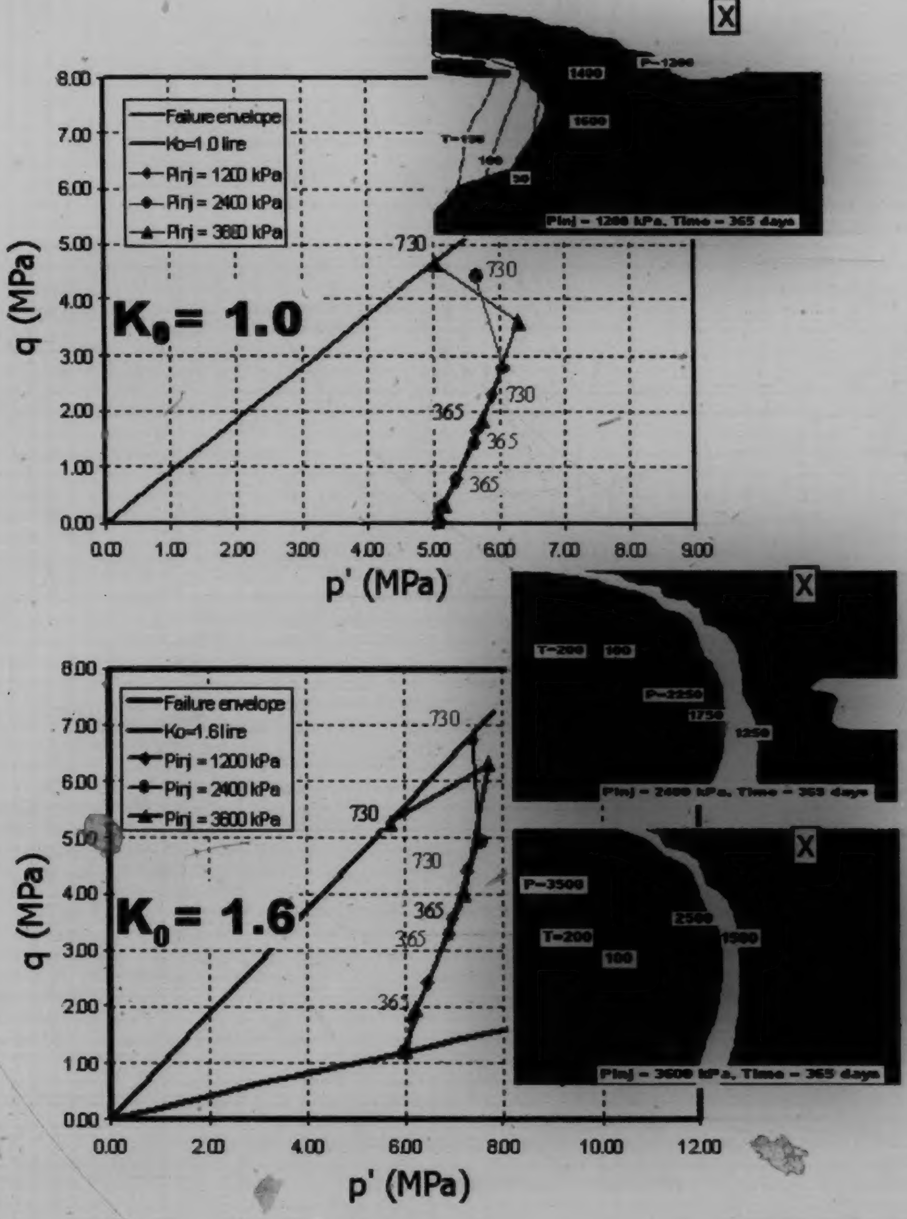

Figure 3-11 Medium depth reservoir model: stress path for element at top of reservoir

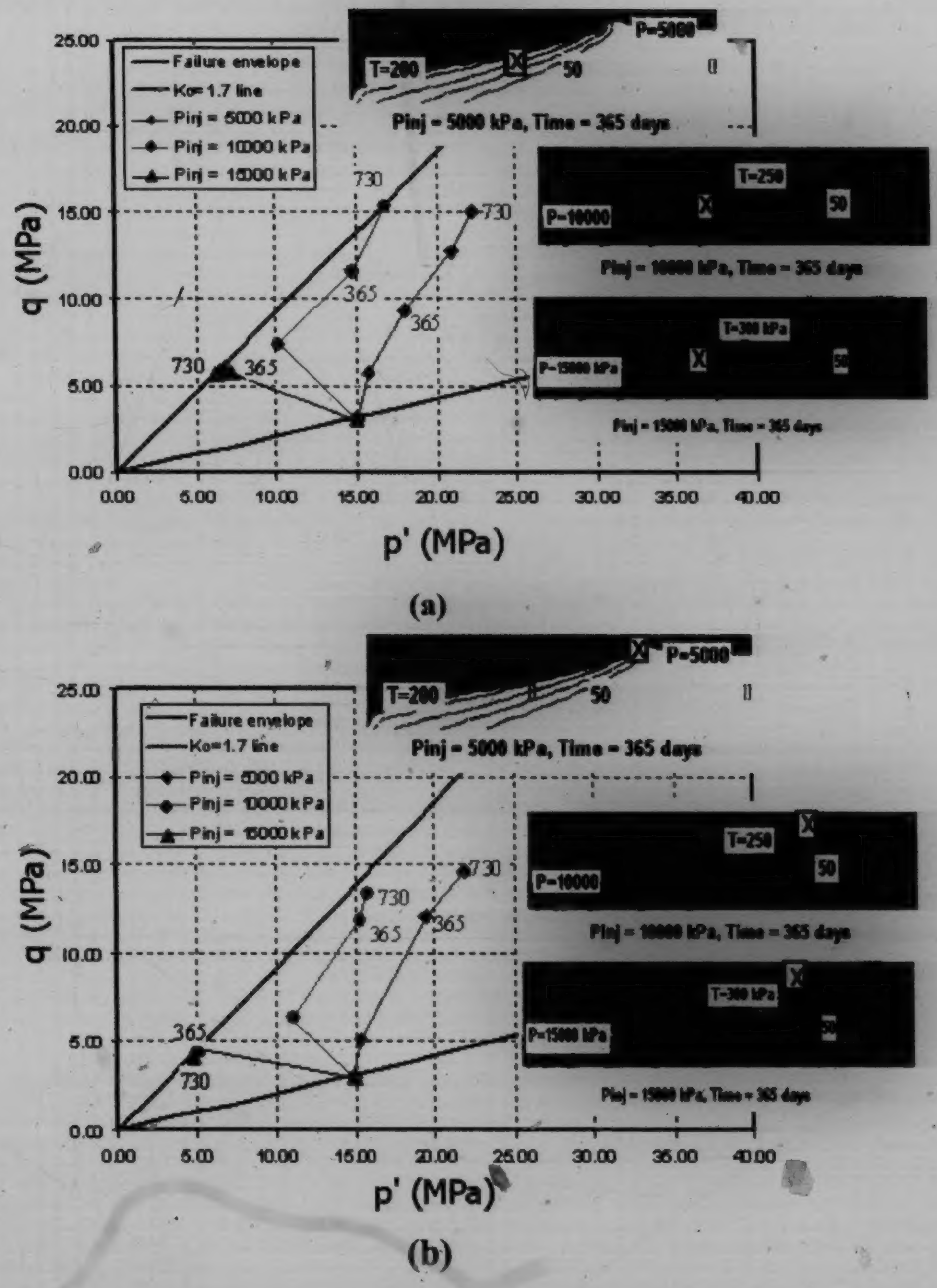

FIGURE 3-12 Deep reservoir model: stress path for element - (a) adjacent to wellpairs and (b) top of reservoir

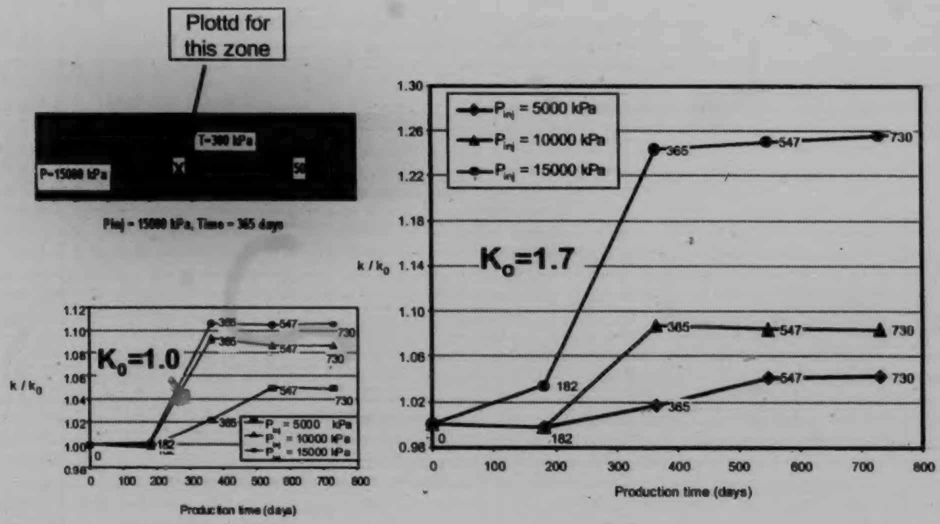

FIGURE 3-13 Change in absolute permeability for deep reservoir model

CHAPTER 4 ISSUES WITH RESERVOIR GEOMECHANICAL SIMULATIONS*

4.1. Introduction

Reasonable prediction of SAGD performance by numerical simulation is an integral component in the design and management of a SAGD project. Conventional reservoir simulation emphasizes multiphase flow in the porous media but generally does not take the interactions between fluid and solid into account. It applies elastic rock compressibility to characterize the coupling mechanism of multiphase flow and rock skeleton. The assumption of this treatment is that the boundary loads and temperature are constant, $\Delta p = \Delta\sigma'$ (Dusseault, 1999). All analytical flow equations in petroleum engineering are based on this assumption. It is clear that the recovery process of conventional oil from sandstones and most carbonate rocks can roughly satisfy this assumption. For the SAGD process, however, volumetric deformations within the reservoir due to pore pressure and temperature changes result in variations of both in situ stress and strain. These stress and strain variations are functions of the in situ boundary conditions. Due to different directional deformation in response to in situ heating, the total stresses in vertical and horizontal directions may also vary. Moreover, the SAGD process is mainly applied in friable or uncemented (unconsolidated) oil sands that geomechanically behave differently to their cemented counterparts. Under these conditions, the assumption used in conventional numerical simulation is no longer effective because the total stress changes within the reservoir.

Although a comprehensive theory of coupled problems between fluids and solids was proposed by Biot in 1941, many research papers on the numerical simulation of these problems were based on single-phase fluid flow in a linearly elastic porous medium under isothermal conditions. Over the last decade, increased research has resulted in a greater understanding of this complex, multiphase physical system and has lead to more realistic analyses of the oil sand recovery process. Ito (1984) and Beattie et al. (1991) expressed the deformation and failure behavior of oil sand as a function of pore pressure. As described above, the integration of stress change should be included in these analyses. Otherwise, it is not possible to understand the real reservoir mechanisms, and to consider potential or favorable operational strategies. Vaziri (1986) gave theoretical expressions of pore fluid pressure under undrained conditions and of the change of soil stress under drained conditions in terms of elastic and thermal properties of multi-phase soil systems. He also developed a finite element code with a set of finite element formulations which link temperature changes to fully coupled stress/deformation and fluid-flow phenomena (1988). Tortike and Farouq Ali (1987), Fung et al. (1994), Settari and Mourits (1995), and Settari and Walters (1999) also conducted research in this field, which are described in Chapter 2 in detail. Settari et al. (2001) summarized the advances in coupled reservoir and geomechanical modeling and presented the results of several case studies in the field. It is shown that coupled reservoir modeling can help better understand the phenomena occurring in the reservoir. They indicated that with the help of coupled reservoir and geomechanical modeling, recovery mechanisms could be better understood, which may influence economic evaluations.

---

* Part of this chapter entitled *Issues with Reservoir Geomechanical Simulations of the SAGD Process* (Li, P., Chalaturnyk, R.J., and Polikar, M.) has been published by the Journal of Canadian Petroleum Technology (JCPT), Volume 43, No. 5, pp. 30-40. May 2004. It was first presented at the 3rd Canadian International Petroleum Conference (the 53rd Annual Technical Meeting of the Petroleum Society), June 11-13, 2002, Calgary, Alberta.

The SAGD process remains one of the most promising technologies for developing the vast in situ oil sands resources. Chalaturnyk conducted an uncoupled reservoir-geomechanical simulation to demonstrate the geomechanical behavior associated with the SAGD process for the UTF Phase A project (Chalaturnyk, 1996; Chalaturnyk and Scott, 1997). As discussed in Chapter 3, a decoupled approach to conduct reservoir geomechanical simulations can illustrate the possible range of geomechanical responses that may be expected during the SAGD process. No feedback from the geomechanical model into the reservoir simulator is incorporated in the decoupled approach and as such, they remain unsatisfactory in terms of understanding the consequences of geomechanics on the bitumen recovery and other economic indicators for the SAGD process, such as SOR.

As presented by Rutqvist et al. (2002), an alternative to develop a single coupled code (which presents significant challenges), is to sequentially couple two existing well-established codes; one to handle the non-isothermal, multiphase fluid flow associated with the SAGD process and one to handle the geomechanical processes. Although, in principle, a sequential coupling of two codes is less efficient than having a single code, an obvious advantage with coupling of existing well-accepted codes is that they are well tested and widely applied in their respective fields. This technique has now been applied successfully by a number of groups. The work of Rutqvist et al. (2002) has succeeded in linking TOUGH2 and FLAC3D to study problems in storage of carbon dioxide in aquifers and nuclear waste isolation. Work at the University of Alberta was successful at sequentially coupling STARS and FLAC, and Chapter 5 will present the methodology for sequentially linking EXOTHERM and FLAC to conduct coupled reservoir geomechanical simulations.

In general, the major process feedback from the geomechanical model into the reservoir simulator is the change in absolute permeability that occurs as a result of the matrix volume changes due either to bulk compressibility or shear induced effects (Table 4-1). This portrays a very simplistic picture of the interaction between geomechanical processes and the multiphase flow considerations associated with the SAGD process. The geomechanical process impacts many more process variables than just absolute permeability and even the incorporation of absolute permeability modifications is complex. This chapter discusses how the volume changes induced through geomechanical processes impact several key process variables of importance to the SAGD process. As the industry moves forward with sequentially coupled simulations of the SAGD process, it will be important to evaluate the importance of these interrelationships, and incorporate them accordingly into the numerical [illegible]dels.

4.2. Geomechanical Behavior in the SAGD Process

In the SAGD process, saturated steam is continuously injected into the bitumen-bearing formation. So, with increasing time of steam injection, the pore pressure and the temperature in the formation around the injector increase. However, both pore pressure and temperature decrease rapidly from the steam chamber values to initial reservoir values over a certain distance outwards from the steam chamber surface.

The geomechanical phenomena of volumetric straining under the combined effect of pore pressure changes (i.e. effective confining stress changes) and shear stress constitutes the primary factor influencing SAGD processes. Scott et al. (1991) outlined the effects of steam stimulation on oil sands pore volume changes. A temperature increase causes thermal expansion of sand grains and matrix, which increase shear stresses. Pore pressure increase decreases the effective confining stress and causes an unloading of the reservoir. These processes combine to result in a net change in the reservoir pore volume and permeability.

For a discussion of the issues associated with the reservoir geomechanical processes of the SAGD process, the reservoir has been subdivided into three zones or regions; drained, partially drained, and undrained. The extent of these regions is based on drainage conditions within that zone that directly impact the pore pressure evolution. The following sections describe the conditions for each zone.

4.3. Geomechanical Zones around a Steam Chamber

Drained, partially drained, and undrained zones have been defined based on the drainage conditions within the reservoir and thus relate directly to the ability for pore pressures to develop or dissipate within the formation. Figure 4-1 shows a schematic representation of the three zones surrounding a steam chamber.

In the SAGD process, the high pore pressure front will generally advance ahead of the high temperature front outside the steam chamber (Chalaturnyk, 1996). This condition creates varying geomechanical behavior in different zones outside the steam chamber. Along the direction normal to the steam chamber, temperature decreases from the highest value at the steam chamber surface to initial reservoir temperature. Thus, the bitumen viscosity has an opposite trend and it increases from the lowest value at the steam chamber surface to the highest value (initial bitumen viscosity) along the same direction. The variation of bitumen viscosity affects the pore pressure dissipation significantly. The water saturation combined with the bitumen mobility (or immobility) also strongly affects the pore pressure dissipation process.

So, in the course of the SAGD process, geomechanical analyses cannot be performed according to either drained or undrained conditions only for all the reservoir material. It should be noted that high water saturation layers will respond immediately to steaming, and the combination of the water-bearing shale and sand partings leads to rapid pressure transmission. These properties make the reservoir geomechanical analysis very complex. Since bitumen viscosity exerts a dominant influence on the fluid mobility within oil sands reservoirs and thus, on pore pressure dissipation, the three zones are defined relative to bitumen viscosity. In the following discussion, initial suggestions for possible ranges of bitumen viscosity for each zone are provided but they should be treated as suggestions only.

4.3.1 Drained Zone

Farouq Ali and Meldau (1979) proposed a steam drive screening criterion in which oil viscosity is an important factor. They indicated that a heavy oil reservoir is appropriate for steam drive process if the oil viscosity is less than 1000 mPa·s (1 mPa·s = 1 cP). However, other researcher gave a range of oil viscosity (200-1000 mPa·s) in their steam-drive screening criterion (Iyoho, 1978). So, it is reasonable to take the maximum value, 1000 mPa·s, as the upper limit of viscosity for the first geomechanical zone (drained zone), which is adjacent to the steam chamber directly. In this zone, with increasing the distance from steam chamber surface, the bitumen viscosity increases until it reaches 1000 mPa·s. It is not very difficult for the pore fluids to flow under some driving forces. However, compared with the viscosity of water or steam, the bitumen viscosity in this zone is still high. Theoretically, the effective stress variation in this zone is dependent on two factors. One is steam injection pressure that can induce pore pressure increase due to pore fluid flow. Another is thermal expansion that induces both pore pressure and total stress increase (Figure 4-2).

However, from a reservoir geomechanical perspective, the significance of this region is that any geomechanical processes do not lead to the development of additional pore pressures. The fluid mobility within this region is sufficient so that any excess pore pressure (above injection pressure) that may want to develop is immediately "drained" away. For instance, shear induced volume changes will only cause a pore volume change but will not lead to changes in pore pressure. This is not the case for partially drained or undrained regions, as discussed subsequently. For reservoir geomechanical simulations in this region or zone of the reservoir, adopting the pressures and temperatures obtained from the reservoir simulator seems appropriate, as no geomechanical processes will likely impact the pore pressure development within this region.

4.3.2 Partially Drained Zone

The drained zone transitions to a partially drained zone as you move away from the steam chamber. Bitumen viscosity begins to rise and ranges from 1000 mPa·s to 20000 mPa·s. Although it is difficult for bitumen to flow, a small amount of bitumen still has the ability to move under certain pressure gradients. So, this zone is correspondent to partially drained condition in geomechanical analysis. The pore pressure change and effective stress variation is also dependent on the same factors as that in the drained zone, but the magnitude of variation is not the same as that in the drained zone (Figure 4-3).

This transition zone between drained and undrained states is difficult to define explicitly. The rate of pore pressure development and the relative movement of pore pressure and temperature inherently control its size. It is likely that a small partially drained region when injection pressures are close to reservoir pressure will increase in size as the injection pressures are raised above the initial reservoir pressure. The complexity in how to treat this region in a sequentially coupled simulation arises from the treatment of the "rate" of the geomechanical process relative to the fluid mobility.

4.3.3 Undrained Zone

The undrained zone lies adjacent to the partially drained zone and extends to far-field area defined by the initial conditions of the reservoir. Bitumen viscosity is greater than 20000 mPa·s. Under the assumption of rich oil sands (high bitumen saturation and low water saturation), pore pressure dissipation is slow due to the low mobility of the pore fluids. If geomechanical processes impact this region, it is postulated that pore pressure will change under undrained conditions. This has significant consequences in the interpretation of the geomechanical response of the reservoir in this region. Geomechanically, shearing under undrained conditions creates conditions of no volume change but lead to changes in pore pressure. The effective stress variation in this zone is also affected by the total stress change induced by thermal expansion of the steam chamber, drained zone, and partially drained zone (Figure 4-3).

The temperature data measured during the UTF Phase A Project provide an excellent case record to examine the size of the drained, partially drained, and undrained zones. Utilizing temperature measurements near well pair A2, the temperature distribution away from the steam injection well AI2 can be computed. Figure 4-4 illustrates the position of the horizontal well pairs and the temperature measurement points within the geotechnical cross-section. Temperature values for time period beyond 400 days after the start of steaming were chosen because it was only after this time the steam chamber growth within the geotechnical cross section followed conventional SAGD steam chamber growth patterns. Prior to this time, the steam chamber was evolving axially along the A1 well pair from a position north of the geotechnical cross section. By extracting temperature values at 450, 500, 550 600, 650, and 700 days, it is possible to examine the evolution of the drained, partially drained, and undrained zones. Figure 4-5 illustrates the temperature distribution relative to the edge of the steam chamber (assuming 200 °C effectively defines the edge of the steam chamber). Utilizing the bitumen viscosity definition of each zone, as described above, Figure 4-6 clearly shows that for UTF Phase A conditions, the drained zone extended a distance of about 8 m beyond the steam chamber. The partially drained zone maintained a thickness of approximately 4 m, which effectively means that the oil sands reservoir beyond a distance of approximately 12 m away from steam chamber behaves in an undrained manner with respect to geotechnical process.

4.4. Reservoir Properties/Processes Modified by Geomechanics

Using the three regions or zones described above as a basis for discussion, the following sections provide a discussion on how geomechanics affect reservoir properties and flow characteristics associated with the SAGD process.

4.4.1 Pore Pressure Transmission and Fluid Flow

Pore pressure transmission requires a finite but often only minute amount of fluid flow. Thus, significant and extensive pressure transmission can occur even though fluid mass travels only a very short distance. The pore pressure response to SAGD can be defined relative to the three zones discussed earlier. Within the steam chamber and the drained zone immediately adjacent to the steam chamber the pore pressure is equal to the steam injection pressure. Pore pressure equilibration is immediate and maintained at injection pressures throughout the SAGD process. If the steam injection pressure is higher than the initial reservoir pressure, the pore pressure decreases from the injection pressure at the drained zone boundary to the initial reservoir pressure at some distance away within the undrained zone.

By definition, the drained zone has sufficient fluid mobility to dissipate any incremental, excess or extra pore pressure (above injection pressure) that could be generated by geomechanical processes. This is not the case for the partially drained or undrained zones. Pore pressure increase within these zones can result from three sources.

The first and most obvious source is conventional pore pressure propagation due to flow (under an imposed gradient) from the steam chamber surface through the drained zone and into these regions. Flow under these conditions would include low viscosity bitumen and water. As the bitumen moved through the partially drained zone, it would cool, become more viscous and would lead to a progressive reduction in fluid mobility. This would retard the migration of pore pressure towards and into the undrained zone.

Pore pressure and temperature data measured during the UTF Phase A project provide an excellent case record to examine the relative position of the pore pressure front with respect to the steam chamber. Utilizing the temperature measurements at Well AT9 and the pore pressure contours developed from all the pore pressure measurements (Chalaturnyk, 1996), the relative position of the pore pressure front over a period of 450 days to 700 days after start of steaming during the Phase A project can be examined. Assuming that the 200°C contour defines the boundary of the steam chamber, the distance from this contour to each magnitude of pore pressure provides a measure of how far out in front of the steam chamber the pore pressure is migrating. Figure 4-7 shows that the injection pressure front tracks along very well with the temperature front remaining approximately 10-15 m in front of the steam injection temperature. Note that this distance correlates very well with the beginning of the undrained zone.

The second source of pore pressure increase is the total stress change caused by temperature increase. Foregoing the issue of rate of total stress change relative to rate of pore pressure dissipation within the partially drained or undrained zones, it is well accepted that a change in total stress under these undrained conditions can lead to pore pressure changes and is generally described by Equation (4-1)

$$\Delta p = B\left[\Delta\sigma_3 + A\left(\Delta\sigma_1 - \Delta\sigma_3\right)\right] \tag{4-1}$$

The parameter B defines the pore pressure change due to hydrostatic or isotropic total stress changes whereas the parameter A defines the pore pressure change due to shear stresses. For dense oil sands, $B \approx 0.7$ and $A \approx -0.35$. The negative A parameter signifies that shearing under undrained conditions will lead to a reduction in pore pressure. Figure 4-8 shows the results of an undrained triaxial compression test on dense, artificial, bitumen saturated oil sands specimens. While these samples do not replicate the in situ diagenetic fabric of McMurray Formation oil sands, these specimens are extremely dense ($I_D = 145\%$). The results show that even for a low initial effective confining stress of 100 kPa, the deviatoric stress at failure reaches 10 MPa and the pore pressure decreases by more than 4 MPa. Clearly, shearing under undrained conditions can lead to a substantial reduction in pore pressure.

The third source of pore pressure change is the difference in volumetric thermal expansion coefficients between the reservoir fluids (particularly bitumen) and the solids. This source of pore pressure change is primarily restricted to the partially drained zone where the temperature is decreasing towards to reservoir temperature. Assessing the relative contribution of this source is difficult because of the competing processes of thermal expansion and bulk volume expansions due to increasing pore pressures (decreasing effective stresses). These two processes tend to balance each other.

Under completely undrained conditions, however, the volume increase due to pore fluid expansion is much larger than that due to oil sand structure expansion and can lead to substantial increases in pore pressure.

4.4.2 Gas Evolution

Generally, in situ bitumen contains varying amounts of dissolved gas. As discussed above, there exists the possibility that geomechanical processes can lead to pore pressure reduction within the undrained zone, as described above and illustrated in Figure 4-8. Therefore, within the undrained zone, if the pore pressure decreases below the saturation pressure due to geomechanical behavior, dissolved gas can nucleate and gradually begin evolving from the bitumen and water phases. In porous media, nucleation takes place on surface of the particles, poorly wetted cavities, and pre-existent trapped gas (Sheng, 1997). This process requires that ~40 CH_4 molecules join before a non-collapsing bubble is generated. The migration or movement of this bubble is seriously retarded by the high viscosity of bitumen (Dusseault, 2001). Gas bubble growth is also strongly controlled by the viscous forces of bitumen. In fact, the gas bubbles cannot grow by overcoming the high viscous resistance of the surrounding bitumen. Therefore, in the area where geomechanical processes induce a pore pressure decrease as a response to SAGD, the state of bitumen is changed from bitumen with solution gas to bitumen with solution gas and entrained gas bubbles.

Gas evolution due to pore pressure decrease in the undrained zone may reduce the absolute permeability. With the expansion of steam chamber, the drained zone may move to the area previously occupied by the undrained zone. Then the evolved gas bubbles may attempt to pass through pore throats. If the actual pressure difference across a pore throat is less than that predicted by Equation (4-2)

$$\Delta p = 2\sigma(1/r_1 - 1/r_2) \tag{4-2}$$

the bubble may plug the pore throat and prevent fluid from flowing, as schematically illustrated in Figure 4-9. Fortunately, geomechanical effects, such as isotropic unloading and shear dilation, can help reduce the pore constrictions.

4.4.3 Porosity

Porosity is perhaps the single most important reservoir parameter modified through geomechanical processes. Almost all reservoir properties utilized in SAGD simulations are linked to porosity. Porosity can be increased or decreased by geomechanical behavior in the SAGD process.

When the mean effective confining stress decreases (pore pressure increases), porosity becomes larger simply due to bulk compressibility increases. Bulk compressibility of oil sands is highly nonlinear, especially in the low effective stress ranges. As the effective stress nears zero, isotropic bulk, rock, and pore compressibilities all increase dramatically (Chalaturnyk, 1996), as illustrated in Figure 4-10. It is important to note that the configuration of the grains or their relative position is, for the most part, unchanged for this mechanism of pore volume change. The grains simply move apart without any relative rearrangement of the grain packing.

While a substantially more complicated process, shear stress induced volume changes (dilation), will also produce changes in porosity. In contrast to bulk compressibility pore volume changes, however, dilation produces substantial relative motion of the grains and significant changes in the pore geometry within dense sand. Clearly the impact of porosity changes due to these two geomechanical mechanisms will create different pore geometry and it seems reasonable to expect that they will influence reservoir properties such as absolute permeability differently.

It is instructive to examine the largest possible range of porosity changes that could be expected given a specific initial state. Based on Graton and Fraser (1935), six simple sphere packing cases exist, in which the tightest packing has the lowest porosity of 25.95% and the loosest packing has the highest porosity of 47.64%. Therefore, the difference between these two values is 21.69%, which means that if the tightest packing is transformed into the loosest packing, the porosity will be increased by 21.69%. In reality, owing to the grain rugosity and irregular packing, such as chaotic packing, haphazard packing, and chance packing (Graton and Fraser, 1935), porosity cannot reach the highest value. The above value helps provide limits on the possible magnitude of porosity change to be expected from geomechanical processes.

Tortike and Farouq Ali (1993) established the following Equation (4-3) to calculate porosity change based on volumetric strain:

$$\phi = \frac{\phi_0 + \varepsilon_v - (1-\phi_0)\alpha_s(T - T_0)}{1 + \varepsilon_v} \tag{4-3}$$

Equation (4-3) makes no distinction of the geomechanical processes involved in achieving a particular volumetric strain, ε_v. Also note that Equation (4-3) includes the thermal expansion coefficient, α_s, of the solids. The reason for this is to adjust for the increase in the volume of solids due to thermal expansion.

4.4.4 Absolute Permeability, k_a

The permeability for a porous medium having orthogonal principal axes is a second-rank symmetric tensor (Equation (4-4)). This is consistent with the reality because the permeability parallel to the bedding plane is often larger than that perpendicular to the bedding plane.

$$[k] = \begin{bmatrix} k_{11} & k_{12} & k_{13} \\ k_{21} & k_{22} & k_{23} \\ k_{31} & k_{32} & k_{33} \end{bmatrix} \tag{4-4}$$

Assuming the principal axes of permeability coincide with the directions of the coordinate system, *[k]* becomes Equation (4-5) (Collins, 1961)

$$[k] = \begin{bmatrix} k_x & 0 & 0 \\ 0 & k_y & 0 \\ 0 & 0 & k_z \end{bmatrix} \tag{4-5}$$

The permeability *k* of an unconsolidated sand can be expressed in terms of the intrinsic properties of the medium as Equation (4-6) (Panda and Lake, 1994)

$$k = \frac{\phi^3}{2\tau(1-\phi)^2 a_v^2} \tag{4-6}$$

Absolute permeability of oil sands increases considerably during isotropic unloading and shear dilation because both the tortuosity of flow and the specific internal surface area decrease and porosity increases. However, shear dilation introduces different variations of k_x, k_y, and k_z. The mathematic expression relating these permeability changes to shear dilation is not available.

Equation (4-6) is difficult to use because the tortuosity and specific internal surface area are not available when geomechanical effects occur. Tortike and Farouq Ali (1993) and Touhidi-Baghini (1998) established Equation (4-7) and Equation (4-8), respectively, relating permeability variation to volumetric strain based on the Kozeny-Carman model

$$\frac{k}{k_0} = \frac{\left[1 + \frac{\varepsilon_v}{\phi_0} - \frac{\alpha_s \Delta T\left(1-\phi_0\right)}{\phi_0}\right]^3}{1+\varepsilon_v} \tag{4-7}$$

$$Ln\frac{k}{k_0} = \frac{B}{\phi_0}\varepsilon_v \tag{4-8}$$

In Equation (4-8), B value was obtained from lab testing results based on outcrop bitumen free oil sands samples. B is equal to 2 and 5 for horizontal and vertical core specimens, respectively. It should be noted that these equations give an isotropic permeability change due to geomechanical behavior. Based on Tortike's equation, the absolute permeability change due to the transformation of packing cases (Graton and Fraser, 1935) can be easily found. Theoretically, if porosity is increased by 8.1% and 21.69%, volumetric strain will be 0.134 and 0.293, and the final permeability becomes 2.12 and 7.46 times larger than the initial values, respectively.

Based on reconstituted Athabasca oil sands specimens, Scott et al. (1991) obtained increases in absolute permeability of approximately 30% and 70% by unloading from initial effective confining stresses of 1000 kPa and 4360 kPa, respectively. They also obtained a 30% increase of permeability for an increase in volume of 3% during shear. Other experimental studies have shown that a two-order of magnitude increase in permeability is possible in stabilized dense sands subjected to shear dilation (Mori and Tamura, 1986). Based on the full strain field analysis, Chalaturnyk (1996) found a maximum shear strain of 3.0% and a volumetric strain of 2.6% between well pairs of A1 and A2 at UTF Phase A site. The absolute permeability within this region increased by 30%, increasing from 7.5 darcies to 9.8 darcies.

To illustrate the impact of absolute permeability variation on SAGD production performance, the two relationships (Equation (4-7) and Equation (4-8)) were applied in sequentially coupled simulations using STARS and FLAC. The two simulators are sequentially coupled in that for each time step, pressure and temperature are passed to FLAC from STARS and a geomechanical simulation is completed. The resulting change in volumetric strain, converted to a change in absolute permeability using Equation (4-7) and (4-8), is passed back to STARS and the next time step in STARS is completed with the updated absolute permeability. This does not fully satisfy the issues in conducting a sequentially coupled simulation but it does provide improved simulations to examine the impact of absolute permeability change on SAGD performance. For the shallow reservoir case (analogous to UTF Phase A) described in Chapter 3, the results of the sequentially coupled simulation are provided in Table 4-1. Again, while not meant to be conclusive, only modest increases in recovery are achieved for this case.

4.4.5 Relative Permeability, k_{rw}, k_{ro}, and k_{rg}

Relative permeability is the ratio of effective permeability to absolute permeability. Experimental test data show that effective permeability varies even more significantly than absolute permeability as geomechanical behavior occurs. During triaxial compression tests, a 50-fold increase in effective permeability to water was measured when the specimen volume had increased by 1% (Wong et al., 1991). Moreover, the effective permeability to water can increase by three orders of magnitude as the result of a 17% increase in pore volume or a 6% increase in total volume brought about by shear dilation (Scott et al., 1991). Figure 3-4, which summarizes the experimental work of

Oldakowski, shows the influence of volumetric strains for several test types on the effective permeability to water.

The improvement of effective permeability also results from isotropic unloading and shear dilation. In the drained zone, the condensed water can occupy the increased pore space rapidly because the mobility ratio of water to bitumen is high. Thus, water porosity and water saturation increase, and as a result, effective permeability to water is improved. In the partially drained zone, isotropic unloading plays an important role initially, and it ceases to dominate the permeability enhancement when water porosity starts to increase by shear dilation. In the undrained zone, gas may come out of solution and bitumen expands. Clearly, effective permeability enhancement in the undrained zone is more complex and is likely less dramatic than illustrated in Figure 3-4.

Oldakowski (1994) obtained an equation describing the relationship between effective permeability to water and water porosity for the specimens containing less than 2% fines (< 45 μm), which is Equation (4-9)

$$\log k_{ew} = -5.868 + 36.20\phi_w \tag{4-9}$$

This equation may be applied in the drained zone and partially drained zone.

The variation of relative permeability of different pore fluids should be calculated based on both the changed effective permeability and absolute permeability. Since shear dilation and isotropic unloading have different impacts on pore geometry, relative permeability increases more significantly due to shear dilation than due to isotropic unloading. Moreover, they induce irreversible and reversible relative permeability changes, respectively (Figure 4-11).

4.4.6 Compressibility

As mentioned previously, with decreasing effective stress, bulk compressibility increases significantly. Chalaturnyk (1996) indicated that isotropic bulk compressibility is a strong function of effective confining stress, especially below 1.0 MPa (Figure 4-10). He also found that McMurray formation oil sands have the following bulk compressibility (Equation (4-10)) (applicable only in the range of σ_m' from 100 kPa to 7,000 kPa).

$$c_b = 0.6 \times 10^{-6} + 2.5(\sigma_m')^{-2} \tag{4-10}$$

In conventional reservoir simulation, rock compressibility is the only coupling factor describing the interactions between fluid flow and solid structures in the reservoir. The purpose of this treatment is to deal with the porosity variation due to the pore pressure variation. It is clear that this treatment is not enough because it does not take plastic deformations into consideration. In coupled numerical simulation, major reservoir parameters, such as porosity, absolute permeability, and effective permeability, are all calculated from appropriate geomechanical principles, which include bulk modulus that is the reciprocal of bulk compressibility. Therefore, rock compressibility is no longer necessary in the reservoir numerical simulation.

4.4.7 Thermal Expansion Effect

In a sequentially coupled reservoir geomechanical simulation, the reservoir simulator provides pore pressure distributions of all the three geomechanical zones to the geomechanical simulator. When these pore pressures are input to the geomechanical simulator together with their corresponding temperatures, the pore pressures within the partially drained zone may rise further due to the net volumetric expansion of pore fluids. In addition, when steam injection pressure is equal to the initial reservoir pressure, the effective stress in the drained and partially drained zone is constant. However, the thermal expansion effect may be significant and could apply a large total stress to shale streaks or shale barriers, if they exist. Thus, these shale streaks or shale barriers can be thermally consolidated. Owing to the decrease of their thickness and volume, pore space of the oil sands around these shale materials may increase. Similar to compressibility, the thermal expansion coefficient of reservoir matrix can be applied in geomechanical simulator instead of reservoir simulator.

4.4.8 Saturation, S_o, S_w, and S_g

Saturations vary significantly when isotropic unloading and shear dilation occurs. The reason is the mobility ratio of water to bitumen. When geomechanical behavior creates an extra pore space, water will occupy it rapidly and thereafter water saturation increases. Correspondingly, oil saturations become lower. This phenomenon mainly occurs within the drained zone and partially drained zone.

4.4.9 Capillary Pressure, p_c

Capillary pressure is defined as the differential pressure between the pressures in the nonwetting phase and the wetting phase. Capillary pressure results from the interfacial tension σ_{12} between the two fluids, which is defined in Equation (4-11) (F is the free surface energy per unit interfacial area and Σ is the two-fluid interfacial area per unit pore volume)

$$\sigma_{12} = dF / d\Sigma \tag{4-11}$$

A generalized relationship on arbitrary porous media is expressed as Equation (4-12) (Scheidegger, 1974)

$$p_c = \sigma_{12} S / \phi \tag{4-12}$$

If the porous medium is unconsolidated, and if S_0 is the particle surface area per unit solid volume, then $S = (1-\phi)S_0$. For spherical particles of uniform diameter d, S_0 is equal to $6/d$, and therefore, Equation (4-12) becomes Equation (4-13)

$$p_c = 6(1-\phi)\sigma_{12} / (\phi d) \tag{4-13}$$

Within the drained and partially drained zones, both isotropic unloading and shear dilation can increase the two-fluid interfacial area per unit pore volume. So, interfacial tension decreases based on Equation (4-11). In addition, with increasing temperature, oil-water interfacial tension also decreases (Sanyal et al., 1974,). Generally, porosity increases due to the two geomechanical processes. As a result, the capillary pressure decreases. According to Leverett (1941), capillary pressure can be modified with permeability and porosity (Equation (4-14))

$$P_c = P_{c0}(S_l)\frac{\sqrt{k_0/\phi_0}}{\sqrt{k/\phi}} \tag{4-14}$$

The decreased capillary pressure reduces the volume of the trapped oil at the end of imbibition, i.e. it reduces the residual oil saturation. In addition, it helps overcome the phenomenon of hysteresis between drainage and imbibition. Another effect of the lower capillary pressure is that it can partially avoid absolute permeability decrease due to the bubble plugging effect.

4.4.10 Enthalpy Transmissibility, T_H

The enthalpy transmissibility is calculated by Equation (4-15)

$$T_H = T_w H_w + T_o H_o + T_g H_g \tag{4-15}$$

It is a function of water, oil, gas transmissibility and their respective enthalpies. However, these transmissibilities are dependent on the effective permeability of fluids, which can be increased in varying degrees within the drained zone and partially drained zone by geomechanical behavior. As discussed above, the effective permeability to water can be increased more significantly than that to bitumen. So, the total enthalpy transmissibility is enhanced greatly by the increased water transmissibility.

4.5. Summary

- In the SAGD process, the reservoir can be divided into three geomechanical zones, i.e., drained zone, partially drained zone, and undrained zone, based on oil viscosity ranges. With the expansion of the steam chamber, the three geomechanical zones propagate simultaneously, and the geomechanical phenomena occurring previously in an undrained zone will eventually play a role when this zone becomes drained.

- Sequentially coupled reservoir-geomechanical simulations of the SAGD process must be sensitive to the presence of drained, partially drained, and undrained zones and the potential for geomechanically influenced pore pressure changes.

- Owing to thermal and pore pressure changes in response to SAGD, isotropic unloading and shear dilation occur with varying degrees in different geomechanical zones.

- Geomechanically induced volume changes that lead to pore pressure reductions may initiate gas evolution within the bitumen and water phases. Gas evolution mainly takes place in the undrained zone as a result of dilative shear.

- Sequentially coupled reservoir geomechanical simulations of the SAGD process must treat the influence on absolute permeability of compressibility induced pore volume changes and shear induced pore volume changes differently.

- Absolute permeability change due to geomechanical behavior is complex and its isotropic variation does affect SAGD production performance based on sequentially coupled simulation of STARS and FLAC.

- Geomechanical processes can lead to significant changes in relative and effective permeability. In a similar manner to absolute permeability, relative permeabilities are likely impacted differently by compressibility induced pore volume changes and by shear induced pore volume changes.

- Pore pressure enhancement due to fluid expansion in the partially drained zone and thermal consolidation of shale zones within both drained and undrained zones need to be included in the geomechanical simulation.

- Within the extra pore space induced by geomechanical behavior, saturation redistribution is dependent upon the mobility of pore fluids and condensed water flow.

- Within the drained and partially drained zones, geomechanical behavior helps lower the capillary pressure, which reduces residual oil saturation and partially overcomes the bubble plugging effect.

- Enthalpy transmissibility improves as a result of water permeability increase due to isotropic unloading and shear dilation.

Table 4-1 Impact of absolute permeability variation due to geomechanics on SAGD production performance

Production results	Constant permeability	Procedure verification	Tortike's relationship		Touhidi-Baghini's relationship
			$K_0 = 1$	$K_0 = 1.5$	$K_0 = 1.5$
Cumulative oil production (10^3 m^3)	71.4	71.5	72.7	73.0	74.4
Cumulative steam injection (10^3 m^3)	110.5	110.8	111.7	112.3	113.8
OSR	0.646	0.647	0.651	0.650	0.654
Recovery factor (%)	63.9	64.0	65.1	65.4	66.6

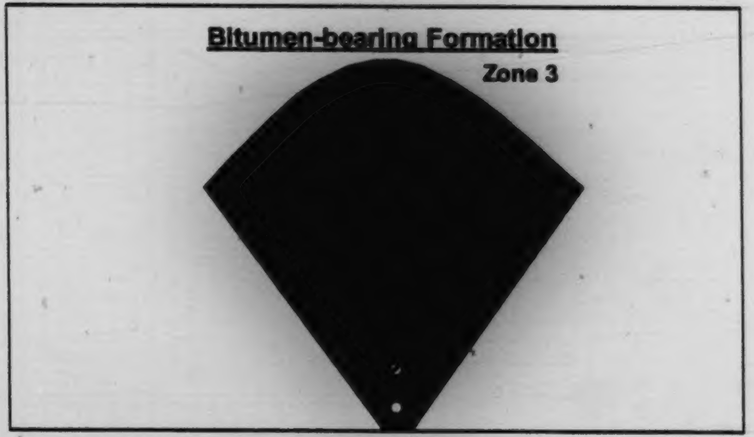
Bitumen-bearing Formation
Zone 3

Zone 1 – Drained zone, $\mu_o \leq 1000$ mPa s

Zone 2 – Partially drained zone, $\mu_o = 1000 – 20,000$ mPa.s

Zone 3 – Undrained zone, $\mu_o \geq 20,000$mPa.s

Figure 4-1 Sketch of the three geomechanical zones

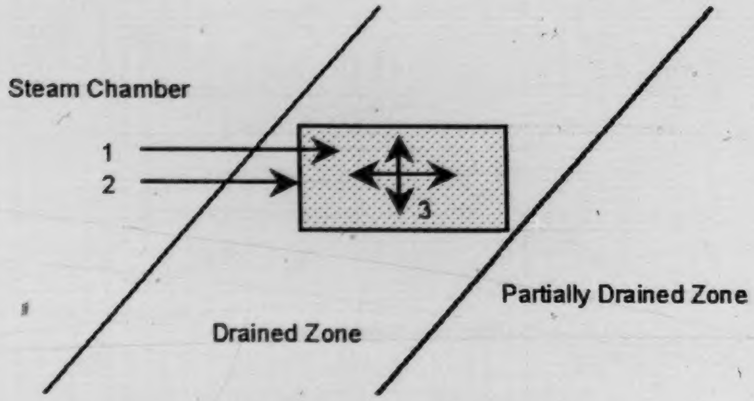
Steam Chamber
1
2
3
Partially Drained Zone
Drained Zone

1. Pore pressure transmission from steam chamber
2. Total stress increase due to thermal expansion
3. Pore pressure increase due to pore fluid expansion

Figure 4-2 Pore pressure generation in the drained zone

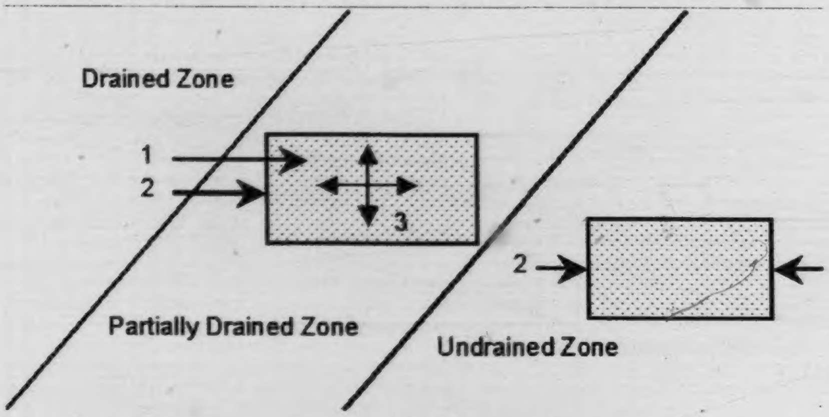
Drained Zone
1
2
3
2
Partially Drained Zone
Undrained Zone

1. Pore pressure transmission from drained zone
2. Total stress increase due to thermal expansion
3. Pore pressure increase due to pore fluid expansion

Figure 4-3 Pore pressure generation in the partially drained and undrained zone

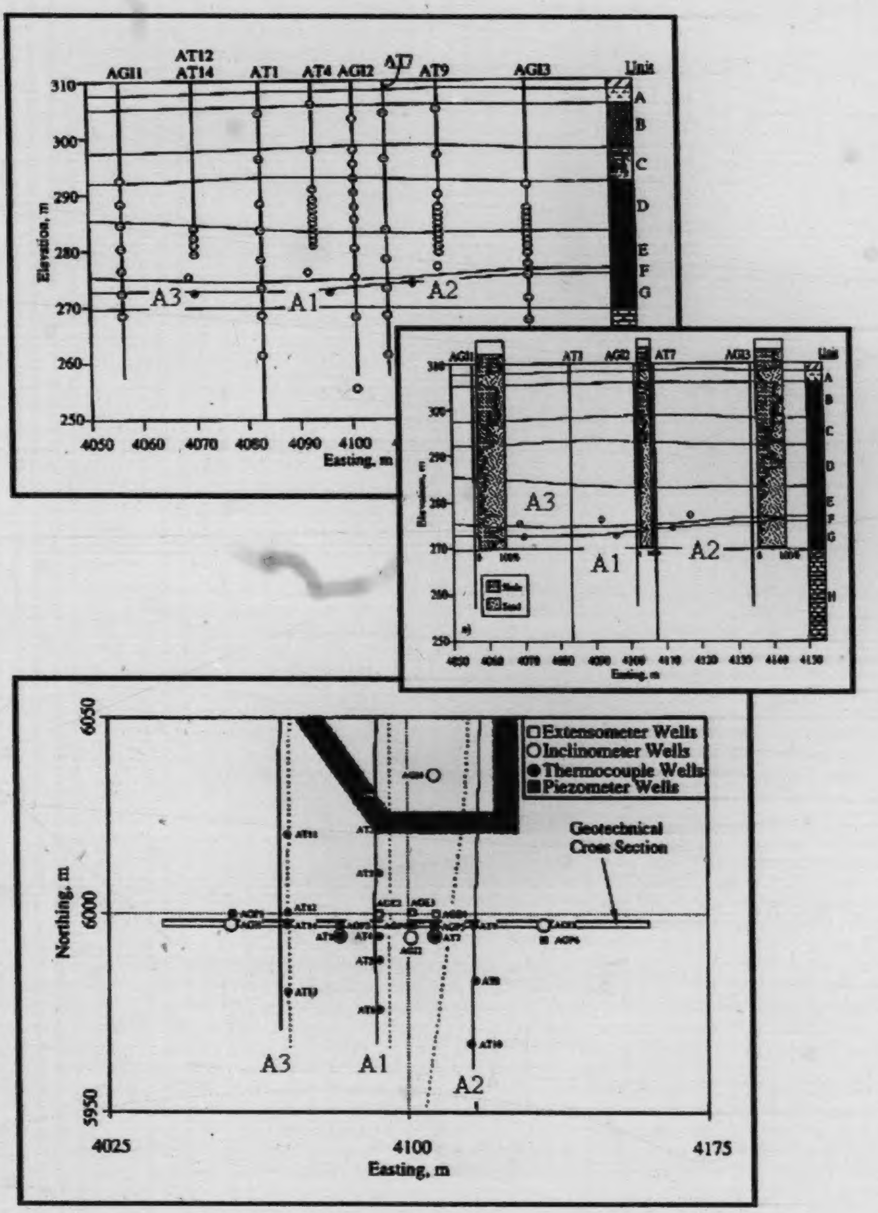
AGI1
AT12
AT14
AT1
AT4
AGI2
AT7
AT9
AGI3
Unit
A
B
C
D
E
F
G
H
A3
A1
A2
Elevation, m
Easting, m
310
300
290
280
270
260
250
4050
4060
4070
4080
4090
4100
4110
4120
4130
4140
4150
Shale
Sand
0
100%
□ Extensometer Wells
○ Inclinometer Wells
● Thermocouple Wells
■ Piezometer Wells
Geotechnical Cross Section
Northing, m
6050
6000
5950
4025
4100
4175

Figure 4-4 Plan view and geotechnical cross-section of UTF Phase A site

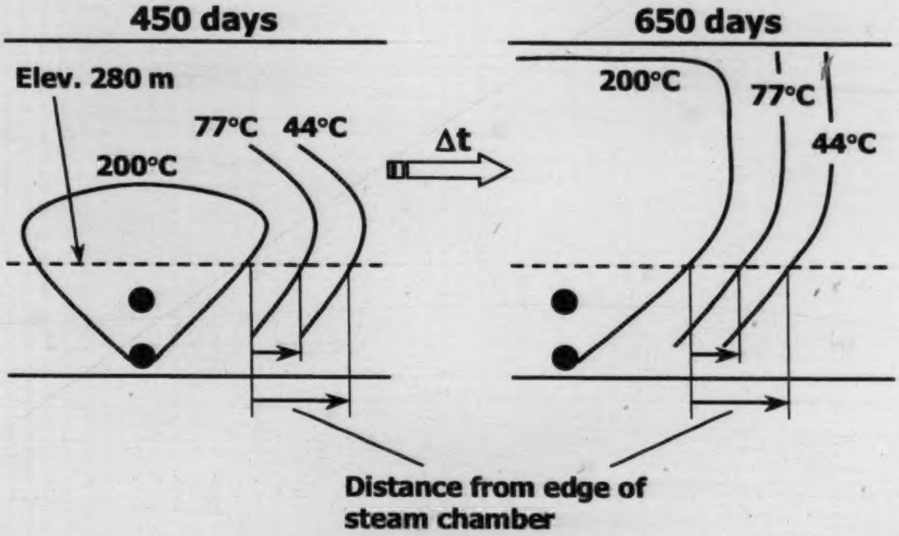
450 days
Elev. 280 m
200°C
77°C
44°C
Δt
650 days
200°C
77°C
44°C
Distance from edge of steam chamber

Figure 4-5 Schematic distance of the outside boundary of three geomechanical zones from edge of steam chamber

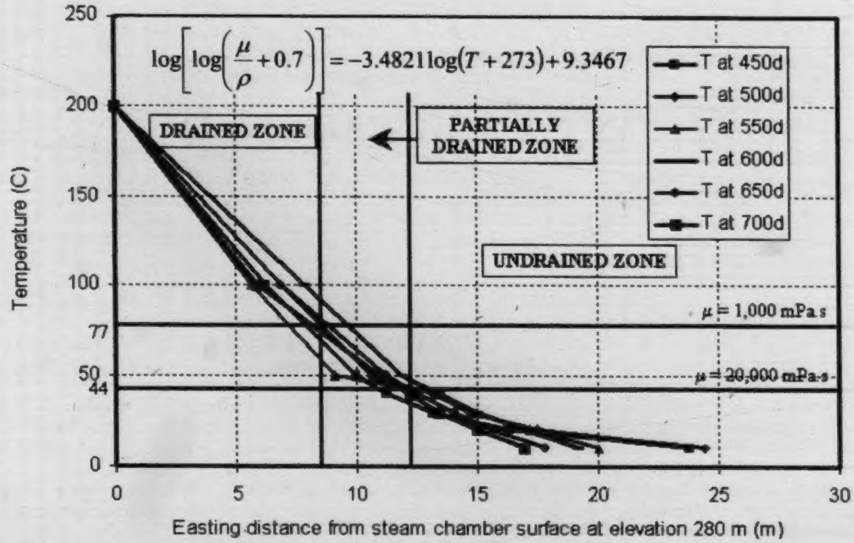

Figure 4-6 The three geomechanical zones in UTF Phase A Project (analytical equation is from Walther formula; density is 1019 kg/m^3 (7°C) and 889 kg/m^3 (220°C) (Butler, 1997); viscosity is 5000000 cp (7°C) and 7 cp (220°C) (Siu, 1991)

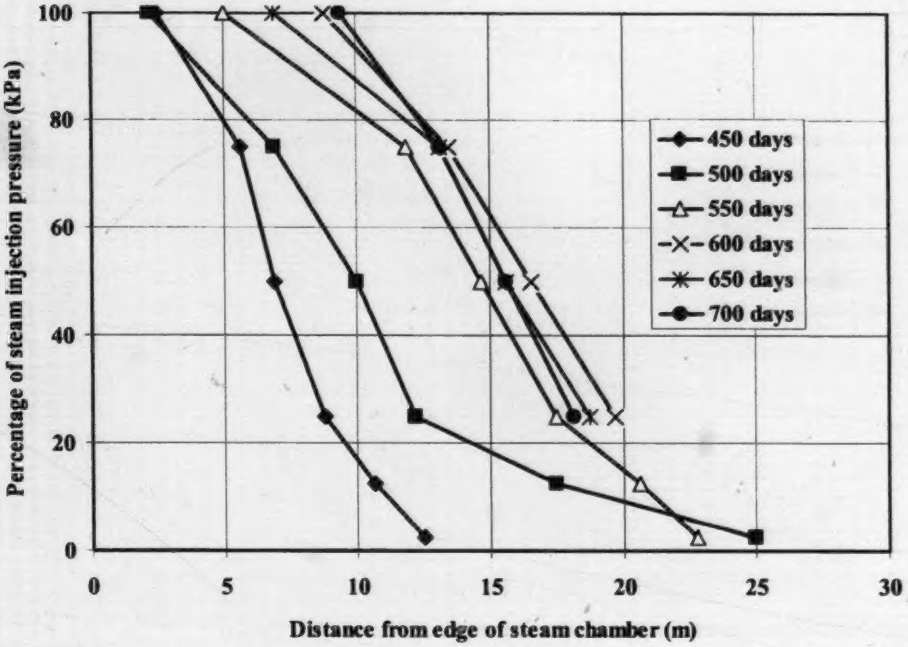

Figure 4-7 Injection pressure front tracks: evolution of pore pressure front in advance of steam chamber, UTF filed data, elevation 280 m (After Chalaturnyk, 1996)

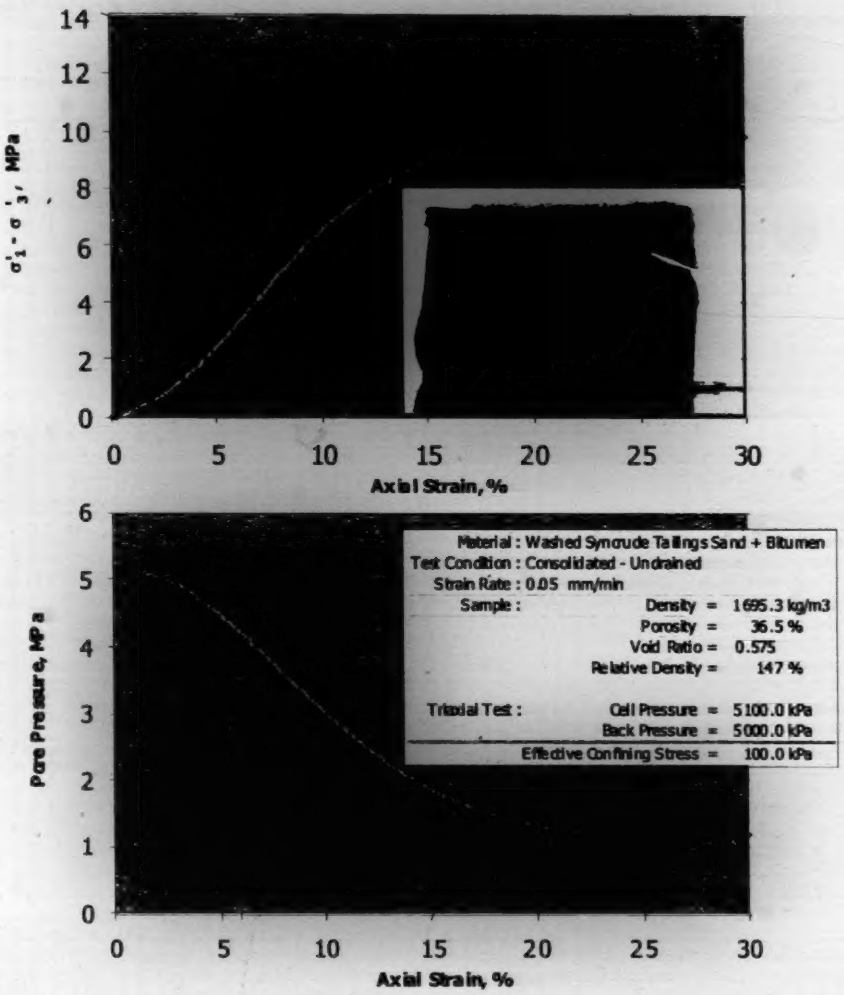

Material : Washed Syncrude Tailings Sand + Bitumen
Test Condition : Consolidated - Undrained
Strain Rate : 0.05 mm/min
Sample : Density = 1695.3 kg/m3
Porosity = 36.5 %
Void Ratio = 0.575
Relative Density = 147 %

Triaxial Test : Cell Pressure = 5100.0 kPa
Back Pressure = 5000.0 kPa
Effective Confining Stress = 100.0 kPa

Figure 4-8 Undrained triaxial compression test

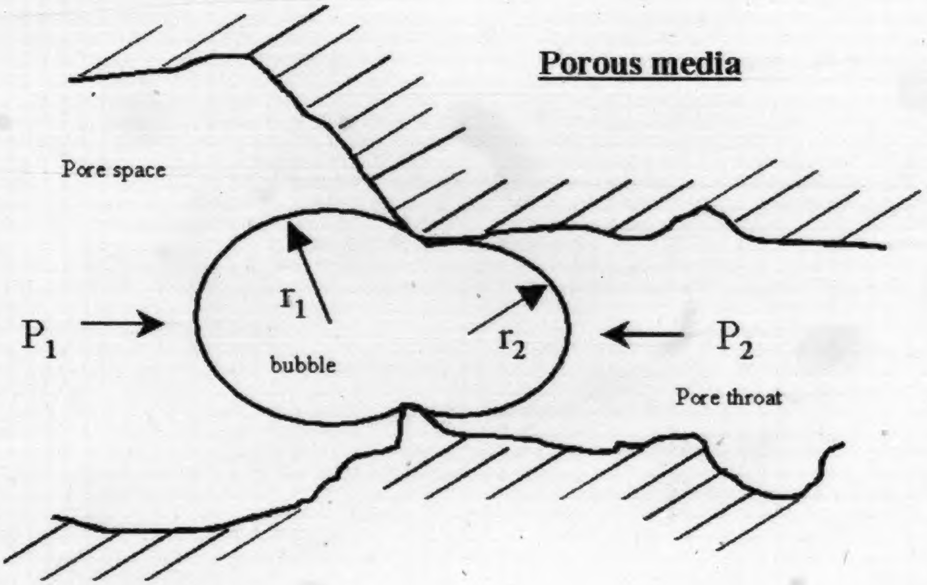
Porous media
Pore space
P_1
r_1
bubble
r_2
P_2
Pore throat

Figure 4-9 Bubble plugging effect (modified after Sheng, 1997)

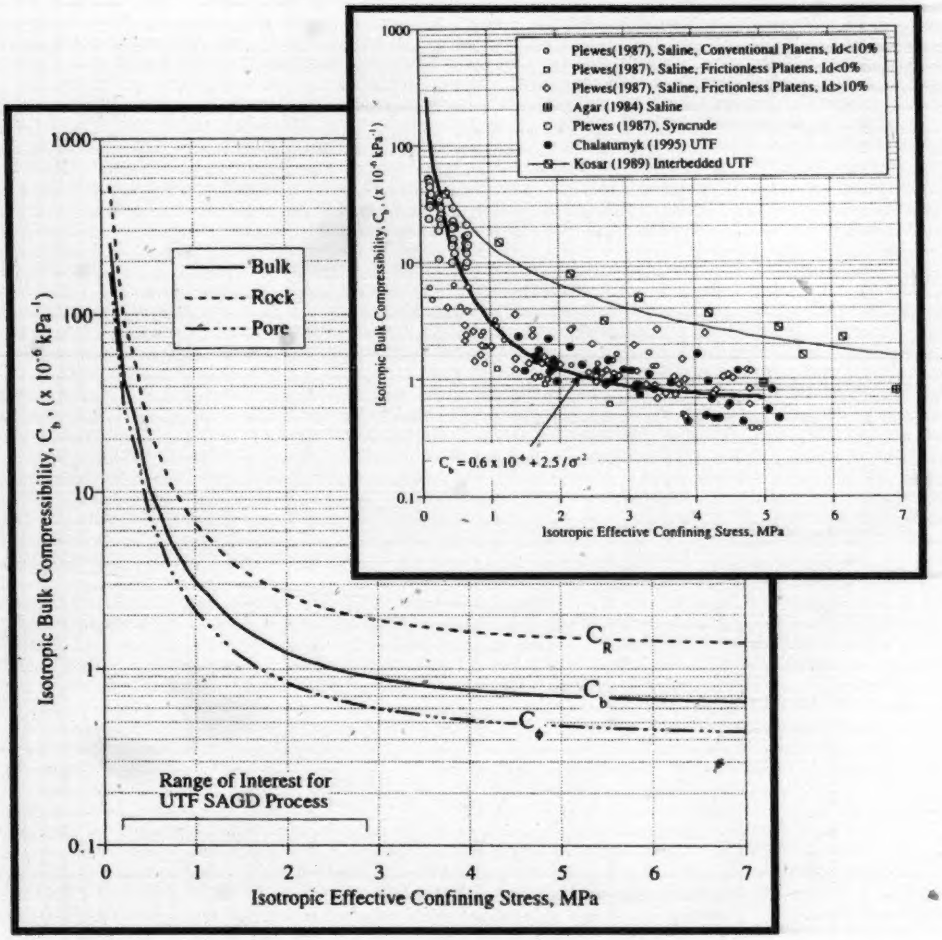

Figure 4-10 Compressibility versus effective stress

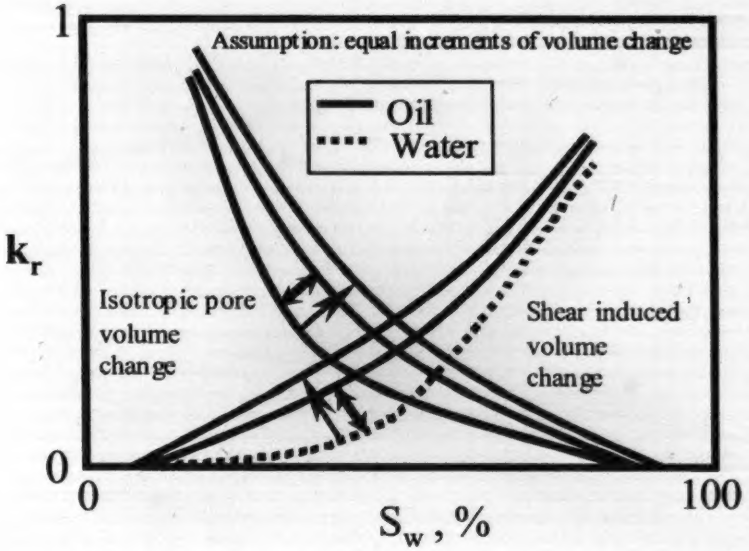

Figure 4-11 Effect of geomechanical behavior on relative permeability

CHAPTER 5 DEVELOPMENT OF THE METHODOLOGY OF THE COUPLED RESERVOIR GEOMECHANICAL SIMULATIONS FOR THE SAGD PROCESS*

5.1 Introduction

In the SAGD process, continuous steam injection and fluid flow can change reservoir pore pressure and temperature, which can increase or decrease the effective stress in the reservoir. The deformations of the oil sand material (skeleton and pores) change the fluid flow related reservoir parameters (Li et al., 2002). Clearly, this coupled problem requires coupled reservoir geomechanical simulations.

In this chapter, two existing well-established codes, EXOTHERM and FLAC, are coupled to characterize both the fluid flow and geomechanical behaviours in the SAGD process. The two codes are linked using sequential execution and data transfer through nonlinear coupling functions. The EXOTHERM code is a thermal reservoir simulator that can be applied to simulate the thermal recovery processes, such as cyclic steam stimulation, steam drive, and SAGD. It has been verified and used by organizations and research groups conducting thermal reservoir simulations. The FLAC (Fast Langrangian Analysis of Continua) is used to simulate the behavior of structures built of soil, rock or other materials which undergo plastic flow when their yield limits are reached. This capability allows the process of dilation or shear induced volume changes to be modeled for the temperature and pressure conditions of the SAGD process. Although the sequential coupling of two codes is less efficient than having a single code, an obvious advantage with coupling of EXOTHERM and FLAC is that both codes are well tested and widely applied in their respective fields.

---

* Part of this chapter entitled *Coupled Reservoir Geomechanical Simulations for the SAGD Process* (Li, P., Chalaturnyk, R.J., and Tan, T.B.) has been published by the Journal of Canadian Petroleum Technology (JCPT) Vol.45, No. 1, pp. 33-40, January 2006. It was first presented at the 4th Canadian International Petroleum Conference (the 54th Annual Technical Meeting of the Petroleum Society), Calgary, Alberta, Canada, June 10-12, 2003.

This chapter describes the methodology to establish the coupling of EXOTHERM and FLAC for modeling thermal-multiphase flow-mechanical process in the SAGD operations. First, the governing equations are presented. Thereafter, the approach to couple EXOTHERM and FLAC, including coupling parameters and numerical procedures, is described. Finally, application cases of the coupled reservoir geomechanical simulations are provided to demonstrate the capabilities of the simulation technique.

5.2 Mathematical Formulation in EXOTHERM

The EXOTHERM model was developed by T.T. & Associates Inc., Calgary, Alberta, Canada. It is designed to operate in the MICROSOFT WINDOWS environment. This is a three dimensional, three phase, fully implicit, and multi-component computer model designed to numerically simulate the phase behaviour of hydrocarbon reservoirs undergoing depletion with steam injection. The code can simulate problems in one, two or three dimensions using either rectangular cartesian (x y z) or cylindrical (r θ z) coordinates, with any combination of oil, gas or water phases, and characterizing the reservoir fluid into one or more components. Interblock mass transfer is represented by Darcy's law with relative permeability, capillary pressure and gravity effects. The transfer of any component between the oil, gas and water phases is calculated using equilibrium ratios. This model is appropriate to simulate the thermal recovery processes, such as cyclic steam stimulation (CSS), steam drive, and SAGD.

In the formulation for EXOTHERM, the hydrocarbon equation (Equation (5-1)) accounts for flow in both the oil and gas phases (Mattax and Dalton, 1990)

$$\begin{aligned} &\nabla\cdot\left(x_v\rho_o\lambda_o\nabla\Phi_o+y_v\rho_g\lambda_g\nabla\Phi_g\right)+q_v \\ &=\frac{\partial}{\partial t}\left[\phi\left(x_v\rho_oS_o+y_v\rho_gS_g\right)\right] \end{aligned} \tag{5-1}$$

The water material-balance equation (Equation (5-2)) involves the water in either the aqueous or the vapour phase:

$$\begin{aligned}&\nabla\cdot\left(\rho_w\lambda_w\nabla\Phi_w+y_w\rho_g\lambda_g\nabla\Phi_g\right)+q_w\\&=\frac{\partial}{\partial t}\left[\phi\left(\rho_wS_w+y_w\rho_gS_g\right)\right]\end{aligned}\qquad(5\text{-}2)$$

The energy equation (Equation (5-3)) is

$$\begin{aligned}&\nabla\cdot\left(k_h\nabla T+\sum_\alpha H_\alpha\rho_\alpha\lambda_\alpha\nabla\Phi_\alpha\right)+q_h\\&=\frac{\partial}{\partial t}\left[\phi\sum_\alpha U_\alpha\rho_\alpha S_\alpha+(1-\phi)\rho_sC_sT\right]\end{aligned}\qquad(5\text{-}3)$$

These continuum differential equations are discretized in space using the finite-difference method. Time is discretized as a first order finite-difference. When this component molar balance equation is satisfied for all cells individually, the model is converged at a time step. The tolerance for convergence is chosen in Control Data Section of the simulator. Typically, values in the range of 0.01 to 0.001 of the maximum molar well rate are chosen.

For coupled reservoir geomechanical simulations, EXOTHERM performs a complete simultaneous solution of the discretized mass- and energy-balance equations at each time step. The calculated pore pressure and temperature at each grid block are saved and ready for input to FLAC.

5.3 Mathematical Formulation in FLAC

The FLAC (Fast Langrangian Analysis of Continua) code (Itasca Consulting Group, 2000) is used to simulate the behaviour of structures built of soil, rock or other materials which undergo plastic flow when their yield limits are reached. FLAC is a two-dimensional explicit finite difference program for engineering mechanics computation. In this research of the SAGD process, the pressure drop along the horizontal well is not considered and the cross sections perpendicular to the SAGD wellpair is assumed constant. Therefore, simulating the SAGD process using FLAC2D (two dimensional plane strain) is considered appropriate.

Running FLAC in its mechanical and thermal mechanical configuration mode, it solves the equation of motion (Equation (5-4))

$$\frac{\partial \sigma_{ij}}{\partial x_j} + \rho_m g = \rho_m \frac{\partial \dot{u}}{\partial t} \tag{5-4}$$

The other set of equations that apply to a solid, deformable body is known as the constitutive relation, or stress/strain law, which can be written as a general form as Equation (5-5) (:= means replaced by)

$$\sigma_{ij} := M(\sigma_{ij}, \dot{\varepsilon}_{ij,} \kappa) \tag{5-5}$$

The strain rate is derived from velocity gradient and strain from displacement gradient as Equation (5-6)

$$\varepsilon_{ij} = \frac{1}{2}\left(\frac{\partial u_i}{\partial x_j} + \frac{\partial u_j}{\partial x_i}\right) \qquad \dot{\varepsilon}_{ij} = \frac{1}{2}\left(\frac{\partial \dot{u}_i}{\partial x_j} + \frac{\partial \dot{u}_j}{\partial x_i}\right) \tag{5-6}$$

The total strain increment consists of elastic, plastic, and thermal expansion parts (Equation (5-7)

$$\Delta\varepsilon = \Delta\varepsilon^e + \Delta\varepsilon^p + \Delta\varepsilon^T \tag{5-7}$$

where the thermal strain is calcualted by Equation (5-8)

$$\Delta\varepsilon^T = \mathrm{I}\beta_T \Delta T \tag{5-8}$$

The effective stress is calculated as Equation (5-9)

$$\sigma' = \sigma + \mathrm{I}\alpha p \tag{5-9}$$

In FLAC, the basic explicit dynamic calculation iterates between solving the equation of motion and the stress-strain constitutive equation using a sufficiently small time step to assure numerical stability. This procedure first invokes the equations of motion to derive new velocities and displacements from stresses and forces. Then, strain rates are derived from velocities, and new stresses from strain rates. The calculation involves the input of pressure and temperature data obtained from EXOTHERM. Meanwhile, the volumetric strain saved at each zone will be used to modify the reservoir parameters, such as permeability and porosity.

5.4 Windows Automation Software AUTOMATE

Automation of the sequentially coupled simulations is achieved using the automation software, AutoMate, which is developed by Los Angeles based Unisyn Software. Users can free themselves from redundant and repetitive tasks with this software. They can develop automated procedures based on a visual metaphor that is a domain previously reserved only for programmers. AutoMate applies a specific "building block" approach enabling users to quickly assemble automated tasks using "dragging and dropping" pre-built actions on his/her machine. When a task is built, the user can assign a "trigger", i.e., the event that induces the task to run. Triggers can be "schedule", "hotkey", or "Window Watcher" (which responds to a certain window appearing on the screen). All this work can be done with little or no programming effort.

The above noted functions of AutoMate can be applied to control the procedure of coupled reservoir geomechanical simulations for the SAGD process. AutoMate can smoothly and successfully link the reservoir simulator, EXOTHERM, the geomechanical simulator, FLAC, and data processing programs written with Visual Basic.

5.5 Methodology of Coupling between EXOTHERM and FLAC

5.5.1 Coupling Categories

Based on the degrees of coupling between reservoir fluid flow and oil sand geomechanics (Settari et al., 2001), the coupled simulations consist of four categories: non-coupled, decoupled, sequentially coupled, and fully coupled. Non-coupled solution means the conventional reservoir simulation, which only applies rock compressibility to consider the interactions between the fluids and solids. Decoupled solution generally has the complete time history of reservoir simulation followed by stress solution but does not include the feedback of geomechanical effects on reservoir simulation. The sequentially coupled solution contains both the explicitly coupled and the iteratively coupled reservoir geomechanical simulations. The stress equations are solved sequentially in each time step or iteration during each time step (Rutqvist et al., 2002). Then, the modified reservoir parameters by geomechanical behaviour are back substituted into the flow equation to continue the next time step. The fully coupled reservoir geomechanical simulation solves the flow equation and stress equation simultaneously based on a unified grid system.

5.5.2 EXOTHERM-FLAC Coupling

In this research, the two codes, EXOTHERM and FLAC, are explicitly and sequentially coupled. In another words, the EXOTHERM and FLAC codes are executed sequentially on compatible numerical grids and linked through external coupling modules (Figure 5-1), which transfer relevant information between the field equations that are solved in respective codes. The coupling between these two codes is based on the concept of effective stress and certain relationships for changes in reservoir parameters as a function of volumetric strain. These functions can be estimated from laboratory data and theoretical relationships. This coupling process includes the effects of oil sand material deformation on porosity and permeability, and the effects of fluid pressure and temperature variation on oil sand material deformation.

5.5.3 EXOTHERM-FLAC Coupling Modules

The coupled reservoir geomechanical simulation starts from EXOTHERM and the updated pore pressures and temperatures are provided to FLAC (Figure 5-1). Because EXOTHERM uses the center of each element and FLAC nodes are located in element corners, data have to be bi-linearly interpolated from the center of grid block to corner locations. A coupling module of Visual Basic (VB) performs the interpolation from EXOTHERM to FLAC and effective stresses are calculated based on thermal expansion coefficient and initial stress data given in the FLAC input deck.

Based on the updated effective stress conditions and constitutive stress-strain relationship given in the FLAC input data file, FLAC internally calculates the elastic and plastic deformation status. Then, it modifies the reservoir porosity and permeability for EXOTHERM based on theoretical or empirical functions, which are material-specific.

The updated porosity and permeability are transferred to EXOTHERM to start the reservoir simulation of the next time step. The data transfer is also performed by a Visual Basic module. No interpolation in space is required because stress and strain are defined in the center of each grid block and so are the modified porosity and permeability, which are identical to EXOTHERM grid system.

5.5.4 Operation Procedure of the Methodology

The strategy and methodology of the coupled reservoir geomechanical simulations for the SAGD process based on these two simulators can be described as follows.

1. Establish the initial start files for both EXOTHERM and FLAC, and then design the following loop to realize the coupled reservoir and geomechanical modeling.
2. After each time step of EXOTHERM, write pressure, temperature, permeability, and porosity distributions into a text file. Meanwhile, write a wait flag to the file.
3. Transform the pressure and temperature data format into that required by FLAC, including the interpolation in space. This is conducted by a VB module.
4. Run FLAC with updated pore pressure and temperature data to calculate the updated stress and strain status and modify porosity and absolute permeability for EXOTHERM.
5. Transform the data format (porosity and permeability) into the format required by EXOTHERM. This is also performed by the VB module.
6. Run EXOTHERM for the next time step with updated porosity and absolute permeability.

Repeat the procedure from step 2 to 6 until the final time step is reached.

This procedure is controlled by AutoMate©.

5.5.5 Coupling Relationships for EXOTHERM and FLAC

In this section, some coupling relationships for EXOTHERM and FLAC are described, particularly for oil sand material of McMurray Formation at the UTF Phase A site. Chalaturnyk (1996) proposed that the Young's modulus of oil sand material varies as a function of minimum effective principal stress (Equation (5-10))

$$E = 343\sigma_3'^{0.875} \quad \text{(MPa)} \tag{5-10}$$

Porosity and absolute permeability can be expressed as a function of volumetric strain (Tortike and Farouq Ali, 1993), which is calculated based on stress-strain relationship defined for oil sands material (Equation (4-3) and (4-7)):

$$\phi = \frac{\phi_0 + \varepsilon_v - (1 - \phi_0)\alpha_s(T - T_0)}{1 + \varepsilon_v}, \tag{4-3}$$

$$\frac{k}{k_0} = \frac{\left[1 + \frac{\varepsilon_v}{\phi_0} - \frac{\alpha_s \Delta T (1 - \phi_0)}{\phi_0}\right]^3}{1 + \varepsilon_v} \tag{4-7}$$

where α_s is the thermal expansion coefficient of solid material.

5.6 Testing of the Methodology

In order to verify the feasibility of the sequentially coupled reservoir geomechanical simulation procedure, two simulation methods are applied. One is the conventional reservoir simulation with EXOTHERM only, and the other is the sequentially coupled reservoir geomechanical simulation with both EXOTHERM and FLAC in which porosity and permeability are not updated. If the two simulation results are the same, then the sequentially coupled reservoir geomechanical simulation method is assumed to be functional.

Table 5-1 is the reservoir parameters and geomechanical parameters used in the simulations. This reservoir condition is defined based on the UTF Phase A site (Siu, et al., 1991). Initial reservoir pressure is 550 kPa and steam injection pressure is 2750 kPa (this injection pressure is only applied for testing the methodology). Figure 5-2 and Figure 5-3 show the grid systems in reservoir simulation and geomechanical simulation, respectively. The geomechanical model has the following boundary conditions:

- Fixed x and y displacement at the base of the model
- Fixed x displacement along both vertical edges of the model
- Fixed formation pressure beyond the reservoir
- Fixed temperature beyond the reservoir
- Fixed saturation beyond the reservoir

Figure 5-4 shows the comparison of steam rates and cumulative steam injections between conventional reservoir simulation and the coupled reservoir geomechanical simulation. Figure 5-5 compares the oil rates and cumulative oil productions for the two simulation methods. Figure 5-6 is the predicted oil recovery factors. It can be seen clearly that the two simulation results are almost the same except very small differences on steam rate and oil production rate over a very short period of time (the difference may result from numerical errors). These comparisons indicate that the sequentially coupled reservoir geomechanical simulation methodology is applicable to predict SAGD production performance. Chapter 8 presents further verifications of the sequentially coupled reservoir geomechanical simulation methodology.

5.7 Application Cases of the Coupling Procedure

UTF Phase A project was the first SAGD operation in the field. This project was a pre-pilot program established for preliminary investigation of the SAGD process at approximately one-tenth pilot scale, to provide added assurance of project feasibility and to confirm a full pilot design basis. Field operations proved that the SAGD process can be successful in the development of oil sand reservoirs. This project obtained very good development results with low steam oil ratio (SOR = 2.5) and high oil recovery (60%) (Komery et al., 1995). The proposed simulation methodology is applied to this reservoir condition to examine the feasibility of coupled reservoir geomechanical simulations for the SAGD process.

The reservoir and geomechanical parameters in Table 5-1 and the grid systems in Figures 5-2 and 5-3 were also applied in the following reservoir geomechanical simulations. The spacing of the SAGD wellpair at UTF Phase A site is 26 m and the thickness of the bitumen-bearing formation is 20 m. Therefore, the grid system is 13 m×20 m and each element is 1 m by 1 m. Owing to the symmetry of the SAGD well configuration, half of the wellpair spacing is applied in horizontal direction. The grid system used in the geomechanical simulation is extended up to the surface in the vertical direction. The boundary conditions are shown in Figure 5-3.

The coupled reservoir geomechanical simulations are performed based on the combination of the following conditions: Steam injection pressure: 1200, 1800, 2400, and 3000 kPa. Initial reservoir permeability: 2500×10^{-3} μm^2 (2500md) and 5000×10^{-3} μm^2 (5000md).

In the SAGD process, steam injection pressure and thermal expansion can induce high pore pressures around the injector at the startup of the process. Hence, the effective stress can become very small around this well. As a result, the volumetric strain is so large that the permeability calculated based on Tortike's equation can also be very large. Based on Touhidi-Baghini (1998), under low confining effective stresses, the maximum and minimum volumetric strain for oil sand material in the McMurray Formation were estimated to be in the range of -0.02 to 0.12. Consequently, a maximum volumetric strain limit of 0.12 was chosen for the analysis. The reason for setting this upper limit was that the in situ effective stress under injection conditions was very low and occasionally, may have exceeded fracture pressure ($\sigma_3' < 0$). As FLAC has no capability to handle fracturing mechanisms, this results in excessively large volumetric strains. This effect was primarily limited to the near wellbore regions during the startup stages of the SAGD process. The volumetric strains in FLAC were not numerically modified but rather, if the volumetric strain exceeded 0.12, then only a value of 0.12 was used in Equations (5-11) and (5-12) to compute porosity and permeability changes. This should provide a conservative estimate of the impact of geomechanical processes on SAGD performance.

The permeability and porosity are updated each time step during the coupled reservoir geomechanical simulations.

5.7.1 Effect of Steam Injection Pressure

Figure 5-7 compares the oil recovery and SOR of the SAGD process based on the initial reservoir permeability of 5000md and the four steam injection pressures. It is clearly seen from Figure 5-7 that the coupled reservoir geomechanical simulations predict higher oil recovery than the conventional reservoir simulations. Moreover, with increasing steam injection pressure, the difference is even larger. For example, when the steam injection pressure is sequentially increased from 1200 kPa, to 1800 kPa, to 2400 kPa, and to 3000 kPa, the oil recovery is increased by 1.7%, 1.5%, 2.3%, and 6.4%. On the other hand, the coupled reservoir geomechanical simulations predict even lower SOR values compared to the conventional reservoir simulations. In fact, isotropic unloading and shear dilation allows for more effective contact between steam and bitumen, which results in the decrease of SOR values. Figure 5-8 shows the same phenomenon when the initial reservoir permeability is 2500md. The reason that the result with steam injection of 1200 kPa is not shown in Figure 5-8 is that under this condition, the SAGD performance was extremely poor; recovery of only 1% were predicted.

5.7.2 Effect of Initial Reservoir Permeability

Two initial reservoir permeability values are applied in this simulation, which are 2500md and 5000md. Figure 5-9 compares the oil production rates of different steam injection pressures for these two initial permeability values. When the initial reservoir permeability is 5000md and steam injection pressures 1200 kPa and 2400 kPa, Figure 5-9 shows that the curves of the oil production rates of the coupled reservoir geomechanical simulations and that of the conventional reservoir simulations are very similar. In contrast, when the initial reservoir permeability is 2500md and steam injection pressures 1800 kPa and 2400 kPa, Figure 5-9 shows that the difference is significant between the curves of the oil production rates of the two simulation techniques. This comparison indicates that the geomechanical behaviour plays an important role when the initial reservoir permeability is relatively low.

5.7.3 Effect of Geomechanical Behavior

The analysis above indicates that geomechanical behavior will affect the production performance of the SAGD process. The reason is that geomechanical behaviour can modify reservoir parameters, such as permeability and porosity, which are key parameters associated to fluid flow in the reservoir.

If the steam injection pressure is higher than the initial reservoir pressure, the reservoir pore pressure will be increased during the SAGD operation. As expected, the higher the steam injection pressure, the higher the reservoir pore pressure. The effective stress within the reservoir varies as a function of the pore pressure and thermal expansion. Thermal expansion causes the total stress to increase. Figure 5-10 shows the vertical effective stress, displacement, and porosity distributions for steam injection pressures of 1800 kPa, 2400 kPa, and 3000 kPa, where the initial permeability is 5000md for all the three cases. This figure demonstrates that with increasing steam injection pressure, the effective stress decreases. The left side is fixed in horizontal direction because of symmetry. That is why the effective stress around the left side is higher than that in the internal area. In the regions with low effective stresses, two major geomechanical processes occur. One is isotropic unloading and the other is shear dilation. Both of them can induce significant deformations of the reservoir material. It is clear from Figure 5-10 that when the steam injection pressure is 3000 kPa, the effective stress within the reservoir is much lower and large displacement occurs around the upper left corner of the reservoir, where thermal expansion of the reservoir material within and around the steam chamber exerts larger horizontal stress. Therefore, the displacement is moving upward because of constraint in the horizontal direction.

Due to deformations occurring in the reservoir, porosity will vary as a function of volumetric strain. In these simulations, the initial porosity is 0.3. Figure 5-10 shows that in some areas, porosity is decreased due to compaction and in some areas, porosity is increased due to isotropic unloading and shear dilation. For example, when the steam injection pressure is 3000 kPa, porosity is increased to greater than 0.35 in the upper left corner of the reservoir where significant displacement occurs. Figure 5-11 shows similar results of simulations with an initial permeability of 2500md.

Figure 5-12 shows the permeability contours of three steam injection pressures, which are 1800 kPa, 2400 kPa, and 3000 kPa. All of them have the same initial reservoir permeability of 5000md. From this figure, it is clearly seen that with increasing steam injection pressure, the permeability increases more significantly. Particularly, for the steam injection pressure of 3000 kPa, the permeability values in the upper left corner of the reservoir are increased to more than 12000md, which is 2.4 times higher than the initial values. The reason of this permeability increment is reservoir deformation as discussed above. Figure 5-13 shows the similar results of simulations with an initial permeability of 2500md. In this case, the maximum permeability increment is only 1.6 times higher than the initial permeability value.

The porosity and permeability increments due to geomechanical behavior influence the production performance of the SAGD process. Hence, these factors should be taken into account in the prediction and evaluation of a SAGD project.

5.8 Characteristics of the Methodology

The methodology of the coupled reservoir geomechanical simulations proposed in this research has the following characteristics:

- It is flexible to apply geotechnical properties of the reservoir material, shale streaks within the reservoir, overburden and underburden with appropriate boundary conditions.

- The geomechanical behavior occurring in the SAGD process, such as compaction, expansion, and shearing, can be characterized by the geomechanical simulator, FLAC.

- It has advantages over the current coupled reservoir geomechanical simulation techniques in the selection of constitutive stress strain relationships. It can apply any models provided by FLAC or established by users.

- The reservoir simulator, EXOTHERM, is applied to perform both the coupled reservoir geomechanical simulations and the conventional reservoir simulations. Therefore, it is convenient to compare the results from these two simulation techniques.

- The coupling procedure is controlled by AutoMate©, which allows the sequentially coupled reservoir geomechanical simulations to be achieved in a straightforward manner.

5.9 Conclusions

- The methodology of sequentially coupled reservoir geomechanical simulations was developed, which is based on the reservoir simulator, EXOTHERM, and the geomechanical simulator, FLAC.

- The simulation procedure is controlled by Windows automation software, AutoMate. It can smoothly and successfully link the two simulators and their coupling modules written with Visual Basic.

- The sequentially coupled reservoir geomechanical simulation procedure is verified by comparing the results of the conventional reservoir simulation and that of the developed procedure.

- This coupled simulation procedure is flexible and easy to use.

- The application cases show that the geomechanical behaviour occurring in the SAGD operations does affect SAGD production performances.

- The geomechanical effects on the SAGD production are dependent on the steam injection pressure. Higher injection pressure induces significant changes of reservoir porosity and permeability.

- For relatively lower initial reservoir permeability, the difference is more obvious between the coupled reservoir geomechanical simulation and the conventional reservoir simulation.

- Permeability variations due to geomechanical behaviour can be anisotropic. This phenomenon needs to be considered in the coupled reservoir geomechanical simulations.

Table 5-1 Reservoir and geomechanical parameters

Reservoir Parameter	Value	Geomechanical parameter	Value
Depth, m	160	Linear thermal expansion coefficient, °C^{-1}	2×10^{-5}
Pay thickness, m	20	Overburden dry density, 10^3kg/m^3	1.7
Porosity, %	30	Wet density, 10^3kg/m^3	3.05
Horizontal permeability, μm^2	2.5 and 5.0	Bulk modulus, 10^5kPa	2.86
Vertical permeability, μm^2	1.25 and 2.5	Shear modulus, 10^5kPa	1.32
Oil saturation, %	85	Shear failure model	Mohr-Coulomb
Oil viscosity, mPa.s	5,000,000	Cohesion, kPa	0
Reservoir pressure, kPa	550	Dilation angle, °	25
Reservoir temperature, °C	8	Friction angle, °	55
Compressibility, kPa^{-1}	5×10^{-6}	Overburden bulk modulus, 10^5kPa	2.08
Volumetric thermal expansion coefficient, °C^{-1}	6×10^{-5}	Overburden shear modulus, 10^4kPa	9.62
Horizontal well length, m	55	$K_o=1$	
Well pair spacing, m	26	$\sigma_x=\sigma_z$ (kPa)	3545
Injector producer spacing, m	5	σ_y (kPa)	3545
Steam quality, %	98		
Steam injection pressure, kPa			
1200	1800		
2400	3000		

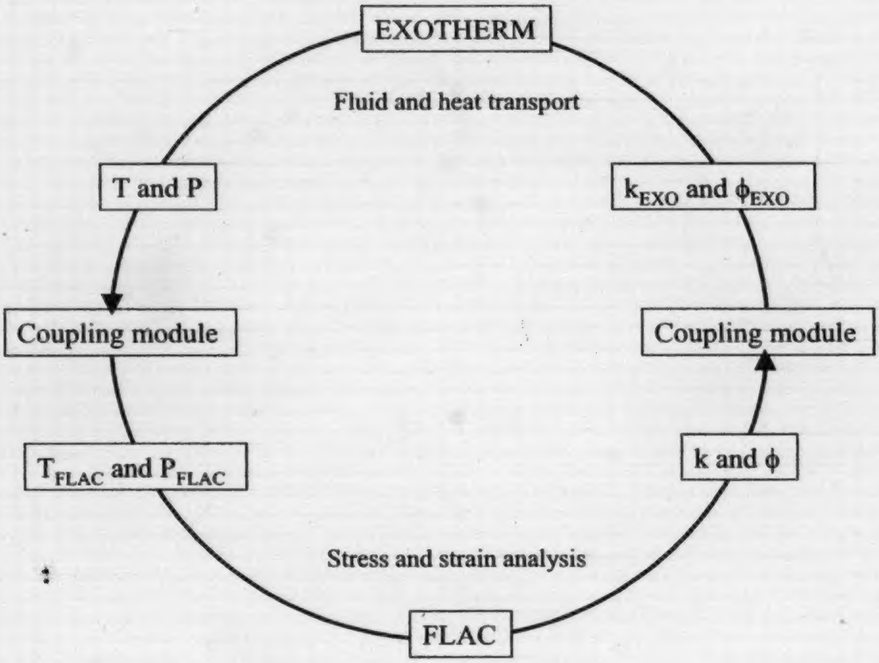
EXOTHERM
Fluid and heat transport
T and P
k_{EXO} and ϕ_{EXO}
Coupling module
Coupling module
T_{FLAC} and P_{FLAC}
k and ϕ
Stress and strain analysis
FLAC

Figure 5-1 Flow chart of the coupled reservoir geomechanical simulation procedure with EXOTHERM and FLAC

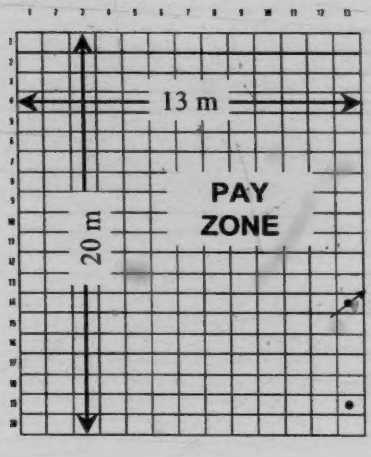
13 m
20 m
PAY ZONE

Figure 5-2 Grid system in reservoir simulator

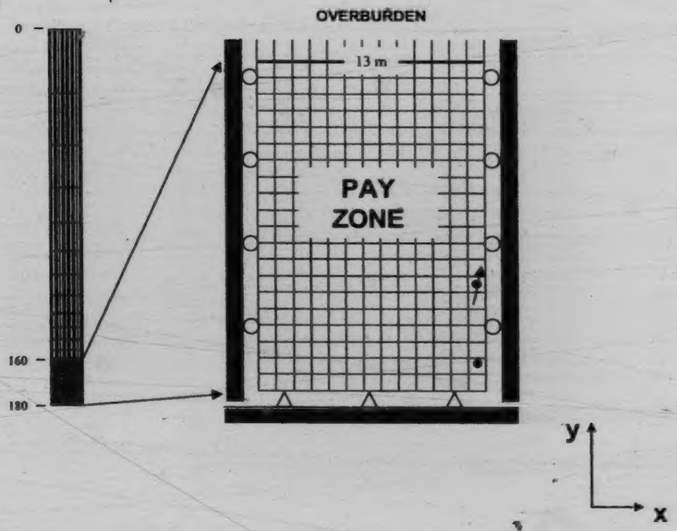
OVERBURDEN
13 m
PAY ZONE
0
160
180
y
x

Figure 5-3 Grid system in geomechanical simulation

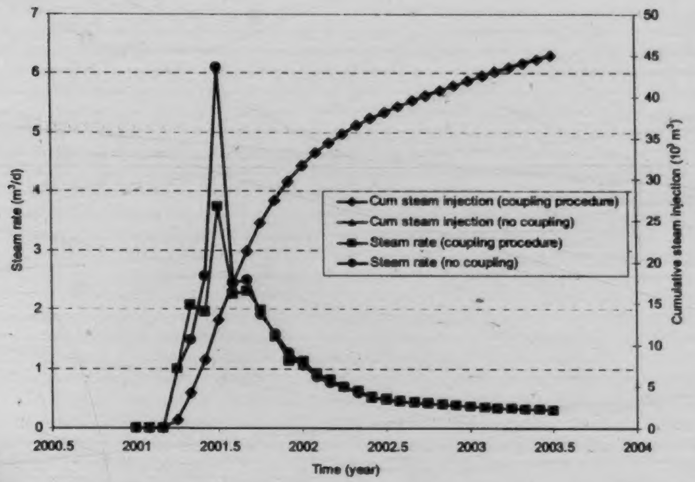

Figure 5-4 Comparison of steam rates and cumulative steam injections between conventional simulation and the coupled simulation

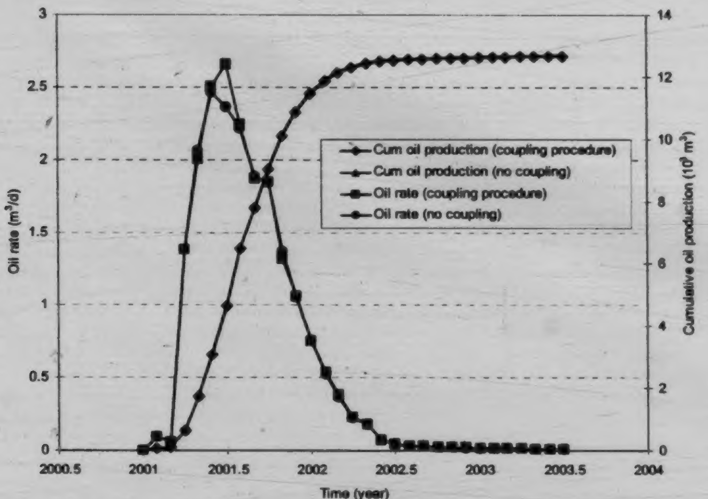

Figure 5-5 Comparison of oil rates and cumulative oil productions between conventional simulation and the coupled simulation

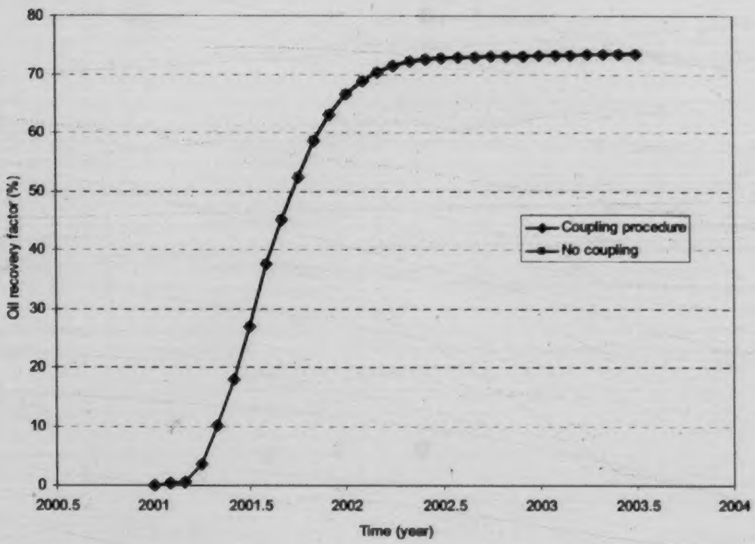

Figure 5-6 Comparison of oil recoveries between conventional simulation and the coupled simulation

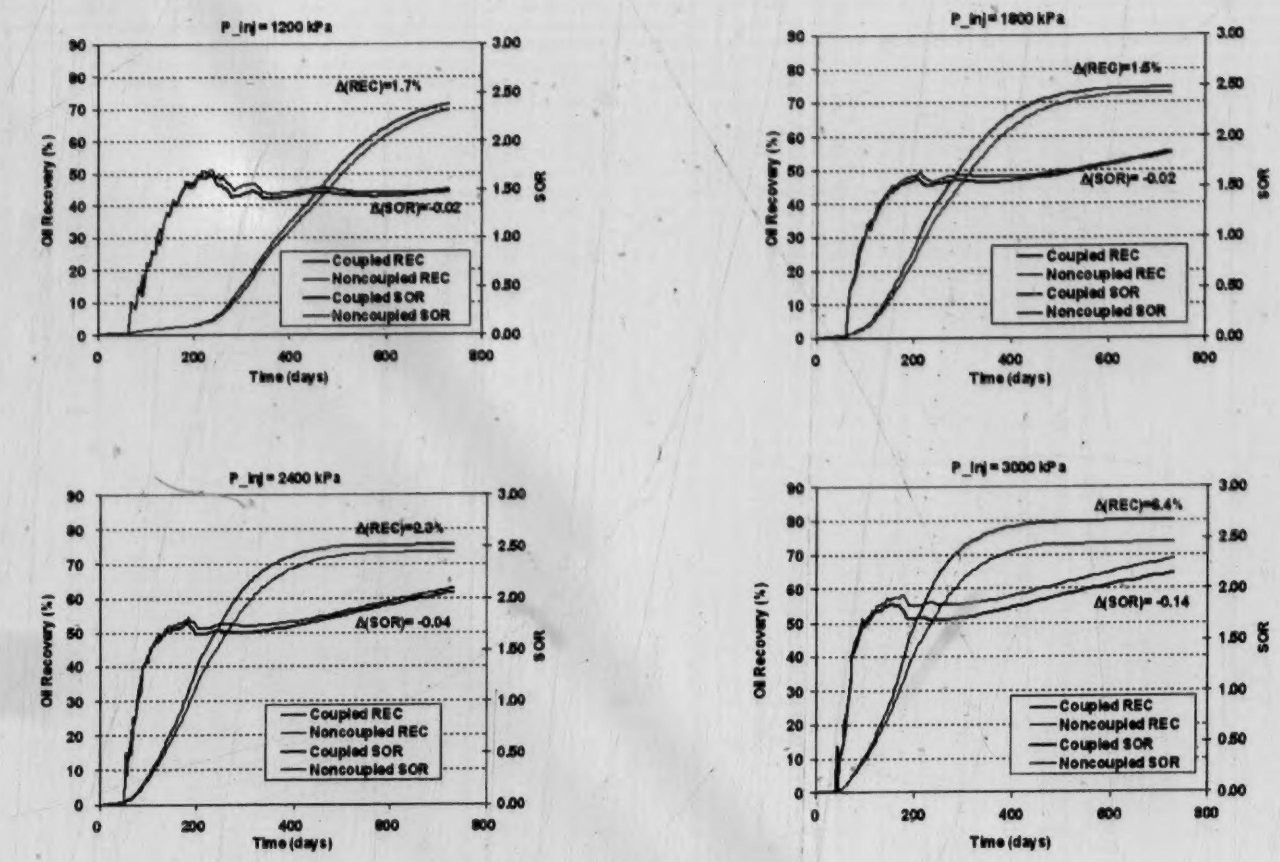

Figure 5-7 Oil recovery and SOR versus time for k_i = 5000md

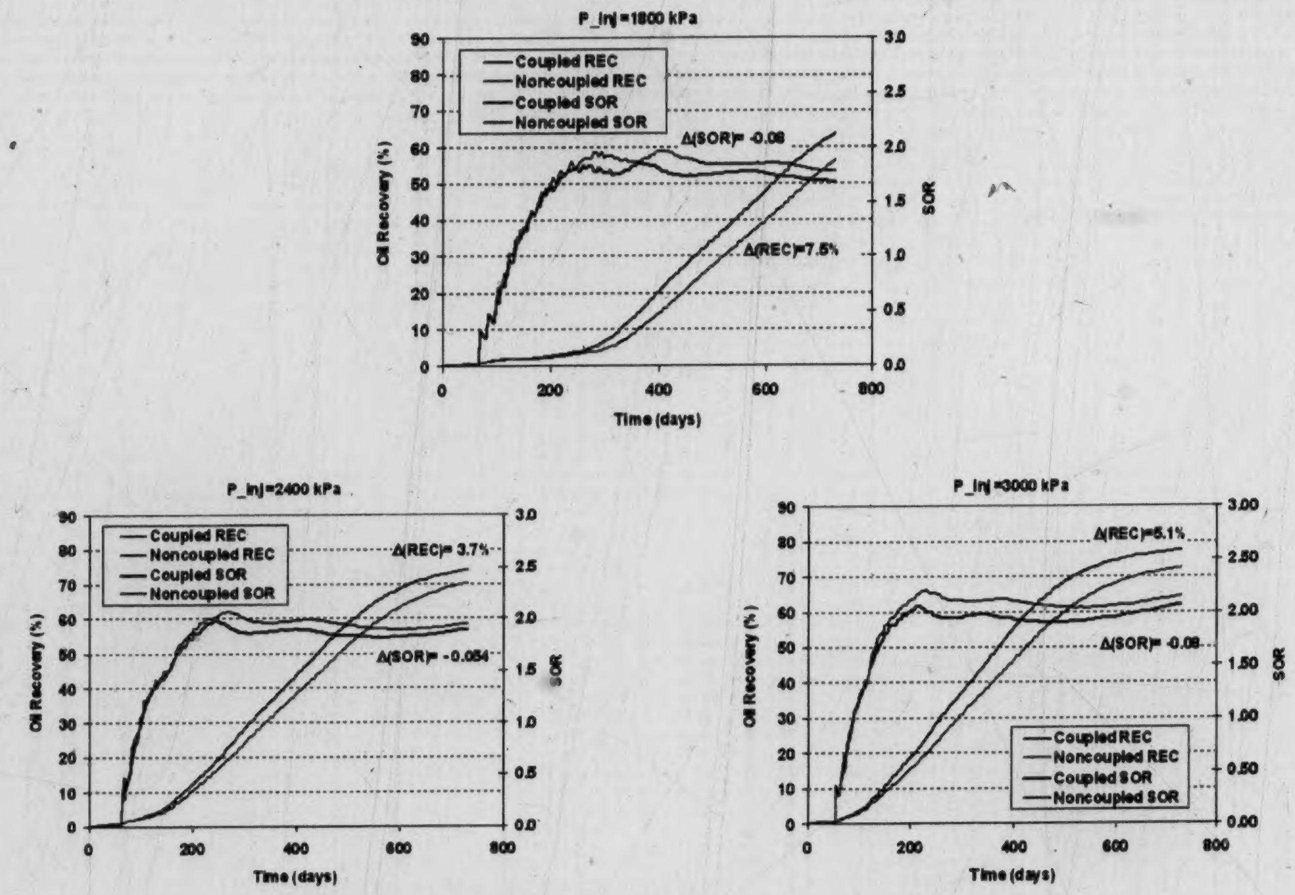

Figure 5-8 Oil recovery and SOR versus time for k_i = 2500md

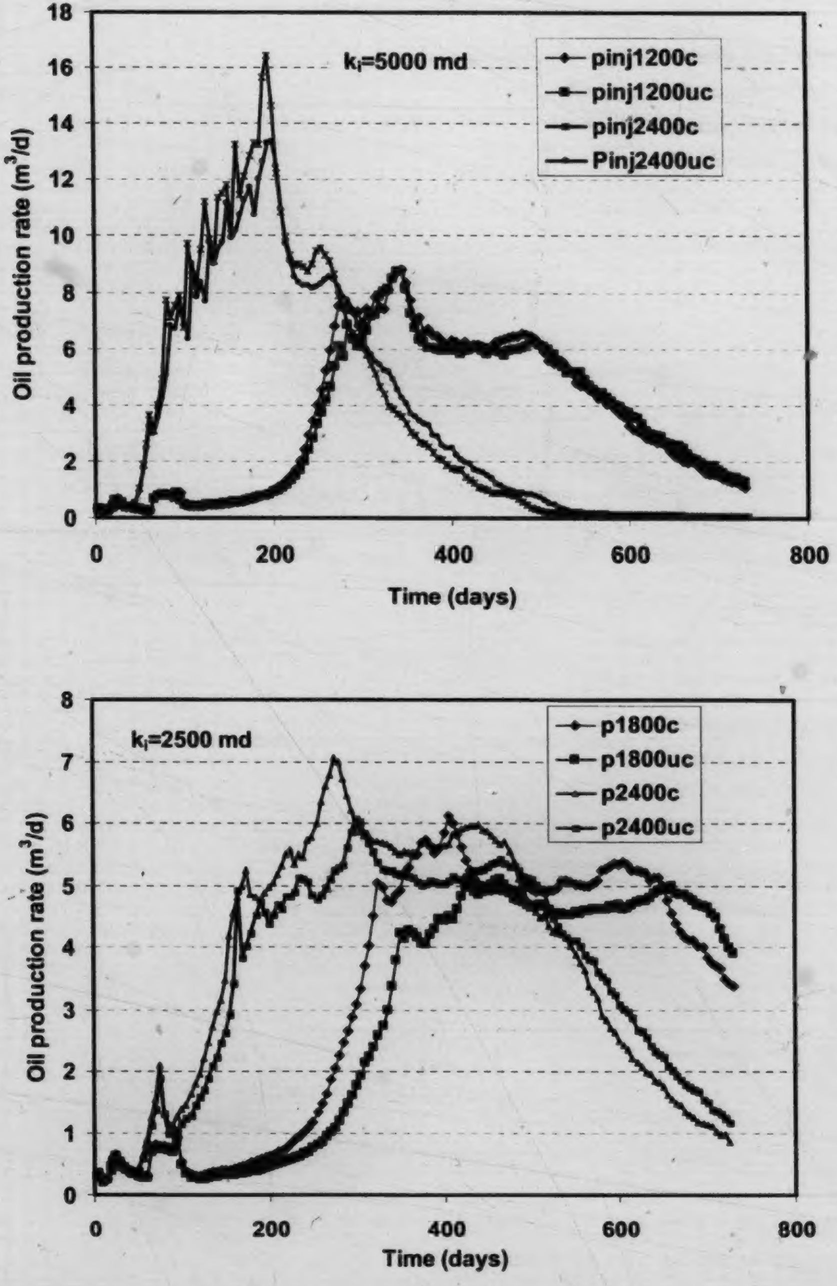

Figure 5-9 Comparison of oil production rates for different simulation techniques

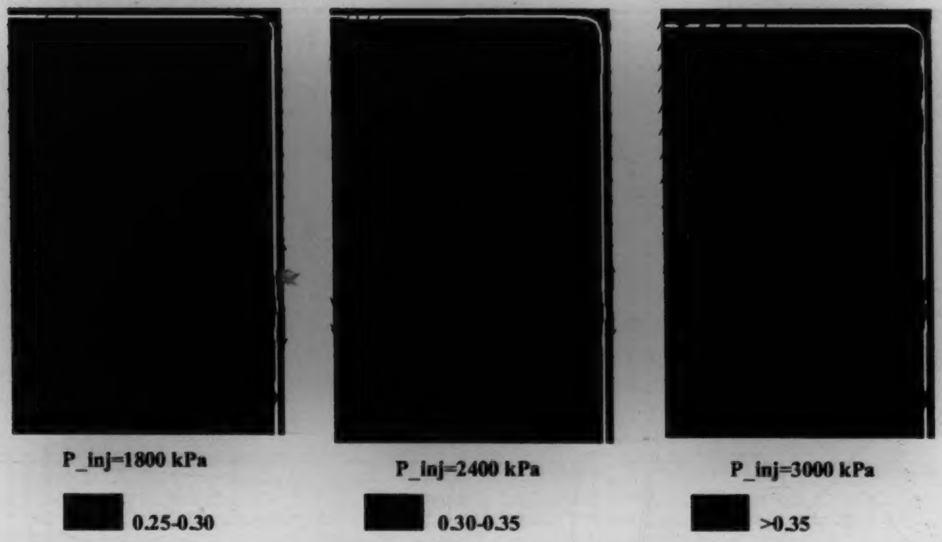

Figure 5-10 Porosity, vertical effective stresses, and displacement fields after the SAGD operation (k_i=5000md)

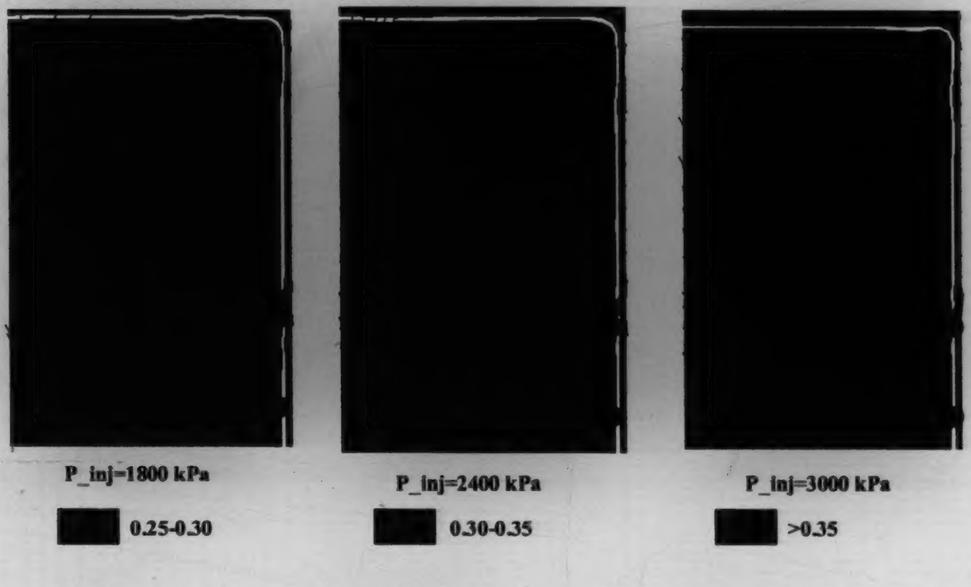

Figure 5-11 Porosity, vertical effective stresses, and displacement fields after the SAGD operation (k_i=2500md)

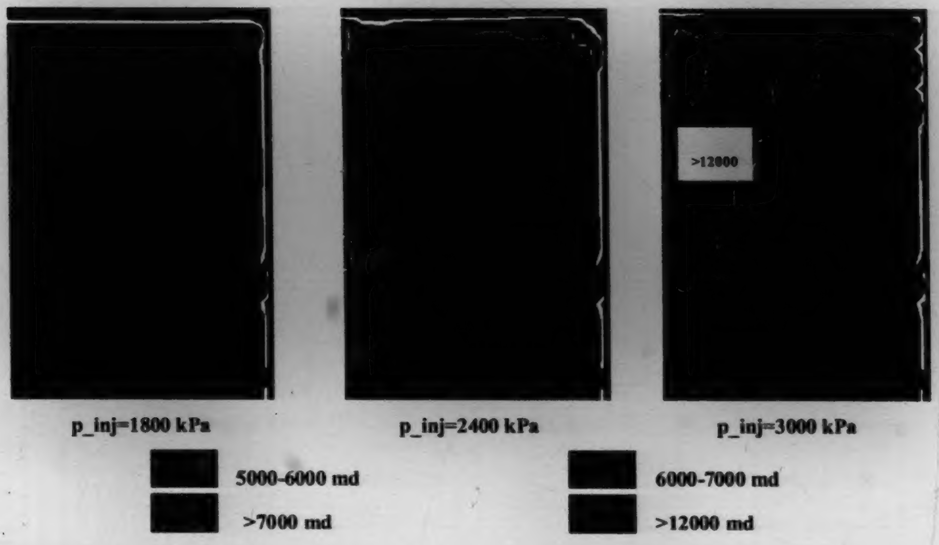

p_inj=1800 kPa p_inj=2400 kPa p_inj=3000 kPa

Figure 5-12 Permeability variation due to steam injection pressure (k_i=5000md)

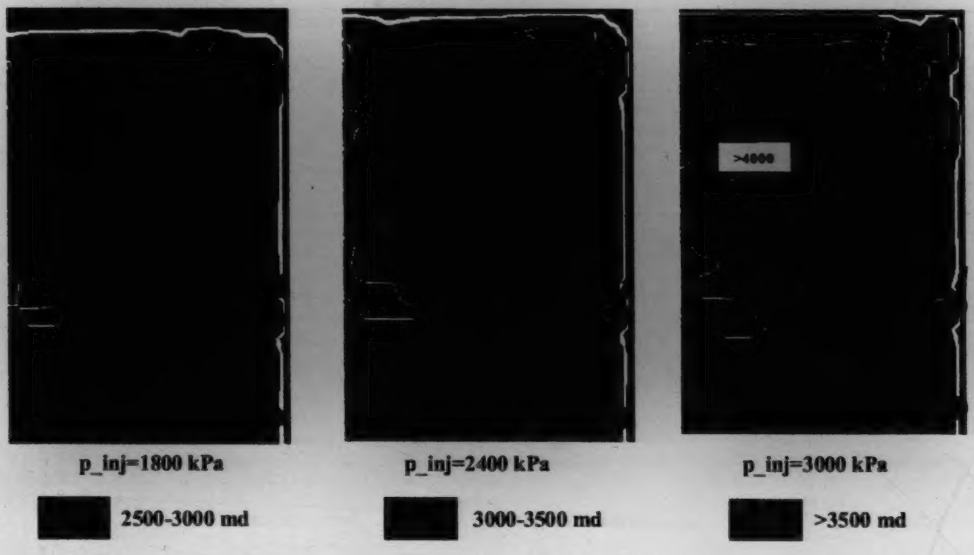

p_inj=1800 kPa p_inj=2400 kPa p_inj=3000 kPa

Figure 5-13 Permeability variation due to steam injection pressures (k_i=2500md)

CHAPTER 6 PERMEABILITY VARIATIONS ASSOCIATED WITH GEOMECHANICAL BEHAVIORS IN SAGD*

6.1 Introduction

Permeability variations of sandstone and other high strength materials experiencing the isotropic unloading and shearing processes have been studied by Scott et al. (1991) and Wong et al. (1991). Oldakowski (1994) conducted a series of tests based on both reconstituted oil sands specimens and in situ oil sands cores to characterize the relationships of permeability and geomechanical processes. Chalaturnyk (1996) summarized the test results on oil sands and provided the relationship between oil sands compressibility and confining effective stress. It is known that oil sands samples can be easily disturbed during sampling process. In order to minimize the disturbance, Touhidi-Baghini (1998) took the test specimens from an exposed outcrop of bitumen free McMurray Formation sandstone, northeast of Fort McMurray. Based on these specimens, experimental studies were conducted on the permeability variation during the shearing process.

This chapter systematically discusses the oil sands permeability variations due to the isotropic unloading and shearing process based on Oldakowski's and Touhidi-Baghini's test results. In addition, some empirical permeability relationships, such as Kozeny-Carman model, Tortike's equation, and Chardabellas's terms, are also discussed.

6.2 Geomechanical Behavior During SAGD

During the SAGD operations, steam is continuously injected into the oil sands reservoir. The steam injection pressure is generally greater than the initial reservoir pore pressure. The steam chamber propagates under the influence of the injection pore pressures and high temperatures. Because of different mechanisms of pore pressure transmission and heat flow, the high pore pressure front is approximately four to five meters in front of the high temperature front, as discussed in Chapter 4. Under these processes, two major geomechanical phenomena may occur. One is an isotropic unloading process and the other is a shearing process. Both of them can induce variations of reservoir permeability. However, the magnitude of these variations is different for each process and is discussed below.

---

* Part of this chapter entitled *Permeability Variations Associated with Shearing and Isotropic Unloading during the SAGD Process* (Li, P. and Chalaturnyk, R.J.) has been published by the Journal of Canadian Petroleum Technology (JCPT), Vol. 45, No. 1, 2006, pp.54-61. It was first presented at the 5th Canadian International Petroleum Conference (the 55th Annual Technical Meeting of the Petroleum Society), Calgary, Alberta, Canada, June 8-10, 2004.

6.2.1 Isotropic Unloading Process

The two concepts, isotropic unloading and anisotropic unloading, need to be clarified first. Isotropic unloading means that the confining effective stress is decreased by the same amount in all directions. So, both pore pressure injection and confining pressure reduction can induce the isotropic unloading process. Anisotropic unloading means that the confining effective stress is decreased by different amount in different directions. Pore pressure injection cannot result in the anisotropic unloading process.

In the SAGD process, reservoir pore pressures are increased due to steam injection and they essentially remain constant within the high pore pressure front. This region includes the entire drained zone and part of the partially drained zone, as discussed in Chapter 4. Pore pressures decrease gradually from the highest pore pressure value to the initial reservoir value in the far field. It is clear that all the regions where the pore pressure is greater than the initial reservoir value undergoes isotropic stress unloading. This process causes the grain packing to become less dense (e.g. porosity increases), but the relative position of grains does not change significantly. It should be noted that any porosity variations induced by the isotropic unloading process are generally recovered when the pore pressure is reduced and the confining stress returns to its original value.

6.2.2 Shearing Process

High steam temperature in the SAGD process induces significant thermal expansion of the reservoir material (Figure 6-1). During the SAGD process, the thermal expansion of the reservoir region within the high temperature front creates a large thermal stress normal to the front surface. The volumetric thermal expansion coefficient α is defined by Equation (6-1)

$$\begin{aligned}\alpha &= -\frac{1}{\rho}\left(\frac{d\rho}{dT}\right)_p \\ &= \frac{1}{V}\left(\frac{\partial V}{\partial T}\right)_p\end{aligned} \tag{6-1}$$

The volumetric thermal expansion coefficient α is related to the linear thermal expansion coefficient β by Equation (6-2)

$$\alpha = 3\beta \tag{6-2}$$

Thermal stress due to the volumetric expansion can be calculated by Equation (6-3)

$$\Delta\sigma_T = -E\,\alpha\,\Delta T \tag{6-3}$$

For SAGD operations in Athabasca oil sands deposits, the net temperature increase can be as high as 250°C. Assuming a coefficient of linear thermal expansion of oil sands of 2×10^{-5} °C^{-1} and Young's modulus, *E*, of 1200 MPa, the induced thermal stress can be as high as 6 MPa. This thermal stress can significantly increase the total stress in regions beyond the high temperature front. Within 10 – 15 m of this front, however, the pore pressure is similar to the injection pressure, resulting in low effective stresses and a reduction in the shear strength of the reservoir material in this region. If the stress state reaches the failure envelope of the material, shear failure occurs. The reservoir material located above the steam chamber may behave differently compared to that laterally adjacent to the steam chamber (Figure 6-2, Figure 6-3, and Figure 6-4). In addition, the shearing process is also dependent upon the in situ vertical and horizontal stress conditions because the magnitude of in situ stresses in different directions and vertical horizontal stress ratio (K_0) can induce different shearing responses for the same steam injection operations.

The shearing process causes reservoir grains to roll, ride, or dilate. Thus, it results in the rearrangement of grains and changes the grain packing style. This mechanism causes significant variations of reservoir parameters, such as porosity and permeability, and in contrast to isotropic unloading can result in substantial variations in absolute permeability. The following sections explore only the variations in permeability.

6.3 Absolute Permeability Variations in Response to Isotropic Unloading

As discussed above, for the isotropic unloading process, dense grain packing becomes less dense directly but the relative position among grains does not change. This makes it possible to relate the permeability variation to isotropic and bulk volumetric strain of the material.

Adhikary (1991) and Oldakowski (1994) conducted a series of tests on reconstituted oil sands specimens to measure the absolute permeability change due to isotropic stress unloading. The initial properties of the specimens are provided in Table 6-1. Figure 6-5 shows the volume change of ten oil sands specimens as a function of isotropic confining effective stresses. It can be seen that, except for PI-3D, all specimens have maximum confining effective stresses of about 4000 kPa. With decreasing effective confining stress, the volume of the specimens (porosity) increases. Although Specimen PI-3D started at the confining effective stress of 1000 kPa, it has the same variation trend of volume change as other specimens. When the confining effective stresses are reduced to about 200 kPa, the volume is increased by 1.2% to 1.5%. Figure 6-6 shows a regression curve of the specimens' volume change as a function of confining effective stresses. Although the tested specimens are reconstituted, the regression curve may be used to approximately calculate the volume change of oil sands material during the isotropic unloading process because the specimens were dense sands and the in situ interlocked property of oil sands does not play an important role in the volume change during isotropic unloading.

Based on the relationship between oil sands compressibility and effective confining stresses, the volumetric strain as a function of isotropic effective stress can be found and is shown in Figure 6-7. The data on Cold Lake oil sands from Scott et al. (1991) and Wong et al. (1991) are also included. All these data indicate that the volume change of oil sand material during the isotropic unloading process is less than 2%. The data of interbedded UTF oil sands from Kosar (1989) show a volumetric strain of about 4.7% due to isotropic unloading. This is not consistent with other testing results because these samples were highly disturbed.

Permeability variation can be expressed as the ratio of the modified permeability during the isotropic unloading process to its initial value. Figure 6-8 is the permeability ratio as a function of volume change for ten specimens from Oldakowski (1994) and Adhikary (1991). It is seen that the permeability ratio increases with increasing the volumetric strain. In addition, for the same volumetric strain, a lower initial permeability results in a larger permeability increases. Only the specimen Sn-3 has untypical variation trend, which is due to operational problems during the experiment. When the initial permeability is greater than 1 μm^2 (which is roughly consistent to the real in situ oil sand conditions), the permeability ratio is less than 1.2 for the maximum volumetric strain. Cold Lake oil sands have the similar permeability variation characteristic, which is shown in Figure 6-9 (Scott et al., 1991).

6.4 Absolute Permeability Variations in Response to Shearing

Absolute permeability measurement on bitumen saturated oil sands specimen is difficult because bitumen cannot flow at room temperature. The extraction of bitumen from oil sands material prior to conducting laboratory experiments is difficult and can disturb the oil sands structure. Therefore, Touhidi-Baghini used bitumen free, McMurray Formation oil sands samples to measure the absolute permeability (Touhidi-Baghini, 1998) during the shearing process. The block samples were taken from the McMurray Formation along the banks of the High Hill River, approximately 60 km east of Fort McMurray, Alberta. They are bitumen free, so it is possible to avoid the disturbance of gas evolution and bitumen extraction. The oil sands specimens used in testing were obtained by coring the block bitumen free sample both vertically and horizontally. If the specimens were drilled perpendicular to the bedding direction, they were called vertical core specimens, such as Vertical T27, T28, T29, T36, T38, and T39. If the specimen were drilled parallel to the bedding direction, they were called horizontal core specimens, such as Horizontal T40, T41, T42, and T43. The specimen properties are listed in Table 6-2. Touhidi-Baghini measured absolute permeability of these oil sands specimens during shearing based on four stress paths (Figure 6-10).

Figure 6-11 and Figure 6-12 show the volumetric strain as a function of axial strain for horizontal and vertical specimens, respectively. In general, the volumetric strain increases with increasing the axial strain. For horizontal specimens, as shown in Figure 6-11, the maximum volumetric strain is about 11% when its axial strain is 10% (Horizontal T43, tested with stress path 4). Meanwhile, for the same axial strain, volumetric strain decreases for specimens tested along stress path 1. Horizontal T40 that is tested with stress path 1 displays contracting behavior for axial strains less than 4%. Vertical specimens exhibit similar behavior (Figure 6-12). The specimens tested with stress paths 2, 3, and 4 (Vertical specimens T38, T36, and T39) reach their maximum volumetric strain at an axial strain of approximately 4%. However, Vertical specimens T27, T28, and T29, which were tested along stress path 1, had a volumetric strain of less than zero when the axial strain is less than about 5%. Their maximum volumetric strain is also much smaller (3 - 4%) compared with other vertical specimens.

Stress path 1 is a shearing loading process because it increases the confining effective stress. Although the shearing process can cause the specimen to dilate and increase its volume, the increasing confining effective stress results in a decrease of the specimen volume. The combination of these two mechanisms controls the variation characteristics of the volumetric strain. In fact, the shear stress causes contraction of the specimen initially and the increase of confining effective stress compresses the specimen. So, the volumetric strain is negative (contraction) at the beginning of shearing. When the volumetric strain reaches the minimum value, shear dilation becomes dominant and the specimen'volume increases as shear stress and axial strain increase. Owing to the effect of increasing confining effective stress, the final volumetric strain is much smaller than that of the specimens tested with stress paths 2, 3, and 4. Stress path 2 has no change of the effective confining stress and the volumetric strain of specimen is only controlled by the shearing process. However, stress paths 3 and 4 involve the isotropic unloading process because the confining effective stress decreases with increasing shear stress and axial strain. This unloading causes specimen volume to increase. This process more significantly affects the specimens tested with stress path 4 because for the same shear stress, the confining effective stress of stress path 4 is smaller than that of stress path 3. Clearly, permeability variations due to shear stresses are stress path dependent.

Figure 6-13 and Figure 6-14 show the absolute permeability variations as a function of volumetric strain for both horizontal and vertical specimens. From these two figures, it is clearly seen that although the initial permeability of these two types of specimens is similar, the variation in permeability by the shearing process is much different. The permeability of vertical specimens can be increased from approximately 2 μm^2 to the maximum value of 7 μm^2 (Vertical T36) for a volumetric strain of 3.2%. In contrast, the permeability of horizontal specimens can be increased from approximately 1.5 μm^2 to the maximum value of 4 μm^2 (Horizontal T43) for a volumetric strain of about 2.5%. The permeability of the specimens tested with stress path 1 is not increased significantly because of the volumetric contraction induced by the loading process. It is noted that when the permeability has reached its maximum value, the additional volume change leads to a decrease in absolute permeability. It is speculated that with increasing volumetric strain, fines migration has occurred and led to pore throat blockage and permeability decreases (Touhidi-Baghini, 1998).

Permeability ratios as a function of volumetric strain are shown in Figures 6-15 and 6-16 for horizontal and vertical specimens, respectively. Except the specimens tested with stress path 1, vertical specimens' permeability (Figure 6-16) can be increased approximately by 400% (Vertical T36), 500% (Vertical T38), and 700% (Vertical T39) for the volumetric strains of 3.2%, 6%, and 10%, respectively. However, Figure 6-15 shows that the maximum horizontal specimens' permeability is increased by about 250% (Horizontal T43) for the volumetric strain of 2.5%. So, for the same volumetric strain, vertical specimen's permeability is increased more significantly than horizontal specimen's permeability.

6.5 Effective Permeability to Water

Oldakowski (1994) measured effective permeability to water and its variations of oil sands specimens during isotropic unloading and shearing processes. These oil sands cores were obtained from wells drilled in 1987 at the AOSTRA Underground Facility Phase A site. The testing results of samples S19, S20, S21, S22, and S23 are analyzed here because these samples have been tested with both isotropic unloading and shearing stress paths. The sample properties are listed in Tables 6-3 and 6-4.

Figure 6-17 shows the relationship of volumetric strain as a function of confining effective stress. Figure 6-18 provides a regression curve fit through all the data points. It is seen that the volume increase is less than 2% when the confining effective stress is reduced from approximately 6000 kPa to 150 kPa.

Because of high bitumen saturation, pore space, and pore throat geometry, the region available for water to flow is very small. Figure 6-19 is the measured effective permeability to water as a function of volumetric strain. The initial effective permeability to water of these five samples is approximately from 10^{-5} μm^2 (Sample S20) to 10^{-4} μm^2 (Sample S19). The variation of effective permeability to water can be clearly shown by the ratio of the altered value to its initial value (Figure 6-20). It is seen from Figure 6-20 that the isotropic unloading process can increase the effective permeability to water more significantly if the initial permeability is small (Sample S20) (Table 6-3). The final effective permeability to water of the five samples is about 2 to 6 times of the initial value for the maximum volumetric strain of 1.6 to 1.8%. The increase of effective permeability to water is greater than that of the absolute permeability for the same volumetric strain due to the isotropic unloading process (Figure 6-8 and 6-20). The reason is that the initial effective permeability to water of Sample S19 to S23 is much smaller than the initial absolute permeability of reconstituted oil sands specimens Sn-1 to Sn-5 and PI-1 to PI-4 (Figure 6-8). This is consistent with the statement that the smaller the initial permeability, the larger the increase of permeability due to the isotropic unloading process.

Effective permeability to water varies differently with the shearing stress paths. Figure 6-21 shows the volume changes of Sample S19 to S23 as a function of axial strain. The shearing stress path was applied to these five samples. The initial confining effective stresses (σ_{3i}') are 3000 kPa, 890 kPa, 1950 kPa, 570 kPa, and 1390 kPa for Samples S19, S20, S21, S22, and S23, respectively. The volumetric strain for Sample S19 is the smallest because of the maximum initial confining effective stress. It is only 3% for the axial strain of 8%. Other samples reach the maximum volumetric strain of about 6% for the axial strain of 5% to 6%. The volumetric strain reaches a maximum value when shear failure occurs. Figures 6-22 to Figure 6-26 show the first derivatives of volumetric strain to the axial strain for Samples S19 to S23, respectively. It is clearly seen that when shear failure occurs, these first derivatives or rate of volume change reach the maximum value.

Figure 6-27 shows the effective permeability to water as a function of volumetric strain for Samples S19 to S23. Effective permeability increases significantly as volumetric strain increases. Particularly, it increases dramatically when shear failure occurs. Using the first derivative of effective permeability to axial strain helps to identify the change in permeability. These results are shown in Figures 6-28 to 6-32. They show that after shear failure, the derivatives increase as axial strain increases. This means that for the same increment of axial strain, effective permeability to water increases more significantly after shear failure than before failure. The magnitude of the improvement of effective permeability to water can be clearly seen in Figure 6-33. For all the samples except Sample S19, which has the highest initial confining effective stress of 3000 kPa, the effective permeability to water is 100 to 500 times higher than their initial value for a volumetric strain of 4% to 6%.

6.6 Discussions

6.6.1 Comparison of Permeability Changes due to Different Geomechanical Behavior

The maximum absolute permeability change due to the isotropic unloading process, based on the reconstituted oil sands specimens, is not more than two times its initial value (Figure 6-8). However, it can be 5 times higher than its initial value due to the shearing process based on vertical specimens (Vertical T38) (Figure 6-16).

The initial effective permeability to water of oil sands core specimens is very low, and its maximum value due to the isotropic unloading process can be 2 to 6 times higher than its initial value (Figure 6-20). In contrast, the shearing process can induce even more significant increase of effective permeability to water, which can be 100 to 500 times higher than its initial value for a volumetric strain of 4% to 6% (Figure 6-33). Therefore, it can be concluded that whatever the initial permeability is for oil sands specimens, the shearing process can induce a significant improvement in oil sands permeability. But the volume change during shear is confining stress dependent and if the confining effective stress is too high, the shearing process may cause oil sands permeability to decrease (Figure 6-34) (Scott et al., 1991). In addition, both the isotropic unloading process and the shearing process play an important role when the initial permeability value is low.

Figure 6-35 shows the effective permeability to water as a function of volumetric strain for both the isotropic unloading and pure shearing process. A comparison of the effects of isotropic unloading and shearing is also shown in Figure 6-33. From Figure 6-21 and Figures 6-22 to 6-26, it is seen that the volumetric strain is less than 2% when shear failure occurs. The effective permeability to water can be greatly increased if shear failure occurs. Before shear failure occurs, the shearing process plays the same role as the isotropic unloading process (Figure 6-33 and 6-35).

6.6.2 Tortike's Equation and Kozeny-Carman Model

Tortike derived an equation based on Kozeny-Carman model to determine the modified permeability as a function of volumetric strain, which is induced by geomechanical behavior. This equation is expressed as follows (Equation (2-2)):

$$\frac{k}{k_0} = \frac{\left(1 + {\varepsilon_v}/{\phi_o}\right)^3}{\left(1 + \varepsilon_v\right)} \tag{2-2}$$

It can be applied to calculate the absolute permeability variations due to the isotropic unloading process. The results are shown in Figure 6-36. This figure shows that Tortike's equation matches the absolute permeability data measured during the isotropic unloading process when the initial value is greater than 1 μm^2. It has a large deviation if the initial permeability is small.

The initial absolute permeability of horizontal specimens from the block oil sands sample is greater than 1 μm^2. Permeability ratio as a function of volumetric strain due to the shearing process and the curve based on Tortike's equation are both plotted in Figure 6-37. It is shown that Tortike's equation matches the absolute permeability data of horizontal specimens very well. However, if Tortike's equation is plotted on a similar figure for vertical specimens, it does not match the testing results (Figure 6-38). When the volumetric strain is less than 4%, Tortike's equation approximately matches the measured absolute permeability data. However, if the axial strain is greater than 4%, a large deviation exists between the measured data and the calculated results from Tortike's equation. The reason is that shear failure occurs at the volumetric strain of about 2% to 4% for vertical specimens. After shear failure, absolute permeability of vertical specimens is improved more significantly and Tortike's equation cannot be used to determine the modified permeability value under this condition. Although the modified absolute permeability of horizontal specimens matches Tortike's equation, it is likely coincidental because the improvement of horizontal permeability due to the shearing process is smaller than that of vertical permeability.

Consequently, it is concluded that if the initial absolute permeability is greater than 1 μm^2, Tortike's equation is applicable to calculate the modified absolute permeability due to the isotropic unloading process. It is also possible to determine the absolute permeability value due to the shearing process before the shear failure occurs. After shear failure, Tortike's equation will induce significant errors in the calculation of the modified absolute permeability due to the shearing process. In addition, if the initial absolute permeability is much smaller than 1 μm^2, Tortike's equation cannot be applied to calculate the modified absolute permeability by both processes.

It should be noted that another expression of absolute permeability as a function of porosity (Equation (6-4))

$$\frac{k}{k_0}=\left(\frac{\phi}{\phi_0}\right)^3\left(\frac{1-\phi_0}{1-\phi}\right)^2 \tag{6-4}$$

based on Kozeny-Carman model (Dullien, 1979) should be similar to Tortike's equation because both of them do not take the variation of tortuosity into account. Tortuosity can be defined as the ratio of the length of a fluid particle's flowing path to the length of a straight line between the beginning and ending points of the path.

Based on the modified Kozeny-Carman model (Collins, 1976), the absolute permeability ratio can be written as Equation (6-5)

$$\frac{k}{k_0}=\frac{C}{C_0}\frac{\phi^3\,\tau_0 S_0}{\phi_0^3\,\tau\,S} \tag{6-5}$$

Although Tortike's equation considered the porosity change, it assumes that the tortuosity is constant during the geomechanical processes, such as isotropic unloading and shearing. The deviation may result from this assumption.

6.6.3 Permeability of Horizontal and Vertical Specimens

Although the vertical and horizontal oil sands specimens were all obtained from the bitumen free block oil sands sample, their permeability varies differently during the shearing process. This difference may result from the internal structures of both types of specimens. The bedding direction in horizontal specimens is consistent with the core specimen axis. In a microscopic scale, the long axis of all the grains is approximately parallel to the bedding direction (side element in Figure 6-2) because this alignment of grains is more stable. During the shearing process, axial stress applied to the specimen is increased gradually. If the shear stress is large enough to cause the specimen to yield, shear dilation occurs and oil sands grains may start to rotate, roll, and dilate relative to each other (Figure 6-39). When the stress path touches the failure envelope, peak state is reached and pore space increases significantly around the shear bands. As shown by Wong (2000), the density of shear bands can occupy 16% to 47% of the specimen body during the triaxial compression tests with Athabasca oil sands specimens. Due to the mechanisms associated with shear dilation, the tortuosity of fluid flow is reduced and absolute permeability improved accordingly.

Similar mechanisms can occur in the vertical specimens during the shearing process. The long axis of most grains in these specimens is also parallel to the bedding direction (top element in Figure 6-2). However, it is perpendicular to the core specimen axis. Thus, when the specimens yield and fail during the shearing process, grain rotation and rolling may induce even more significant reductions of tortuosity (Figure 6-39) than that of horizontal specimens. That is why absolute permeability of vertical specimens is much larger than that of horizontal specimens for the same volumetric strain.

6.6.4 Calculation of Absolute Permeability due to Shearing

Touhidi-Baghini (1998) defined the following general equation (Equation (6-6)) for absolute permeability:

$$k = C\,D_s^2\,\frac{\phi^a}{(1-\phi)^b} \tag{6-6}$$

where C is a function of the particle shape and pore shape and D_s is the mean size of the solid particles. The constants a and b are determined from experimental data. Based on this equation and the assumption that C is constant, the following equation (Equation (6-7)) was derived to calculate the oil sands permeability:

$$Ln\frac{k}{k_0} = C_{n_1}\,\varepsilon_v \tag{6-7}$$

where

$$C_{n1} = \left[\frac{(1-\phi_0)\,a + b\,\phi_0}{\phi_0}\right] \tag{6-8}$$

using the Chardabellas terms of $a = b = B$, Touhidi-Baghini (1998) obtained the following equation (Equation (4-8)):

$$Ln\frac{k}{k_0} = \frac{B}{\phi_0}\,\varepsilon_v \tag{4-8}$$

The average initial porosity is 0.339 for both horizontal and vertical specimens. Values of $B = 2$ and $B = 5$ were applied to obtain a good agreement with the experimental results for the horizontal and vertical specimens, respectively. The parameter C_{nl} was computed to be 5.9 and 14.76 (Figure 6-40 and Figure 6-41) accordingly. It is possible to apply these equations to calculate the improved absolute permeability due to the shearing process in the field if the confining effective stress and the stress path are approximately consistent with that used in the testing.

It should be noted that although the shape factor C in Equation (6-6) was assumed as a constant, the parameter C_{nl} was chosen as 5.9 and 14.76 to match the testing results of horizontal and vertical specimens, respectively. The reason is that as discussed above, horizontal and vertical specimens change their pore shapes and tortuosity differently. The different selection of B values or C_{nl} values actually has taken the different pore shape and tortuosity changes into consideration.

The variation of effective permeability to water due to the isotropic unloading process cannot be matched by Tortike's equation (Figure 6-42). However, Equation (6-7) can be applied to fit the test data with B value of 6 ($C_{nl} = 81.69$), as shown in Figure 6-42.

Figure 6-43 shows the effective permeability to water modified by the shearing process as a function of volumetric strain. The calculation results from Equation (6-7) are also shown in this figure. The water porosity of the oil sands specimens S19 to S23 varies from 6.1% to 9.3% with an average value is 8.1%. If B is set to 7.5 ($C_{nl} = 92.59$), the calculated results match the test results very well. This is consistent with the discussion above that if the initial permeability and porosity are very small, shearing has a more significant impact on absolute permeability.

6.6.5 Water Relative Permeability

The effect of isotropic unloading and the shearing process on relative permeability to water can be discussed based on the testing results and the proposed calculation methods discussed above. Porosity change as a function of volumetric strain can be expressed as Equation (6-9) (Touhidi-Baghini, 1998)

$$\phi = \frac{\varepsilon_v + \phi_0}{1 + \varepsilon_v} \tag{6-9}$$

$$\phi_w = \frac{\varepsilon_v + \phi_{w0}}{1 + \varepsilon_v} \tag{6-10}$$

$$S_w = \frac{\phi_w}{\phi} \tag{6-11}$$

Because the tests were conducted at the room temperature or the initial reservoir temperature (Oldakowsi, 1994), the increased porosity due to the isotropic unloading and the shearing process can be considered as the increase of water porosity (Equation (6-10)). In the triaxial test, pore pressure is measured through the water which transfer the pressure from the pore space to the pressure sensor. Most part of the pore space is occupied by bitumen which is very viscous and cannot flow under the test temperature. Therefore, water will flow into the increased pore space. The ratio between the improved water porosity and the improved total porosity is the modified water saturation (Equation (6-11)). The absolute permeability change due to the isotropic unloading process is determined by Tortike's equation and the change of effective permeability to water due to isotropic unloading is determined by Equation (6-7) with a C_{nl} value of 81.69. The ratio of these two numbers provides the water relative permeability change as a result of isotropic unloading. Correspondingly, absolute permeability change for horizontal specimens because of shearing is calculated by Equation (6-7) with the C_{nl} value of 5.9 and that for vertical specimens with the C_{nl} value of 14.76. The modified value of effective permeability due to shearing can be computed using Equation (6-7) with a C_{nl} value of 92.59. Therefore, the water relative permeability change as a result of shearing is determined by the ratios of modified water effective permeability and absolute permeability.

Figure 6-44 shows the variations of water relative permeability curves as a result of isotropic unloading and shearing. It can be clearly seen that the improvement of water relative permeability due to the isotropic unloading process is much smaller than that due to the shearing process. Water relative permeability for both horizontal and vertical specimens can be greatly increased by the shearing process. If the following theoretical equation (Equation (6-12)):

$$k_{rw} = \frac{k_w}{k} = \left(\frac{S_w - S_{wi}}{1 - S_{wi}} \right)^n , \tag{6-12}$$

from Petroleum Production Handbook (1962) is used with the exponent n = 3.70 (Oldakowski, 1994), the predicted water relative permeability curves shown in Figure 6-44 are much smaller than that modified by geomechanical processes. For these theoretical calculations, the initial water saturations are 20.97% and 23.96% at the beginning of the isotropic unloading and shearing processes, respectively. It should be noted that if the temperature increases, the relative permeability to oil also increases as a function of the isotropic unloading and shearing processes. Meanwhile, the relative permeability to water will decrease accordingly.

6.6.6 Field Applications

As discussed above, both the isotropic unloading process and the shearing process can improve reservoir permeability. The shearing process plays an even more important role in this aspect. In the SAGD operations, steam injection pressure is the key factor to induce both the isotropic unloading process and shearing process. Even if the steam injection pressure similar to the initial reservoir pressure is applied, the pore pressure in the partially drained zone can still be increased significantly due to the thermal expansion effect.

Clearly, to realize the benefits that may accrue from the geomechanical behavior of an oil sands formation, higher steam injection pressure is required. It helps reduce the confining effective stress and the higher temperatures produce greater shear stress in the reservoir material around the interface between the drained zone and the partially drained zone. As a result, the shearing process will induce larger improvement on reservoir permeability (including absolute permeability and relative permeability), particularly for low permeability reservoirs. In addition, high steam injection pressure helps the gas lifting process, increasing oil production rate, and reducing the entire operation period. It should be indicated, however, that geomechanical behavior is but one factor in the selection of steam injection pressure. The practical steam injection pressure should be determined based on all the aspects associated with the economic benefit of the SAGD process (Li and Chalaturnyk, 2003).

6.7 Conclusions

- Isotropic stress and shear stress changes are two major geomechanical processes during the SAGD operations. The former occurs within the high pore pressure front and the latter predominantly around the interface between the drained zone and the partially drained zone.

- The shearing process induces more significant improvements on absolute permeability and effective permeability to water compared to the isotropic unloading process. Particularly, after shear failure, oil sands permeability increases dramatically.

- Tortike's equation is applicable for the isotropic unloading process if the initial absolute permeability is greater than 1 μm^2. Otherwise, it may induce significant errors. Tortike's equation is not appropriate to calculate the modified absolute permeability due to the shearing process, especially after shear failure occurs.

- The absolute permeability of vertical specimens increases more significantly than that of the horizontal specimens for the same volumetric strain. This may result from the significant decrease of tortuosity for vertical specimens.

- Geomechanics induced absolute permeability and effective permeability to water can be determined based on Equation (6-7) with different C_{nl} values for geomechanical cases.

- Water relative permeability increases due to the isotropic unloading and shearing processes. The shearing process produces more significant improvement, particularly after shear failure.

Table 6-1 Specimen conditions after consolidation for isotropic unloading tests

Specimen	Bulk density (g/cm^3)	Dry density (g/cm^3)	Relative density (%)	Porosity ϕ_0 (%)	Void ratio e_0	Max. effective conf. stress (kPa)
Sn1-D	2.05	1.69	92	36.7	0.58	4030
Sn2-D	2.05	1.69	92	36.7	0.58	4120
Sn3-D	2.02	1.64	79	38.3	0.62	4240
Sn5-D	2.03	1.65	79	38.3	0.62	4360
Pl2-D	2.03	1.66	82	37.9	0.61	4400
Pl3-D	2.05	1.68	89	37.1	0.59	1000
Pl1	2.00	1.6	70	39.5	0.65	4040
Pl2	2.02	1.63	80	38.4	0.62	3990
Pl3	2.01	1.62	77	38.7	0.63	4280
Pl4	2.01	1.62	77	38.8	0.63	4160

Table 6-2 Specimen properties from block oil sand sample

Sample	Stress path	Initial confining stress (kPa)	Density (g/cm^3)	Relative density (%)	Initial porosity (%)
Vertical T27	1	150	1.757	128	33.8
Vertical T28	1	200	1.734	120	34.7
Vertical T29	1	210	1.753	127	34.0
Vertical T38	2	250	1.744	124	34.1
Vertical T36	3	250	1.757	128	33.6
Vertical T39	4	250	1.750	126	33.9
Horizontal T40	1	250	1.783	137	32.7
Horizontal T41	2	250	1.754	127	33.8
Horizontal T42	3	250	1.729	119	34.7
Horizontal T43	4	250	1.758	129	33.6

Table 6-3 Isotropic unloading after consolidation under 5.6 to 6.0 MPa

(Stress path referring to Figure 7-1)

Specimen	Stress path	Initial bulk density (g/cm^3)	Initial porosity (%)	Disturb. index (%)	Initial water porosity (%)	Initial perm. to water (darcy)	Effective Conf. pressure change (kPa)	Volume change (%)	Perm. to water change (%)
S19	Au	2.06	36.2	5.8	8.9	2.1×10^{-4}	5860 to 140	1.72	106
S20	Ap	2.08	34.9	7.4	8.3	5.3×10^{-6}	5720 to 150	1.59	500
S21	Au	2.09	34.5	3.6	5.4	7.7×10^{-5}	5960 to 160	1.60	258
S22	Ap, Au	2.07	35.9	6.2	7.2	1.2×10^{-5}	5610 to 120	1.62	500
S23	Au	2.08	35.3	7.6	6.9	5.3×10^{-5}	5660 to 120	1.73	214

Table 6-4 Specimen conditions at the beginning of shear tests

(Stress path referring to Figure 7-1)

Specimen	Stress path	Effective confining stress (kPa)	Bulk density (g/cm^3)	Porosity (%)	Disturb. index (%)	Water saturation (%)	Water porosity (%)	Effective permeability to water (darcy)
S19	Dp	3000	2.06	36.5	6.7	25.4	9.3	2.5×10^{-4}
S20	Dp	890	2.07	35.4	8.9	25.3	9.0	1.9×10^{-5}
S21	Du	1950	2.08	35.0	5.1	17.4	6.1	1.8×10^{-4}
S22	Du	570	2.05	36.7	8.6	22.8	8.4	4.9×10^{-5}
S23	Du	1390	2.07	35.9	9.5	21.5	7.7	1.4×10^{-4}

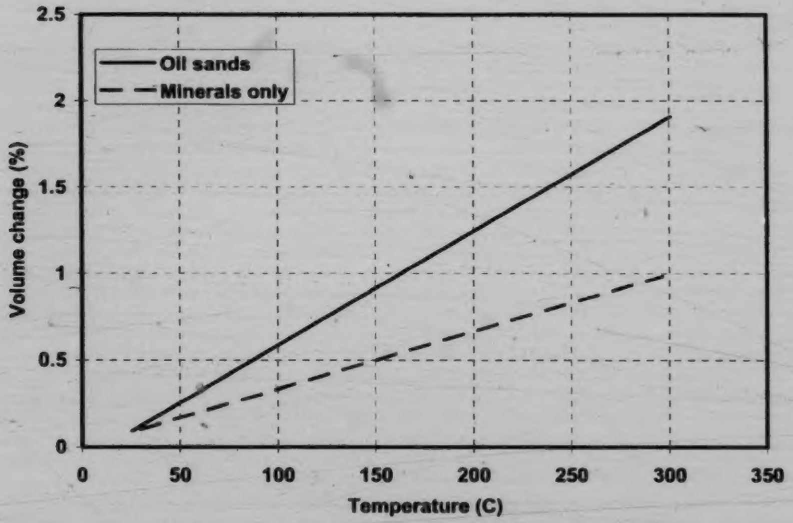

Figure 6-1 Thermal expansion of oil sands (After Scott et al., 1991)

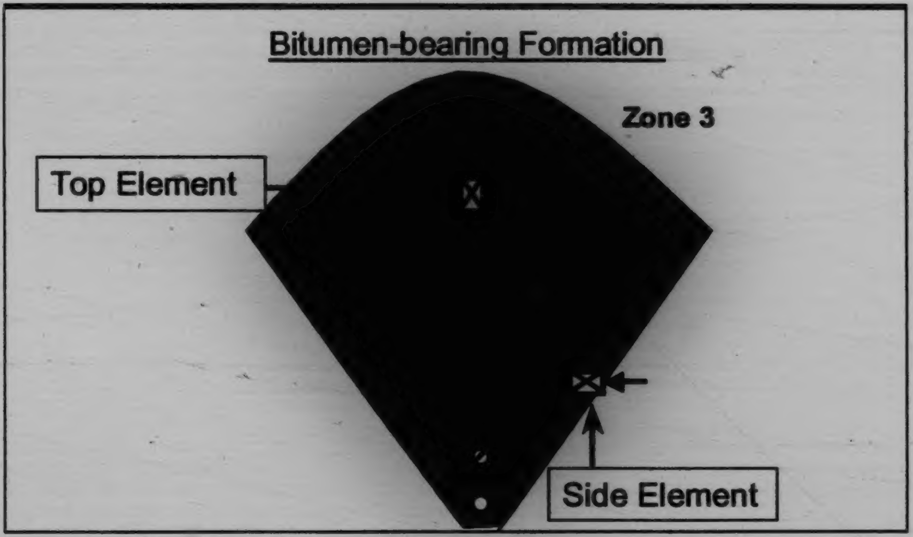
Bitumen-bearing Formation
Zone 3
Top Element
Side Element

Figure 6-2 Shearing in the SAGD process

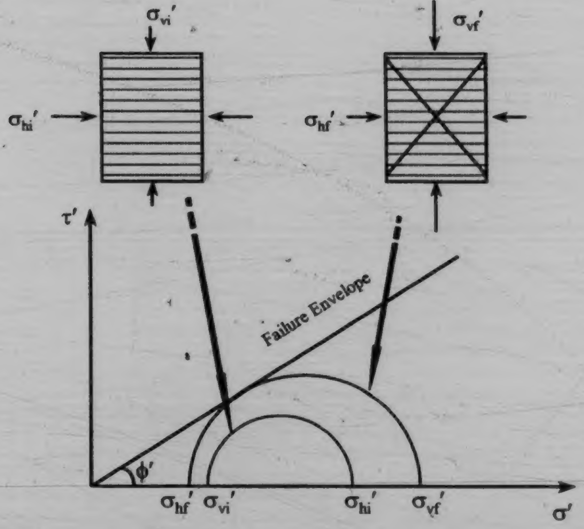
σ_{vi}'
σ_{vf}'
σ_{hi}'
σ_{hf}'
τ'
Failure Envelope
ϕ'
σ_{hf}'
σ_{vi}'
σ_{hi}'
σ_{vf}'
σ'

Figure 6-3 Schematic shear failure of top element as deviatoric stress increases - the shear plane has a large angle to the bedding direction

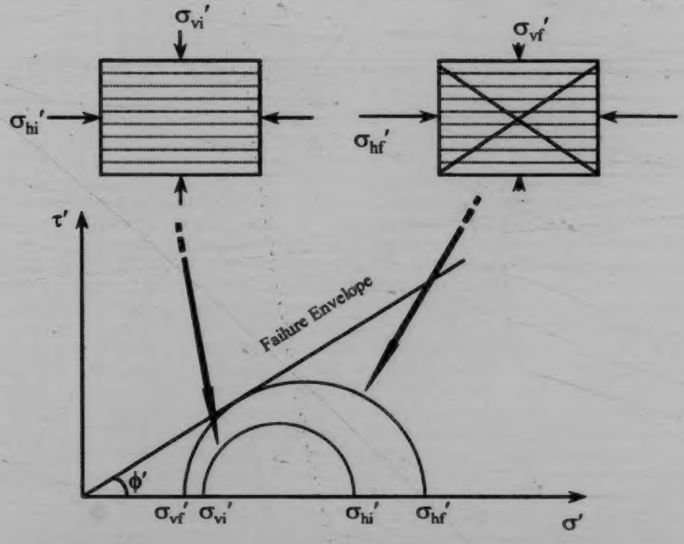
σ_{vi}'
σ_{vf}'
σ_{hi}'
σ_{hf}'
τ'
Failure Envelope
ϕ'
σ_{vf}'
σ_{vi}'
σ_{hi}'
σ_{hf}'
σ'

Figure 6-4 Schematic shear failure of side element as deviatoric stress increases - the shear plane has a small angle to the bedding direction

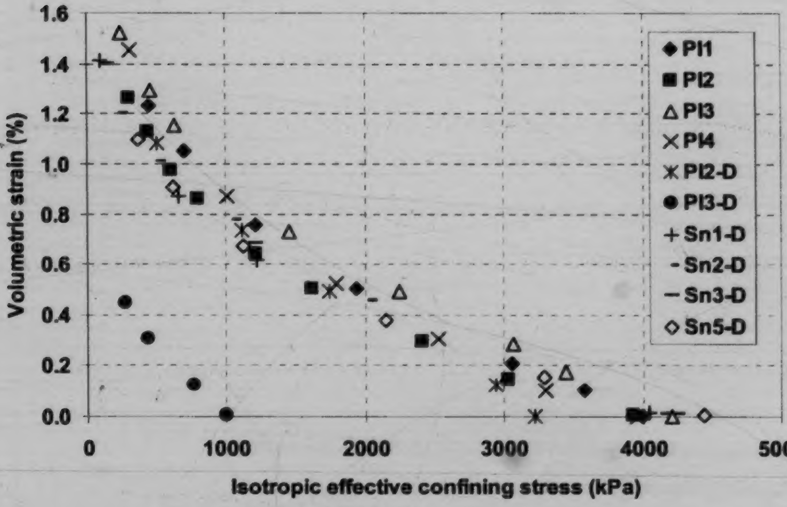

Figure 6-5 Volume change vs. confining effective stress (after Oldakowski, 1994)

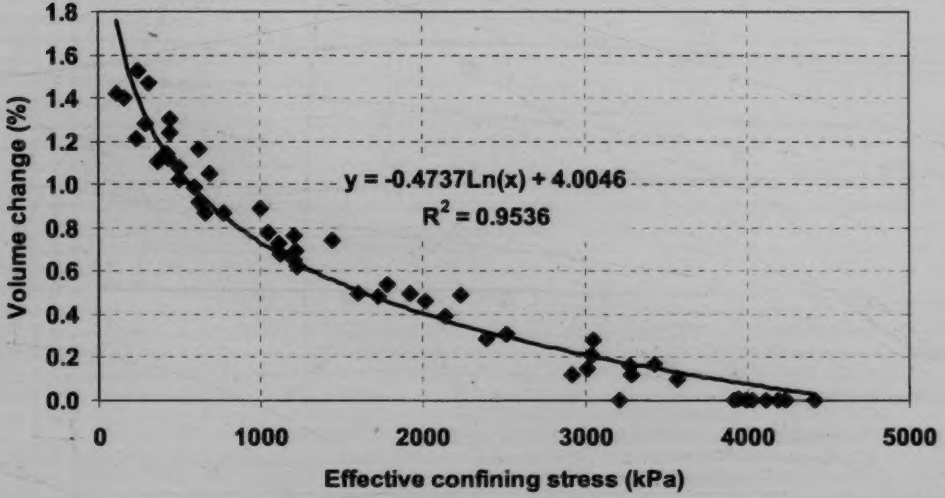

Figure 6-6 Regression curve through all the data (with exception of PI3-D) shown in Figure 6-5

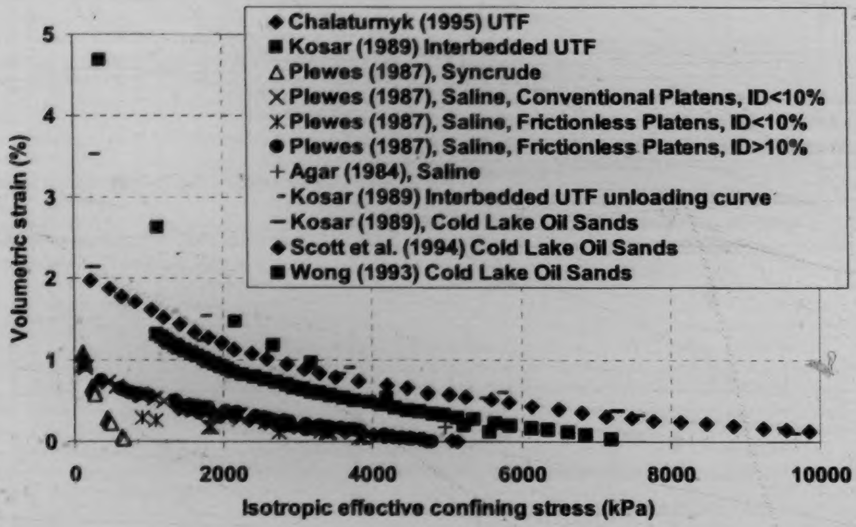

Figure 6-7 Volumetric strain vs. isotropic confining effective stress (After Chalaturnyk, 1996)

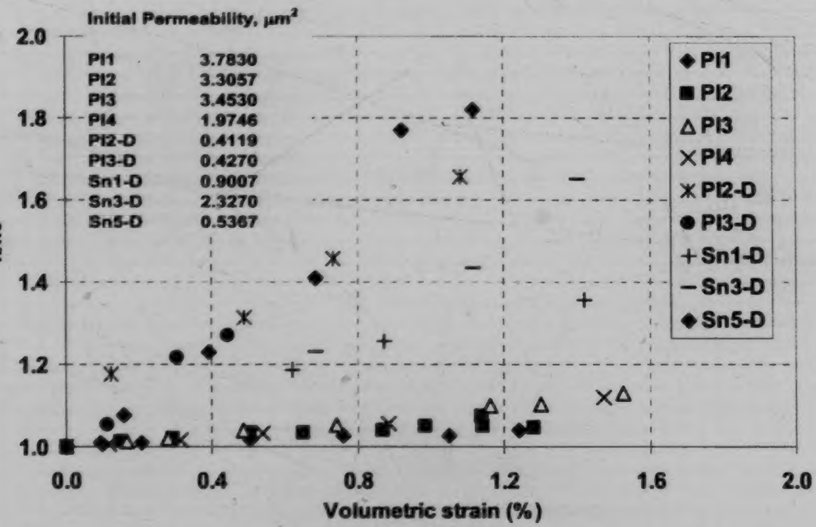

Figure 6-8 Absolute permeability ratio vs. volumetric strain from isotropic unloading test (after Oldakowski, 1994)

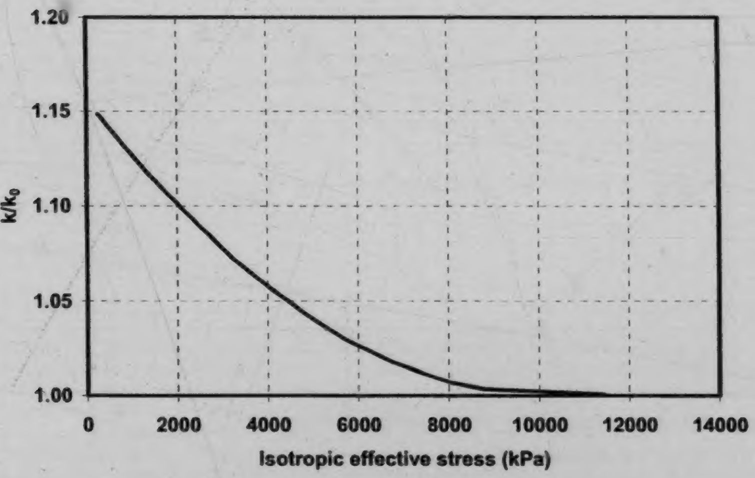

Figure 6-9 Absolute permeability ratio vs. isotropic effective stress (After Scott et al., 1991)

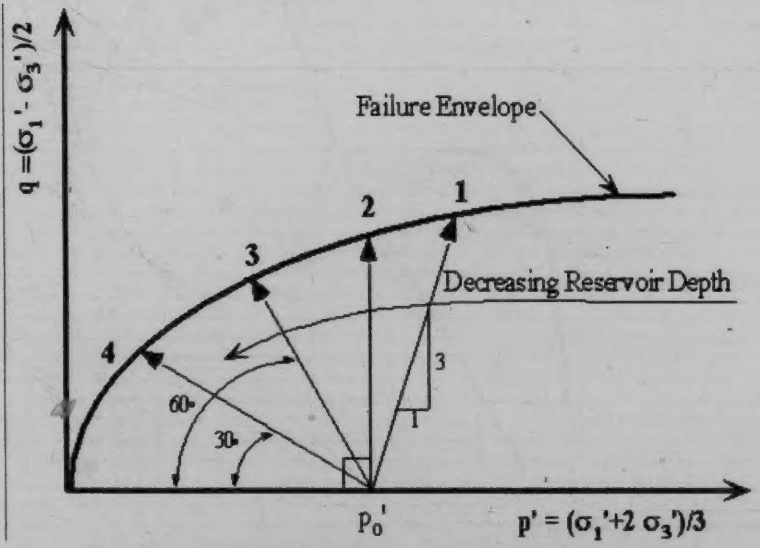
q =(σ$_1$' - σ$_3$')/2
Failure Envelope
1
2
3
4
Decreasing Reservoir Depth
3
1
60°
30°
p$_0$'
p' = (σ$_1$'+2 σ$_3$')/3

Figure 6-10 Stress paths for absolute permeability test during shearing (after Touhidi-Baghini, 1998)

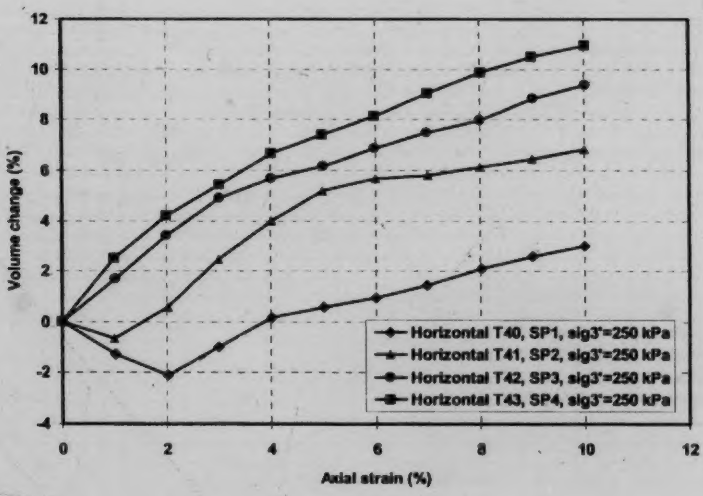

Figure 6-11 Volume change vs. axial strain for horizontal specimens

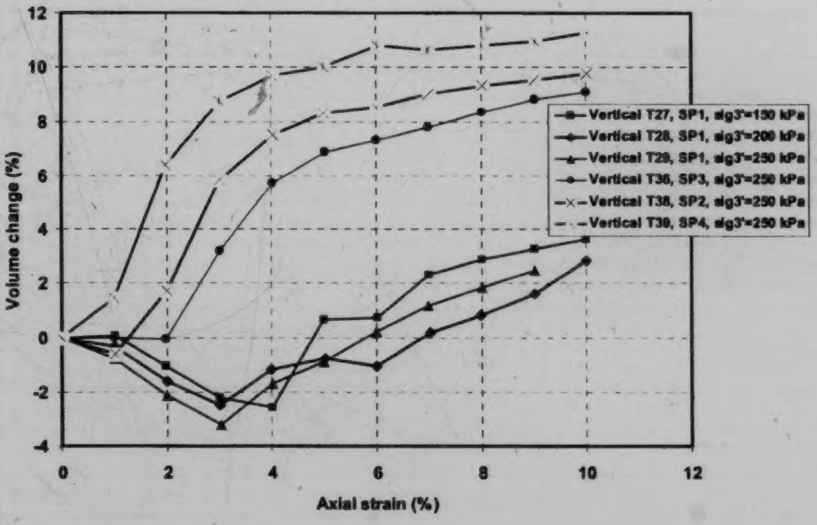

Figure 6-12 Volume change vs. axial strain for vertical specimens

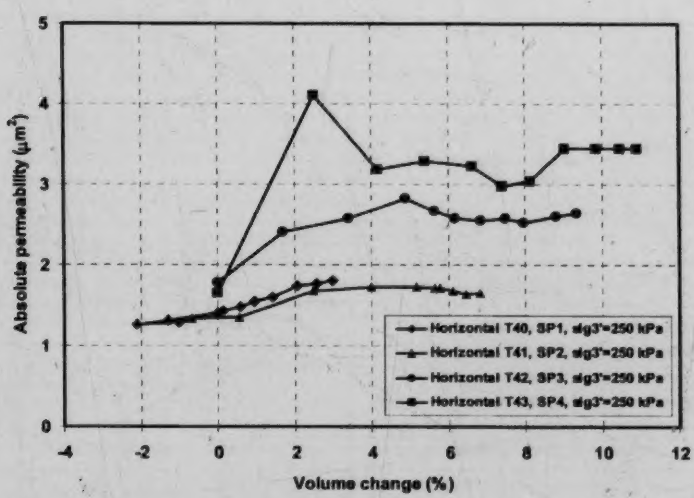

Figure 6-13 Absolute permeability change during shearing for horizontal specimens

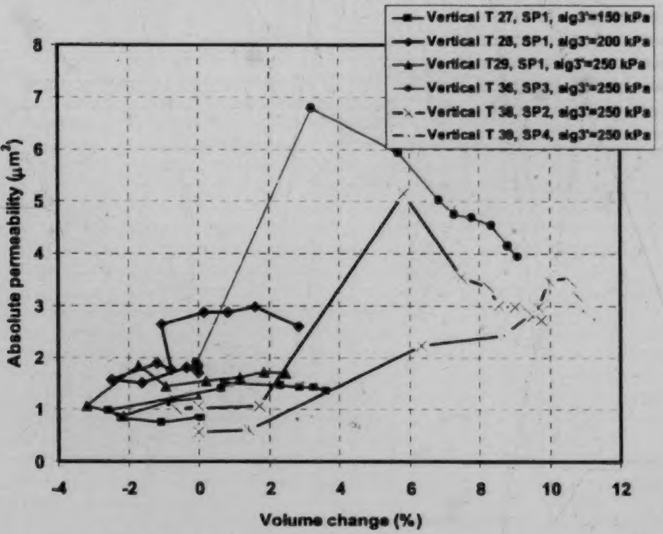

Figure 6-14 Absolute permeability change during shearing for vertical specimens

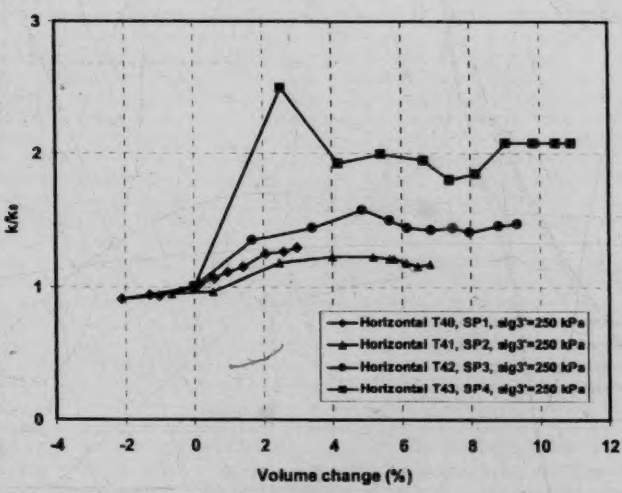

Figure 6-15 Absolute permeability ratio vs. volume change for horizontal specimens

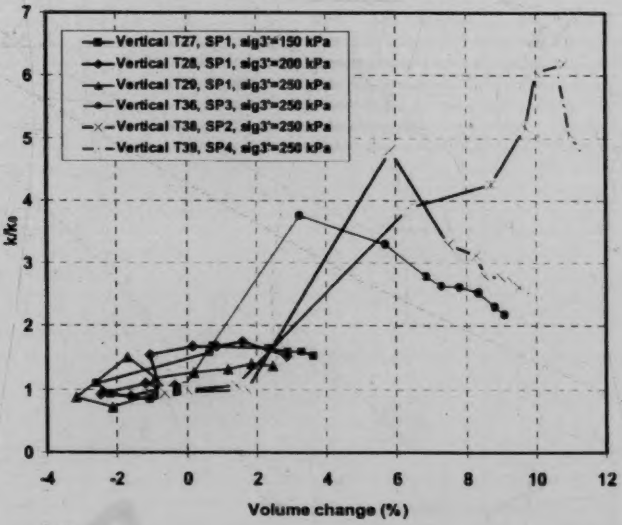

Figure 6-16 Absolute permeability ratio vs. volume change for vertical specimens

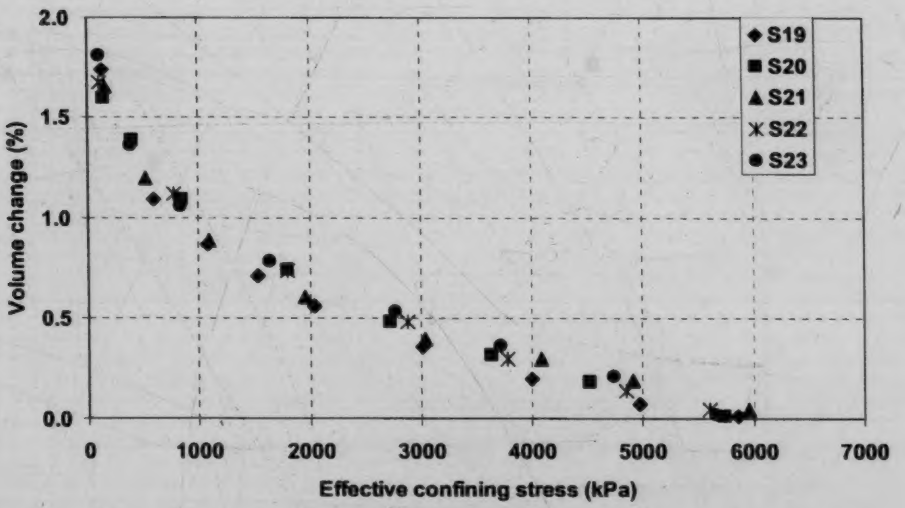

Figure 6-17 Volume change vs. effective confining stress (after Oldakowski, 1994)

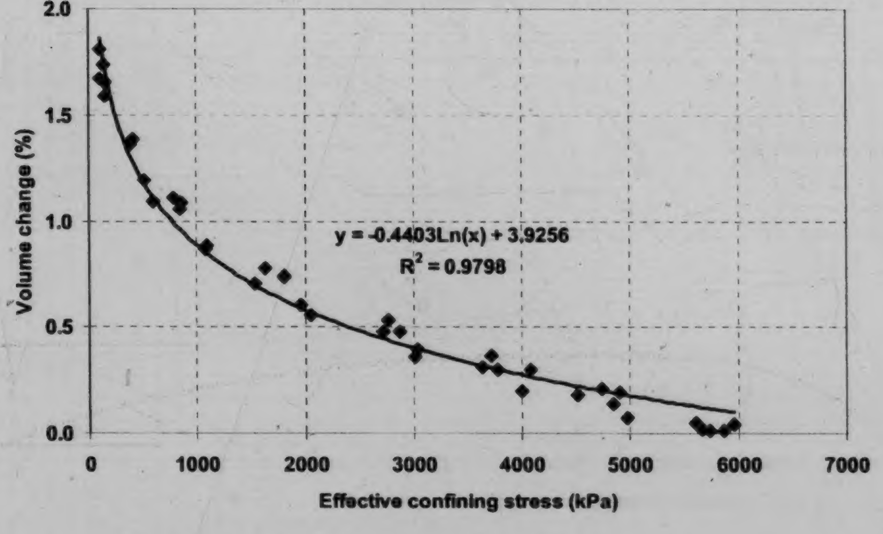

Figure 6-18 Regression curve through all the data shown in Figure 6-17

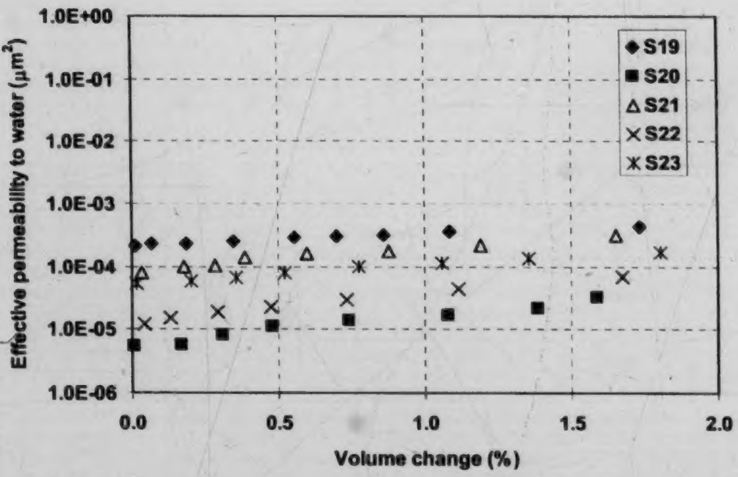

Figure 6-19 Effective permeability to water vs. volume change (after Oldakowski, 1994)

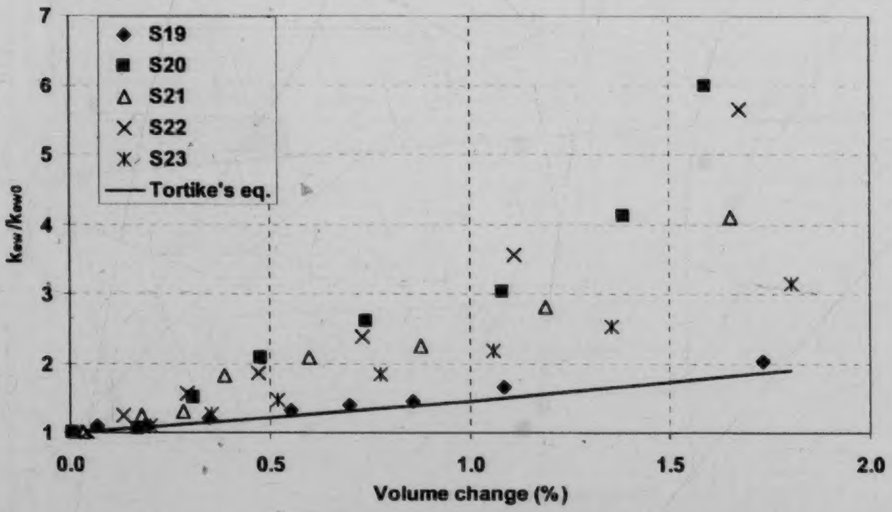

Figure 6-20 Effective permeability ratio vs. volume change including the curve with Tortike's equation

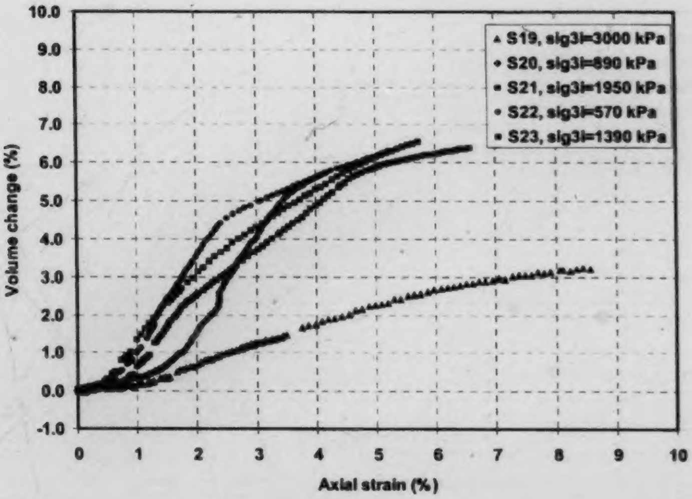

Figure 6-21 Volume change vs. axial strain during shearing (after Oldakowski, 1994)

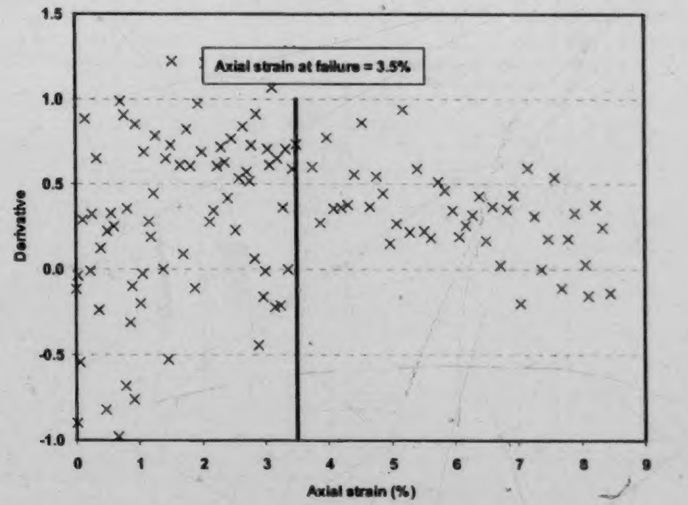

Figure 6-22 Derivative of volume change to axial strain for specimen S19

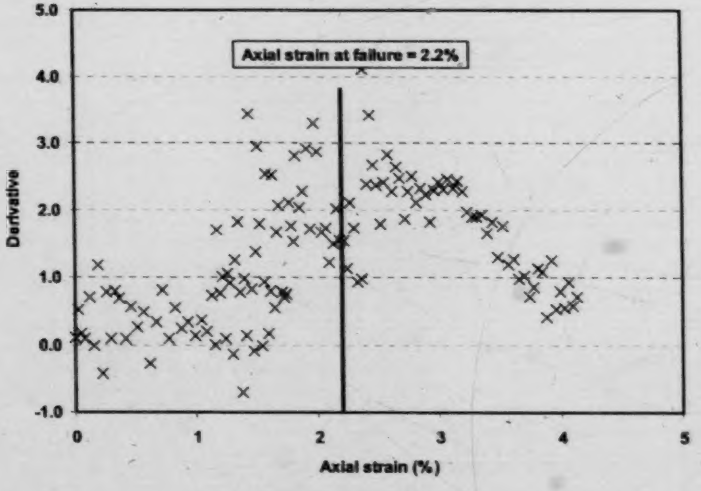

Figure 6-23 Derivative of volume change to axial strain for specimen S20

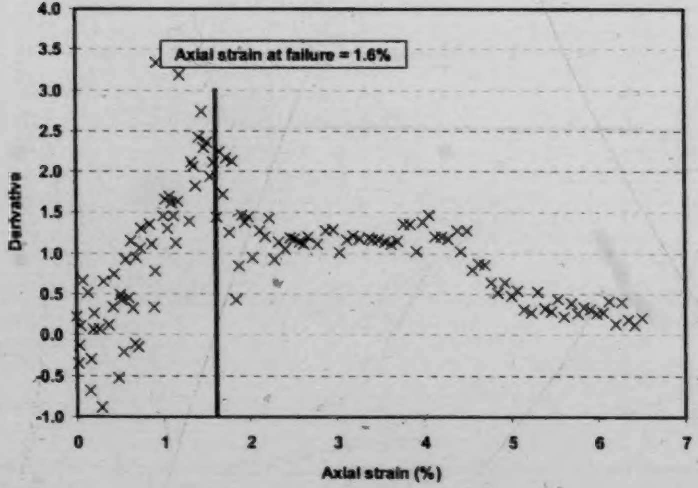

Figure 6-24 Derivative of volume change to axial strain for specimen S21

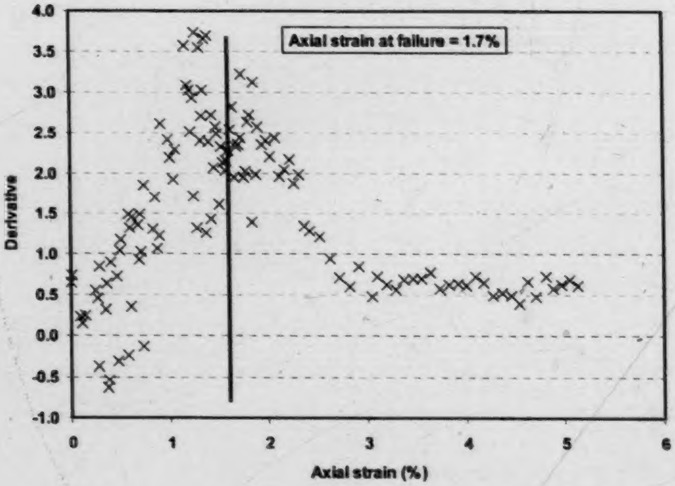

Figure 6-25 Derivative of volume change to axial strain for specimen S22

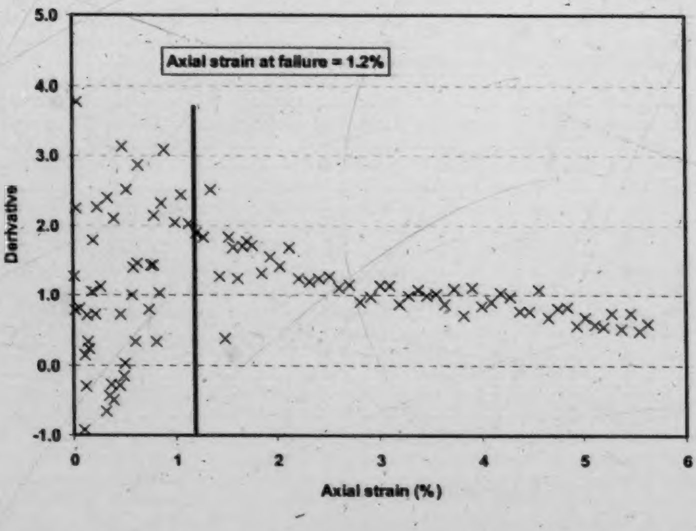

Figure 6-26 Derivative of volume change to axial strain for specimen S23

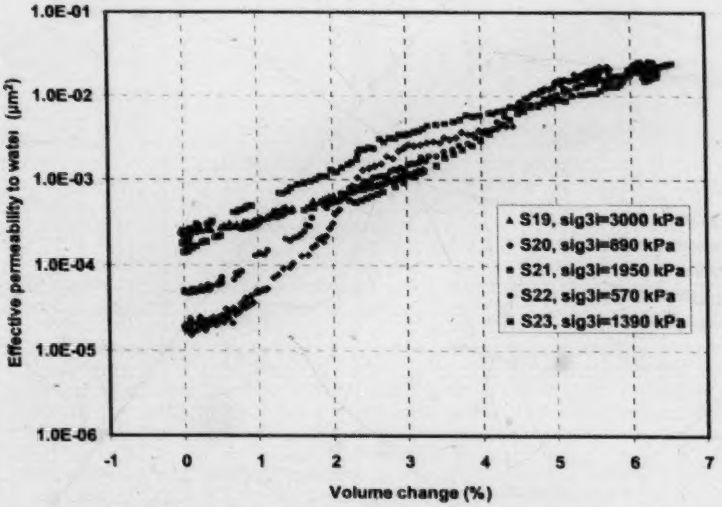

Figure 6-27 Variation of effective permeability to water vs. volume change during shearing (after Oldakowski, 1994)

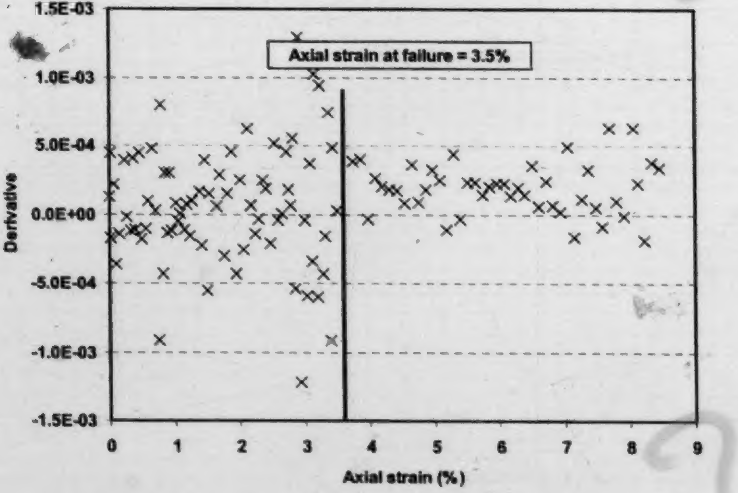

Figure 6-28 Derivative of water effective permeability to axial strain for specimen S19

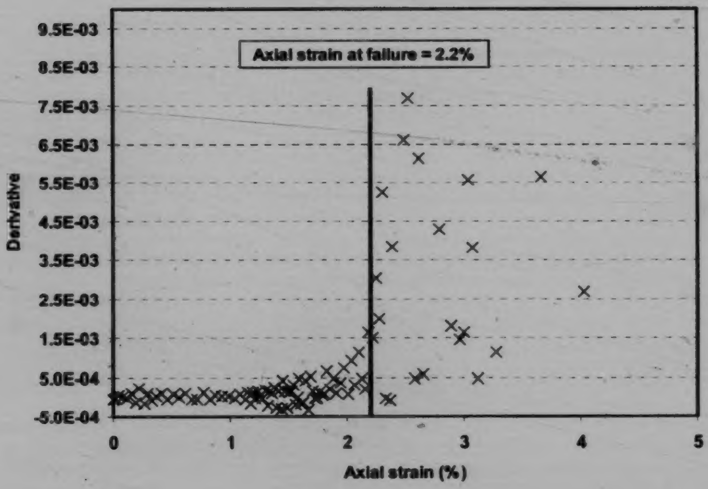

Figure 6-29 Derivative of water effective permeability to axial strain for specimen S20

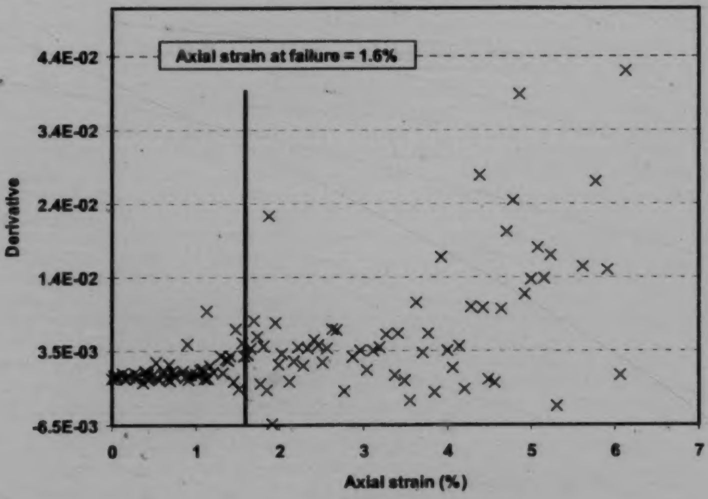

Figure 6-30 Derivative of water effective permeability to axial strain for specimen S21

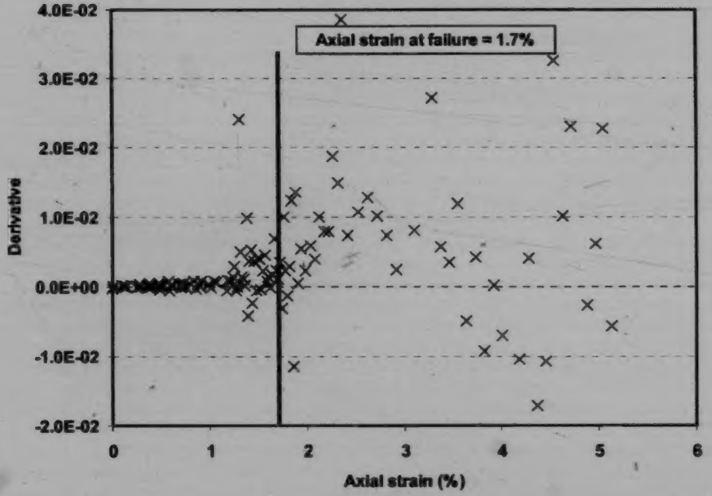

Figure 6-31 Derivative of water effective permeability to axial strain for specimen S22

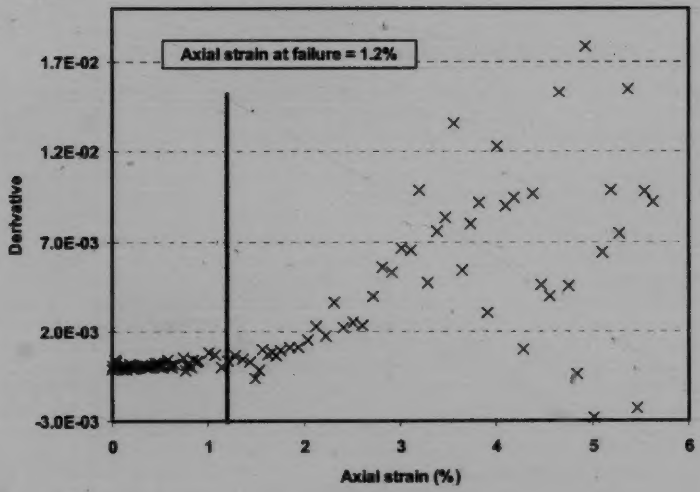

Figure 6-32 Derivative of water effective permeability to axial strain for specimen S23

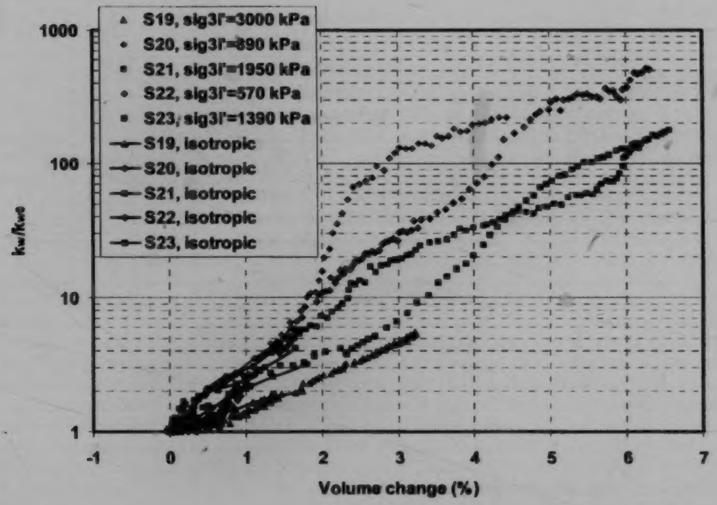

Figure 6-33 Comparison of water effective permeability ratio due to isotropic unloading and shearing

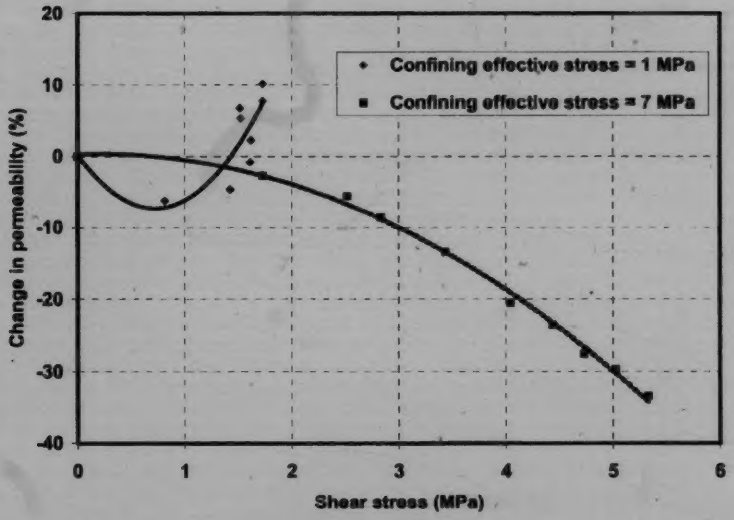

Figure 6-34 Impact of confining effective stress on change in permeability (Scott et al., 1991)

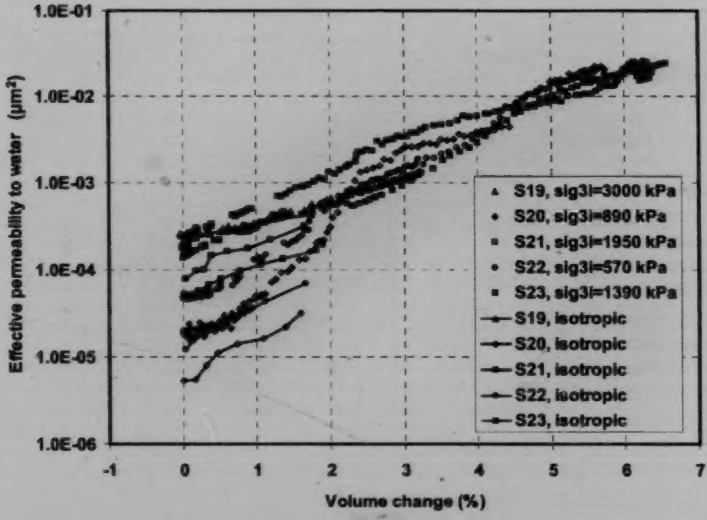

Figure 6-35 Comparison of effective permeability to water due to isotropic unloading and shearing

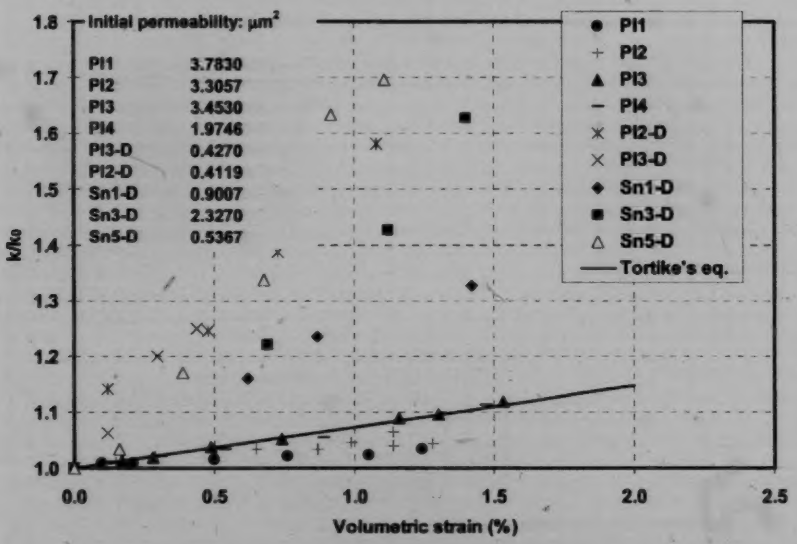

Figure 6-36 Absolute permeability ratios from isotropic unloading test and Tortike's equation

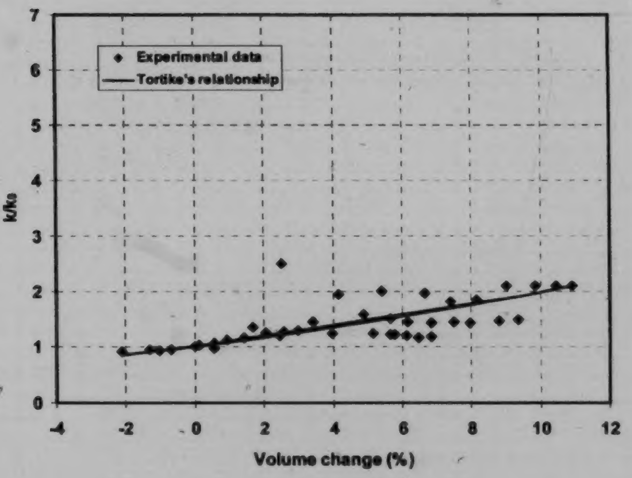

Figure 6-37 Absolute permeability ratios from shearing test of horizontal specimens and Tortike's equation

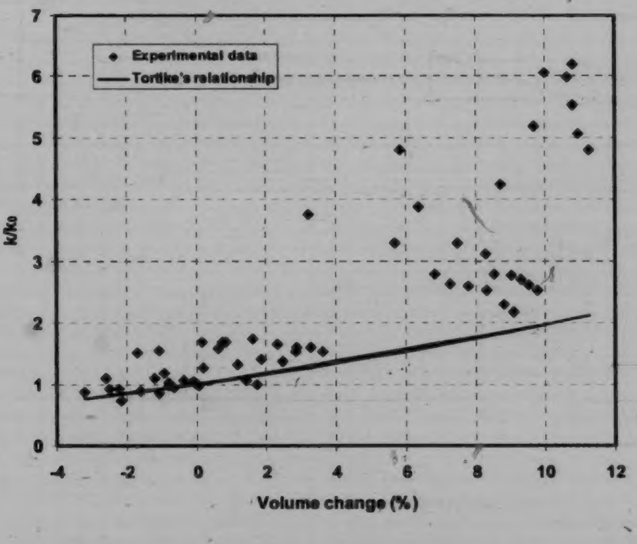

Figure 6-38 Absolute permeability ratios from shearing test of vertical specimens and Tortike's equation

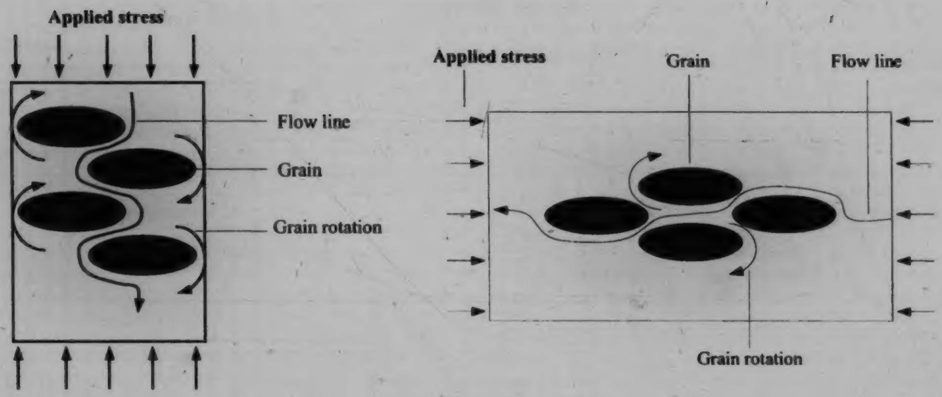
Applied stress
Flow line
Grain
Grain rotation
Applied stress
Grain
Flow line
Grain rotation

Figure 6-39 Tortuosity change for vertical (left) and horizontal (right) specimens

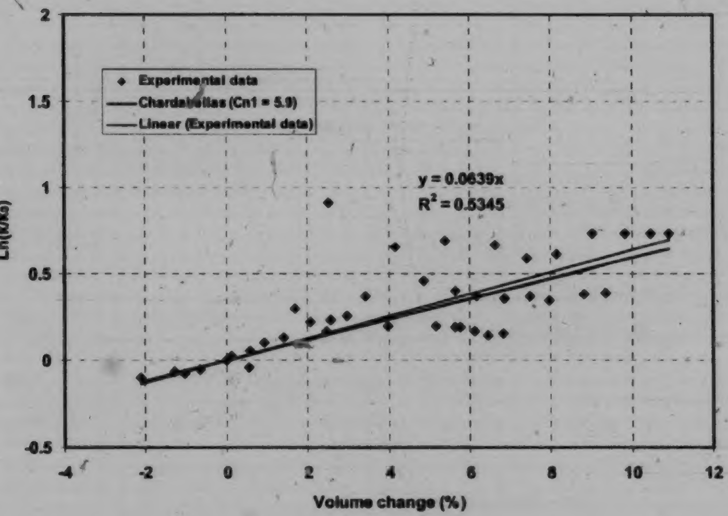

Figure 6-40 Determination of absolute permeability due to shearing for horizontal specimens

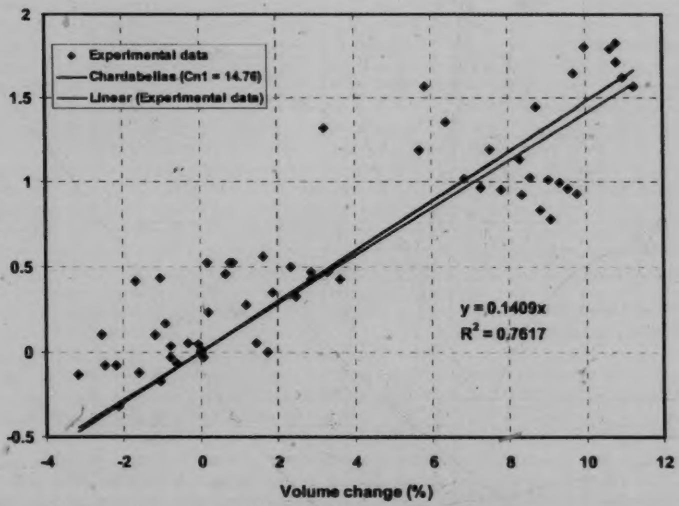

Figure 6-41 Determination of absolute permeability due to shearing for vertical specimens

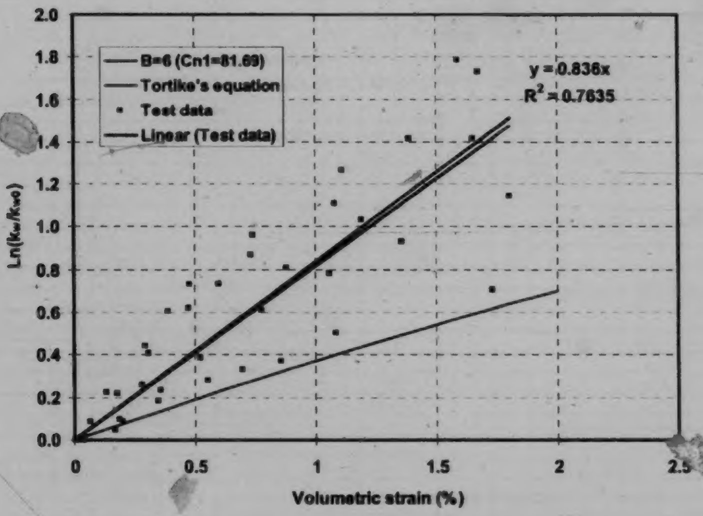

Figure 6-42 Determination of absolute permeability due to the isotropic unloading process

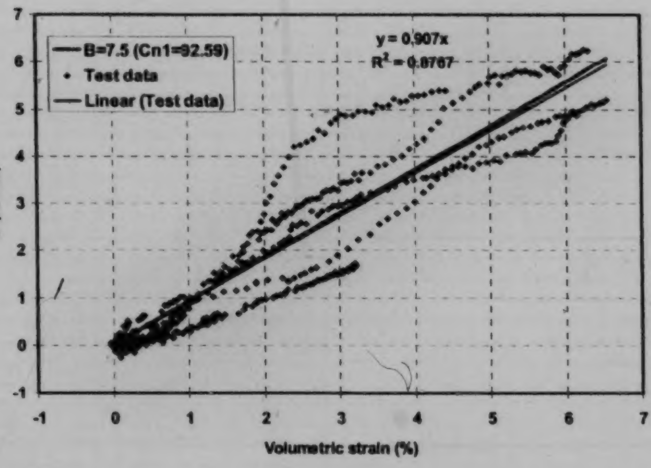

Figure 6-43 Determination of effective permeability to water due to the shearing process

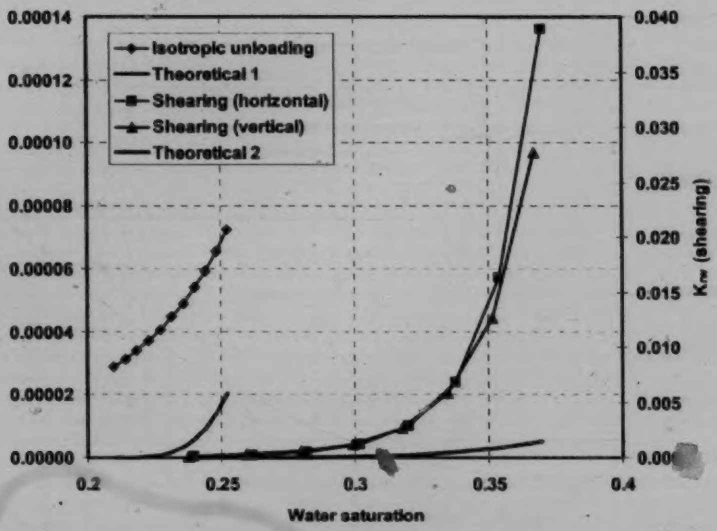

Figure 6-44 Impact of isotropic unloading and shearing on water relative permeability

CHAPTER 7 GEOMECHANICAL MODEL OF OIL SANDS*

7.1 Introduction

The geomechanical properties of oil sands have been studied extensively since 1970s (Dusseault, 1977; Agar, 1982; Kosar, 1989; Oldakowski, 1994; Chalaturnyk, 1996; Samieh and Wong, 1997; Touhidi-Baghini, 1998). The major objective is to improve the surface mining efficiency, understand the reservoir deformational behaviors regarding in situ recovery and hydraulic fracturing, and predict the in situ recovery performance. With increasing experience in sampling and testing, good quality data have been obtained from lab testing. In this chapter, the most recent laboratory testing results from Oldakowski (1994), Samieh and Wong (1997), and Touhidi-Baghini (1998) are analyzed and simulated in order to obtain a representative geomechanical model of oil sands material.

7.2 Laboratory Testing On Oil Sands

7.2.1 Oldakowski's Lab Tests

Oldakowski (1994) conducted a series of triaxial compression tests with different stress paths based on drilled oil sands cores to characterize the stress-strain relationship of oil sands material. These oil sands cores were obtained from wells drilled at the AOSTRA Underground Facility Test Phase A site in 1987. In total, 23 oil sands samples were obtained from wells AT3 and AGI4 (Figure 4-4) at two stratigraphic units, E and D, which consist of the richest oil sands at the UTF site.

Oldakowski applied four different effective stress paths or, in terms of total stress, seven stress paths during the tests. These stress paths in the p'-q' space are shown in Figure 7-1.

Typical testing results are shown in Figures 7-2 and 7-3.

---

* Part of this chapter entitled *Geomechanical Model of Oil Sands* (Li, P. and Chalaturnyk, R.J.) has been published in the International Thermal Operations and Heavy Oil Symposium (ITOHOS) (SPE 97949), Calgary, Alberta, Canada, November 1-3, 2005.

7.2.2 Samieh and Wong's Lab Tests

Samieh and Wong (1997) provided consolidated drained triaxial compression test results with different boundary conditions (confining stresses). Oil sand specimens were obtained from an exploration well at the OSLO lease 41 site, which is approximately 10 km north of Fort McMurray.

In total, six drained triaxial compression tests were conducted with confining stresses of 50 kPa, 100 kPa, 300 kPa, 450 kPa, 600 kPa, and 750 kPa. During these tests, the applied confining stresses were kept constant and axial strain increased based on designed strain rate. Typical testing results are shown in Figure 7-4.

7.2.3 Touhidi-Baghini's Lab Tests

It is known that oil sands samples can be easily disturbed during sampling process. To overcome the potential for disturbance, Touhidi-Baghini (1998) used intact, relatively undisturbed bitumen free block samples of McMurray Formation sand to obtain specimens for triaxial compression tests with permeability measurement. These block samples were taken from the McMurray Formation along the banks of the High Hill River, approximately 60 km east of Fort McMurray. They are bitumen free but with intact oil sands structure and fabric. Triaxial compression tests were conducted along four different stress paths (Figure 6-10).

Figures 7-5 and 7-6 show the testing results based on stress path 1 (Specimen Horizontal T40).

It can be seen that all the testing results based on different researchers demonstrate the strain softening behavior of oil sands material. Consequently, it is reasonable that a strain-softening model is utilized to characterize the geomechanical behavior of oil sands.

7.3 FLAC Numerical Experiments of Laboratory Tests

Drained triaxial compression tests on dense sand under low confining pressures typically show a response of the form illustrated in Figure 7-7. The specimen exhibits a marked peak in its deviatoric stress-axial strain curve, and, thereafter, deviatoric stress decreases and is continuing to decrease at the end of the test. Volumetrically, the specimen contracts slightly initially, but then expands or dilates strongly until the end of the test. Strain softening from a peak deviatoric stress is a familiar feature of the observed stress strain behavior of dense sand (Touhidi-Baghini, 1998). It is plausible to describe the stress-strain behavior of oil sands material with the strain-softening model because oil sands have an even higher density than ordinary dense sands.

The approach chosen to quantify the parameters of a strain-softening model was to perform numerical experiments with the same testing conditions as those applied in the laboratory. The numerical experiment approach was applied to match the relationship between stress and strain and that between volumetric strain and axial strain. Strain-softening model parameters were modified until satisfactory matches were obtained with experimental results. The geomechanical simulator, FLAC, was used for the numerical experiments, which are discussed below.

Axisymmetry allows half of the sample to be modeled in the numerical experiments. The grid system (7 × 14 = 98 blocks) was applied in these numerical experiments (Figure 7-8). Touhidi-Baghini (1998) investigated the effect of grid systems on the simulation results and found that the grid systems of 98 blocks were sufficient to minimize gridding effects.

The numerical experiments were conducted based on the following steps:

1) set up the same oil sands model and boundary conditions as that used in the lab tests;

2) apply the strain softening Mohr-Coulomb model and related model parameters, such as modulus of elasticity, friction angle, dilation angle; and

3) run the numerical experiments with the same stress paths as in the laboratory. Adjust the model parameters and relationships to obtain a good match to the laboratory tests.

A total of 26 numerical experiments were performed, including 12 of Oldakowski's tests, 6 of Samieh and Wong's tests, and 8 of Touhidi-Baghini's tests. The matches obtained with experimental data for typical stress paths, stress strain relationships, and volumetric strain as a function of axial strain are shown in Figures 7-9 to 7-15. Other results of the numerical experiments are shown in Appendix A.

7.4 Geomechanical Model of Oil Sands

Given the reasonable matches between the numerical and laboratory experiments, the geomechanical model, which is the strain softening Mohr-Coulomb model, applied in the FLAC simulation can be considered as a representative model for oil sands material. The modulus of elasticity varies as a function of confining effective stress and it can be expressed by Equation (7-1).

$$E = K_E P_a (\sigma_3' / P_a)^{0.5} \tag{7-1}$$

where K_E is a constant. In the 26 numerical experiments, 14 applied the relationship from Samieh and Wong (1997) and K_E is equal to 950. These 14 numerical experiments obtained good matches to the laboratory experiments done by Samieh and Wong (1997) and Oldakowski (1994). In addition, four of these twenty-six numerical simulations applied the K_E value of 650 to 1250 to match the laboratory test data, which were obtained by Oldakowski (1994). To match Touhidi-Baghini's data (1998), the K_E value of 314 and 460 were applied for horizontal cores and vertical cores, respectively. It should be noted that Touhidi-Baghini applied a low confining effective stresses (250 kPa) to do his tests. In contrast, Samieh and Wong (1997) and Oldakowski (1994) conducted the their tests with a large range of confining effective stresses (50 kPa to 3000 kPa). So, it is plausible that the relationship of modulus of elasticity applied to match the laboratory data from them is appropriate to represent the oil sands behavior (Figu[illegible]-16) (Equation (7-2).

$$E = 950 P_a (\sigma_3' / P_a)^{0.5} \tag{7-2}$$

In order to test the general applicability of the model parameter values, the maximum friction angle and dilation angle obtained from Touhidi-Baghini's tests were used in numerical experiments to match Samieh and Wong's and Oldakowski's tests. Very good matches were obtained with only a minor adjustment in these two parameters required to obtain the match to Oldakowski's tests. Consequently, the following relationships (Equations (7-3) and (7-4)) for peak friction angle and dilation angle have been chosen for use in the oil sands model (Figures 7-17 and 7-18)

$$\phi_p' = 55 - 14.93\log\left(\sigma_3' / P_a\right) \tag{7-3}$$

$$\psi_p' = 25.8 - 12.05\log\left(\sigma_3' / P_a\right) \tag{7-4}$$

The post peak behavior of oil sands is characterized by variations of friction angle and dilation angle as a function of plastic shear strain. The numerical matches of the test results from Oldakowski, Samieh and Wong, and Touhidi-Baghini produced similar relationships for the post-peak friction angle and dilation angle. The following equations (Equations (7-5) and (7-6)) have been chosen to represent the post peak behavior of oil sands (Figures 7-19 and 7-20)

$$\phi_r' = 55.9 - 2.03\gamma_p \tag{7-5}$$

$$\psi_r' = 27.3 - 1.53\gamma_p \tag{7-6}$$

7.5 Concluding Remarks

- A great number of laboratory tests done by different researchers, such as Oldakowski, Samieh and Wong, and Touhidi-Baghini, show that oil sands material reflects a strain softening stress strain behavior.
- Totally 26 numerical experiments were performed with the geomechanical simulator, FLAC, to match the corresponding laboratory tests.

- The strain softening Mohr-Coulomb model was established for oil sands material based on the 26 numerical experiments. The modulus of elasticity, the maximum friction angle, and the maximum dilation angle vary as a function of confining effective stress expressed as Equations (7-2), (7-3), and (7-4), respectively. The post-peak friction angle and dilation angle vary as a function of plastic strain expressed as Equations (7-5) and (7-6), respectively

$$E = 950 P_a (\sigma_3^{'} / P_a)^{0.5} \tag{7-2}$$

$$\phi_p' = 55 - 14.93 \log\left(\sigma_3^{'} / P_a\right) \tag{7-3}$$

$$\psi_p' = 25.8 - 12.05 \log\left(\sigma_3^{'} / P_a\right) \tag{7-4}$$

$$\phi_r^{'} = 55.9 - 2.03 \gamma_p \tag{7-5}$$

$$\psi_r^{'} = 27.3 - 1.5 \gamma_p \tag{7-6}$$

Note that these empirical relationships (Equations 7-2 to 7-6) are applicable over the range 0.03 MPa $\leq \sigma_3' \leq$ 3.0 MPa. Caution should be exercised in applying these relationships outside this stress range.

- This strain softening Mohr-Coulomb model can be applied in the coupled reservoir geomechanical simulations for different recovery techniques of oil sands resources. It should be noted that this geomechanical model of oil sands was obtained based on the lab tests with shallow oil sands samples and lower confining stress conditions. Application of the model should take this limitation into consideration.

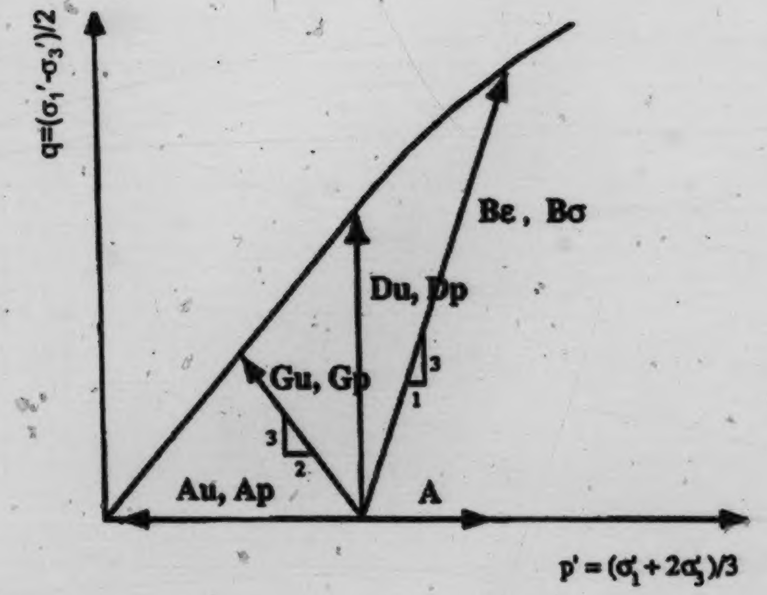

A - Isotropic Compression

Au - Isotropic Unloading by Pore Pressure Injection

Ap - Isotropic Unloading by Decreasing Confining Pressure

Bε - Compression

Bσ - Compression

Dp - Constant p', Compression with Decreasing Confining Pressure

Du - Constant p', Compression with Pore Pressure Injection

Gp - Confining Stress Unloading, Compression with Decreasing Confining Pressure (Constant σ_1' and σ_1)

Gu - Confining Stress Unloading, Compression with Pore Pressure Injection (Constant σ_1')

Figure 7-1 Stress paths (after Oldakowski, 1994)

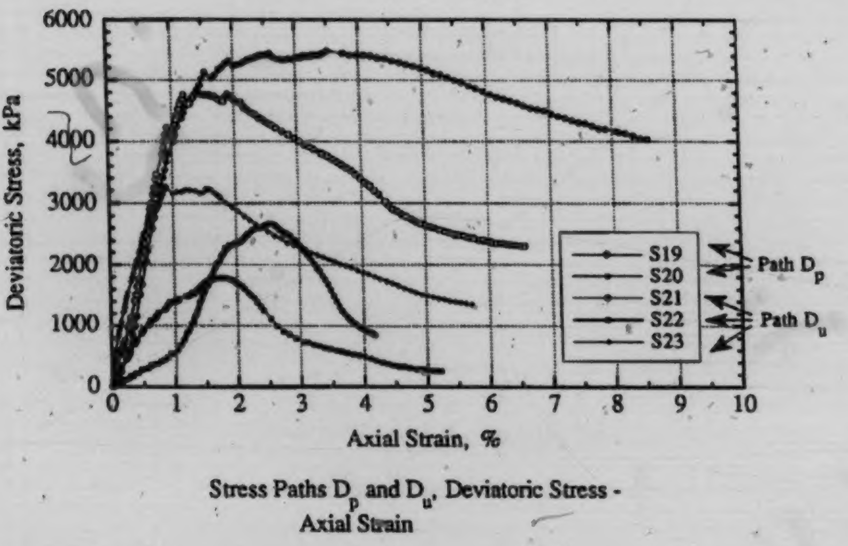

Figure 7-2 Typical stress strain relationships (Oldakowski, 1994)

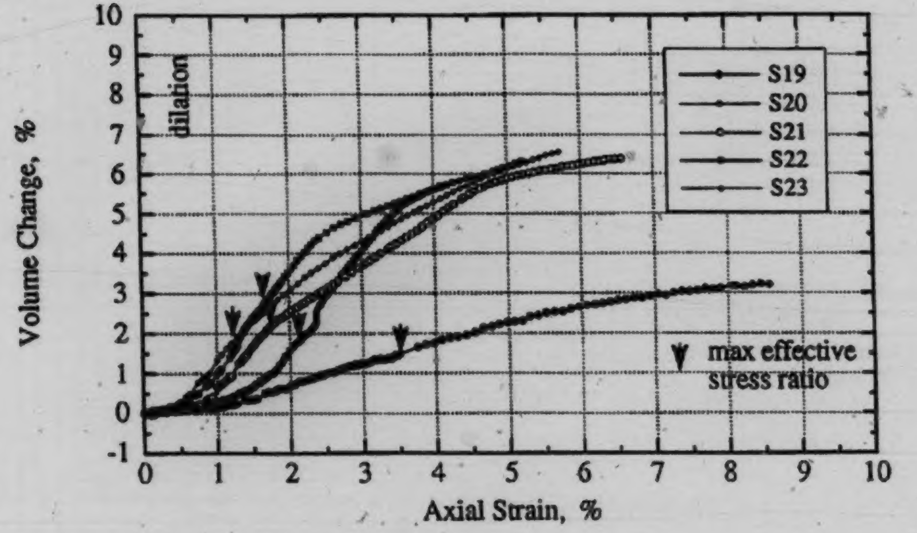

Figure 7-3 Volume change versus axial strain of oil sands (Oldakowski, 1994)

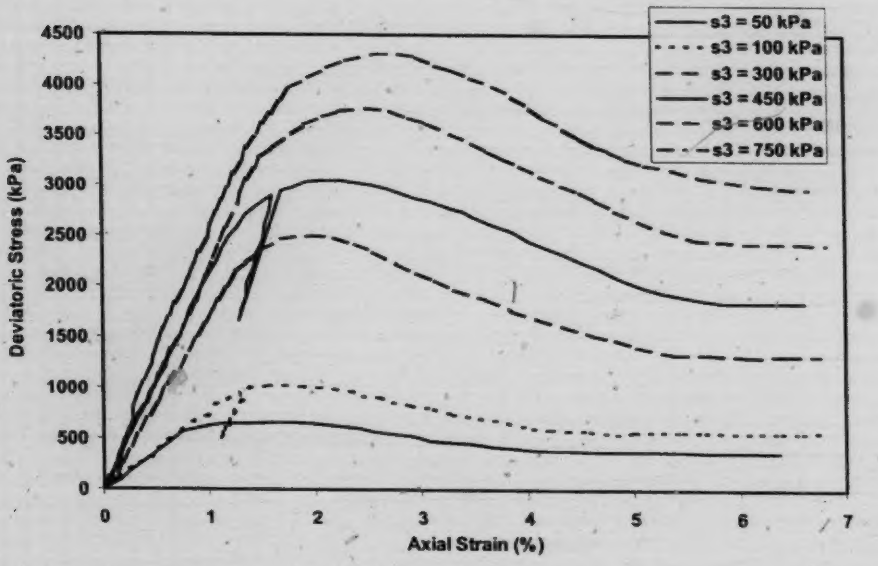

(a)

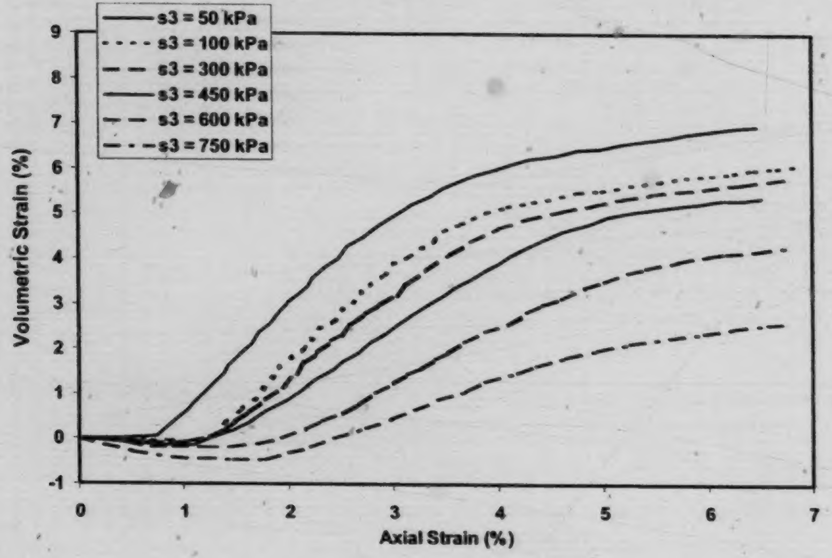

(b)

Figure 7-4 Deviatoric stress and volumetric strain versus axial strain (Samieh and Wong , 1997)

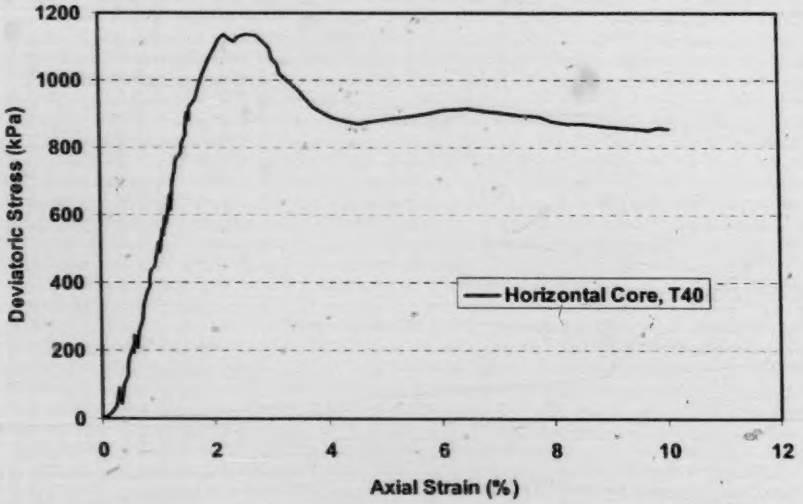

Figure 7-5 Typical stress strain relationship (Stress path 1) (Touhidi-Baghini, 1998)

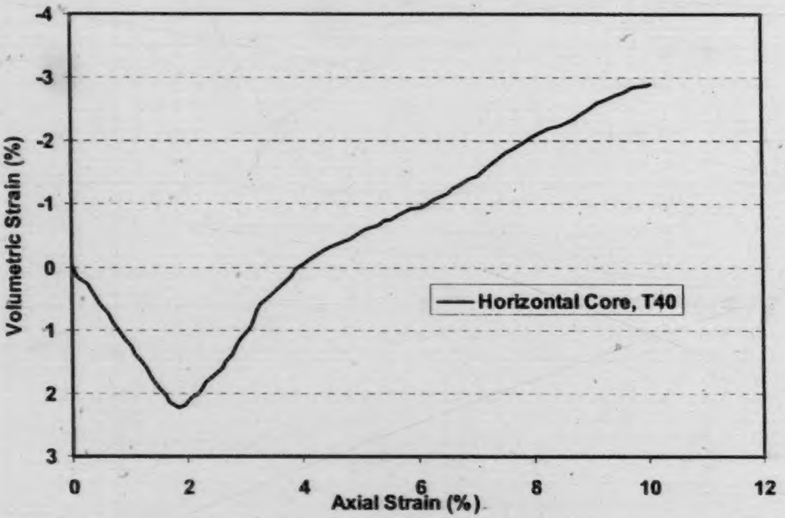

Figure 7-6 Volumetric strain versus axial strain (Stress Path 1) (Touhidi-Baghini, 1998)

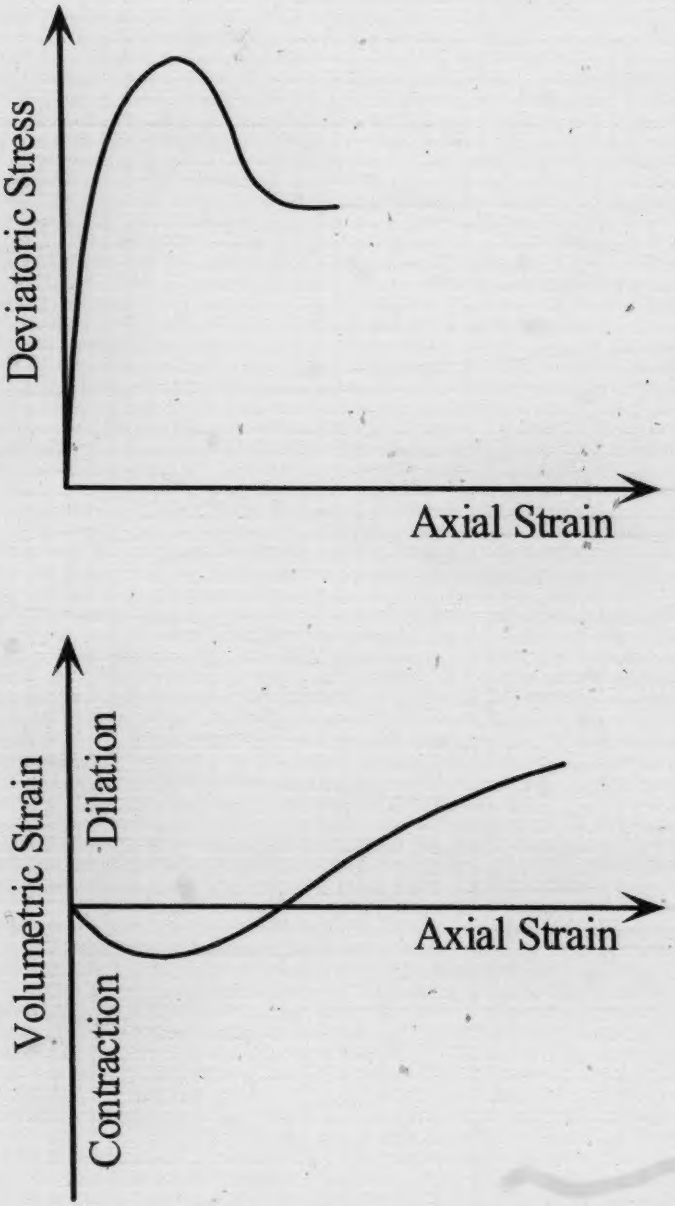

Figure 7-7 Typical drained triaxial test results on dense sands (After Touhidi-Baghini, 1998)

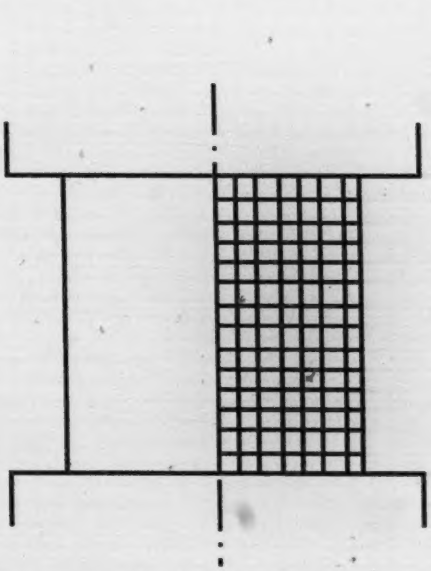

Figure 7-8 Oil sands model in FLAC

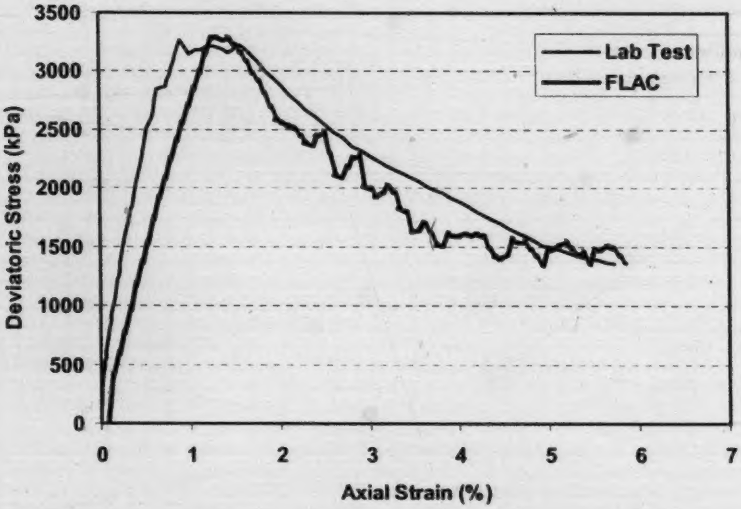

Figure 7-9 Deviatoric stress versus axial strain, Stress Path 2 (Initial σ_3' = 1390 kPa), Lab tests simulated by FLAC (Oldakowski's sample S23)

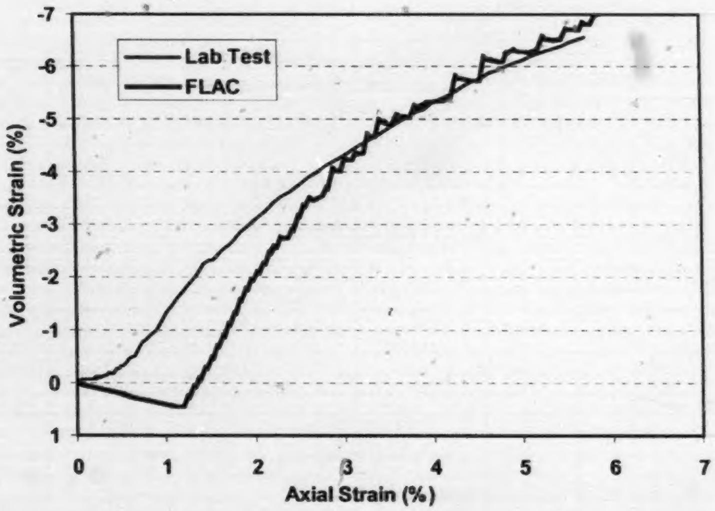

Figure 7-10 Volumetric strain versus axial strain, Stress Path 2 (Initial σ_3' = 1390 kPa), Lab tests simulated by FLAC (Oldakowski's sample S23)

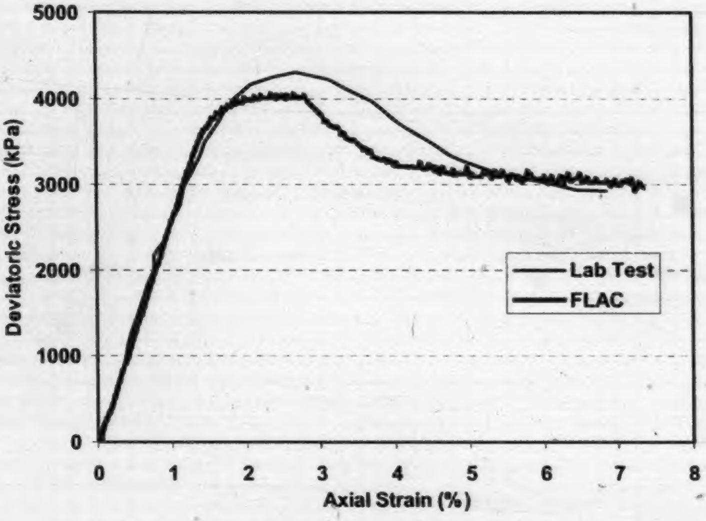

Figure 7-11 Deviatoric stress versus axial strain, Lab tests simulated by FLAC (Samieh and Wong's sample, σ_3' = 750 kPa)

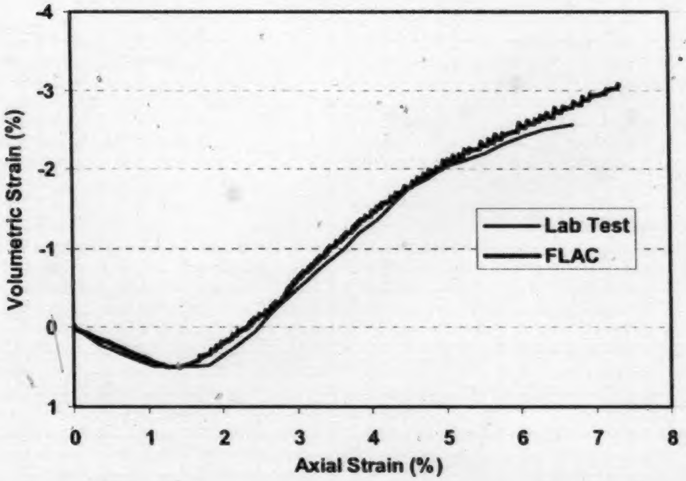

Figure 7-12 Volumetric strain versus axial strain, Lab tests simulated by FLAC (Samieh and Wong's sample, $\sigma_3' = 750$ kPa)

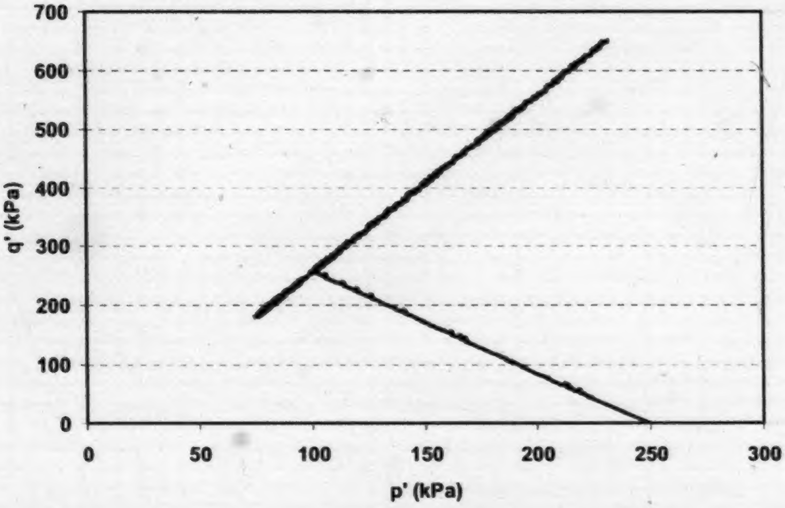

Figure 7-13 Deviatoric stress versus mean effective stress, Stress Path 3 (Initial $\sigma_3' = 250$ kPa), (Touhidi-Baghini's Vertical Core, T36)

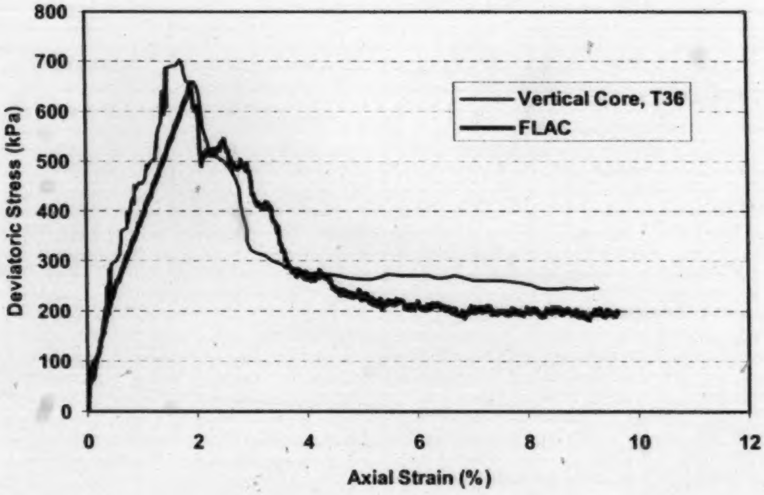

Figure 7-14 Deviatoric stress versus axial strain, Stress path 3 (Initial $\sigma_3' = 250$ kPa), Lab tests simulated by FLAC (Touhidi-Baghini's Vertical Core, T36)

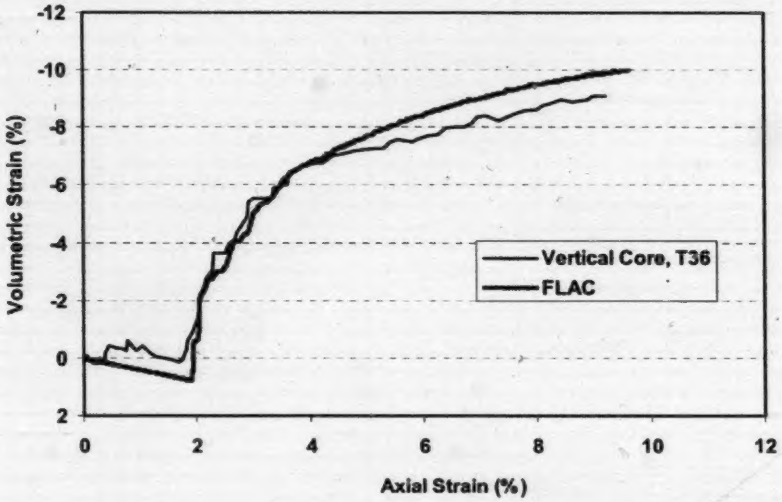

Figure 7-15 Volumetric strain versus axial strain, Stress path 3 (Initial $\sigma_3' = 250$ kPa) (Touhidi-Baghini's Vertical Core, T36)

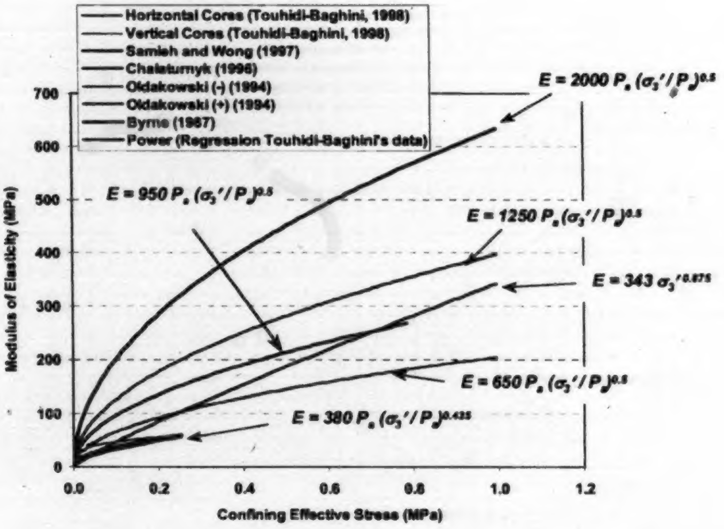

Figure 7-16 Summarized modulus of elasticity for oil sands

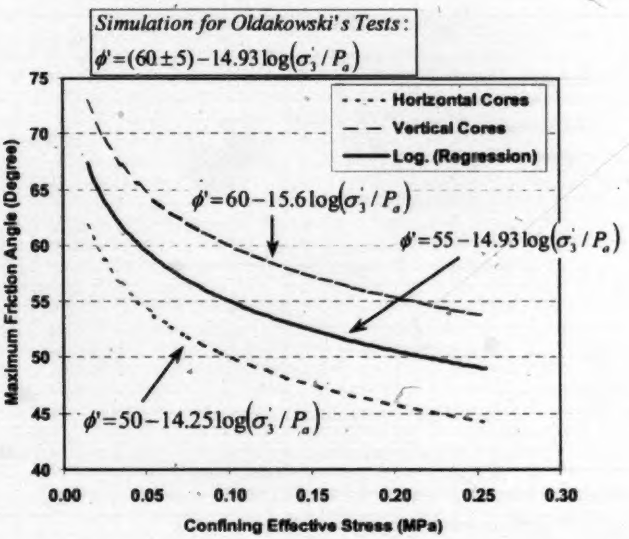

Figure 7-17 Summarized maximum friction angle for oil sands

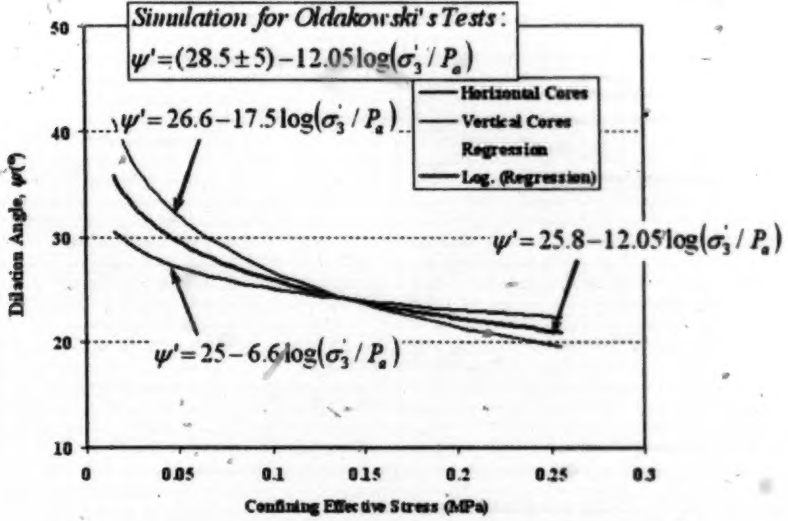

Figure 7-18 Summarized maximum dilation angle for oil sands

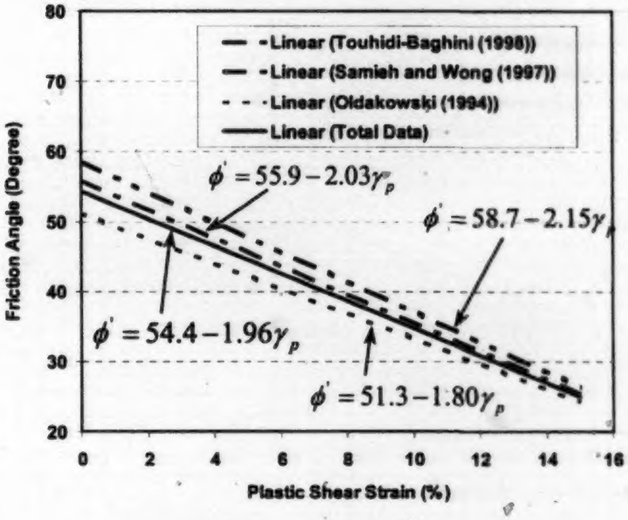

Figure 7-19 Summarized post peak friction angle for oil sands

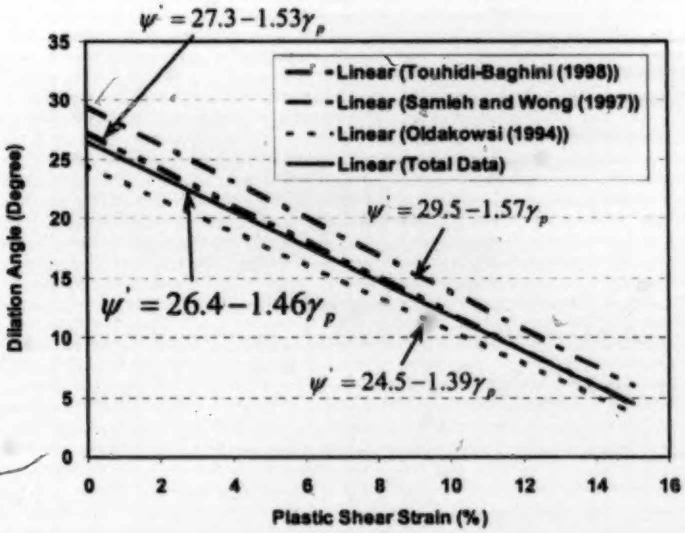

Figure 7-20 Summarized post peak dilation angle for oil sands

CHAPTER 8 HISTORY MATCH OF THE UTF PHASE A SAGD PROJECT WITH COUPLED RESERVOIR GEOMECHANICAL SIMULATION*

8.1 Introduction

The methodology of the coupled reservoir geomechanical simulations has been developed and tested successfully as discussed in Chapter 5. However, the methodology needs to be verified based on a practical field application of the SAGD process. Fortunately, the Underground Test Facility (UTF) Phase A project led by the Alberta Oil Sands Technology and Research Authority (AOSTRA) provided a variety of data measured in the field over the period of the SAGD operation, which can be used in the history match of the SAGD process to verify the methodology. The available data include bottomhole pressures of each injector and producer, reservoir pressure, temperature, vertical strain, vertical displacement of the reservoir top, horizontal displacement, horizontal strain, and volumetric strain inside the reservoir during the SAGD operation.

The objective of this chapter is to present the static and dynamic data of UTF Phase A project, including field survey on geomechanical behaviors. Then, establish the oil sands reservoir model and geomechanical model based on the available and assumed reservoir properties. Thereafter, conduct the coupled reservoir geomechanical simulations and compare the SAGD production performances obtained from the field and the coupled simulation. Finally, sensitivity studies are performed to obtain a good history match and the feasibility of the sequentially coupled simulation technique is discussed.

---

[*] Part of this chapter entitled *History Match of the UTF Phase A Project with Coupled Reservoir Geomechanical Simulation* (Li, P. and Chalaturnyk, R.J.) has been submitted to the Journal of Canadian Petroleum Technology (JCPT) for publication and is now under the peer-review process. It was first presented at the 6th Canadian International Petroleum Conference (the 56th Annual Technical Meeting of the Petroleum Society) (CIPC Paper 2005-164), Calgary, Alberta, Canada, June 8-10, 2005. Also, this paper obtained the Dr. R.M. Butler Memorial Best Paper Presented at CIPC 2005 Second Runner-up Award.

8.2 Project and Reservoir Description

AOSTRA initiated a feasibility study on the construction of an Underground Test Facility (UTF) in 1982, which were based on two discrete but complementary technologies: (1) the Shaft and Tunnel Access Concept (SATAC) and (2) horizontal well technology for in situ recovery of oil sands reservoir. Detailed design of the UTF was completed in January 1982 and construction began in June 1984. The SAGD process was selected for initial piloting at UTF in 1985. Field operation of the Phase A SAGD project started in November 1987 and the whole production period terminated in October 1990.

The AOSTRA Underground Test Facility (UTF) is located 60 km northwest of Fort McMurray, Alberta, Canada, within the area of Township 93 and Range 12. It is about 20 km west of the Syncrude Canada surface mining operation area.

The overall downward stratigraphy consists of 15 m surface Quaternary deposits (Muskeg, Pleistocene till and outwash), 34 m Grand Rapids Formation (predominantly sands), 75 m Clearwater Formation (predominantly clayshales, occasional siltstone beds), 3 m Wabiskaw sands member (sands, some shales), 36 m McMurray Formation (oil sands with variable amounts of clayshales which reduce in frequency with depth), and Massive limestone. The oil sands-limestone contact shows an unconformity surface. The vertical stratigraphic column is shown in Figure 8-1. Rottenfusser et al. (1989) provided a detailed geological characterization of the Phase A reservoir including stratigraphy, description of the stratigraphic units, depositional interpretation, and reservoir parameters. The bottom Clearwater Formation and McMurray oil sands formation were informally divided into units of A to H from top to bottom of the formation, each of which can be correlated throughout the Phase A site. These units are discussed below.

Unit A consists of a medium to coarse grained, light grey, friable, salt and pepper sand and forms the Wabiskaw Member of the Clearwater Formation. It represents the offshore marine bar deposits.

Unit B is composed of light to dark grey soft shales mixed with sand. The shales are generally bioturbated with sand filled horizontal burrows and sand lenses. It was deposited in a marine lower shoreface environment and represents the uppermost unit in the McMurray Formation.

Unit C consists of fine to medium grained dark brown, oil sand interbedded with light brown shale. The upper part of this unit is bioturbated with vertical and horizontal burrows. A shale zone with no bioturbation forms the base of this unit. It belongs to the tidal flat zone deposition environment.

Unit D consists of dark brown, bitumen saturated oil sands with cross bedding dips of approximately 20° interbedded with shale laminae. The shale is moderately bioturbated with horizontal and vertical burrows. This unit forms the upper portion of the tidal channel sediments and contains channel sands at the very bottom of the unit.

Unit E is the main pay zone with the Phase A site. It consists of interbedded oil sands and shale breccia. This unit is dominantly associated with channel sedimentary facies.

Unit F is dominantly shale, grey to light brown in color and thinly bedded with an abrupt contact with the overlying oil sands. It is associated with channel abandonment facies and was deposited under conditions of very low water flow at the top of the basal fluvial/estuarine sequence. A massive, structureless mudstone was formed and distributed sporadically throughout the McMurray Formation.

Unit G is extremely variable but generally consists of bitumen saturated, medium to coarse sands. The unit is strongly bioturbated and contains occasional light grey, bioturbated shale clasts. It forms the fluvial/estuarine regional depositional regime.

Shale barriers within the oil sands formation may affect the SAGD production performance. Particularly, when these barriers are continuous within the reservoir, they will affect the development of the steam chamber significantly (Chalaturnyk, 1996). In the Phase A oil sands reservoir, the Unit F is continuous across the pilot area. It separated the injectors and producers for two of the well pairs, Al and A3. The other well pair, A2, was deliberately drilled so that both wells were above the barrier (Edmunds, 1991). The wellpairs are 55 m long drilled from north to south and their spacing is 26 m. The effect of Unit F on the SAGD production performance will be discussed later.

Typical oil sands reservoir properties are as follows. The average oil sands porosity is 35%. Horizontal permeability is 1 to 10 darcies. The bitumen saturation is about 85%. Initial reservoir pressure and temperature are 550 kPa and 8°C, respectively. Bitumen viscosity under reservoir temperature is 5×10^6 cP and it can be reduced to 7 cP at 220°C (Gittins et al., 1992).

8.3 Geotechnical Instrumentation

Under the co-sponsorship of AOSTRA and CANMET (Canada Centre for Mineral and Energy Technology), an extensive program of geotechnical instrumentation was installed to monitor ground response to the steaming operations. The program was designed to measure the temperature, pore pressure, displacement and effective stress fields (by inference) within the steaming zone and adjacent to the tunnels (Laing et al., 1988).

In total, 14 dedicated thermocouples (AT series), 4 inclinometers (AGI series), 3 extensometers (AGE series), and 5 piezometers (AGP series) were installed (Figure 8-2). Several wells, AT1 and AT7, were also used as inclinometer wells. Piezometers were installed in wells AT4, AT9, AT12 and AT14 and a traversing thermocouple string was used to measure temperature in wells AGI1, AGI2, AGI3, and AGI4. Most instrumentation was placed within a west-east plane at the midpoint of the horizontal wellpairs because it was anticipated that the steam chamber would begin development reasonably uniformly along a horizontal well. This instrumented section was called the geotechincal cross-section (Chalaturnyk, 1996).

The temperature measurement points, the location of the inclinometer wells (measure horizontal displacement), extensometer modules (measure vertical strain), and piezometer locations within the geotechnical cross section are shown in Figure 8-3, 8-4, 8-5, and 8-6, respectively.

8.4 Operation History of UTF Phase A Project

The three well pairs were started up in a staggered fashion. The middle pair, named Al, was steamed first to prove out the operating plan and the underground production equipment, The A2 and A3 pairs were tied in and started up about 6 months later (Edmunds, 1991).

8.4.1 Al Well Pair

Steam circulation began in AI1 and APl on December 1, 1987. Wellhead injection pressure was 2400 kPa and 2050 kPa for AI1 and AP1, respectively. Steam was injected to the annulus and bitumen/condensate produced from tubing. The circulation rate is two times the calculated condensation rate. In early January 1988, temperature increase above AI1 was observed. This response decreased along the well. On January 20, 1988, steam was injected to the tubing and fluid produced from the annulus. Thus, the temperature response was improved.

Steam circulation was operated continuously until April 20, 1988. Bitumen cut was up to 20% and pressure communication between the AI1 and AP1 was not observed. This may be due to the barrier effect of the Unit F. When hot water was injected into AI1 just below fracture pressure, it could flow into AP1 through permeable silts with a slug of warm bitumen. Therefore, bitumen had become hot enough to mobilize at this time. On April 23, 1988, normal SAGD operation mode started. Steam was injected into AI1 tubing at a constant injection pressure and liquid production came out of AP1 tubing. Thereafter, the oil rate was increased and OSR improved. Bitumen cut reached 35% and maintained through A1 life. On mid May 1988, the well pair A1 was shut in to allow work on the other two well pairs. In the third week of June 1988, operation recommenced and continued without serious incident for the next 27 months. Peak bitumen production was reached in September 1989, which was substantially higher than all previous predictions (Edmunds, 1991).

8.4.2 A2 Well Pair

On August 4, 1988, steam circulation started. For both AI2 and AP2, steam was injected to the tubing and fluids were taken from the annulus. A slightly higher pressure was used in AI2 than in AP2. On September 6, 1988, steam circulation was interrupted. The circulation was resumed on October 13, 1988. Thermal communication was detected on November 3, 1988 and warm bitumen began flowing from AP2. Therefore, thermal circulation process was converted to normal SAGD mode on November 10, 1988. No shale barrier existed between AI2 and AP2. So, during most of the production period, annulus to annulus pressure differential across the well pair was less than 200 kPa. In

February 1989, steam injection rate and oil production rate reached their peak value, which were not as high as A1 well pair but still more than satisfactory. In October 1990, production from the well pair was in a gentle decline.

8.4.3 A3 Well Pair

From June 1988 to May 1989, AI3 was operated in the cyclic steam stimulation process including three months shut in period. Steam was injected to the tubing at restricted rate until the pressure reached 2500 kPa. Then, steam was shut off. When the pressure fell to about 2000 kPa, steam injection started again. In late April 1989, the lower wellhead cycle limit was reduced to 1900 kPa, some improvement was noted. On May 15, 1989, the CSS process in AI3 stopped. The CSS steam chamber of AI3 had coalesced with that of A1 well pair. During the following 16 months, AI3 was placed on steam trap production control and flowed continuously for 16 months until September 15, 1990. AI3 consumed the majority of UTF underground operating, engineering, and maintenance resources. The steam circulation operation for AP3 started on June 24, 1989. The CSS process began on October 4, 1989 and communication with AI3 was detected on October 18, 1989.

On April 3, 1990, steam injection stopped, while AP1, AP2, AP3, and AI3 continued producing under steam trap control until October 1990.

8.5 Base Case Reservoir Model and Geomechanical Model

The UTF Phase A project involved three wellpairs. So, all the three wellpairs need to be included in the reservoir model. In addition, the wellpair spacing is approximately 25 to 26 m. In the trial simulation, a smaller reservoir model was applied. The distance between wellpair A2 and the east boundary is 30 m and that is 20 m between wellpair A3 and the west boundary. It was found that these boundary conditions affect the simulation result significantly. So, a lager reservoir model was established, in which the distances between wellpair A2 and the east boundary and between wellpair A3 and the west model boundary were all equal to 60 m. This boundary condition does not affect the simulation results. After the SAGD operation, the distance between the steam chamber and the boundary line is 30 – 40 m. Similarly, the distance between the 50% of the chamber pressure front and the boundary line is greater than 10 m.

The base case reservoir model and grid system used in the reservoir simulator, EXOTHERM, is shown in Figure 8-7 (right). The formation Units C, D, E, F, and G are also shown in this figure. The model has the dimension of 170 m by 29 m. It was divided into 42 grid blocks in horizontal direction and 20 grid blocks in vertical direction. Smaller grid blocks were applied for the region close to the wellpairs and Unit F, which is a mudstone layer with very low permeability. The major reservoir parameters are shown in Table 8-1. The reservoir is divided into two major layers. It consists of an upper oil sands layer (Unit C and D) and a lower oil sands layer (Unit E, F, and G). The Unit F within the lower layer is a mudstone bed. The typical Athabasca oil sands permeability is 1000 – 10000 md (Siu et al., 1991) or 5000 – 12000+ md (Edmunds et al., 1991). In addition, the history match value of UTF Phase A project provided a vertical permeability of 5000 md and a horizontal permeability of 10000 md (Siu et al., 1991). These permeability values were obtained from the history match with conventional reservoir simulation techniques, which do not take the geomechanical effect into account. So, it is possible that these values are unrealistically large. In this chapter, the horizontal absolute permeability of the upper and lower oil sands units are assumed to be 3000 md and 5000 md, respectively, which combined the reservoir geology description and took the well-accepted permeability range (1000 – 10000 D) into consideration. The shale permeability was found to be extremely low, typically in the range of 10^{-6} to 10^{-3} md (Butler, 1997; Magara; Soeder, 1986). In this chapter, the mudstone bed (Unit F) permeability was assumed to be 10^{-3} md.

The base case geomechanical model and its grid system used in the geomechanical simulator, FLAC, are shown in Figure 8-7 (left). In horizontal direction, it is the same as the reservoir model. However, it is extended to the ground surface and has extra 16 grid blocks above the reservoir model in vertical direction. So, this model has a dimension of 170 m by 163 m. The major geomechanical parameters are shown in Table 8-2. The average Young's modulus (modulus of elasticity, E) can be expressed in Equation (7-2), which was proposed by Samieh and Wong (1997).

$$E = 950\,P_a(\sigma_3^{'} / P_a)^{0.5} \tag{7-2}$$

The lower and upper bound of the Young's modulus is approximately expressed in Equation (8-1) and (8-2)

$$E = 650\,P_a(\sigma_3^{'} / P_a)^{0.5} \tag{8-1}$$

$$E = 1250\,P_a(\sigma_3^{'} / P_a)^{0.5} \tag{8-2}$$

The strain-softening model was applied in the geomechanical simulation to characterize the stress strain behavior of oil sands. The modulus of elasticity, friction angle, and dilation angle can be determined based on the relationships proposed in Chapter 7.

The permeability and porosity variations of oil sands material as a function of volumetric strain during the SAGD operation are based on Equation (6-7) and (6-9). These equations have been discussed in Chapter 6.

$$Ln\frac{k}{k_0} = C_{n_1}\ \varepsilon_v \tag{6-7}$$

where C_{nl} is constant. For the block specimens with porosity of about 0.34, C_{nl} is 5.9 and 14.76 for horizontal specimens and vertical specimens, respectively. The isotropic permeability change of oil sands can be found by taking an average of these C_{nl} values. So, C_{nl} is 10.33.

$$\phi = \frac{\phi_0 + \varepsilon_v}{1 + \varepsilon_v} \tag{6-9}$$

Tensile failure and shear failure can improve the permeability of the mudstone layer. However, the magnitude of permeability improvement is not available for the McMurray mudstone layer (Unit F). It is assumed that when shear failure occurs, the mudstone permeability is increased to 100 md and when tensile failure occurs, its permeability is increased to 1000 md. These modifications are illustrated in Figure 8-8. The shear failure is estimated based on the failure index (or factor of safety) proposed by Chalaturnyk

(1996). The cohesion of the lower McMurray shale is 0 kPa. So, the tensile failure occurs when the minimum principal effective stress is less than 0 kPa.

8.6 History Match with Reservoir Geomechanical Simulation

8.6.1 Oil Production, Steam Oil Ratio, and Oil Recovery Factor

The conventional reservoir simulation with EXOTHERM only (uncoupled simulation) and the coupled reservoir geomechanical simulation with both EXOTHERM and FLAC (coupled simulation) provide different SAGD production performances. Because the field production performance is still confidential, it is not feasible to compare the simulation performance and the field production performance. So, the production performance comparison is based on the uncoupled and the coupled simulation results. The cumulative oil production and cumulative steam injection are shown in Figure 8-9. From Figure 8-9, it can be seen that the cumulative oil production predicted by the coupled simulation technique is 26.8×10^3 m^3, which is 2.6 times higher than that predicted by the uncoupled simulation technique. Similarly, the cumulative steam injection based on the coupled simulation technique is also two times higher than that predicted by the uncoupled simulation technique. Oil production rate and steam injection rate shown in Figure 8-10 vary frequently over the whole production period. It is clear that the coupled simulation predicted a higher oil production rate and steam injection rate than the uncoupled simulation. The instant steam oil ratio (ISOR) and cumulative steam oil ratio (CSOR) are shown in Figure 8-11. Before the production time of 469 days, both ISOR and CSOR based on the coupled simulation technique are all higher than that based on the uncoupled simulation technique. However, after this time, the coupled simulation provided lower steam oil ratios than the uncoupled simulation technique. The oil recovery factor predicted by the coupled simulation is about 37%, but it is only 14% based on uncoupled simulation (Figure 8-12). The oil recovery factor of 37% based on the coupled reservoir geomechanical simulation is smaller than the field value of 50%. The reason is that the reservoir model has a larger volume than that used to calculate the field recovery factor.

It is clear that the difference of the oil production performances predicted by coupled and uncoupled simulations results from the geomechanical effect. The coupled reservoir geomechanical simulation technique has taken the geomechanical effect into account.

However, the uncoupled reservoir simulation does not fully incorporate the geomechanical effect. In the uncoupled reservoir simulation, the reservoir permeability is constant and the mudstone bed (Unit F) is impermeable. After 699 days of the SAGD operation, the steam chamber only developed at the A2 wellpair (Figure 8-13) because both the injector and producer are above the Unit F. When the SAGD operation stopped at 1035 days, the steam chamber did not form at wellpairs A1 and A3 (Figure 8-14). However, in the coupled simulation process, geomechanical behavior induced significant permeability improvement in the oil sands material and the mudstone bed (Figures 8-15 and 8-16). As a result, the mudstone bed became permeable and hot bitumen/condensate could flow to the producers of wellpairs A1 and A3. Steam chamber was formed and developed gradually around all the three wellpairs (Figure 8-13 and 8-14). That is why the coupled simulation obtained a much better production performance than the uncoupled simulation.

The coupled simulation technique may be further modified if the field production performance could be compared with the coupled reservoir geomechanical simulation results.

8.6.2 Injection and Production Pressures

In the field, all injection and production pressures were monitored at the wellhead locations as part of the "steam trap" process control procedures. For the history match of the coupled reservoir geomechanical simulations, the wellhead pressures were adjusted to equivalent reservoir injection and production pressures. Friction and head losses of approximately 200 kPa have been assumed between the wellheads and the reservoir (Edmunds et al., 1991). The change in pressure rather than its absolute value was considered to assess the geomechanical response of the reservoir. The initial reservoir pore pressures at the wellpair locations within the geotechnical cross-section were chosen as reference pore pressures (Chalaturnyk, 1996). The change in pressure is the difference between the absolute downhole pressure and the initial reservoir pore pressure at the wellpair locations.

With the base case reservoir model, the steam injection pressure in each injector and production pressure in each producer over the whole period of the SAGD process were obtained based on the coupled reservoir geomechanical simulation technique. Bottomhole pressures in well AI1, AP1, AI2, AP2, AI3, and AP3 obtained from field measurement and the coupled simulation technique are compared in Figures 8-17, 8-18, 8-19, 8-20, 8-21, and 8-22, respectively. The field injection and production pressure histories have been simplified, which retained significant pressure fluctuations (Chalaturnyk, 1996). From these figures, it can be seen clearly that the coupled reservoir geomechanical simulation process almost produced the same well pressure histories as those measured in the field. In another words, the well pressure histories obtained from the coupled simulation technique match the real well pressure histories. Some small differences, such as the pressure curves in well AP3, may result from the thermal expansion effect of the pore fluids at AP3 when steam injection was operated in AP1. The pressure difference between the injector and producer may result from the different treatment on subcool between the field and the simulation.

8.6.3 Reservoir Pressure Field

Figure 8-23 shows the reservoir pore pressure distribution at 500 days, in which the upper figure was obtained from field measurement and the lower figure was plotted based on the coupled reservoir geomechanical simulation. From Figure 8-23, it can be seen that at time of 500 days, the steam chamber in the field is smaller than that in the coupled reservoir geomechanical simulation. This can also be seen from the high pore pressure comparison at the time of 700 days (Figure 8-24).

The reason is that in the field, the steam chamber propagated from the heel (north end) to the toe (south end) of the horizontal well and the geotechnical cross section "feels warm" at about 350 days of the SAGD operation. When the steam chamber touched the geotechnical cross section, it was small. However, over the same period of time based on the coupled simulation process, the steam chamber has been propagating upwards and sideways continuously since the beginning of normal SAGD operation (after the steam circulation process). That is why the simulated steam chamber is relatively larger than that defined based on the field survey. The field steam chamber evolution from 400 days to 500 days of the SAGD operation is shown in Figure 8-25. The heel-to-toe steam chamber propagation process can be clearly seen from this figure.

8.6.4 Reservoir Temperature Field

The reservoir temperature distribution obtained from the coupled reservoir geomechanical simulation basically matches that obtained from the field survey (Figures 8-26 and 8-27). However, it is still clear that the steam chamber predicted by the coupled simulation technique is a little larger than that obtained from the field survey. The reason has been discussed above. Therefore, It should be noted that when the pressure drop along the horizontal injector is small, the SAGD process can be treated as a 2D problem. However, when the pressure drop along the horizontal injector is significant, 3D reservoir model may be required for the simulation of the SAGD process.

8.6.5 Vertical Strain

Field survey data of vertical strain within the geotechnical cross section were obtained from the extensometers in wells AGE2, AGE3, and AGE4. The locations of these wells are shown in Figure 8-5. Well AGE2 was located directly above wellpair A1 in order to measure vertical strains resulting from vertical growth of the steam chamber. Five anchors comprising four measurement modules were installed in AGE2. Well AGE3 was located approximately 6 m east of wellpair A1. Well AGE3 measured vertical strain resulting from horizontal and at later times, vertical growth of the steam chamber. Seven anchors comprising six extensometer measurement modules were installed in AGE3. Well AGE4 was located approximately 12 m east of wellpair A1, close to the midpoint between A1 and A2. Well AGE4 measured vertical strains resulting from horizontal and at later times, vertical growth of the steam chamber. Six anchors comprising five measurement modules were installed in AGE4. These measurement modules in well AGE2, AGE3, and AGE4 were located at specific elevations (Table 8-3). These extensometer modules measure the relative displacement between adjacent anchors. Vertical strain at each module elevation can also be found accordingly. It should be noted that these measurements applied LVDT-based extensometer modules grouted in three vertical boreholes, which was accurate to ±0.2 mm and had a linear range of ±25 mm (Chalaturnyk, 1996).

In the coupled reservoir geomechanical simulations, the vertical strains can be obtained at the same locations where the extensometer modules exist in the field. So, the vertical strains obtained from field survey can be compared with that obtained from the coupled simulation results.

The vertical strains obtained from the field survey and from the coupled reservoir geomechanical simulations are compared in the period of 200 days to 700 days. Because the steam chamber in the field reached the geotechnical cross section at approximately 375 days and that in the coupled reservoir geomechanical simulation process did not develop until 200 days of SAGD operation, so the comparison started from 200 days of the SAGD process.

The vertical strains in well AGE2 will be compared with that predicted by the coupled simulation and discussed in detail below. The vertical strains in other two wells, AGE2 and AGE4, can also be compared with the simulated results and interpreted based on the similar mechanisms occurring in well AGE2. The comparisons for these two wells are shown in Appendix B.

Figure 8-28 compares the vertical strains measured at module 245 (Elevation 280.5 m) with that obtained from the coupled reservoir geomechanical simulation. It can be seen that in the period up to about 290 days, module 245 recorded a maximum extensional vertical strain of 0.09% for a pore pressure increase of approximately 2000 kPa. However, the simulated volumetric strain with the base case model shows a compressive behavior with a minimum vertical strain of –0.4%. The reason is that over this period of time, the steam chamber in the field did not reach the geotechnical cross section and the pore pressure front approached module 245 but the thermal front was still some distance away from the module. So, the extensional vertical strain was measured as a result of isotropic unloading due to pore pressure increase. In contrast, for the coupled reservoir geomechanical simulation, the steam chamber started to propagate upwards and sideways at approximately 200 days after the SAGD process was started. Hence, the oil sands material at the location of module 245, which is just above the steam injection well AI1, was compressed due to the thermal expansion effect. From 300 days to approximately

450 days, the temperature increased within the module and the oil sands formation was compressed. The compressive vertical strain reached a value of –0.88%. However, the simulated vertical strain showed an extensional behavior from time 245 days to 320 days and then approximately maintained a constant value (0.08%) in the period of 320 days to 470 days. This phenomenon indicated that the thermal front reached the location of module 245 much earlier in the simulation than in the field. Beyond time 450 days, field module measurement showed an extensional behavior up to 600 days, which was consistent with the variation trend in the coupled simulation. The instability beyond 600 days may result from field operations (temporary shut in wells or repairs). If the difference of the steam chamber development in the field and in the coupled simulation is taken into account, the vertical strain measured by module 245 is comparable to that obtained in the coupled simulation.

The similar comparisons for module 244 (Elevation 283.5 m), module 249 (Elevation 286.5 m), and module 250 (Elevation 289.5 m) are shown in Figures 8-29, 8-30, and 8-31, respectively. From these figures, it can be seen that the variation trends of vertical strains obtained from the field survey and from the coupled reservoir geomechanical simulations are similar except the field measurement at the location of module 249. The vertical strain measured by the module 249 shows a compressive behavior and reached –0.85% at 700 days. However, the coupled simulation with the base case reservoir model indicates an extensive behavior at the location of module 249 and the vertical strain reached 0.81% at 700 days. The reason of this obvious difference at the location of module 249 may result from local lithology differences. From elevation 282.9 m (close to module 244) to 289.9 m (close to module 250), the measured pore pressure at time 500 days varied from 2200 kPa to 2290 kPa. Correspondingly, this measured pore pressure at time 600 days varied from 2400 kPa to 2596 kPa and beyond this time, it was constant and equal to 2600 kPa (Chalaturnyk, 1996). This variation of the pore pressure indicates that the reservoir material at the location of module 249 consists of mudstone or contains a large portion of mudstone material because thermal expansion of the fluids within the mudstone material induces pore pressure increase, which cannot be dissipated rapidly. Probably this is the reason that the vertical strain based on field survey shows the compressive behavior, and that based on the coupled reservoir geomechanical simulation shows an extensive behavior (shear dilation process).

In the coupled reservoir geomechanical simulation, the reservoir material was considered as homogeneous oil sands. From Figures 8-28, 8-29, 8-30, and 8-31, it can be seen clearly that the vertical strains at the four locations of module 245, 244, 249, and 250 have a similar variation trend. However, with increasing the elevation from module 245 up to 250, the extensive vertical strains occur at 245 days, 270 days, 320 days, and 320 days, respectively. This is due to the propagation of thermal front. When the thermal front touches the location of each module, shear dilation occurs. Field survey also demonstrated the similar variation of vertical strains as a function of elevation and operation time.

In addition, workovers, shut-in, and module repairs can also induce some inconsistence between field survey and the coupled simulation results.

Sensitivity Analysis

The history matches on vertical strains at different elevations of well AGE2, AGE3, and AGE4 show that the simulated values with the base case reservoir model were generally larger than the values obtained in field survey. In general, small modulus of elasticity and large thermal expansion coefficient result in high vertical strains. Therefore, three sensitivity cases were taken into account in the coupled reservoir geomechanical simulation. The first case applied the upper E bound (high E value), which is different from that applied in the base case as shown in Equation (8-3). The difference is the coefficient in the relationship between the modulus of elasticity (E) as a function of volumetric strain. The second case applied a low value of thermal expansion coefficient. The base case applied a volumetric thermal expansion coefficient of 6×10^{-5} °C^{-1} while this sensitivity case applied a low volumetric thermal expansion coefficient of 3×10^{-5} °C^{-1}. The third case lumped the two cases above.

The coupled simulation results show that in most cases, the difference of vertical strains between Case 1 and the base case is not so significant. In another words, it can be seen that the predicted vertical strains at different elevations of the three wells, AGE2, AGE3, and AGE4, based on the high E value are similar to those predicted in the base case. Therefore, the variation of the modulus of elasticity from Equation (8-1) to (8-3) does not affect the vertical strains significantly.

Case 2 applied a smaller thermal expansion coefficient of the reservoir material than that in the base case. This variation affects the vertical strain significantly. Almost in all the elevations with extensometers at wells AGE2, AGE3, and AGE4, the vertical strains predicated in Case 2 are smaller than that obtained in the base case. Only a couple of the extensometers showed the opposite (see Appendix B). This may result from the boundary effect. In the FLAC simulation, the overburden was assumed as elastic material and pore pressures cannot be dissipated to the overburden. At the top of the reservoir, the pore pressure would be increased more significantly for high thermal expansion coefficient case than that for the lower thermal expansion coefficient case because when the thermal expansion coefficient is larger, the expansion of the oil sands material within the steam chamber can apply a much larger thermal stress to the top reservoir material. As a result, the reservoir material in this region can be greatly compacted and/or even crushed for the case with larger thermal expansion coefficient. The similar results of wells AGE3 and AGE4 are shown in Appendix B.

Case 3 is a combination of Case 1 and Case 2. In another words, it applied a lower thermal expansion coefficient and the upper E bound (high E value). As discussed above, the high modulus of elasticity value does not affect the vertical strains significantly. So, it is expected that the vertical strains of Case 3 should be close to that of Case 2. The coupled simulation results do reflect this expectation. It is shown from Figures 8-28 to 8-31 that the vertical strains of Case 3 are approximately consistent with those of Case 2 although Case 3 can have higher or lower values than Case2 for a few elevations.

8.6.6 Vertical Strain in the Geotechnical Cross Section

Figures 8-32 and 8-33 show the vertical strains in the geotechnical cross-section at time 550 days and 679 days, respectively. The regions outside the dotted line have been estimated based on the behavior measured at wells AGE2, AGE3, and AGE4. So, the field data within the dotted line are more reliable. Outside this region, the data become less representative. It is shown that the lower part of the reservoir formation have the similar vertical strains for both the field survey and coupled reservoir geomechanical simulation. For example, at 550 days, all the vertical strains between wellpairs A1 and A2 have increased to approximately 2.0%. However, the upper part of the reservoir formation has different vertical strains. The field survey showed smaller vertical strains than the coupled reservoir geomechanical simulation. This is due to limited data and the assumptions applied in these plots. It was assumed that vertical strain was equal to zero at the upper (Elevation 300 m) and lower (Elevation 270 m) boundaries and that vertical strain behavior above wellpairs A3 and A2 was identical to that above wellpair A1 (Chalaturnyk, 1996).

8.6.7 Horizontal Displacement

The field data were obtained from inclinometer surveys in wells AGI1, AT1, AGI2, AT7, and AGI3, which are shown in Figure 8-4. For each well, the horizontal displacements measured in the field and calculated from the coupled reservoir geomechanical simulation are compared at time 375 days, 550 days, and 679 days. The coupled reservoir geomechanical simulation also applied lower thermal expansion coefficients and upper E bound (high E value) to do sensitivity studies. It should be noted that as calibrated in well AGI2, horizontal displacements measured during Phase A are, on average, only accurate to ±5 mm. This error amounts to approximately 20% of the maximum horizontal displacement measured during the Phase A steaming trials (Chalaturnyk, 1996). The comparison of horizontal displacements for well AGI1 is discussed below. These comparisons for other wells can be found in Appendix B, in which the explanation for some differences is similar to those described in well AGI1.

Well AGI1 is located to the west of and about 15 m away from wellpair A3. The horizontal displacements of well AGI1 at time 375 days, 550 days, and 679 days are shown in Figures 8-34, 8-35, and 8-36, respectively. At 375 days, field survey obtained approximately the same horizontal displacement as that from the base case simulation for the elevation interval from 270 m to 280 m (base case is the initial simulation case without sensitivity analysis). The horizontal displacement in this interval is very small because of the liquid production from well AI 3. However, within the elevation interval of approximately 280 m to 300 m, field survey obtained a smaller horizontal displacement. In contrast, the coupled simulation predicted a negative horizontal displacement (> 10 mm). The reason is that the steam chamber propagation process in the field is different from that in the coupled reservoir geomechanical simulation. At this time, the real steam chamber was just touching the geotechnical cross section, but the simulated steam chamber developed approximately at 200 days within the geotechnical cross section.

At time 550 days, the field survey and the coupled reservoir geomechanical simulation obtained a very similar variation trend in horizontal displacements. However, the coupled simulation from the base case obtained a maximum horizontal displacement of approximately 22 mm, which is about seven times of that obtained from the field survey (Figure 8-35). This difference is even larger at time 679 days (Figure 8-36). As discussed above, the reason is that the steam chamber propagation modes were different between the field and the simulation.

Sensitivity Analyses

As shown above, the field survey obtained smaller horizontal displacements compared to that from the coupled reservoir geomechanical simulations. The major reason is the difference of steam chamber propagation modes. Also, it was thought that certain reservoir geomechanical properties might affect the magnitude of horizontal displacement. For example, thermal expansion coefficient and modulus of elasticity can play important roles in the calculation of horizontal displacement. So, the sensitivity studies on these two parameters were performed. Field survey and the simulation results based on low thermal expansion coefficient and combined low thermal expansion coefficient and high modulus of elasticity are shown in Figures 8-37 to 8-39. These figures show that thermal expansion coefficient affect the horizontal displacement more significantly than the modulus of elasticity. The combined effect of low thermal expansion coefficient and high modulus of elasticity is similar to that with low thermal expansion coefficient only.

8.6.8 Horizontal Strain within the Geotechnical Cross Section

The horizontal strain fields within the geotechnical cross-section based on the field survey at 550 days and 679 days are shown in Figure 8-40 and 8-41, respectively. They are compared with the horizontal strain fields obtained from the coupled reservoir geomechanical simulations. Both figures show that the simulated horizontal strain within the same area of the oil sands reservoir is up to ten times larger than that from the field survey. Although at 550 days, the steam chamber in the field has crossed the geotechnical cross section, the steam chamber within this section only developed for a shorter period of time (less than 200 days). However, in the coupled reservoir geomechanical simulation, the steam chamber has propagated for over 350 days. Thus, the different steam chamber propagation modes within the geotechnical cross-section result in the different horizontal strain distributions.

8.6.9 Volumetric Strain within the Geotechnical Cross Section

Figure 8-42 and 8-43 show the comparisons of volumetric strain distributions based on field survey and the coupled reservoir geomechanical simulations at time 550 days and 679 days, respectively. From these comparisons, it is seen that the coupled simulation obtained larger volumetric strains than the field survey data. The reason has been discussed above, that is, the steam chamber propagation modes are different in these two cases.

8.6.10 Surface Heave and Vertical Displacement of the Reservoir Top

Figure 8-44 compares the vertical displacements at the reservoir top based on both the coupled reservoir geomechanical simulation and the field survey. The surface heave from the coupled simulation is also shown in this figure. It is seen that the maximum vertical displacement at the reservoir top can be as high as 163 mm at 550 days. However, the two field measurement data were 78 mm and 100 mm, respectively. At 679 days, the maximum vertical displacement at the reservoir top is 210 mm based on the coupled simulation, and one field measurement value is 174 mm. Clearly, the coupled simulation obtained larger vertical displacement at the reservoir top than the field measurements. The difference is 50 mm to 60 mm. This may be induced by the different steam chamber propagation modes in both cases. The surface heave based on the coupled simulation at 679 days is 177 mm approximately.

8.7 Conclusions

- The coupled reservoir geomechanical simulation technique was successfully applied to history match the field production performance of the UTF Phase A Project.

- Reservoir pressure and temperature distributions based on the coupled simulation are similar to those obtained from the field measurements.

- The vertical and horizontal strains in the geotechnical cross section were not fully matched. This difference may be induced by complex reservoir properties and also the limitation of the 2D simulation. Within the geotechnical cross-section, the steam chamber development based on the coupled reservoir geomechanical simulation is different from that in the field.

- The horizontal displacements obtained from the coupled simulation are larger than the field measurements. In addition to the different steam chamber development modes, thermal expansion coefficient and the modulus of elasticity are studied and the thermal expansion coefficient affects the simulation results more significantly than the modulus of elasticity.

- The simulated surface heave and vertical displacement at the reservoir top based on the coupled simulation are a little larger than the field measurements.

- The field production data should be applied to compare the oil production (rates and cumulative value) and steam injection (rates and cumulative value) with the same data obtained from the coupled simulation.

- It is of great importance to develop the 3D reservoir geomechanical simulation methodology for the history match of the SAGD process when the pressure drop along the wellbore is significant.

Table 8-1 Reservoir properties in the coupled reservoir geomechanical simulation

Formation Properties														
Formations	Top Depth (m)	Bottom Depth (m)	Thickness (m)	Porosity (%)	Horizontal Permeability	Vertical Permeability	Gas Saturation	Bitumen Saturation	Water Saturation	Initial Pressure	Initial Temperature	Heat Capacity (kJ/kg.C)	Thermal Conductivity (W/m.C)	Rock Compressibility (1/kPa)
Overburden	0	134	134								7	1920	146	
C and D	134	149	15	0.3	3000	1500	0	0.8	0.2	500	7	1865	173	5.00E-06
E	149	159	10	0.35	5000	2500	0	0.85	0.15	550	7	1865	173	5.00E-06
F	159	160	1	0.1	0.001	0.001	0	0.85	0.15	550	7	1920	146	5.00E-06
G	160	163	3	0.35	5000	2500	0	0.85	0.15	550	7	1865	173	5.00E-06
H	163										7	2412	301	
Fluid Properties														
Fluid	Molucular Weight	Density (kg/m3)	Viscosity (10^3 um^2) (at 7 C)	Compressibility (1/kPa)	Thermal Expansion Coefficient (1/C)	GOR (m3/m3)								
Bitumen	500	2065	5000000	4.50E-07	6.41E-04	3								
Water	18	1000	1.44	5.80E-07	1.93E-04									
Well Data														
Well	Depth (m)	Horizontal Length (m)	Injector-Producer Spacing (m)	Steam Circulation Time (Days)	Well Radius (m)	Steam Injection Pressure (kPa)	Injection Steam Quality (%)	Maximum Steam Injection Rate (m3/day)	Maximum Liquid Production Rate (m3/day)	Maximum Steam Production Rate (m3/day)	Steam Trap Temperature difference [C]			
Injector	155	55	5	145	0.1	2400	0.95	80						
Producer	160	55				2050			150	0.5	5			

Note: Oil sands permeability is From Siu et al. (1991) and Edmunds et al. (1991). Mudstone layer permeability is from Pooladi-Darvish (2002).

Table 8-2 Reservoir geomechanical properties in the coupled reservoir geomechanical simulation

Formations	Overburden	C and D	E	F	G	H	Note
Lithology	Mixed Lithology	Oil Sands	Oil Sands	Mudstone	Oil Sands	Limestone	Chalaturnyk, 1996
Formation Top Depth[1] (m)	0	134	149	159	160	163	Laing, et al., 1988
Thickness (m)	134	15	10	1	3	N/A	Laing, et al., 1988
Bulk Density, ρ_b (kg/m^3)	2245	2245	2245	2245	2245	N/A	Chalaturnyk, 1996
Young's Modulus, E (MPa)	800	740.39	760.27	553.00	765.50	N/A	Chalaturnyk, 1996; Li and Chalaturnyk, 2004
Poisson's Ratio, ν	0.3	0.3	0.3	0.3	0.3	N/A	Assumption
Calculated Bulk Modulus[2], K (MPa)	667	617	634	461	638	N/A	
Calculated Shear Modulus[2], G (MPa)	308	285	292	213	294	N/A	
Coefficient of Linear Thermal Expansion, α (°C^{-1})	2.0E-05	2.0E-05	2.0E-05	2.0E-05	2.0E-05	N/A	Chalaturnyk, 1996
Peak Friction Angle, ϕ_p (°)	N/A	32.06	31.72	48.00	31.63	N/A	Chalaturnyk, 1996; Li and Chalaturnyk, 2004
Peak Cohesion, c_p (MPa)	N/A	0	0	0	0	N/A	
Peak Dilation Angle, ψ_p (°)	N/A	7.29	7.01	10.00	6.94	N/A	Chalaturnyk, 1996; Li and Chalaturnyk, 2004
Residual Friction Angle, ϕ_r (°)	N/A	TBD	TBD	46	TBD	N/A	Chalaturnyk, 1996; Li and Chalaturnyk, 2004
Residual Cohesion c_r (MPa)	N/A	0	0	0	0	N/A	Assumption
Residual Dilation Angle, ψ_r (°)	N/A	TBD	TBD	0	TBD	N/A	Li and Chalaturnyk, 2004
In Situ Stresses and Formation Pressures							
Vertical Stress Gradient, σ_v/z (kPa/m)	22.00	22.00	22.00	22.00	22.00	22.00	Chalaturnyk, 1999
Min Horizontal Stress Gradient, σ_h/z (kPa/m)	22.00	26.40	26.40	26.40	26.40	26.40	Assumption
Max Horizontal Stress Gradient, σ_h/z (kPa/m)	22.00	33.00	33.00	33.00	33.00	33.00	Assumption
Vertical Stress (Top Layer), σ_v (MPa)	0.00	2.95	3.28	3.50	3.52	3.59	
Vertical Stress (Bottom Layer), σ_v (MPa)	2.95	3.28	3.50	3.52	3.59		
Min Horizontal Stress (Top Layer), σ_h (MPa)	0.00	3.54	3.93	4.20	4.22	4.30	
Min Horizontal Stress (Bottom Layer), σ_h (MPa)	3.54	3.93	4.20	4.22	4.30		
Max Horizontal Stress (Top Layer), σ_h (MPa)	0.00	4.42	4.92	5.25	5.28	5.38	
Max Horizontal Stress (Bottom Layer), σ_h (MPa)	4.42	4.92	5.25	5.28	5.38		
Formation Pressure(Top Layer), P_f (kPa)	0.00	460.00	535.00	585.00	590.00	605.00	Chalaturnyk, 1996

Notes:

1 Depth relative to ground surface

2 Bulk modulus is equal to E/(3(1-2v)) and shear modulus is equal to E/(2(1+v)); E is Young's modulus and v is Poisson's ratio

3 Only single phase (water) considered in FLAC simulation

Table 8-3 Extensometer modules and their elevations in wells AGE2, AGE3, and AGE4 within the geotechnical cross section

AGE2		AGE3		AGE4	
Module No.	Elevation (m)	Module No.	Elevation (m)	Module No.	Elevation (m)
250	289.5	243	295.6	239	291
249	286.5	242	290.6	241	286
244	283.5	236	285.6	247	281
245	280.5	238	280.6	246	276
		240	275.6	235	271
		248	270.6		

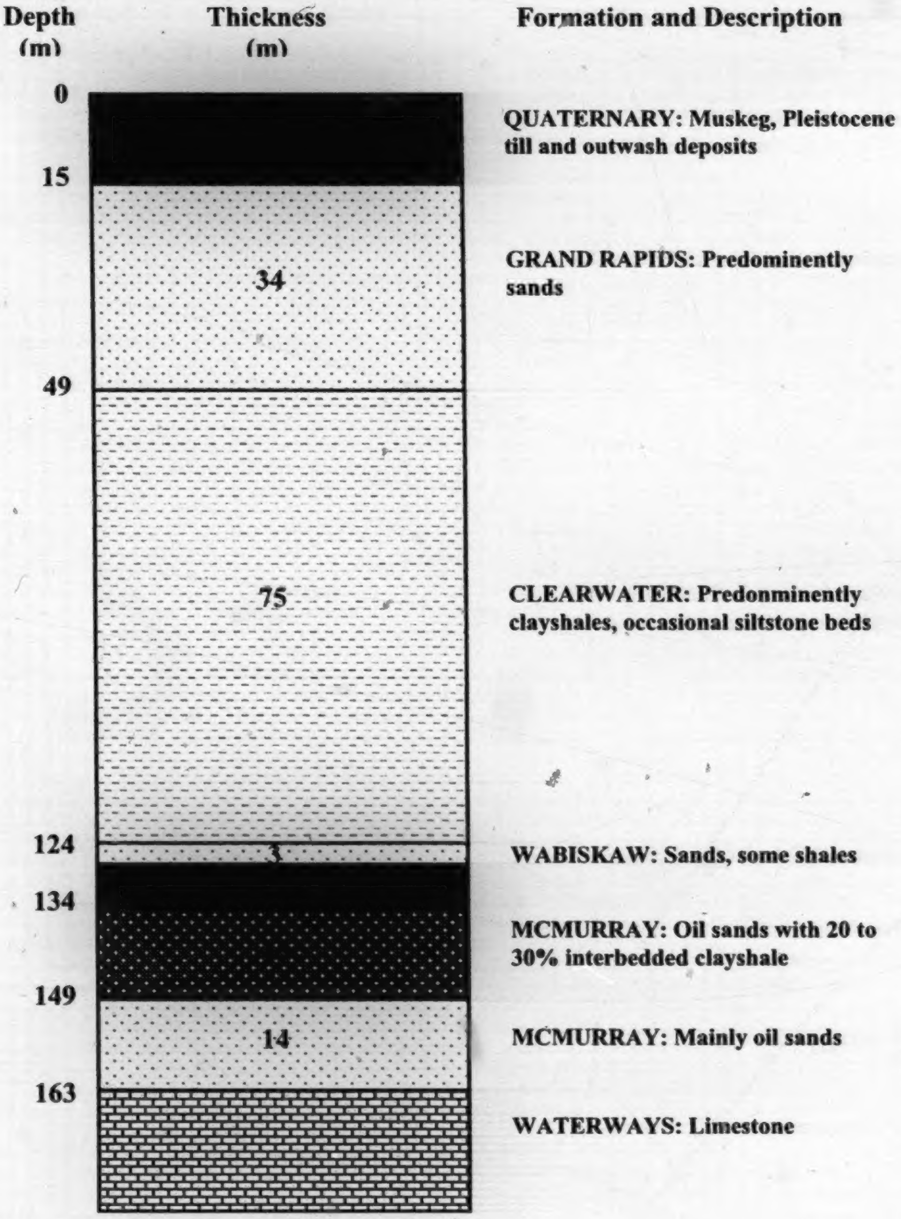
Depth (m)
Thickness (m)
Formation and Description
0
15
49
124
134
149
163
34
75
3
14
QUATERNARY: Muskeg, Pleistocene till and outwash deposits
GRAND RAPIDS: Predominently sands
CLEARWATER: Predonminently clayshales, occasional siltstone beds
WABISKAW: Sands, some shales
MCMURRAY: Oil sands with 20 to 30% interbedded clayshale
MCMURRAY: Mainly oil sands
WATERWAYS: Limestone

Figure 8-1 Vertical stratigraphic column

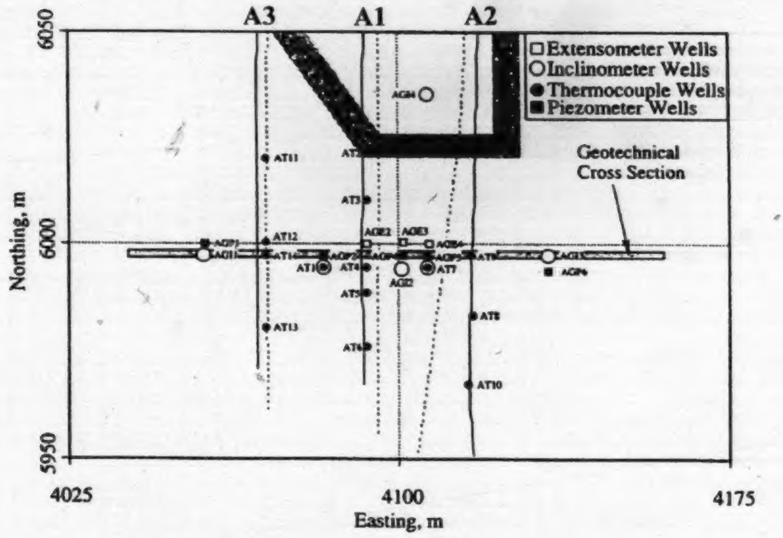
A3
A1
A2
□ Extensometer Wells
○ Inclinometer Wells
● Thermocouple Wells
■ Piezometer Wells
Geotechnical Cross Section
AT11
AT12
AT13
AT3
AT4
AT5
AT6
AT7
AT8
AT10
AGI4
AGE2
AGE3
AGI2
Northing, m
6050
6000
5950
4025
4100
4175
Easting, m

Figure 8-2 Plan view of instrument well locations

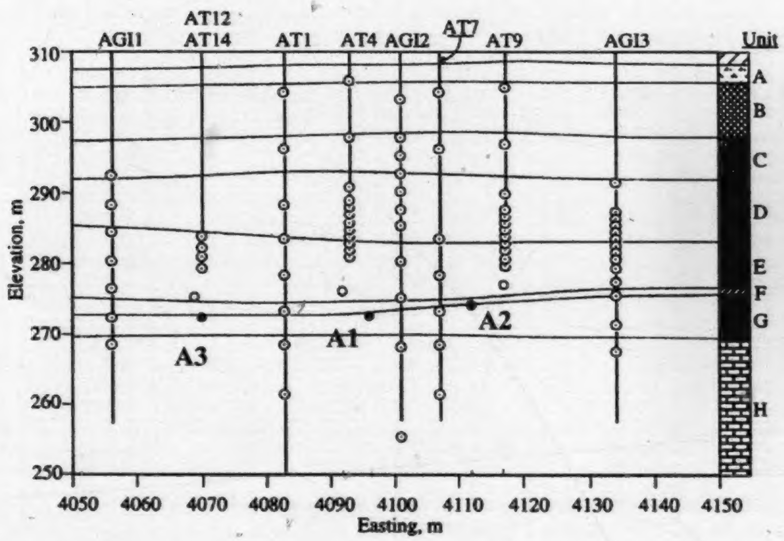
AGI1
AT12
AT14
AT1
AT4
AGI2
AT7
AT9
AGI3
Unit
A
B
C
D
E
F
G
H
A3
A1
A2
Elevation, m
310
300
290
280
270
260
250
4050
4060
4070
4080
4090
4100
4110
4120
4130
4140
4150
Easting, m

Figure 8-3 Temperature measurement points in the geotechnical cross section

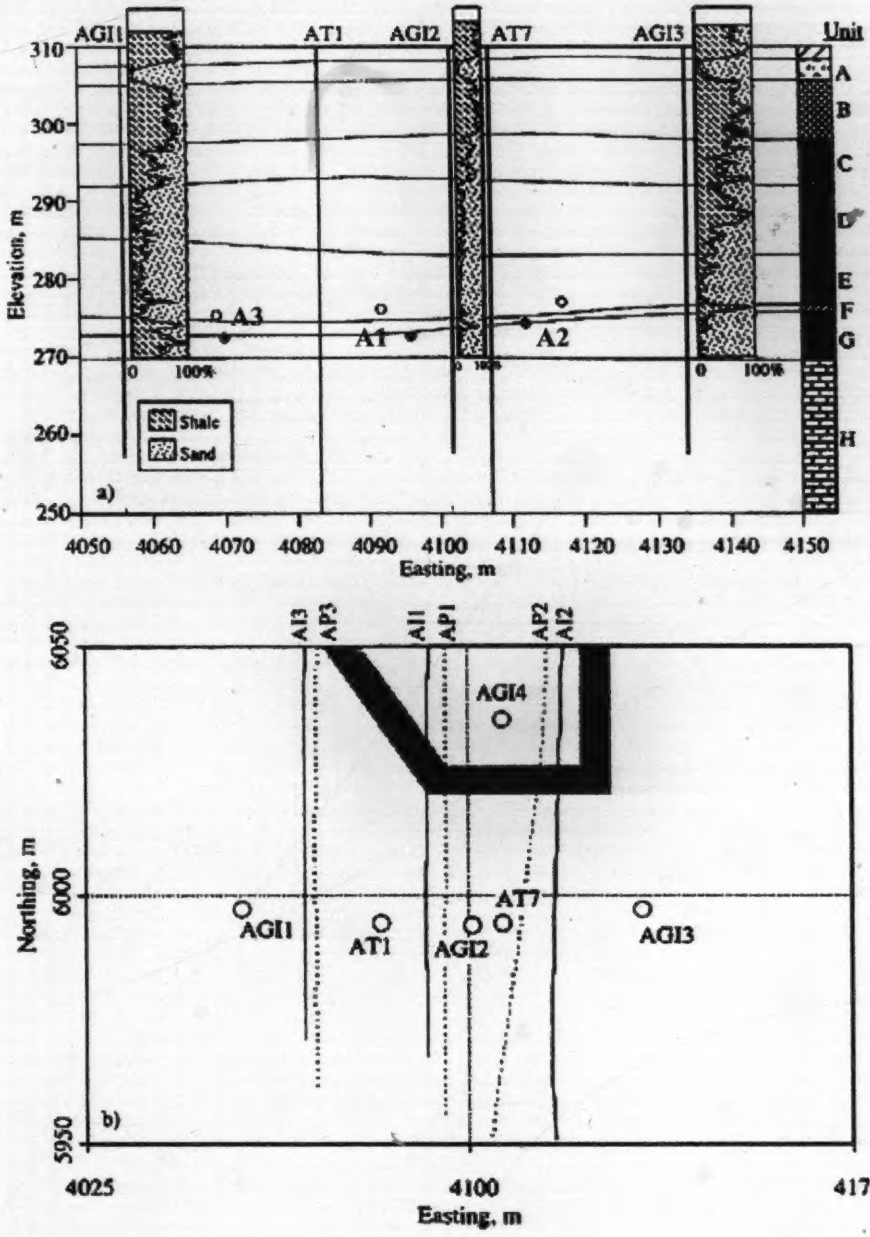

Figure 8-4 Location of inclinometer wells within the geotechnical cross section

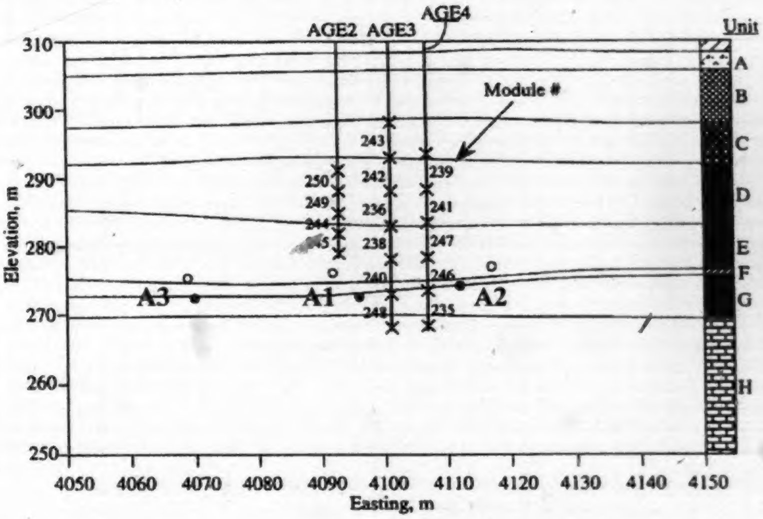
AGE2
AGE3
AGE4
Unit
A
B
C
D
E
F
G
H
Module #
243
250
242
239
249
236
241
244
245
238
247
240
246
248
235
A3
A1
A2
310
300
290
280
270
260
250
Elevation, m
4050
4060
4070
4080
4090
4100
4110
4120
4130
4140
4150
Easting, m

Figure 8-5 Extensometers modules within the geotechnical cross section

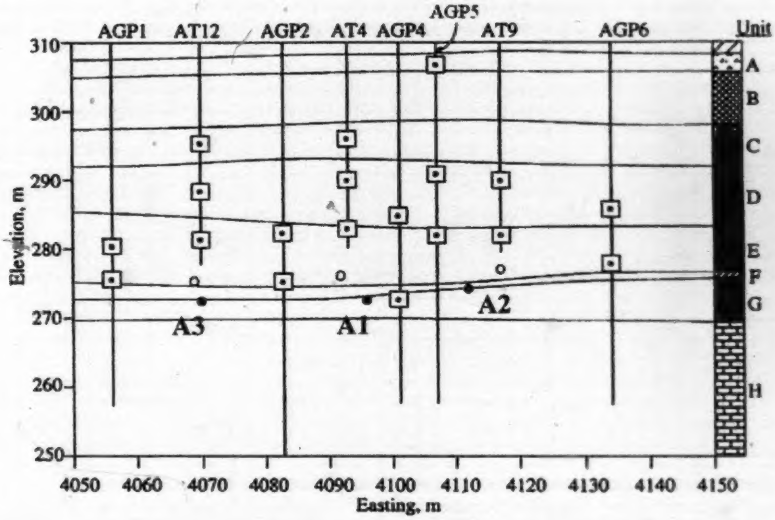
AGP1
AT12
AGP2
AT4
AGP4
AGP5
AT9
AGP6
Unit
A
B
C
D
E
F
G
H
A3
A1
A2
310
300
290
280
270
260
250
Elevation, m
4050
4060
4070
4080
4090
4100
4110
4120
4130
4140
4150
Easting, m

Figure 8-6 Piezometer locations within the geotechnical cross section

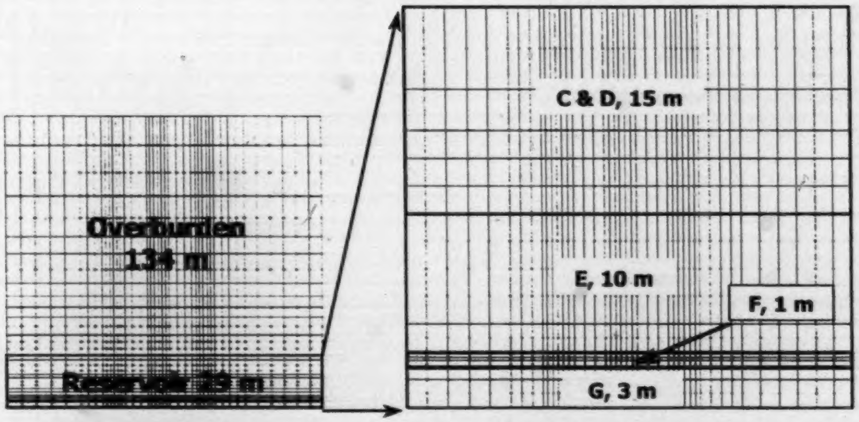
Overburden
134 m
Reservoir 29 m
C & D, 15 m
E, 10 m
F, 1 m
G, 3 m

Figure 8-7 Grid systems in reservoir geomechanical simulations (Note – the letters C, D, E, F, and G refer to stratigraphic units)

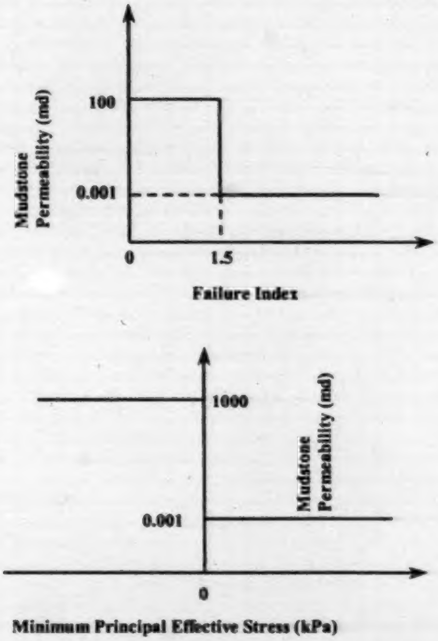

Figure 8-8 Assumptions for Unit F permeability change under tensile failure and shear failure conditions

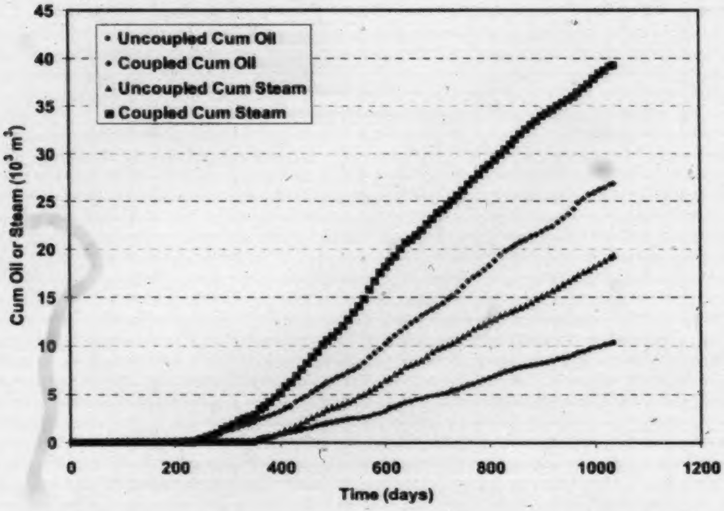

Figure 8-9 Cumulative oil production and steam injection

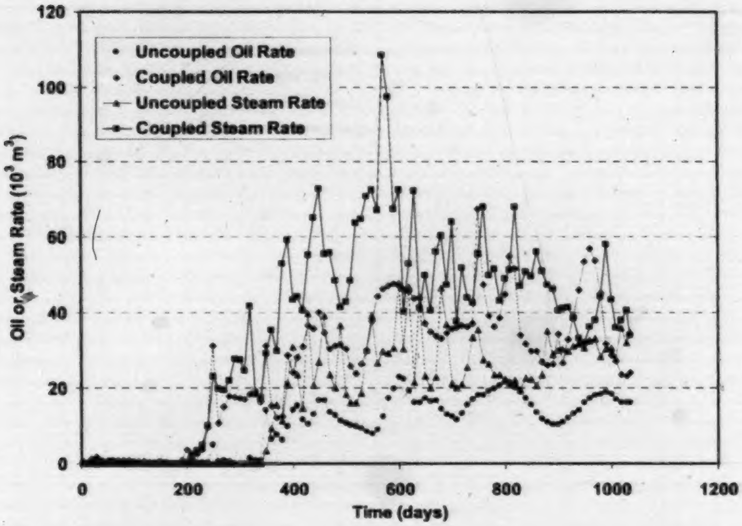

Figure 8-10 Oil production rate and steam injection rate

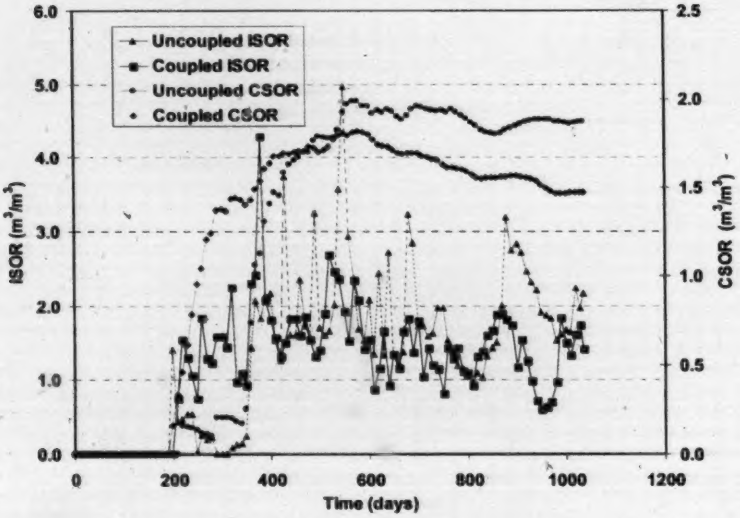

Figure 8-11 CSOR and ISOR

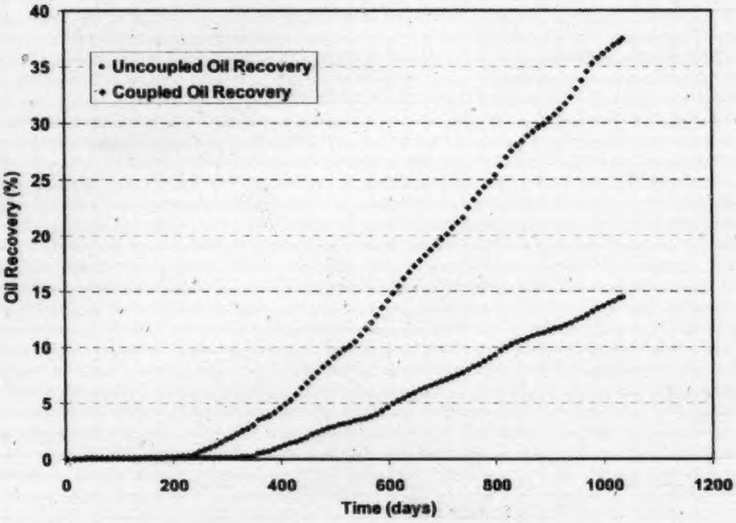

Figure 8-12 Cumulative oil recovery

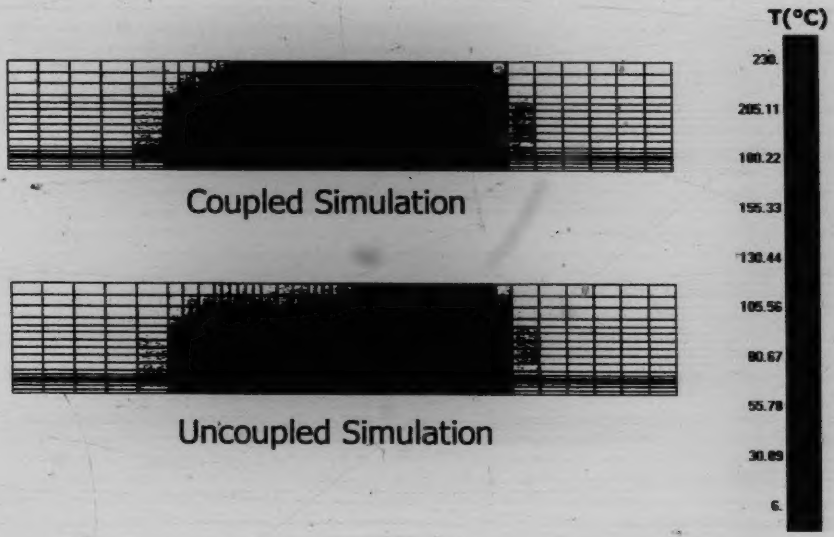

Coupled Simulation

Uncoupled Simulation

Figure 8-13 Temperature distribution (699 days)

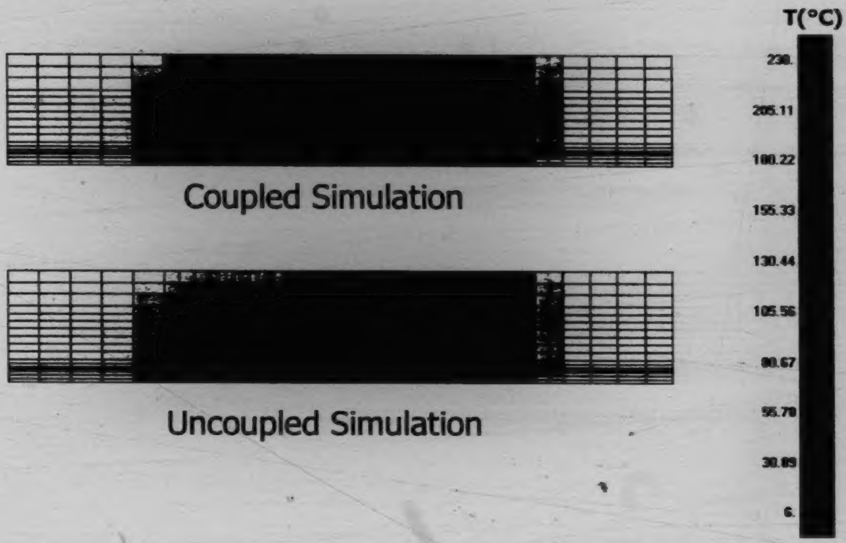

Coupled Simulation

Uncoupled Simulation

Figure 8-14 Temperature distribution (1035 days)

Figure 8-15 Permeability distribution (coupled simulation time 699 days)

Figure 8-16 Permeability distribution (coupled simulation time 1035 days)

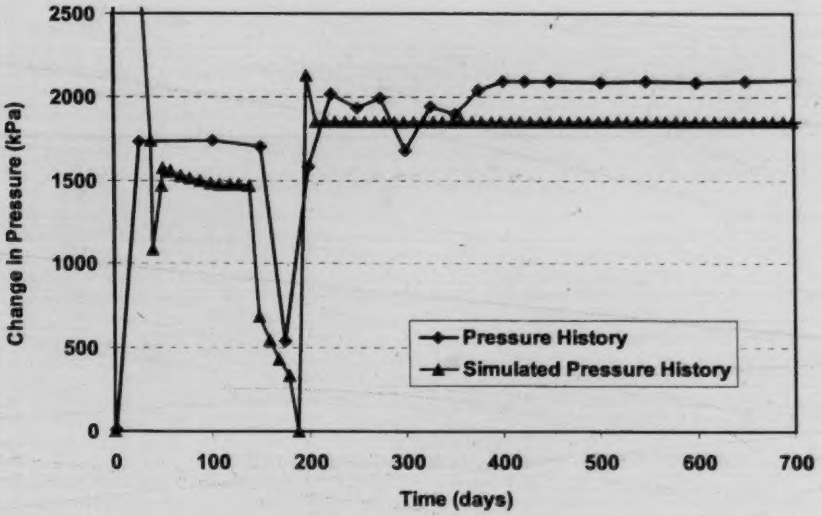

Figure 8-17 History match of AI1 well pressures

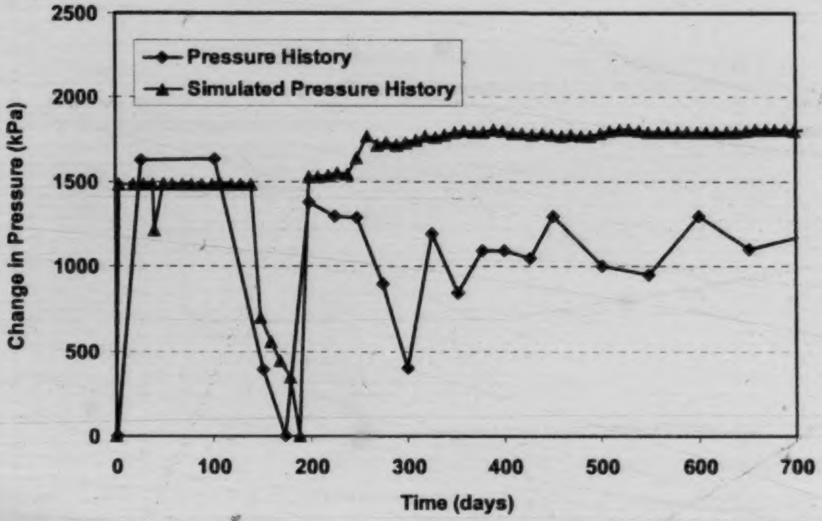

Figure 8-18 History match of AP1 well pressures

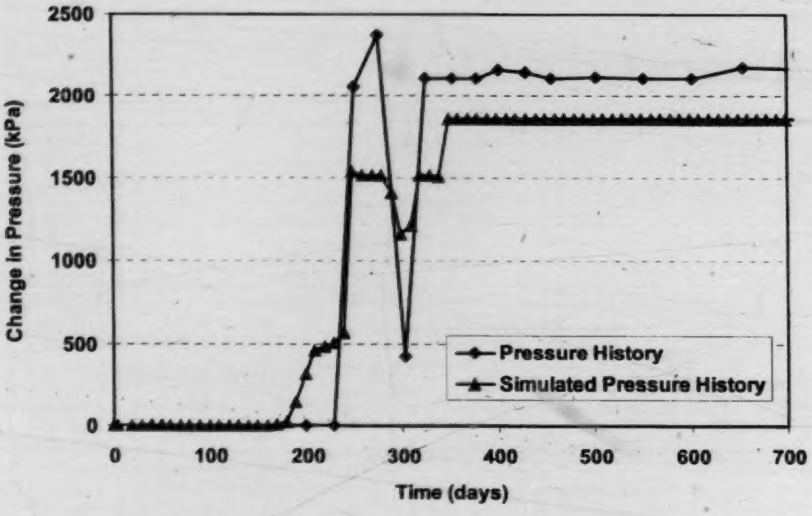

Figure 8-19 History match of AI2 well pressures

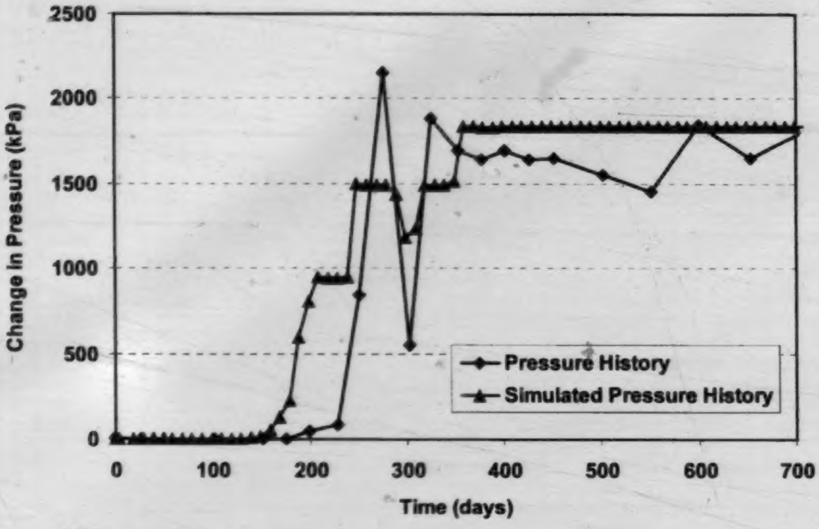

Figure 8-20 History match of AP2 well pressures

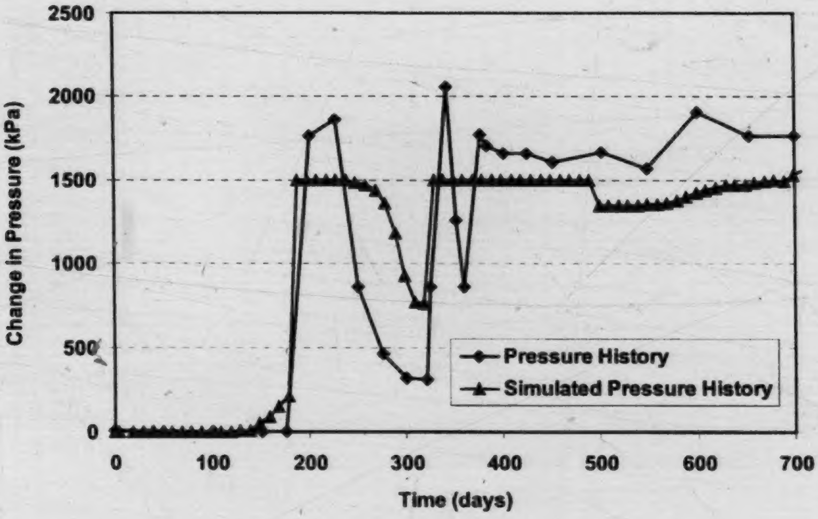

Figure 8-21 History match of AI3 well pressures

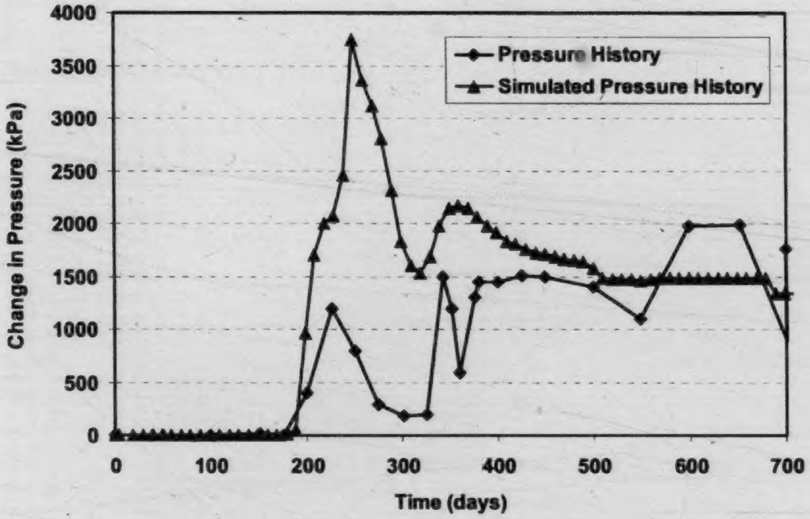

Figure 8-22 History match of AP3 well pressures

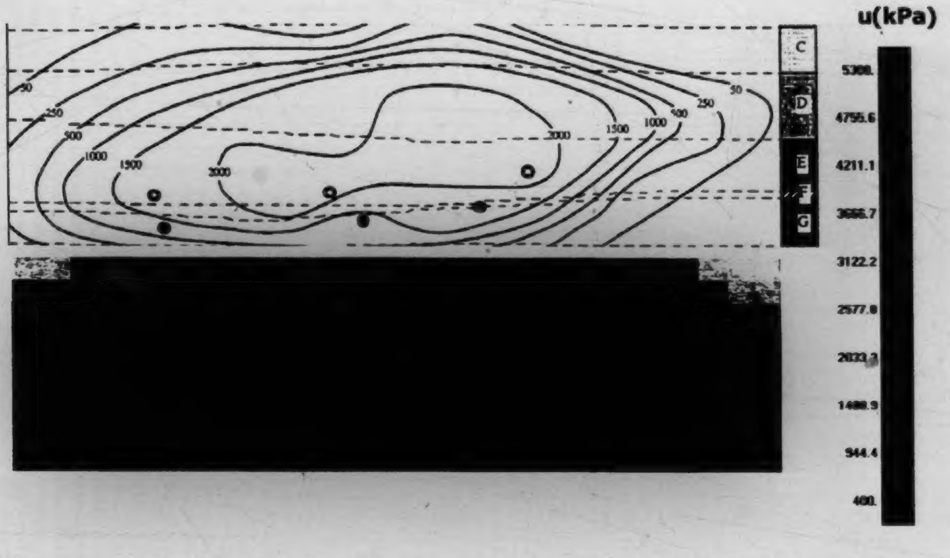

Figure 8-23 History match of pore pressure field (500 days) (contour lines in unit of kPa)

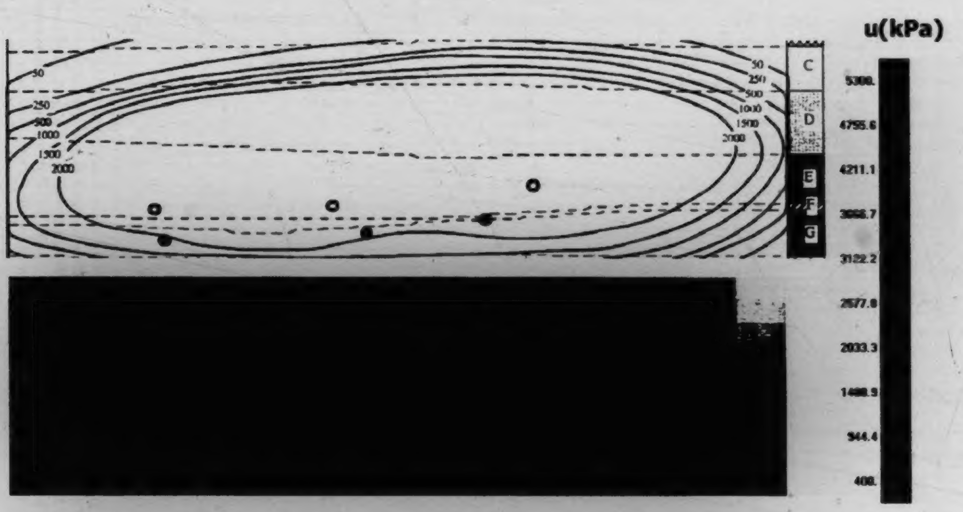

Figure 8-24 History match of pore pressure field (700 days) (contour lines in unit of kPa)

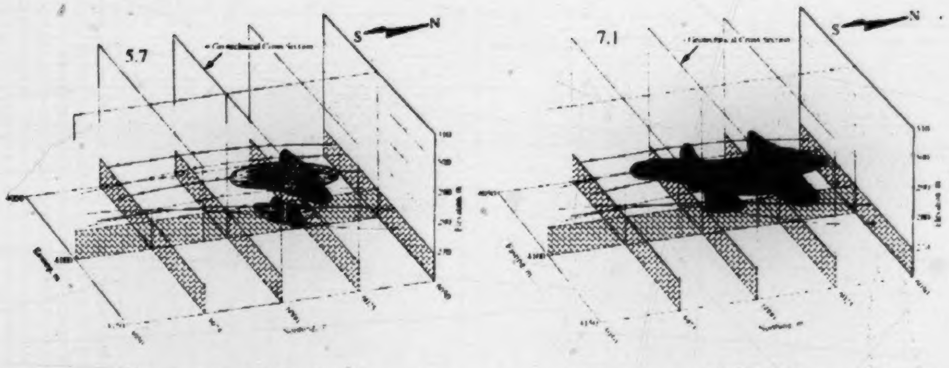

Time = 400 days **Time = 500 days**

Figure 8-25 Field steam chamber evolution

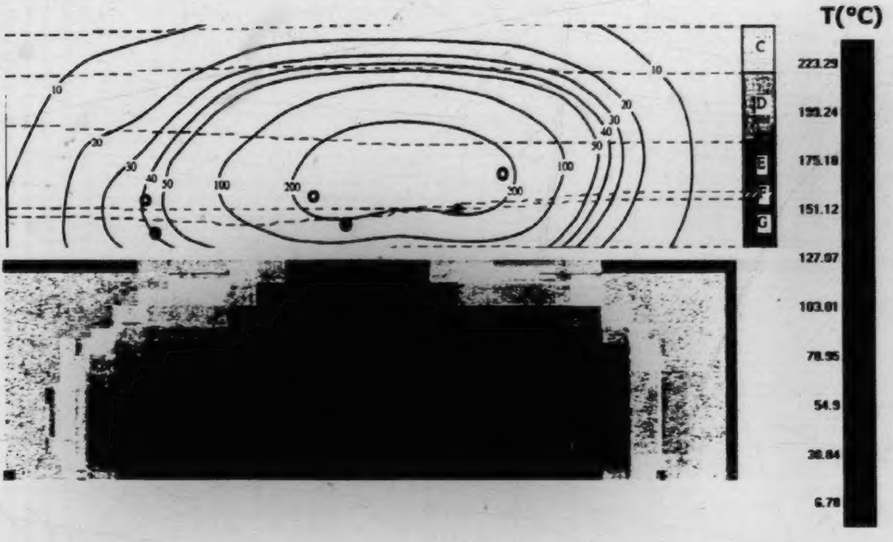

Figure 8-26 History match of reservoir temperature field (500 days) (contour lines in unit of °C)

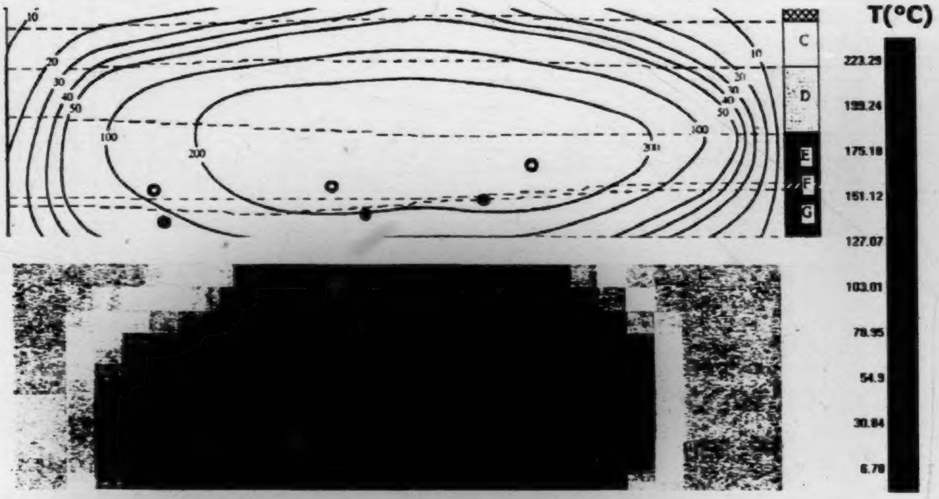
T(°C)
223.29
199.24
175.18
151.12
127.07
103.01
78.95
54.9
30.84
6.78
C
D
E
F
G
10
20
30
40
50
100
200

Figure 8-27 History match of reservoir temperature field (700 days) (contour lines in unit of °C)

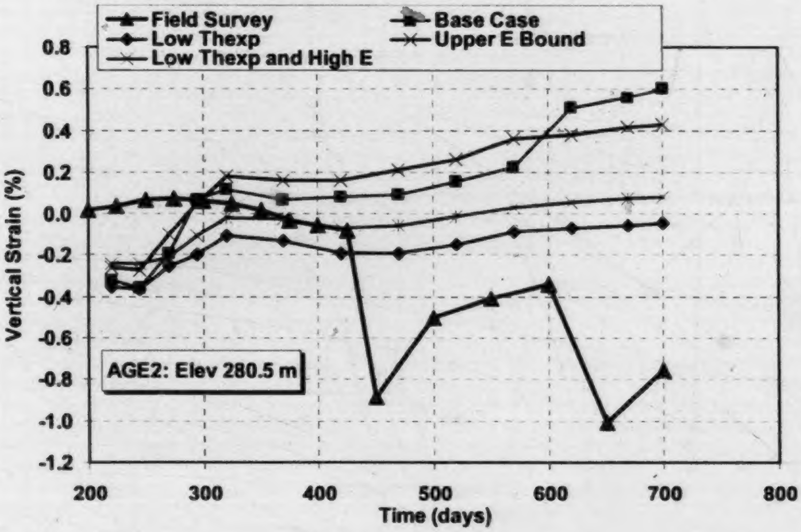

Figure 8-28 Vertical strain for AGE2 (Elevation 280.5 m)

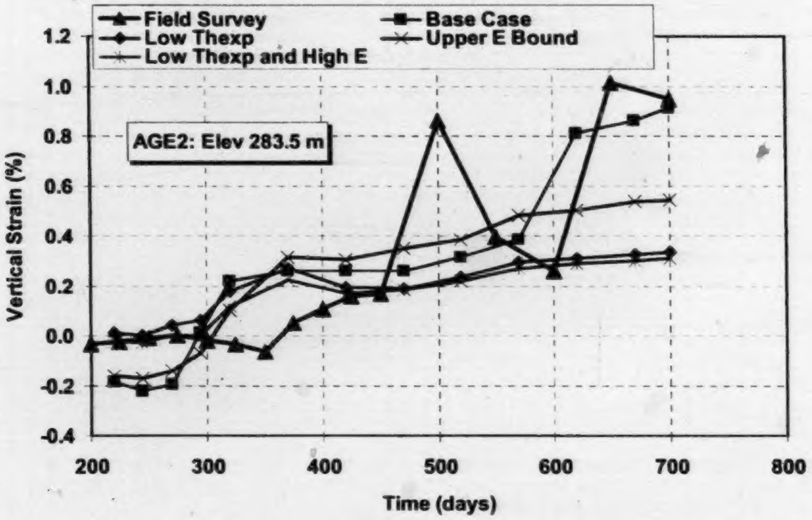

Figure 8-29 Vertical strain for AGE2 (Elevation 283.5 m)

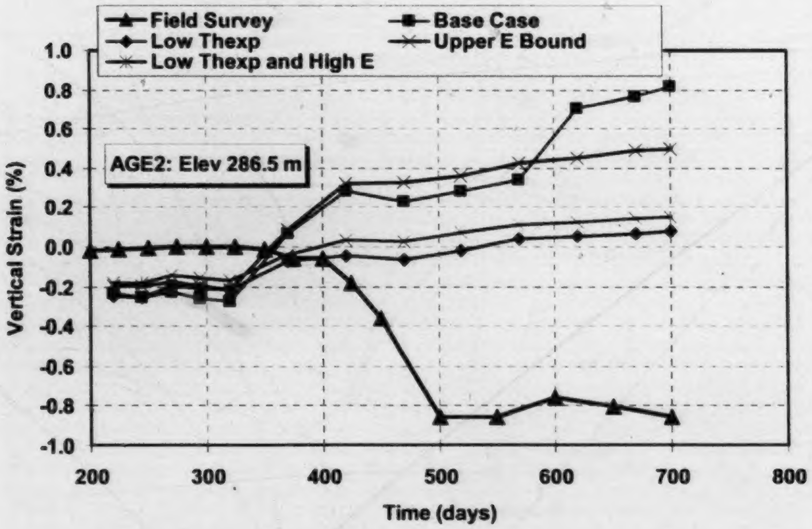

Figure 8-30 Vertical strain for AGE2 (Elevation 286.5 m)

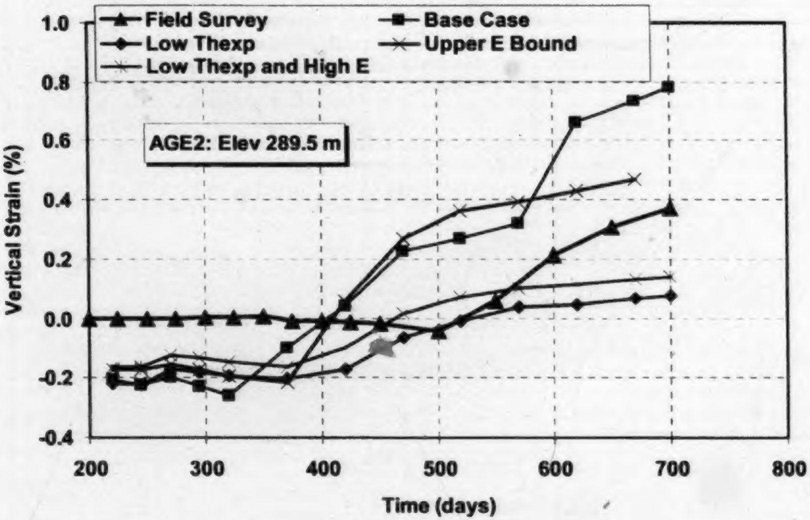

Figure 8-31 Vertical strain for AGE2 (Elevation 289.5 m)

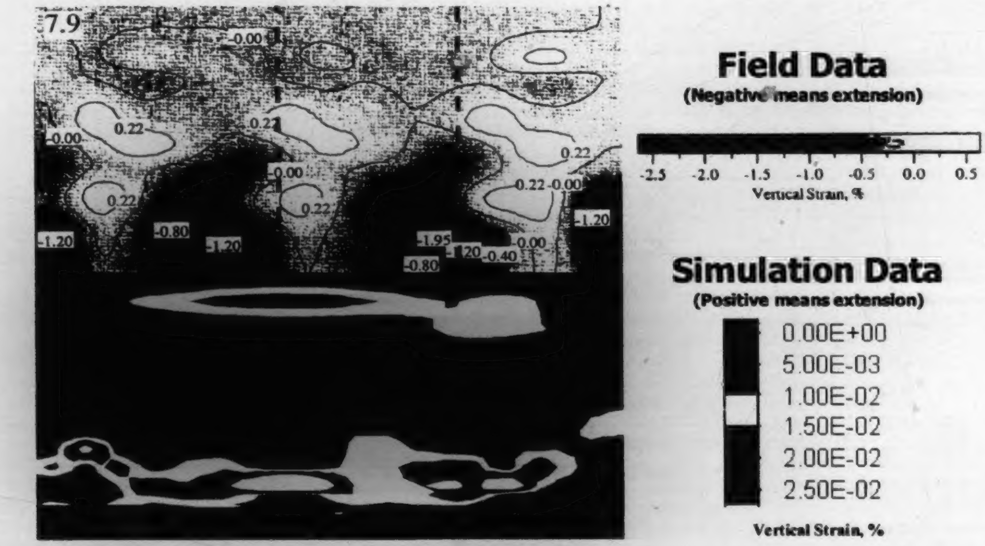

Figure 8-32 Vertical strain in the geotechnical cross section (550 days) (Field data from Chalaturnyk, 1996)

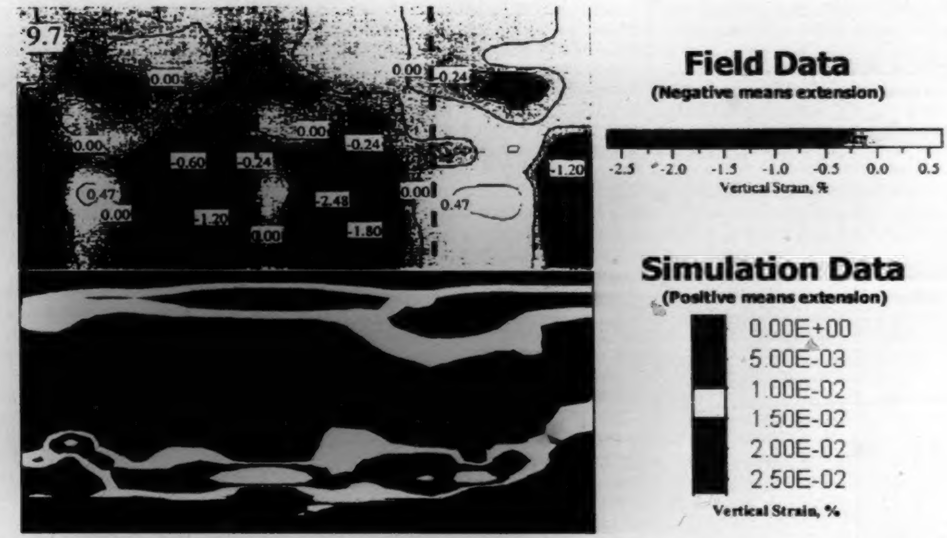

Figure 8-33 Vertical strain in the geotechnical cross section (679 days) (Field data from Chalaturnyk, 1996)

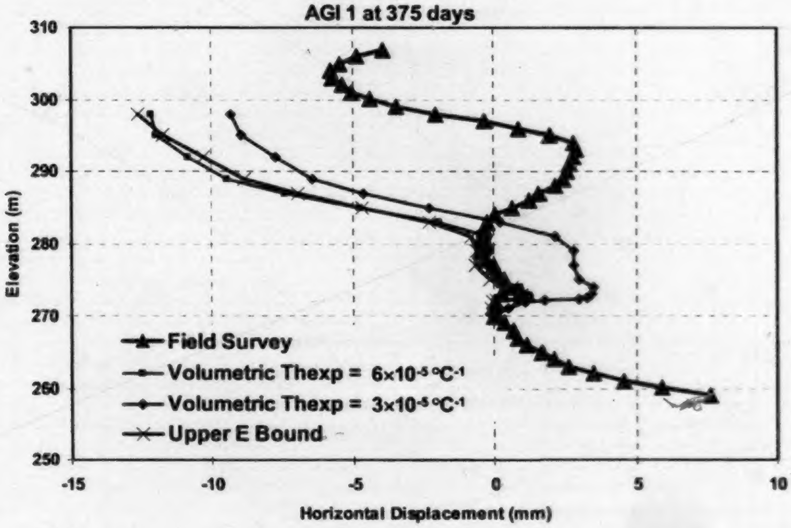

Figure 8-34 Horizontal displacement at AGI1 (375 days)

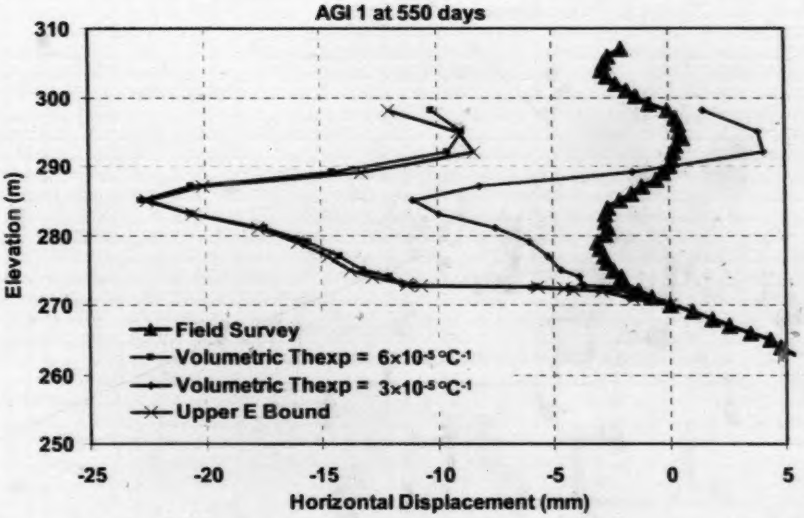

Figure 8-35 Horizontal displacement at AGI1 (550 days)

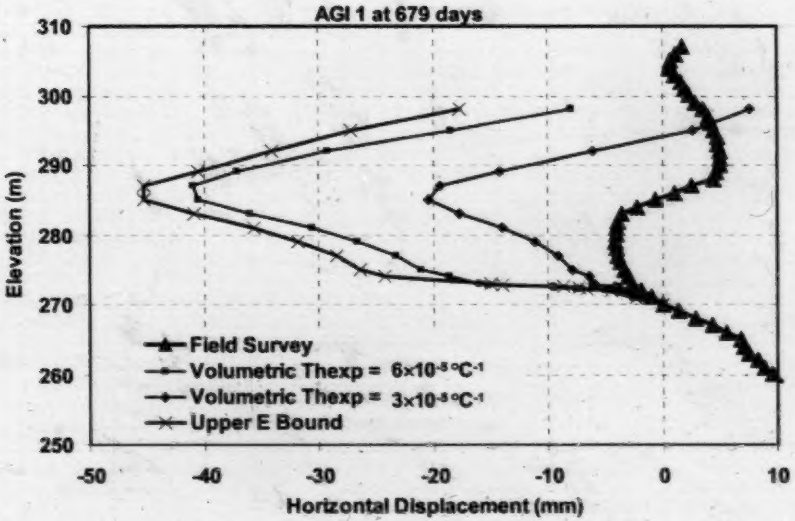

Figure 8-36 Horizontal displacement at AGI1 (679 days)

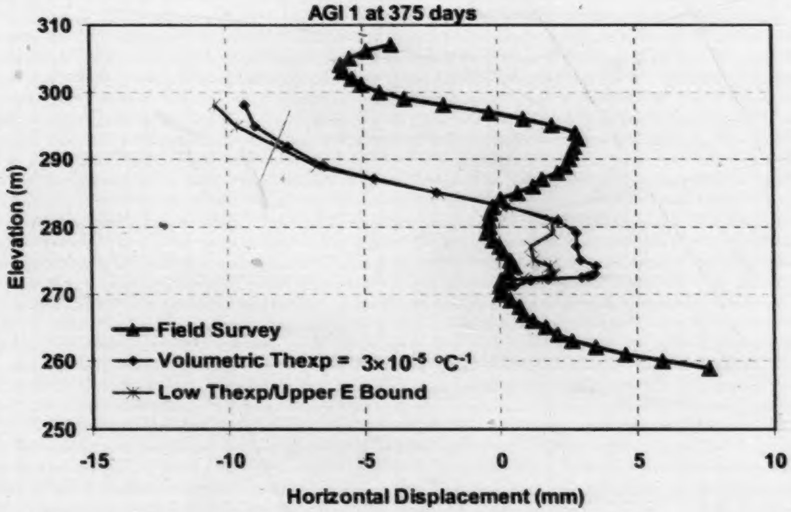

Figure 8-37 Horizontal displacement at AGI1 (sensitivity study) (375 days)

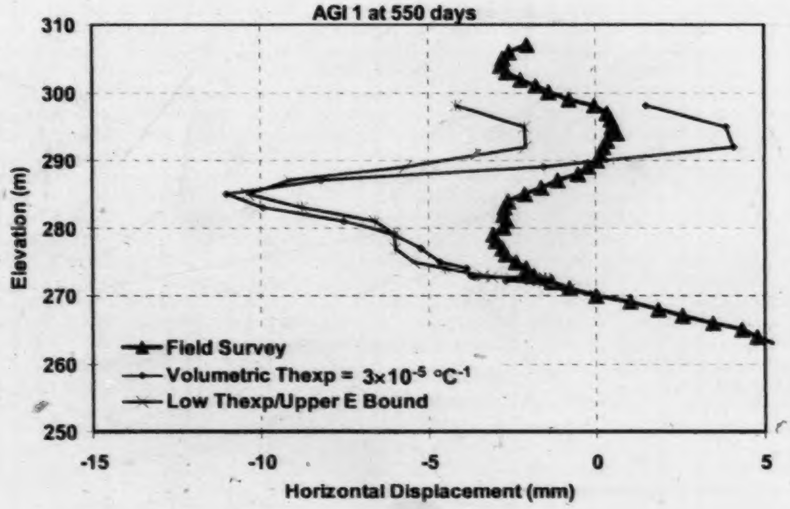

Figure 8-38 Horizontal displacement at AGI1 (sensitivity study) (550 days)

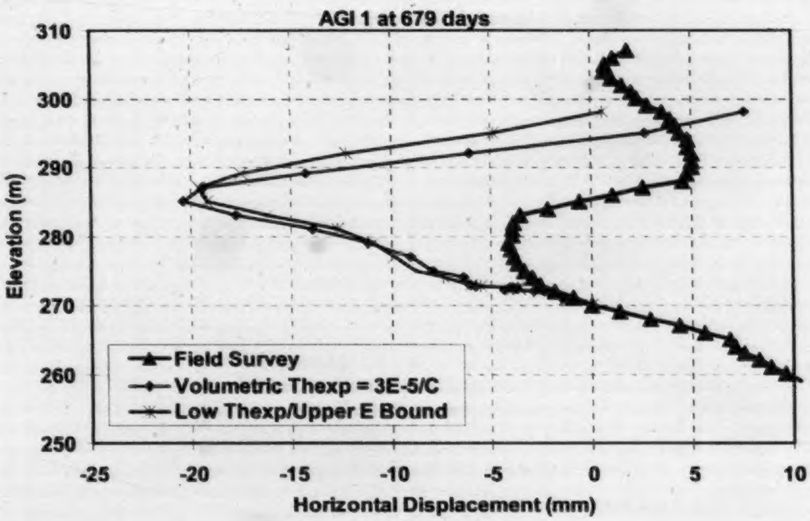

Figure 8-39 Horizontal displacement at AGI1 (sensitivity study) (679 days)

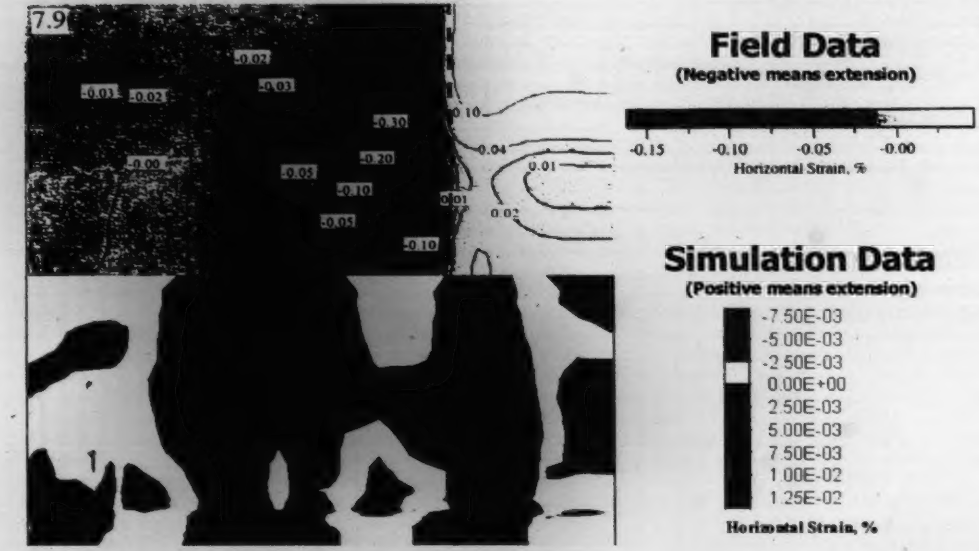

Figure 8-40 Horizontal strain in the geotechnical cross section (550 days) (Field data from Chalaturnyk, 1996)

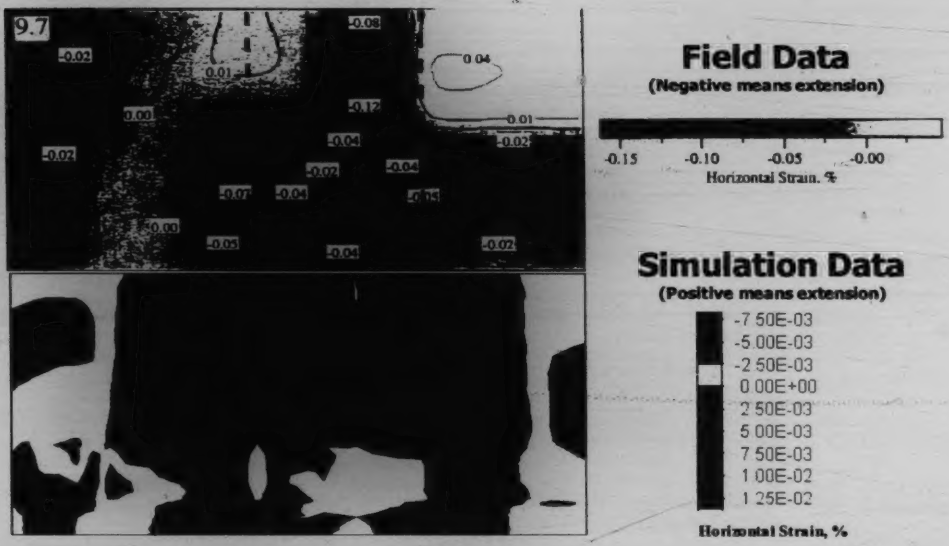

Figure 8-41 Horizontal strain in the geotechnical cross section (679 days) (Field data from Chalaturnyk, 1996)

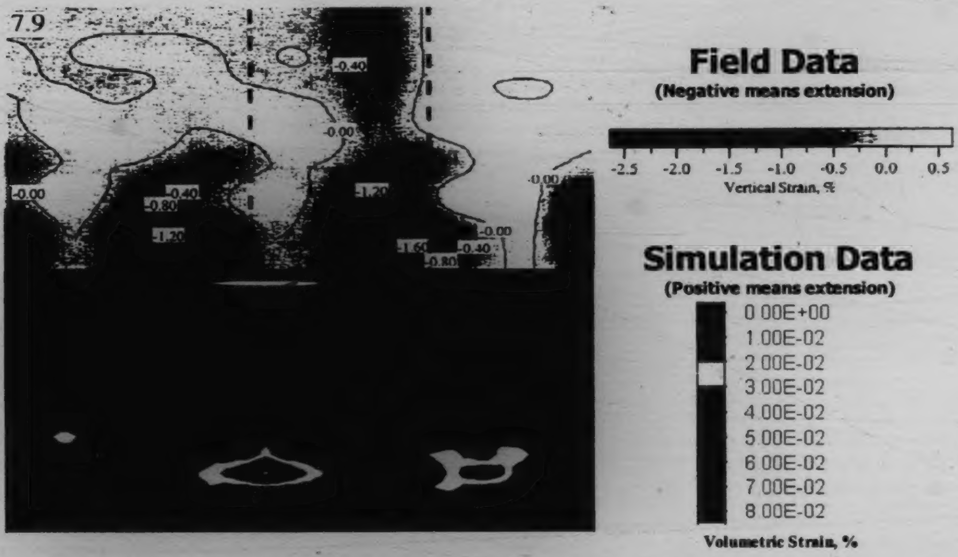

Figure 8-42 Volumetric strain in the geotechnical cross section (550 days) (Field data from Chalaturnyk, 1996)

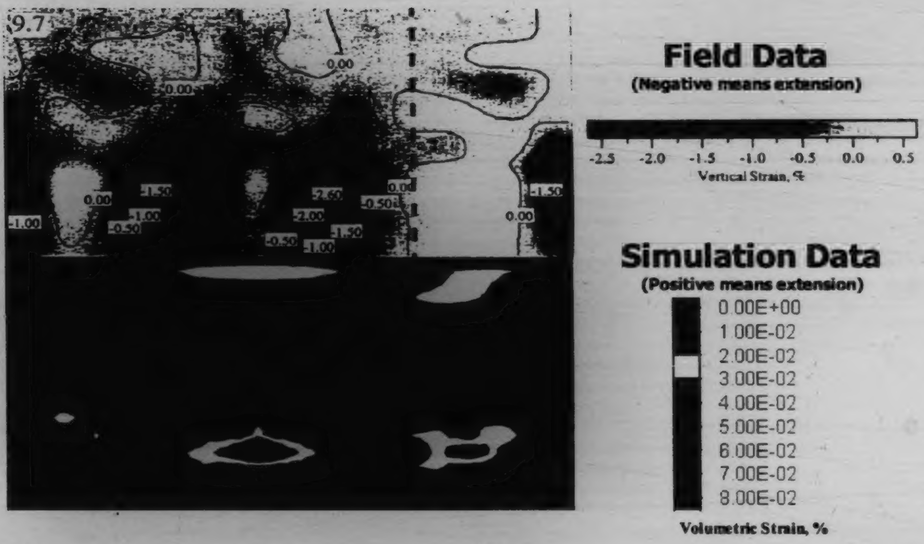
9.7
0.00
0.00
-1.50
0.00
-1.00
-0.50
-1.00
-2.50
-2.00
-0.50
-0.50
-1.00
-1.50
0.00
-1.50
0.00
Field Data
(Negative means extension)
-2.5
-2.0
-1.5
-1.0
-0.5
0.0
0.5
Vertical Strain, %
Simulation Data
(Positive means extension)
0.00E+00
1.00E-02
2.00E-02
3.00E-02
4.00E-02
5.00E-02
6.00E-02
7.00E-02
8.00E-02
Volumetric Strain, %

Figure 8-43 Volumetric strain in the geotechnical cross section (679 days) (Field data from Chalaturnyk, 1996)

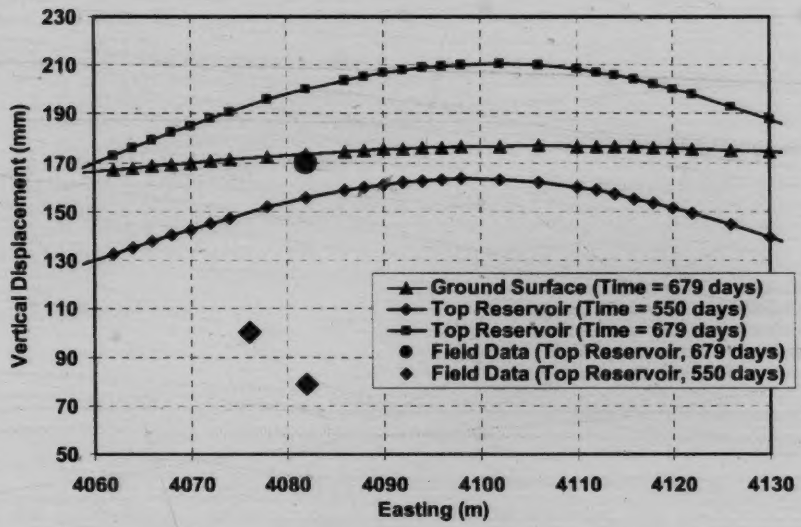

Figure 8-44 Vertical displacement and surface heave

CHAPTER 9 GAS-OVER-BITUMEN GEOMETRY AND ITS SAGD PERFORMANCE ANALYSIS WITH COUPLED RESERVOIR GEOMECHANICAL SIMULATION*

9.1 Introduction

The AEUB (2003a) has stated that almost one-third of the area of Athabasca oil sands deposits has both oil sands reservoirs and gas pools as shown in Figure 9-1. Associated gas is defined as the gas that is in pressure communication with bitumen within a region of influence either directly or through a connecting water zone. Nonassociated gas is defined as the gas that is not in pressure communication with bitumen. As a result of an exhaustive geological study conducted in the region (AEUB, 2003b), the relationship between gas and bitumen has been divided into seven cases, which are:

1) McMurray C Channel / McMurray Channel Gas / Top Water and McMurray C Channel / McMurray Channel Bitumen;
2) McMurray B Gas / Top Water and McMurray Channel Bitumen;
3) Gas / Top Water above McMurray A2 Mudstone and McMurray Channel Bitumen;
4) Wabiskaw D Valley-fill Gas / Top Water and Wabiskaw D Valley-fill bitumen;
5) Wabiskaw D Sand Gas and McMurray Channel / Wabiskaw D Bitumen;
6) Wabiskaw C Sand Gas / Top Water and McMurray Channel / Wabiskaw D and C Bitumen;

---

* Part of this chapter entitled *Gas-Over-Bitumen Geometry and Its SAGD Performance Analysis with Coupled Reservoir Geomechanical Simulation* (Li, P. and Chalaturnyk, R.J.) has been accepted by the Journal of Canadian Petroleum Technology (JCPT) for publication. It was first presented at the 5th Canadian International Petroleum Conference (the 55th Annual Technical Meeting of the Petroleum Society), Calgary, Alberta, Canada, June 8-10, 2004.

7) Wabiskaw A Gas / Top Water and McMurray / Wabiskaw D, C and A Bitumen.

The simulation results discussed in this chapter focuses on one of those cases: an oil sand reservoir with nonassociated gas pool, where a mudstone layer separates the gas pool from an underlying bitumen reservoir (such as Case 3).

For the gas-over-bitumen SAGD geometries, the effect of gas pool depressurization on the SAGD production performance has been discussed since the early 1990's and is still an area of active research (AEUB, 2000; Pooladi-Davirsh and Mattar, 2002). The role played by geomechanics has been discussed in the process of gas pool depressurization, repressurization, and wellbore stability analysis (AEUB, 2000). However, detailed assessment of the mudstone geomechanical behavior was not taken into account in the prediction of SAGD production performance.

Chapter 5 describes the coupled reservoir geomechanical simulation technology which involves both the reservoir simulator, EXOTHERM, and the geomechanical simulator, FLAC. This coupled reservoir geomechanical simulation approach is adopted to study the effect of the mudstone permeability and steam injection pressure on the SAGD production performance. The geomechanical properties of oil sands are summarized in Chapter 7 based on 26 numerical experiments that match the lab testing results done by different researchers. The geomechanical behaviour of mudstone layer and its permeability variations after failure are discussed in Chapter 8.

9.2 Geomechanical Properties of Oil Sands

The geomechanical properties of oil sands have been described in Chapter 7 in detail. The modulus of elasticity as a function of effective confining stress was obtained by numerically matching the results of the experimental tests (Figures 9-2 and 9-3). It is summarized in Chapter 7 that the relationship from Samieh and Wong (1997) is appropriate to represent the modulus of elasticity variation behavior of oil sands (Equation (7-2))

$$E = 950 P_a (\sigma_3' / P_a)^{0.5} \tag{7-2}$$

The values of the maximum friction angle and dilation angle for strain softening geomechanical model were derived by matching the experimental results of Touhidi-Baghini (1998). Based on this numerical matching, the following relationships (Equations (7-3) and (7-4)) were obtained

$$\phi' = 55 - 14.93\log\left(\sigma_3' / P_a\right) \tag{7-3}$$

$$\psi' = 25.8 - 12.05\log\left(\sigma_3' / P_a\right) \tag{7-4}$$

To test the robustness of these relationships, Equations (7-3) and (7-4) were used drectly in matching the experimental results obtained by Samieh and Wong (1997). Remarkably good fits were obtained for their test results and only minor adjustments were required to match the results from Oldakowski (1994). Consequently, the relationships described in Equations (7-3) and (7-4) were adopted for the simulation studies.

9.3 Geomechanical Properties of Mudstones

In the Athabasca oil sands deposits, four stratigraphic mudstones/shales units exist. From oldest to youngest, they are the McMurray B Mudstone, McMurray A Mudstone, Wabiskaw D Shale and Wabiskaw T-21 Marker. These are thought to be sealing layers preventing or restricting pressure communication between underlying and overlying sands with contained gas and bitumen zones (AEUB, 2003b).

McMurray B2 and A2 Mudstones (found at the base of the McMurray B2 and McMurray A2 sand sequences, respectively) are the most significant sealing layers in the Athabasca area (AEUB, 2003b). The B2 mudstone at the base of the B2 sand sequence is 1 to 2 m thick, nonfissile, and exhibits abundant trace fossils. The A2 mudstone at the base of the A2 sand sequence is 1 to 2 m thick. The A2 mudstone is also nonfissile and exhibits abundant trace fossils (AEUB, 2003b). Based on these geological descriptions, it has been assumed that the mudstone layers have low porosity and very low permeability values.

In the SAGD process, pore pressure and thermal “fronts” move or propagate upwards and sideways within the oil sands reservoir (Li et al., 2002). When these fronts approach a low permeability and low porosity mudstone layer, very high pore pressures can be produced. Agar (1984) proposed the following equation to calculate the pore pressure response due to undrained heating of oil sands (Equation (9-1)):

$$B_T = \frac{\Delta u}{\Delta T} = \frac{\beta_u - \beta_{DR} + C_c(\Delta\bar{\sigma} / \Delta T)}{C_u + C_c} \tag{9-1}$$

When the undrained heating is conducted with constant total stresses, Equation (9-1) can be expressed as Equation (9-2).

$$B_T = \frac{\Delta u}{\Delta T} = \frac{\beta_u - \beta_{DR}}{C_u + C_c} \tag{9-2}$$

β_u and C_u are expressed as Equation (9-3) and (9-4), respectively

$$\beta_u = \beta_w \phi_w + \beta_B \phi_B + \beta_s (1-\phi) \tag{9-3}$$

$$C_u = C_w \phi_w + C_B \phi_B + C_s (1-\phi) \tag{9-4}$$

If the mudstone layer is saturated with water only, the bitumen porosity becomes zero. Based on the assumption of $\phi_w = 0.1$, $\beta_s = 5 \times 10^{-5}$ °C^{-1}, $\beta_w = f(T)$, $C_w = 4.5 \times 10^{-7}$ kPa^{-1}, and $C_s = 2.7 \times 10^{-5}$ kPa^{-1}, pore pressure can be increased roughly to 4 MPa, 11 MPa, and 27 MPa for the temperature increase from 0 to 50 °C, 100 °C, and 200 °C, respectively.

Butler (1986) postulated that the same mechanism might occur in oil sands where high pore pressures can be achieved by thermal expansion of pore fluid. High permeability of oil sands allows the high pore pressure to dissipate quickly. For regions of low permeability, however, high pore pressures may remain.

Because mudstone layers have very low permeability values, high pore pressures cannot be relieved in a short period of time. The potential magnitude of these high pore pressures may lead to hydraulic fracture of the mudstone layer. Hydraulic fracturing takes place when pore pressure exceeds the minimum effective stress plus the tensile strength of the mudstone. When hydraulic fracturing or tensile failure occurs, the local permeability of the mudstone increases significantly. This concept is consistent with Butler's statement that low permeability parts of the reservoir may, because of thermal expansion within the pores, be preferentially disrupted with a resulting improvement in permeability.

In addition, shear stresses within a mudstone layer may also lead to failure. Elevated temperature and pore pressure within the mudstone layer leads to volumetric expansion and lower effective confining stresses. These processes can significantly reduce the strength of a mudstone layer (Wong, 1998) resulting in even more amenable conditions for shear failure. After shear failure, the permeability of a mudstone layer may increase or decrease depending on whether the mudstones are ductile and remain sealing after deformation or whether they deform in a brittle manner to create permeable leak paths (Ingram and Urai, 1999). It is postulated that due to the overconsolidated nature of the McMurray A and B mudstone layers, it is likely that they will demonstrate brittle shear failure behaviour.

For this study, it has been assumed, as discussed above, that both tensile and shear failure, if it occurs, will increase the permeability of the mudstone layer during SAGD operations.

9.4 Linking Parameters of Reservoir and Geomechanical Simulators

9.4.1 Oil Sands Reservoir

As described by Li, Chalaturnyk, and Tan (2003), the reservoir simulator, EXOTHERM, and the geomechanical simulator, FLAC, are executed sequentially on compatible numerical grids and linked through external coupling modules, which transfer relevant information between the field equations that are solved in respective codes. After each time step, pore pressure and temperature data produced by EXOTHERM are transferred into FLAC, and then FLAC performs the geomechanical simulation and updates previous permeability and porosity values.

Li and Chalaturnyk (2004) investigated the permeability variations due to isotropic unloading and shearing. They indicated that the permeability of oil sands as a function of volumetric strain can be calculated by Equation (6-7)

$$Ln\frac{k}{k_0} = C_{n_1}\ \varepsilon_v \tag{6-7}$$

where C_{nl} is constant. For the block specimens with porosity of about 0.34, C_{nl} is 5.9 and 14.76 for horizontal specimens and vertical specimens, respectively. The isotropic permeability change of oil sands can be found by taking an average of these C_{nl} values. So, C_{nl} is 10.33.

The porosity variations can be calculated by equation (4-3)

$$\phi = \frac{\phi_0 + \varepsilon_v - (1 - \phi_0)\alpha_s(T - T_0)}{1 + \varepsilon_v} \tag{4-3}$$

where α_s is the thermal expansion coefficient of oil sands, which is much smaller than the first term. So, the second term is negligible. Equation (4-3) can be simplified into Equation (6-9), which is used in the numerical simulations presented in this chapter.

$$\phi = \frac{\phi_0 + \varepsilon_v}{1 + \varepsilon_v} \tag{6-9}$$

9.4.2 Mudstone Layer

As discussed previously, tensile failure and shear failure can alter the permeability of the mudstone layer. Unfortunately, experimental data are unavailable regarding the magnitude of permeability improvement for the McMurray mudstone layer. For the simulations presented in this chapter, it is assumed that when shear failure occurs, the mudstone permeability is increased to 10 md and when tensile failure occurs, its permeability is increased to 1000 md. These modifications are schematically illustrated in Figure 9-4. During SAGD operations, the injected steam will flow to the top thief water zone rapidly if failure occurs. The shear failure is estimated based on the failure index (or factor of safety) proposed by Chalaturnyk (1996). The failure index is defined as the equation shown in Figure 9-5. The cohesion of the mudstone layer is assumed as 100 kPa, and the tensile strength is also assumed to be 100 kPa. So, the tensile failure occurs when the minimum principal effective stress is less than –100 kPa.

9.5 Numerical Simulation

9.5.1 Reservoir Model and Geomechanical Model

An oil sands reservoir model was established based on the Athabasca Wabiskaw-McMurray Regional Geological Study (AEUB, 2003). Well 00/04-13-079-07W4/0 has top gas, top water, A2 Mudstone, and bitumen bearing formation, which is illustrated in Figure 9-6. The stratigraphic representation developed for the modelling study is shown in Figure 9-7. Above the gas sands, all formations are combined as the overburden. The thickness of each layer is also shown in Figure 9-7. It should be noted that the water layer is assumed as a thief zone and a constant pressure boundary is set at the right side of the water layer.

Reservoir properties and geomechanical properties used in EXOTHERM and FLAC simulations are shown in Tables 9-1 and 9-2. The grid systems for both simulators are plotted in Figure 9-8. Smaller grid blocks are used for the mudstone layer and in the area adjacent to the horizontal wells. The mudstone layer is divided into 10 grid blocks in vertical direction and each block is 0.2 m thick.

9.5.2 Base Case: Mudstone Permeability = .001 md

The conventional reservoir simulations do not account for the complex geomechanical interactions between fluid flow and stress strain behaviour. Sequentially coupled reservoir geomechanical simulations performed in this chapter update the reservoir permeability and porosity each time step including reservoir geomechanical responses. For the base case simulation, the mudstone layer has been assigned a permeability of 0.001 md. Sequentially coupled reservoir geomechanical simulations have shown that a mudstone permeability of 0.001 md is sufficient to allow pore pressure dissipation to occur and prevent the development of high thermal induced pore pressures – the mudstone layer does not fail in either tension or shear. Consequently, no preferential flow path develops through the mudstone layer and steam does not leak to the top thief water zone.

The simulations allow the comparison of the results from conventional versus coupled simulations. The SAGD production performance based on these two simulation techniques are compared in Figure 9-9, 9-10, and 9-11. As a result of modest permeability and porosity improvements within the oil sands, the coupled simulation obtained slightly higher oil production and steam injection rates. In addition, the OSR is almost the same over most of the production period. Oil recovery based on coupled simulation is predicted to be slightly higher. The reason for the small difference between these two simulations is that oil sands has a large initial permeability, and the permeability improvement due to geomechanics does not play a critical role. The maximum permeability increment due to geomechanics is 277 md during the SAGD process. Consequently, the improvement in flow performance is minimal.

9.5.3 Evolution of Failure within Mudstone Layer

It has been reported that shale permeability was found to be extremely low, typically ranging from 10^{-6} to 10^{-3} md (Magara; Borst; and Soeder, 1986). The maximum shale permeability reported in the literature was 0.05 md (Pooladi-Darvish, 2002). In the Athabasca area, McMurray A2 and B2 mudstone are the sealing layers. Mudstone is fine-grained, detrital sedimentary rock made up of silt and clay sized particles. It is distinguished from shale by lack of fissility, which is a property of splitting along closely spaced planes more or less parallel to bedding (AEUB, 2003b). So, mudstone permeability should be smaller than shale permeability. To illustrate the evolution of the possible failure process in a mudstone layer, the following discussion presents the results from a coupled simulation using a mudstone permeability of 0.00001 md.

During the SAGD process, when the steam chamber is approaching the mudstone layer, high pore pressure front preferentially migrates laterally under the mudstone layer and cannot propagate into the mudstone layer given its low permeability. However, the pore pressure inside the mudstone layer can still be increased to a very high value by thermal expansion of fluids when the high temperature front propagates into it. These temperature-induced high pore pressures cannot be relieved in a short period of time because of the low permeability. Geomechanically, when these high pore pressures exceed the total stress, tensile failure will occur. This behaviour can be clearly seen in the coupled reservoir geomechanical simulation process discussed below.

At a simulation time of 1399 days, the pore pressures in lower left corner (above the steam injector) of the mudstone layer are predicted to increase from an initial value of 1750 kPa to more than 7000 kPa (Figure 9-12). The FLAC simulation shows that the failure index in this region is approximately equal to 1.0 (Figure 9-13), which means that shear failure has occurred. Consequently, the mudstone permeability increases as shown in Figure 9-14, in accordance with the model shown in Figure 9-4. When the simulation time reaches 1639 days, the pore pressures in the middle left side of the reservoir model has increased to more than 7700 kPa (Figure 9-15). Correspondingly, both tensile failure and shear failure criteria are satisfied (Figure 9-16 and 9-17). Because of tensile failure, the permeability in that area is increased to 1000 md (Figure 9-18). Figure 9-19 shows the modified permeability distribution when the simulation time is 2369 days. As well, a number of grid blocks have experienced shear failure and the corresponding permeability has increased to 10 md. Two regions in the lower right corner have experienced tensile failure (Figure 9-20) and the corresponding permeability is increased to 1000 md. After 20 years of the SAGD operation, the modified permeability distribution in the mudstone layer is shown in Figure 9-21. The failure index after the operation is finished is shown in Figure 9-22, and it shows that the two-meter mudstone layer has reached failure conditions almost through the entire thickness. The ramifications for this type of process, if applicable under field conditions, is that if the thickness of the mudstone layer is less than 1.8 m, the whole mudstone layer will fail, for the assumptions and reservoir properties assumed in the simulations.

9.5.4 Effect of Mudstone Permeability

To study the sensitivity or influence of the mudstone permeability on SAGD production performance, seven different mudstone permeabilities were taken into account. The seven permeability values were 0.1 md, 0.01 md, 0.001md, 0.0001 md, 0.00001 md, 0.000001 md, and 0 md. These coupled simulations were performed based on the properties in Tables 9-1 and 9-2.

When the mudstone permeability is equal to 0.1 md, 0.01 md, 0.001 md, and 0.0001 md, the mudstone layer has failure occurring at the lowest grid block, with 0.2 m thickness, over the period of SAGD operations. Some cases only have shear failure and some cases have both the tensile failure and shear failure. Figure 9-23 shows the modified permeability distribution due to geomechanics in the SAGD process for the case with mudstone permeability of 0.0001 md. These coupled simulation results shows that when the mudstone permeability is greater than 0.0001 md, the high pore pressures generated by thermal expansion of pore fluids are able to dissipate before reaching fracture conditions. The steep pore pressure gradient associated with these high pore pressures accelerates the diffusion of pore pressure within the mudstone layer. The lower region of the mudstone layer cannot rapidly relieve the high pore pressure and consequently, this region undergoes failure. As described previously, when the mudstone permeability is 0.00001 md, 90% of the mudstone layer (1.8 m) from the bottom to the top experiences failure. Only 10% of the upper part (0.2 m) of the mudstone layer does not fail (Figure 9-21). In all cases where the mudstone layer does not fail, the predicted SAGD production is nearly identical for all different mudstone permeabilities as shown in Figures 9-24, 9-25, and 9-26, which compare the SAGD production parameters (oil and steam rate, cumulative oil production and steam injection, oil recovery and OSR, respectively) for simulations with mudstone permeability of 0.1 md and 0.00001 md.

If the permeability of the mudstone layer is even lower, such as 0.000001 md or an unrealistic value of 0 md, the mudstone layer will completely fail (Figures 9-27 and 9-28) over the period of SAGD operations. In this case, the SAGD production performance will become worse because of the steam loss to the top thief water zone and the corresponding pressure decrease inside the steam chamber. Figures 9-29, 9-30, and 9-31 compare the SAGD production performance for two mudstone permeabilities of 0.00001 md and 0.000001 md. For the higher permeability case, the mudstone layer did not fail completely during SAGD. However, for the lower permeability case, the mudstone layer fails completely after 1719 days of the SAGD operation (Figure 9-27). Prior to 1719 days, the predicted SAGD production performance is similar for both cases. After this time, the SAGD production performance of the lower permeability case becomes much different from that of the higher permeability case. It is clear that the steam injection rate is increased to a maximum value and the oil production rate decreases rapidly (Figure 9-29). Correspondingly, the OSR is also decreased to a much smaller value (Figure 9-31). After the SAGD operation is finished, the cumulative steam injection for the low permeability case is almost doubled compared to the high permeability case. For the low permeability case, the cumulative oil production decreases by approximately 25% (Figure 9-30), and the oil recovery is decreased approximately by 20% (Figure 9-31).

9.5.5 Effect of Steam Injection Pressures

The steam injection pressure is directly related to the geomechanical behaviour occurring inside the mudstone layer during the SAGD operations. For the simulations presented above, the steam injection pressure was 2500 kPa. To examine the influence of this parameter, the steam injection pressure was increased to 5000 kPa. With a mudstone permeability of 0.001 md, the higher steam injection pressure causes failure in only the lower 0.2 m thick mudstone layer, as shown in Figure 9-32.

High steam injection pressure simulations were also conducted for a mudstone permeability of 0.0001 md. These simulations show that when the SAGD operation time is equal to 4519 days, shear failure can reach the top of the mudstone layer (Figure 9-33) producing the modified permeability distribution shown in Figure 9-34. In contrast, for almost double the operation time (7305 days), low pressure steam injection simulation only predicts failure in the lower 0.2 m layer of mudstone (Figure 9-23).

Figures 9-35, 9-36, and 9-37 provide a comparison of several SAGD production variables. These comparisons show that the SAGD performance with higher steam injection pressure becomes worse after the shear failure across the mudstone layer at time of 4519 days. At this point, the steam injection rate reaches a maximum value, the oil production rate rapidly decreases to zero (Figure 9-35), and consequently, the OSR becomes zero (Figure 9-37). Before the time of 4519 days, the cumulative steam injection and oil production are larger for the high pressure case than for the low injection pressure case. However, after 4519 days, cumulative steam injection rises rapidly and cumulative oil production becomes a constant for the high pressure case, and the final cumulative oil production and oil recovery are smaller than those of the low pressure case (Figure 9-36 and 9-37).

9.6 Summary

In this chapter, the geotechnical properties of oil sands summarized in Chapter 7 were used to characterize the stress-strain behavior of oil sands. The following concluding remarks were made based on the coupled reservoir geomechanical simulations:

- Mudstone permeability plays a very important role in the SAGD operations based on the gas-over-bitumen geometries presented in this chapter. If the mudstone permeability is sufficiently large, injected steam will flow into a top thief water zone without any difficulty. However, if the mudstone permeability is sufficiently low, shear failure or even tensile failure during the SAGD process may occur and negatively affect the integrity of the mudstone layer and the SAGD production performance. Therefore, an ideal gas-over-bitumen SAGD geometry with a mudstone layer between the bitumen and gas pool should have a mudstone permeability that not only prevents significant steam loss to the top thief water zone but also avoids large pore pressure generation in the mudstone layer.

- Shear or tensile failure is possible under high steam injection pressures. For the same mudstone permeability, low steam injection pressure may not induce failure inside the mudstone layer, but high steam injection pressure may cause failure and worsen the SAGD production performance. Optimization of the steam injection pressure for a SAGD project should account for this complex mudstone behavior.

- Conventional reservoir simulations cannot characterize the tensile and shear failure behavior during the SAGD process. However, coupled reservoir geomechanical simulation techniques can provide valuable and in certain cases, critical input to the optimization and design of a SAGD project.

Table 9-1 Reservoir properties in EXOTHERM simulation

Formation	Overburden	McM* Gas Sands	McM* Water Sands	McM* Mudstone	McM* Oil Sands
Thickness (m)	300	15	10	2	50
Porosity (%)	-	34	34	10	34
Horizontal Permeability (md)	-	1100	1100	0.001	1100
Vertical Permeability (md)	-	550	550	0.001	550
Gas Saturation	-	0.9	0	0	0
Bitumen Saturation	-	0	0	0	0.85
Water Saturation	-	0.1	1.0	1.0	0.15
Initial Pressure (kPa)	-	1700	1700	1750	1800
Initial Temperature (°C)		11	11	11	11
Heat Capacity (kJ/kg. °C)		990	2267	1920	1865
Thermal Conductivity (kJ/D.m. °C)		124	295	146	173
Rock Compressibility (kPa^{-1})		2E-6	2E-6	2E-6	2E-6
	Gas	Bitumen	Water		
Density (kg/m^3)	0.67	1008	1000		
Viscosity at 10 °C (mPa.s)	0.0142	2000000	1.1		
Compressibility (kPa^{-1})		4.5E-7	5.7E-7		
Thermal Expansion Coefficient ($°C^{-1}$)		6.41E-4	4.5E-4		
Injector/Producer Length (m)	Well Spacing (m)	Wellpair Spacing (m)	Well Radius (m)	Injection Pressure (kPa)	Steam Quality (%)
700	5	100	0.1	2500	98

* McM – McMurray Formation

Table 9-2 Geomechanical properties in FLAC simulation

Formation	Overburden	McM* Gas Sands	McM* Water Sands	McM* Mudstone	McM* Oil Sands
Lithology	Mixed	Sands	Sands	Mudstone	Sands
Top Depth (m)	0	300	310	315	317
Thickness (m)	300	10	5	2	50
Bulk Density (kg/m3)	2195	2195	2195	2195	2195
Young's Modulus (MPa)	300	683	690	80	756
Poisson's Ratio	0.3	0.3	0.3	0.3	0.3
Linear Thermal Expansion Coefficient (C^{-1})	2E-5	2E-5	2E-5	2E-5	2E-5
Peak Cohesion (MPa)	-	0	0	0.1	0
Peak Friction Angle (°)	-	TBD**	TBD**	33	TBD**
Peak Dilation Angle (°)	-	TBD	TBD	10	TBD
Residual Cohesion (MPa)	-	0	0	0	0
Residual Friction Angle (°)	-	TBD**	TBD**	10	TBD**
Residual Dilation Angle (°)	-	TBD**	TBD**	0	TBD**
Vertical Stress Gradient (kPa/m)	22	22	22	22	22
Minimum Horizontal Stress Gradient (kPa/m)	22	22	22	22	22
Maximum Horizontal Stress Gradient (kPa/m)	26.4	26.4	26.4	26.4	26.4
Initial Reservoir Temperature (°C)	-	11	11	11	11

* McM – McMurray Formation

** TBD – To be determined (parameters vary as a function of stresses and are calculated based on the relationships described in Chapter 7).

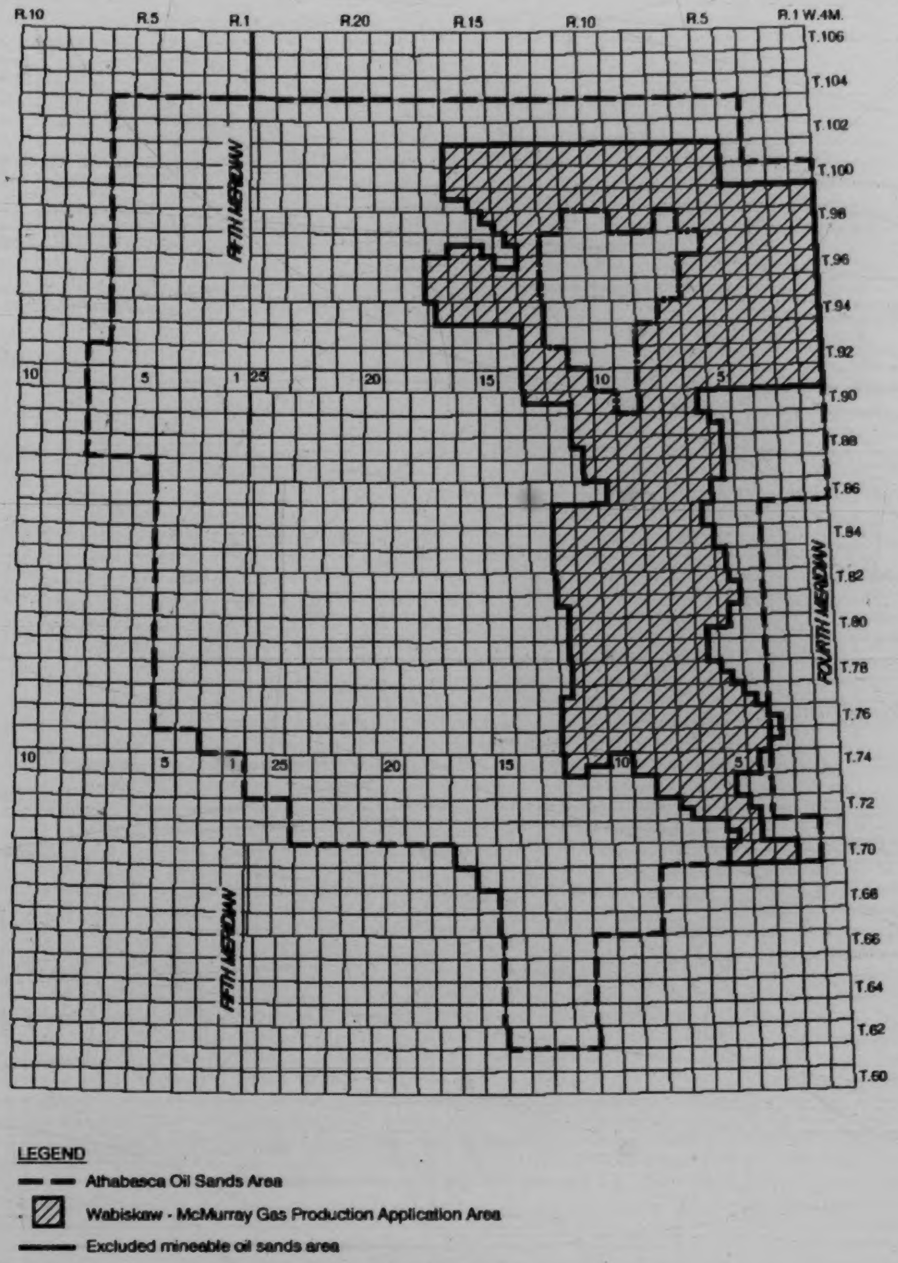
R.10
R.5
R.1
R.20
R.15
R.10
R.5
R.1 W.4M.
T.106
T.104
T.102
T.100
T.98
T.96
T.94
T.92
T.90
T.88
T.86
T.84
T.82
T.80
T.78
T.76
T.74
T.72
T.70
T.68
T.66
T.64
T.62
T.60
FIFTH MERIDIAN
FOURTH MERIDIAN
10
5
1
25
20
15
10
5
LEGEND
Athabasca Oil Sands Area
Wabiskaw - McMurray Gas Production Application Area
Excluded mineable oil sands area

Figure 9-1. Athabasca oil sands reserves and gas production area (Alberta Energy and Utilities Board, 2003b)

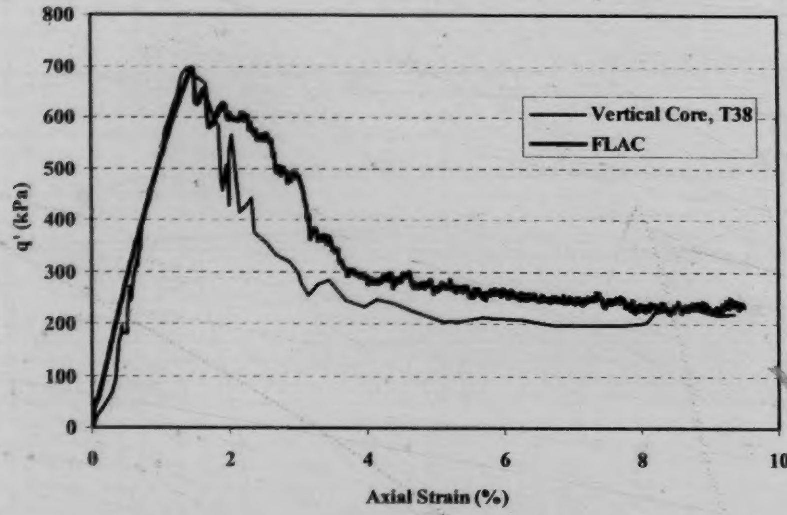

Figure 9-2. Numerical experiment match of deviatoric stress versus axial strain (experimental data from Toughidi-Baghini, 1998)

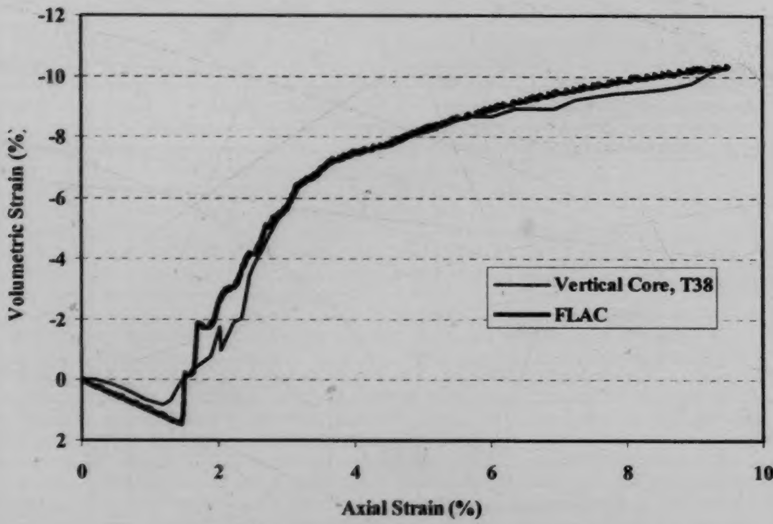

Figure 9-3. Numerical experiment match of volumetric strain versus axial strain (experimental data from Toughidi-Baghini, 1998)

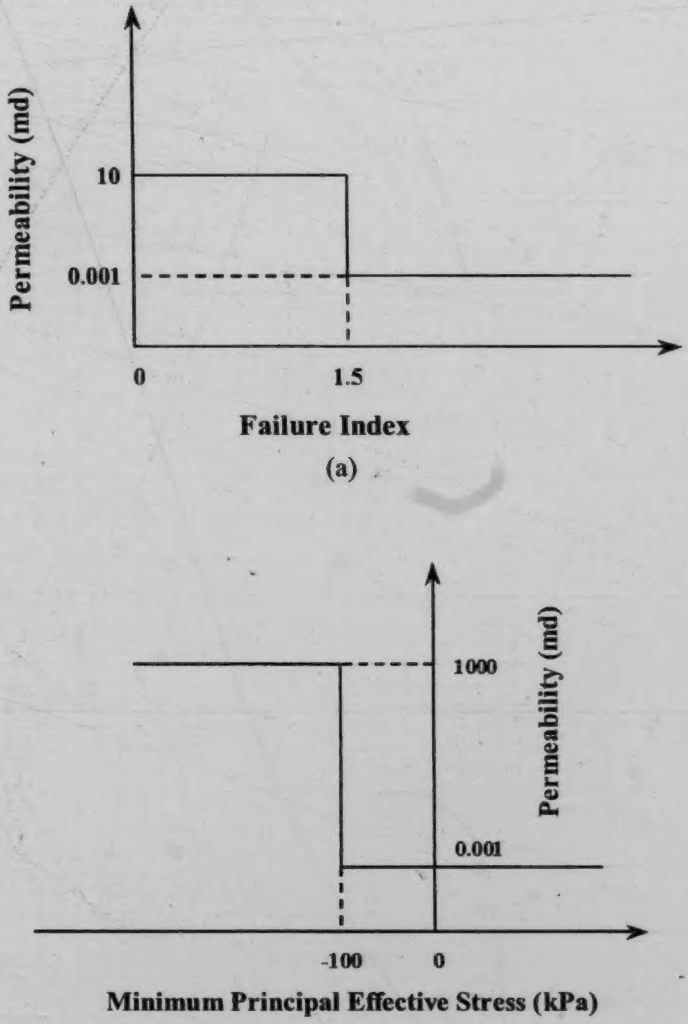

(a)

(b)

Figure 9-4.Assumed permeability improvements due to (a) shear failure and (b) tensile failure

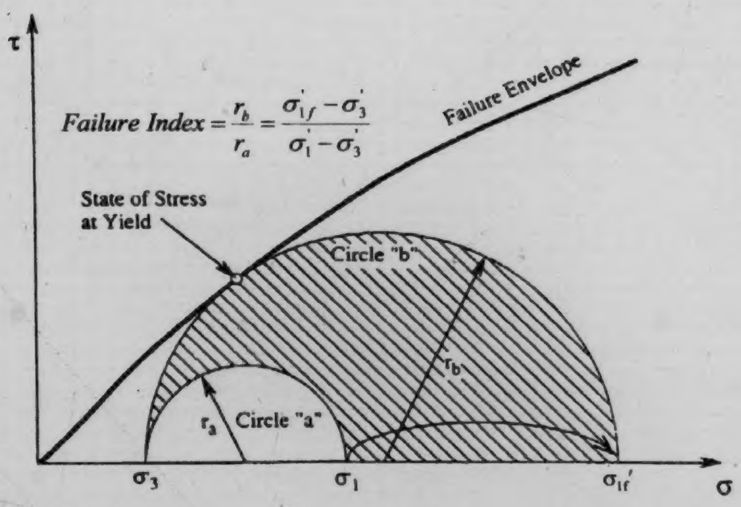
τ
Failure Envelope
$Failure\ Index = \frac{r_b}{r_a} = \frac{\sigma'_{1f} - \sigma'_3}{\sigma'_1 - \sigma'_3}$
State of Stress at Yield
Circle "b"
r_b
r_a
Circle "a"
σ_3
σ_1
σ_{1f}'
σ

Figure 9-5. Definition of failure index (modified from Chalaturnyk, 1997)

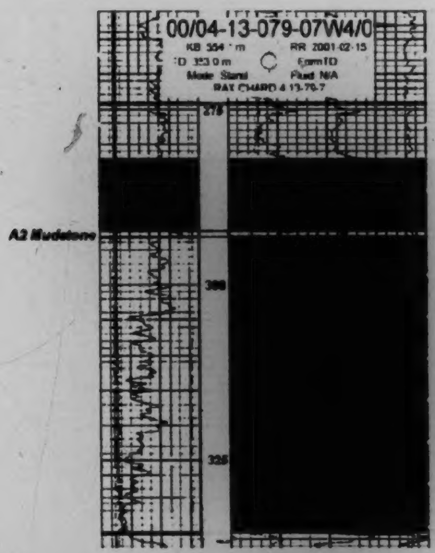

Figure 9-6.Top gas and top water overlying bitumen bearing formation with A2 mudstone unit (Alberta Energy and Utilities Board, 2003b)

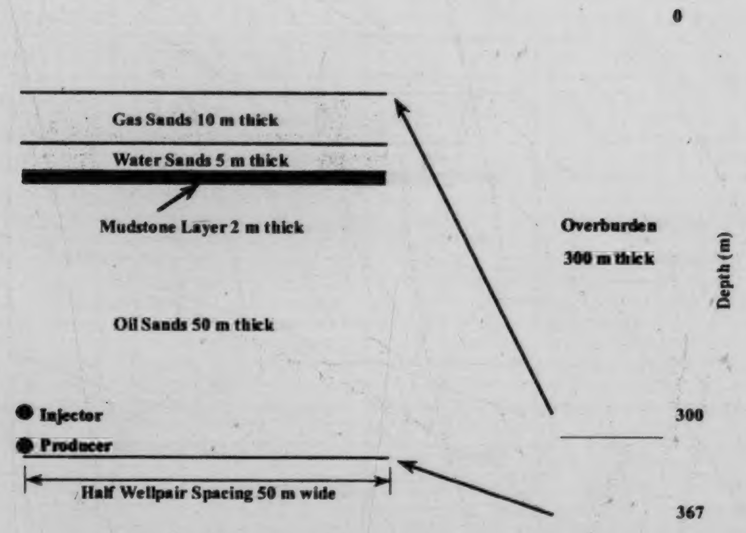
0
Gas Sands 10 m thick
Water Sands 5 m thick
Mudstone Layer 2 m thick
Overburden
300 m thick
Depth (m)
Oil Sands 50 m thick
Injector
Producer
300
Half Wellpair Spacing 50 m wide
367

Figure 9-7. Stratigraphical scheme of the reservoir model

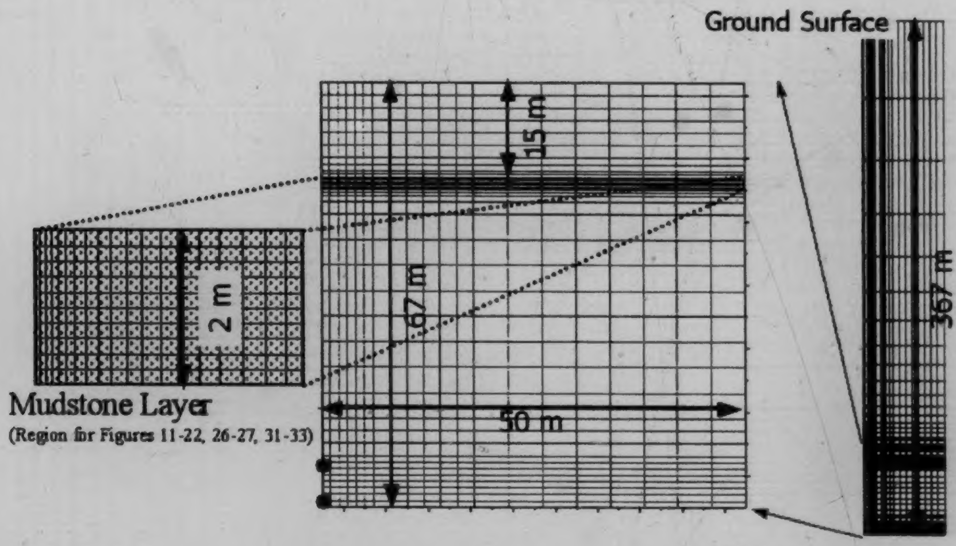
Ground Surface
15 m
2 m
67 m
367 m
50 m
Mudstone Layer
(Region for Figures 11-22, 26-27, 31-33)

Figure 9-8. Grid system used in EXOTHERM (middle) and FLAC (right)

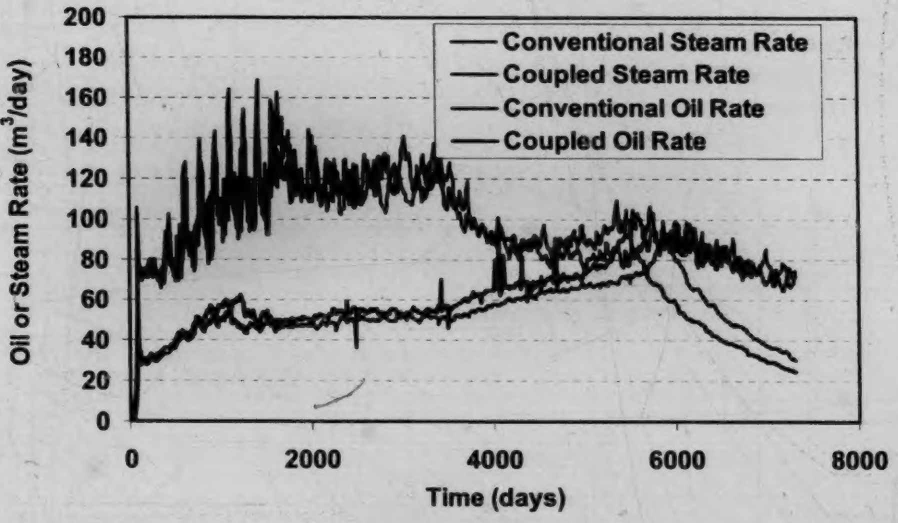

Figure 9-9. Oil rates and steam rates for conventional and coupled simulation

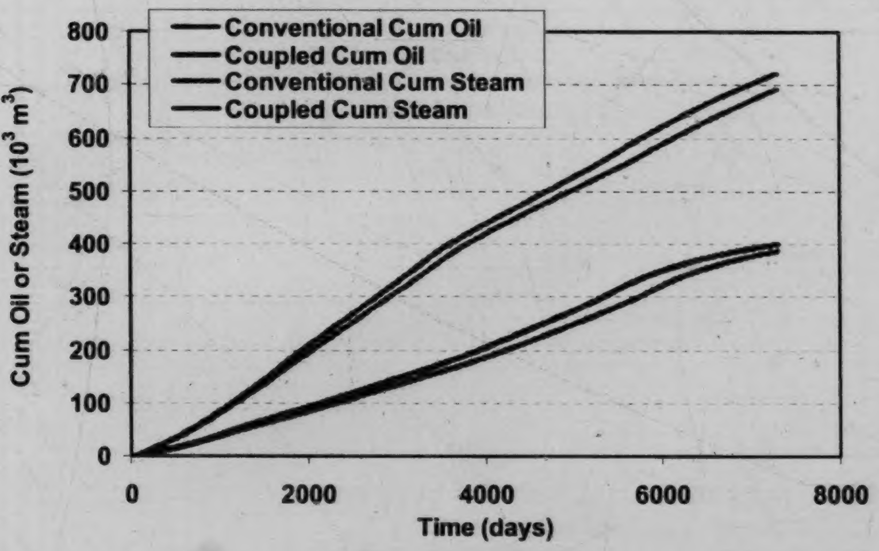

Figure 9-10. Cumulative steam injection and oil production for conventional and coupled simulation

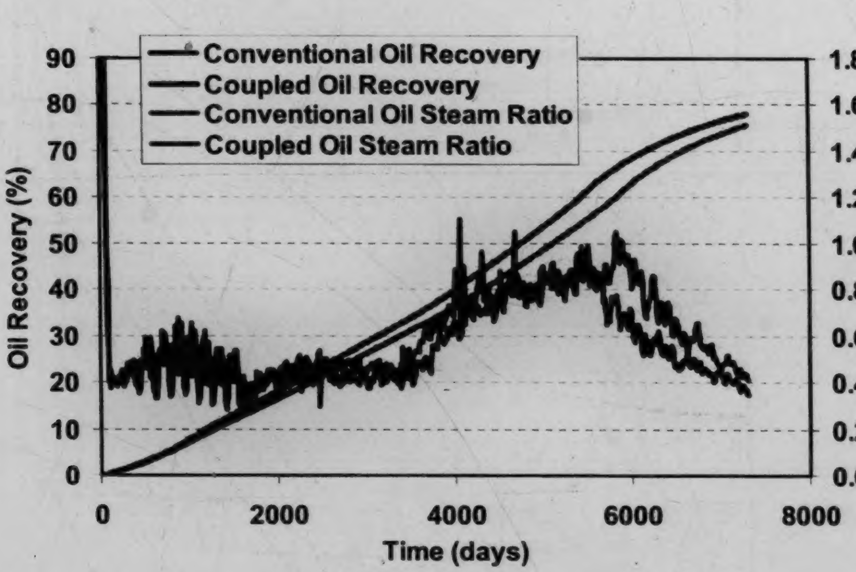

Figure 9-11. Oil recovery and OSR for conventional and coupled simulation

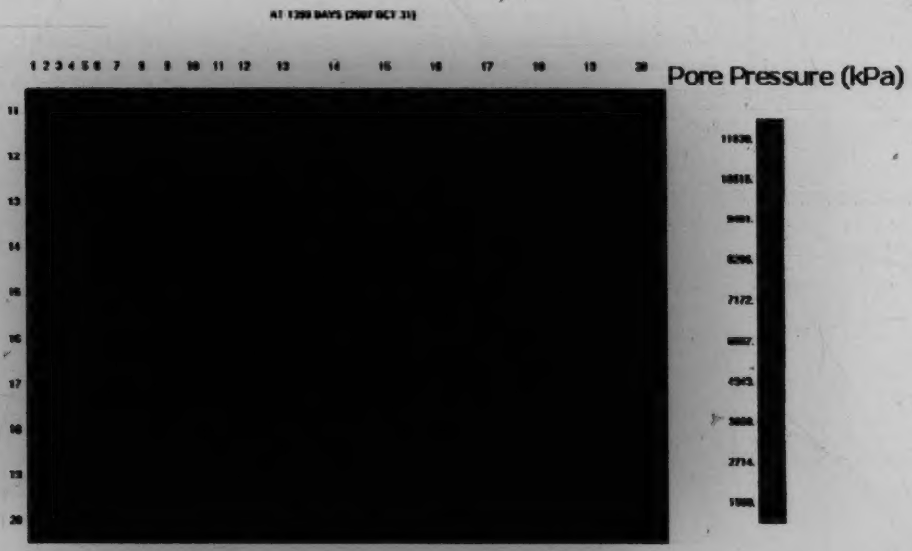

Figure 9-12. Pore pressure distribution in the mudstone layer (Initial k_MS = 0.00001 md, P_inj = 2500 kPa, time =1399 days)

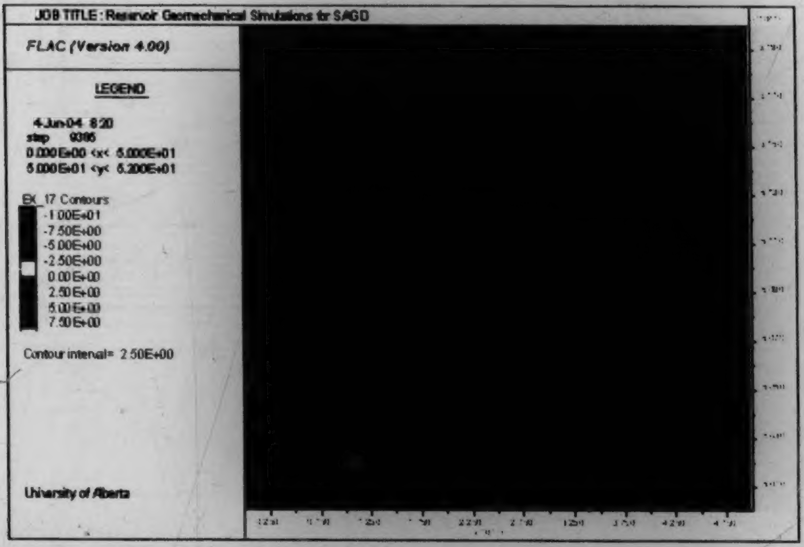

Figure 9-13. Failure index (EX_17) in the mudstone layer (Initial k_MS = 0.00001 md, P_inj = 2500 kPa, Time =1399 days)

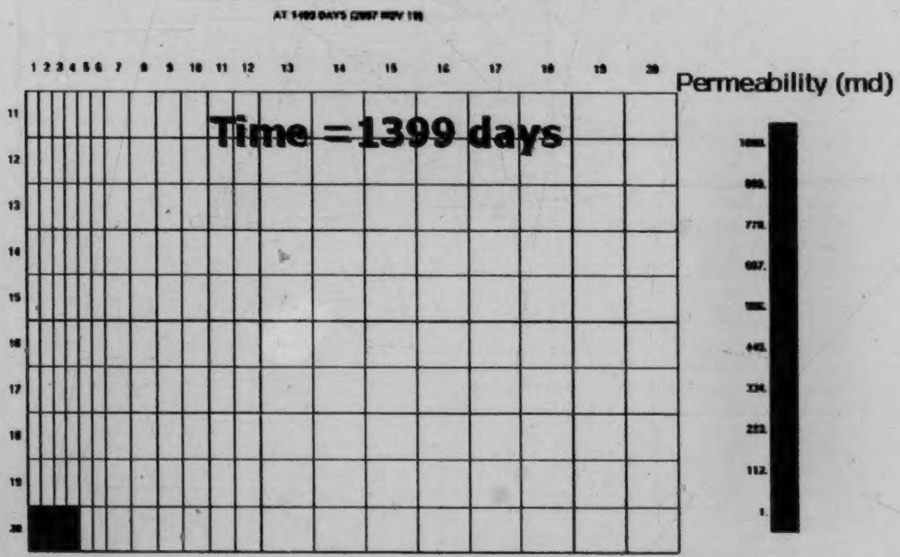

Figure 9-14. Permeability distribution in the mudstone layer (Initial k_MS = 0.00001 md, P_inj = 2500 kPa, Time =1399 days)

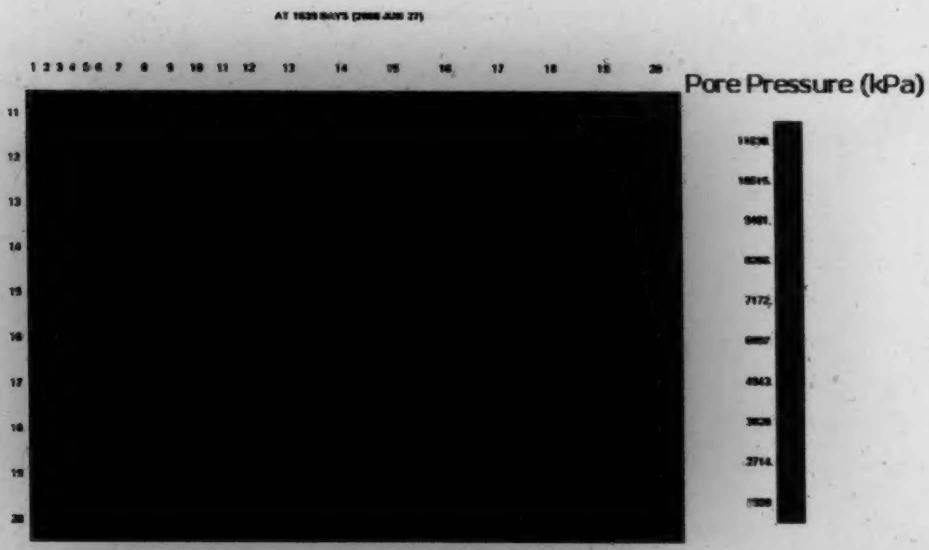

Figure 9-15. Pore pressure distribution in the mudstone (Initial k_MS = 0.00001 md, P_inj = 2500 kPa, Time = 1639 days)

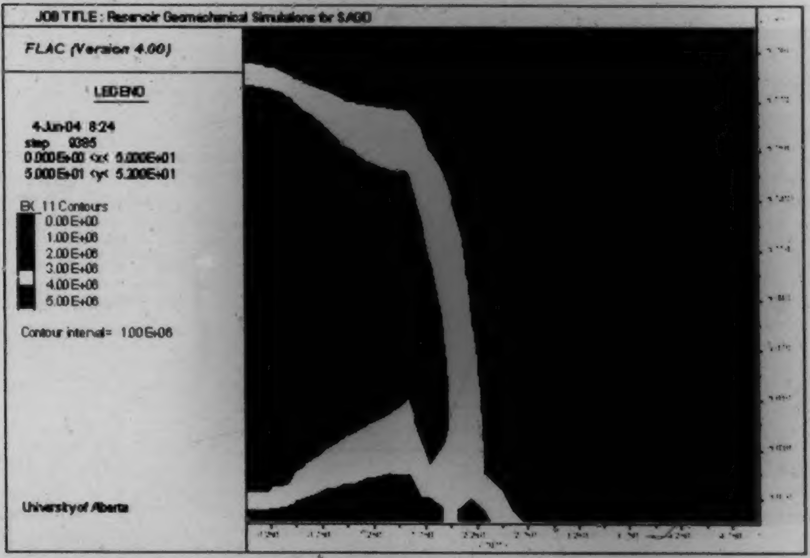

Figure 9-16. Minimum effective principal stress (EX_11, unit: Pa) in the mudstone layer (Initial k_MS = 0.00001 md, P_inj = 2500 kPa, Time = 1639 days)

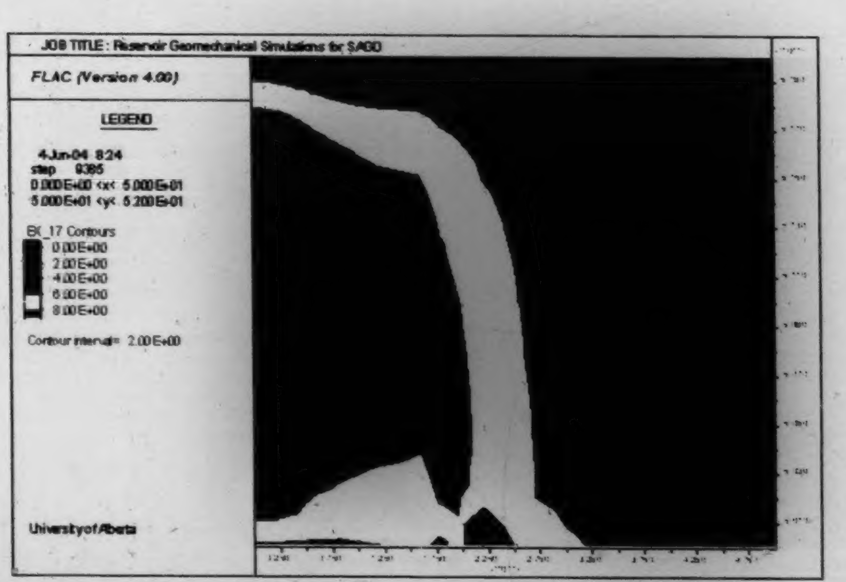

Figure 9-17. Failure index (EX_17) in the mudstone layer (Initial k_MS = 0.00001 md, P_inj = 2500 kPa, Time = 1639 days)

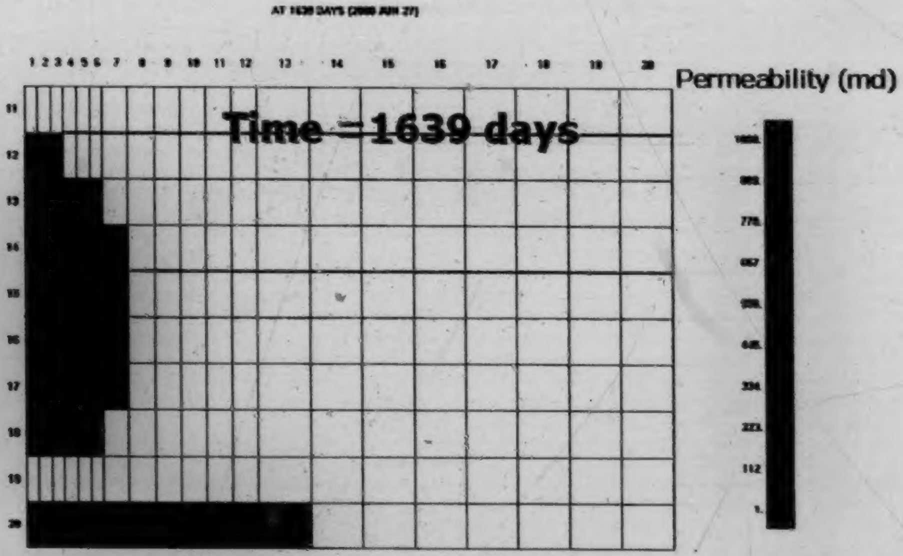

Figure 9-18. The modified permeability distribution (Initial k_MS = 0.00001 md, P_inj = 2500 kPa, Time = 1639 days)

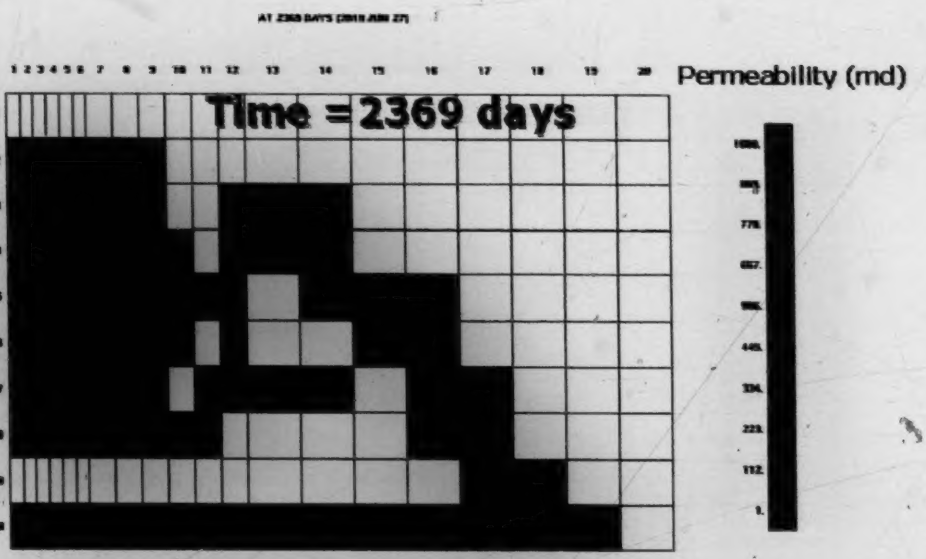

Figure 9-19. The modified permeability distribution (Initial k_MS = 0.00001 md, P_inj = 2500 kPa, Time = 2369 days)

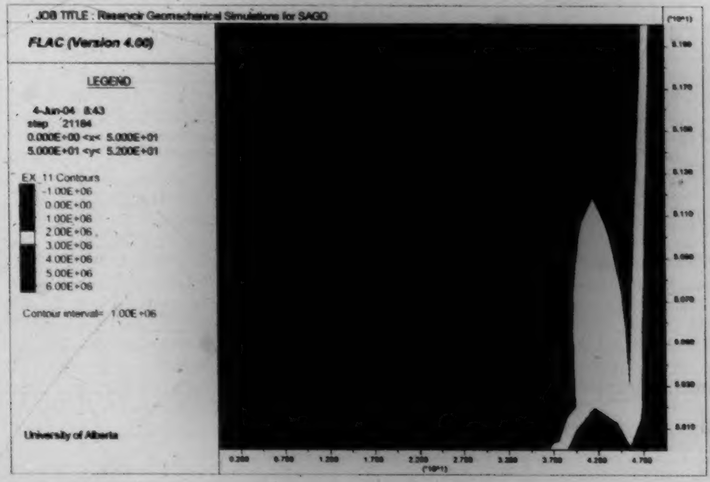

Figure 9-20. Failure index (EX_17) in the mudstone layer (Initial k_MS = 0.00001 md, P_inj = 2500 kPa, Time = 2369 days)

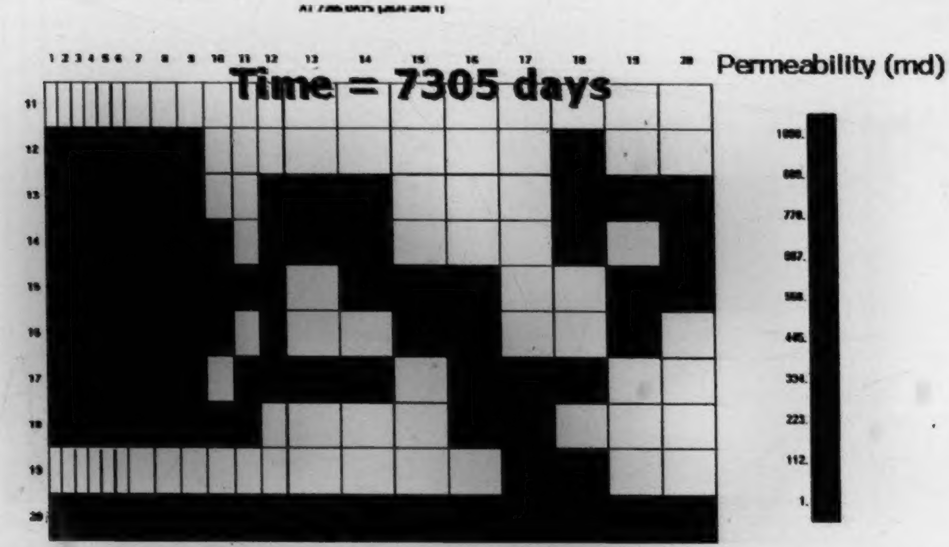

Figure 9-21. The modified permeability distribution (Initial k_MS = 0.00001 md, P_inj = 2500 kPa, Time = 7305 days)

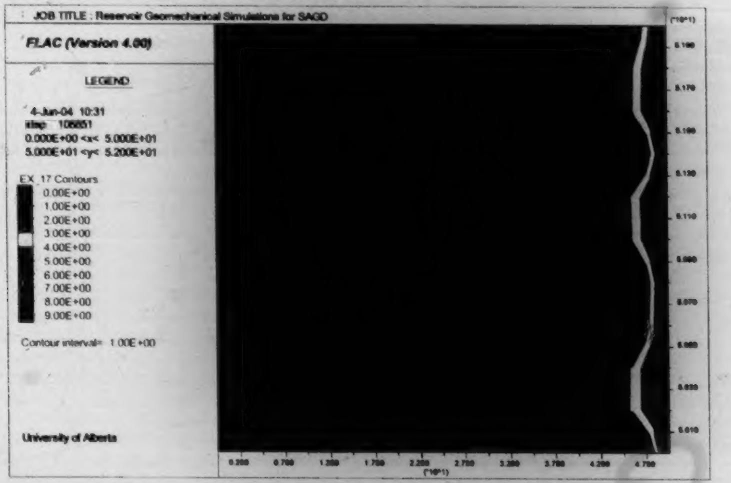

Figure 9-22. Failure index (EX_17) in the mudstone layer (Initial k_MS = 0.00001 md, P_inj = 2500 kPa, Time = 7305 days)

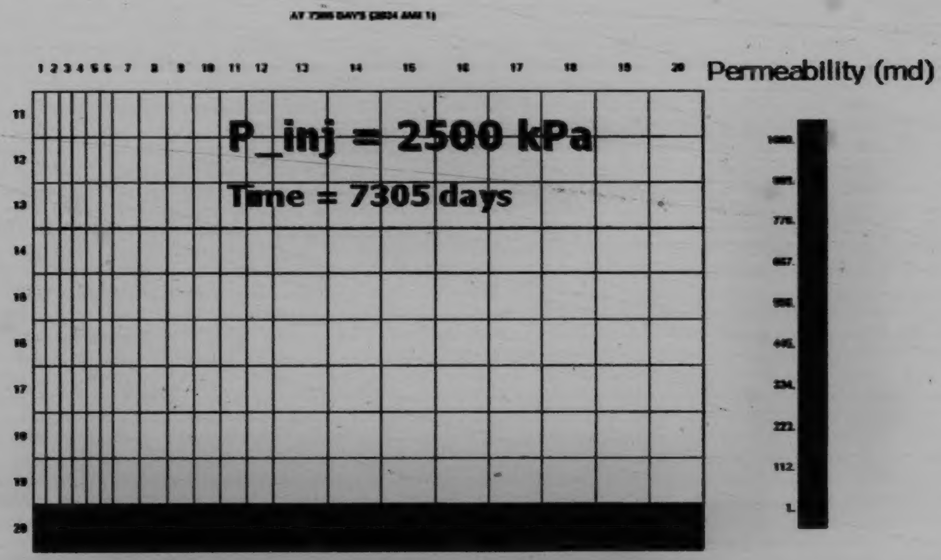
Permeability (md)
P_inj = 2500 kPa
Time = 7305 days

Figure 9-23. The modified permeability in the mudstone layer (Initial k_MS = 0.0001 md, P_inj = 2500 kPa, Time = 7305 days)

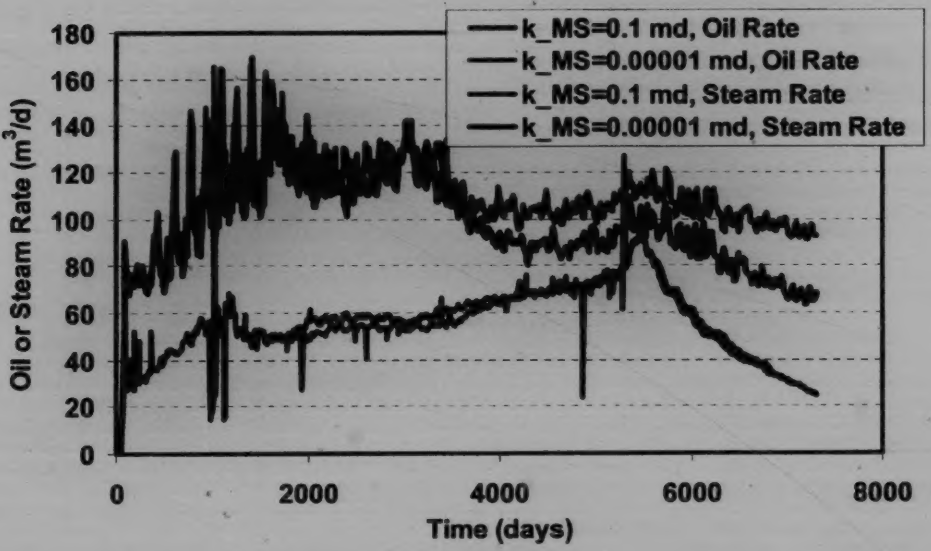

Figure 9-24. Oil and steam rate comparison for mudstone permeability of 0.1 md and 0.00001 md

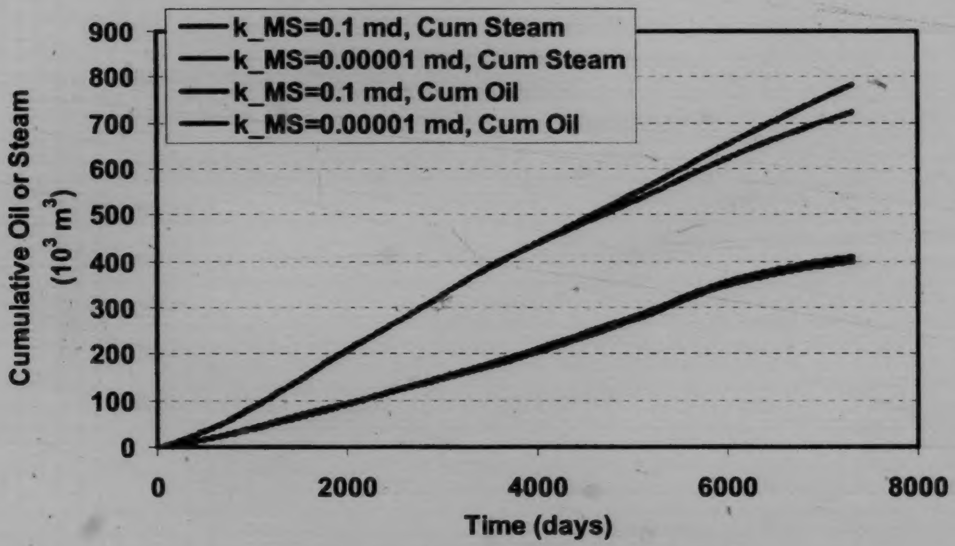

Figure 9-25. Cumulative oil production and steam injection for mudstone permeability of 0.1 md and 0.00001 md

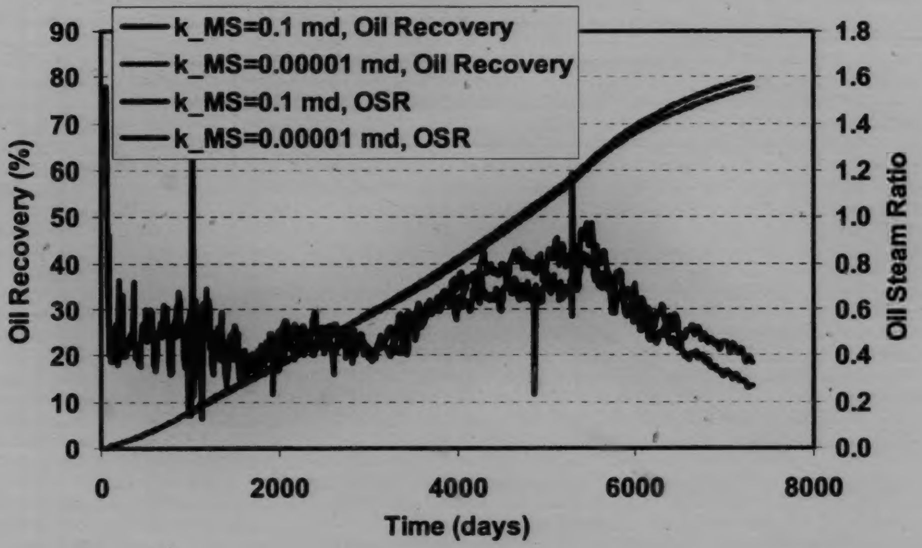

Figure 9-26. Oil recovery and OSR for mudstone permeability of 0.1 md and 0.00001 md

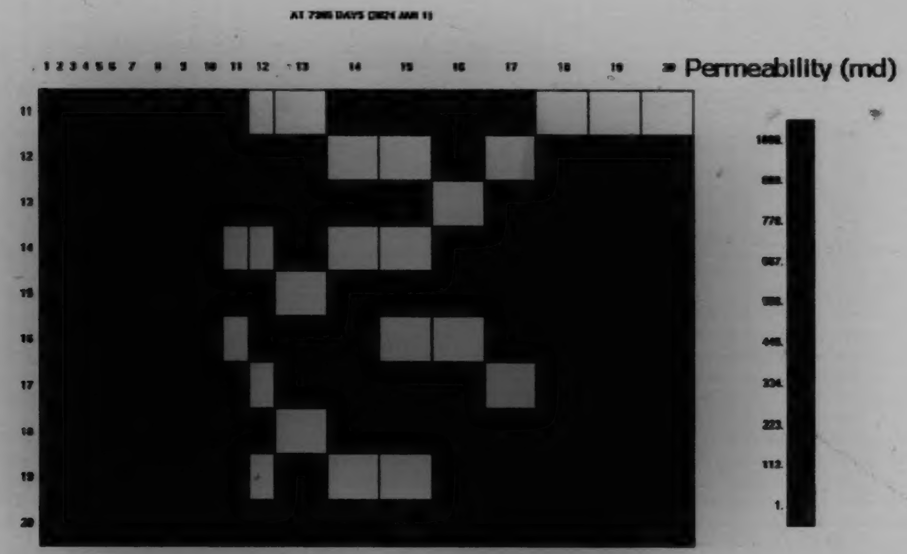

Figure 9-27. The modified permeability distribution (Initial k_MS = 0.000001 md, P_inj = 2500 kPa, and Time = 7305 days)

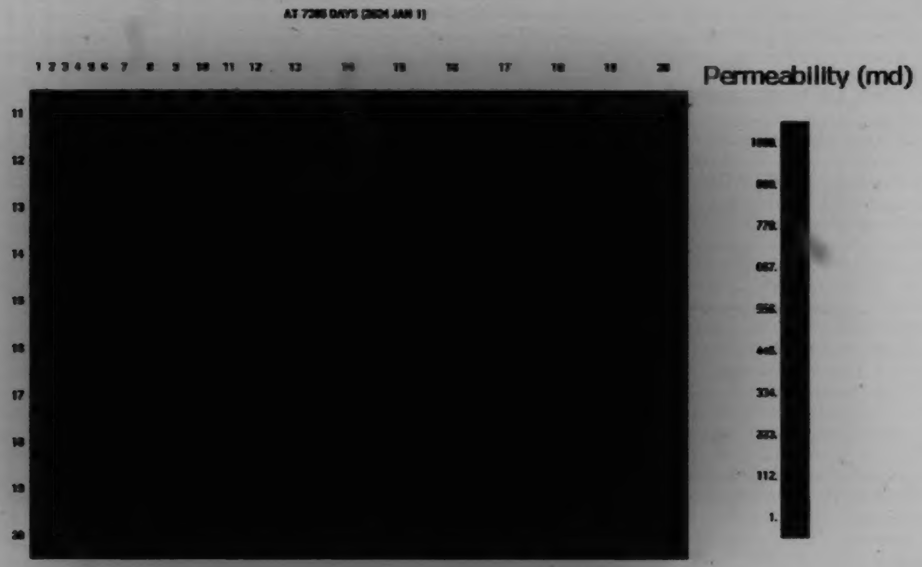

Figure 9-28. The modified permeability distribution (Initial k_MS = 0 md, P_inj = 2500 kPa, and Time = 7305 days)

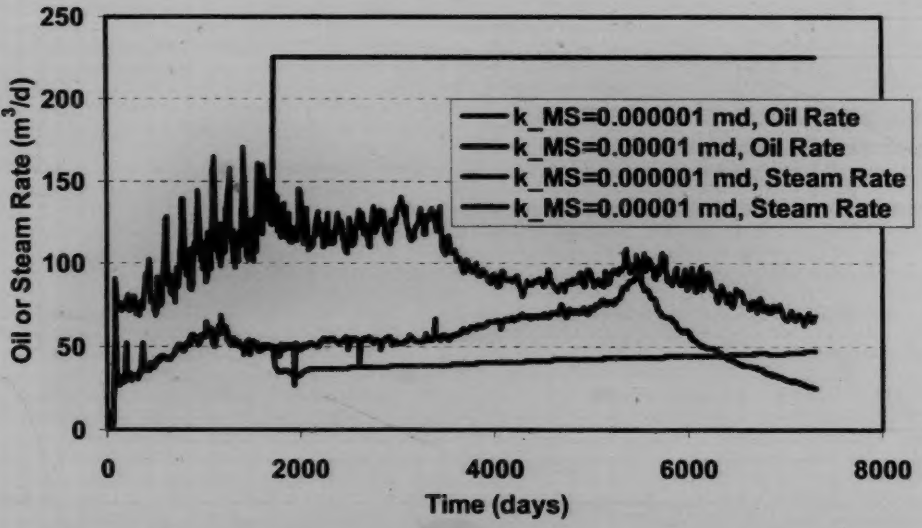

Figure 9-29. Oil rate and steam rate for mudstone permeability of 0.00001 md and 0.000001 md (Mudstone failure occurs at time 1719 days for k_MS = 0.000001 md)

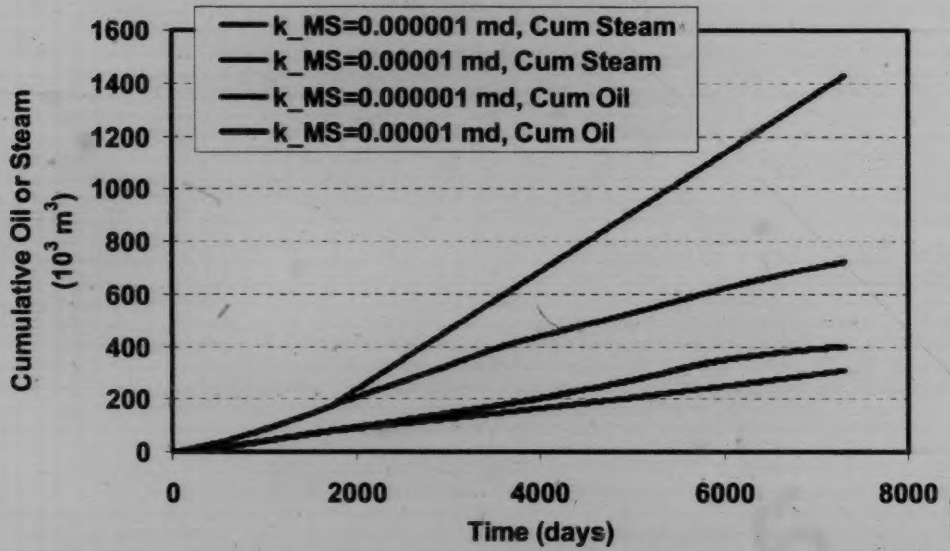

Figure 9-30. Cumulative oil production and steam injection for mudstone permeability of 0.00001 md and 0.000001 md (Mudstone failure occurs at time 1719 days for k_MS = 0.000001 md)

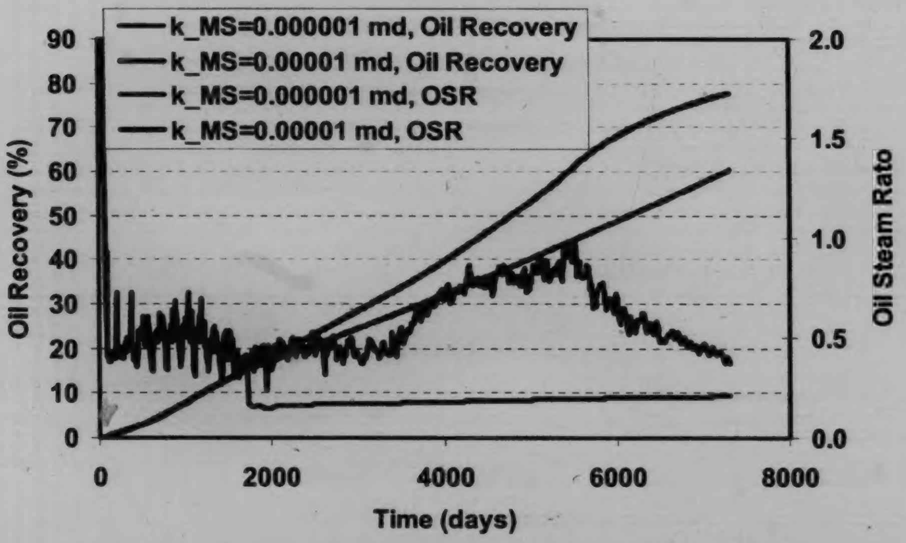

Figure 9-31. Oil recovery and OSR for mudstone permeability of 0.00001 md and 0.000001 md (Mudstone failure occurs at time 1719 days for k_MS = 0.000001 md)

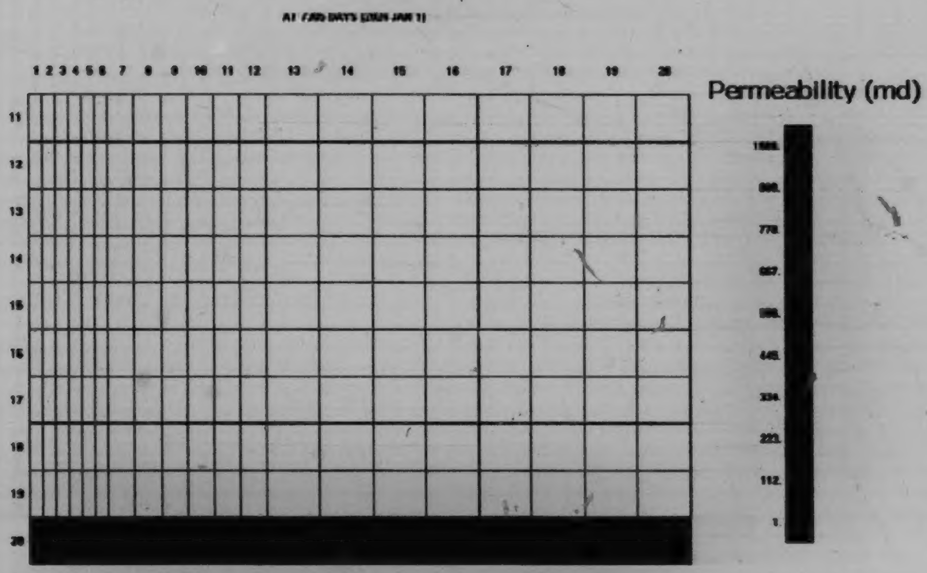
1 2 3 4 5 6 7 8 9 10 11 12 13 14 15 16 17 18 19 20
11
12
13
14
15
16
17
18
19
20
Permeability (md)
1000.
889.
778.
667.
556.
445.
334.
223.
112.
1.

Figure 9-32. The modified permeability distribution (Initial k_MS = 0.001 md, P_inj = 5000 kPa, and Time = 7305 days)

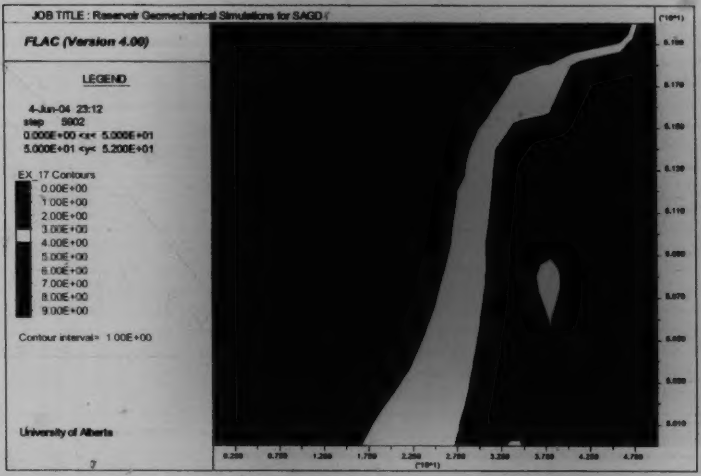

Figure 9-33. Failure index (EX_17) distribution (Initial k_MS = 0.0001 md, P_inj = 5000 kPa, and Time = 4519 days)

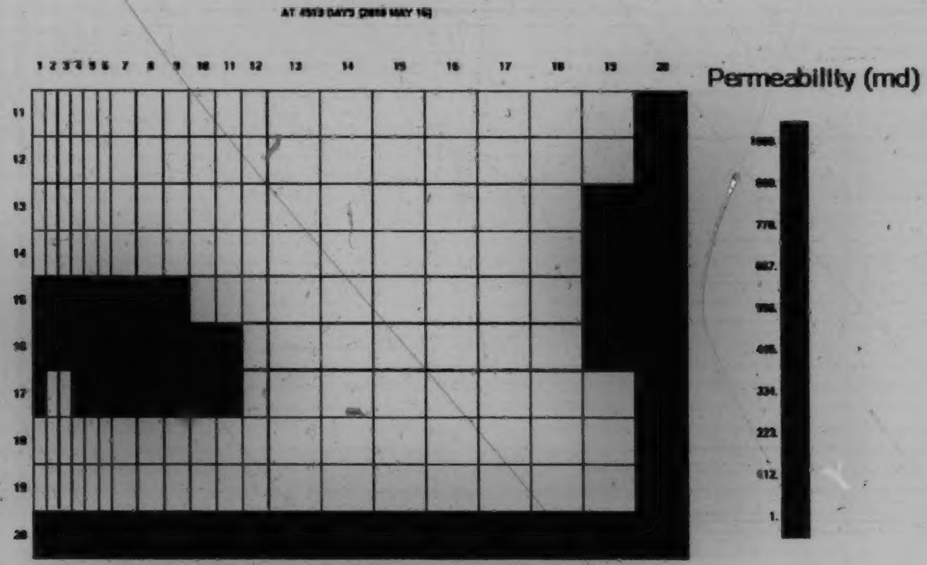

Figure 9-34. The modified permeability distribution (Initial k_MS = 0.0001 md, P_inj = 5000 kPa, and Time = 4519 days)

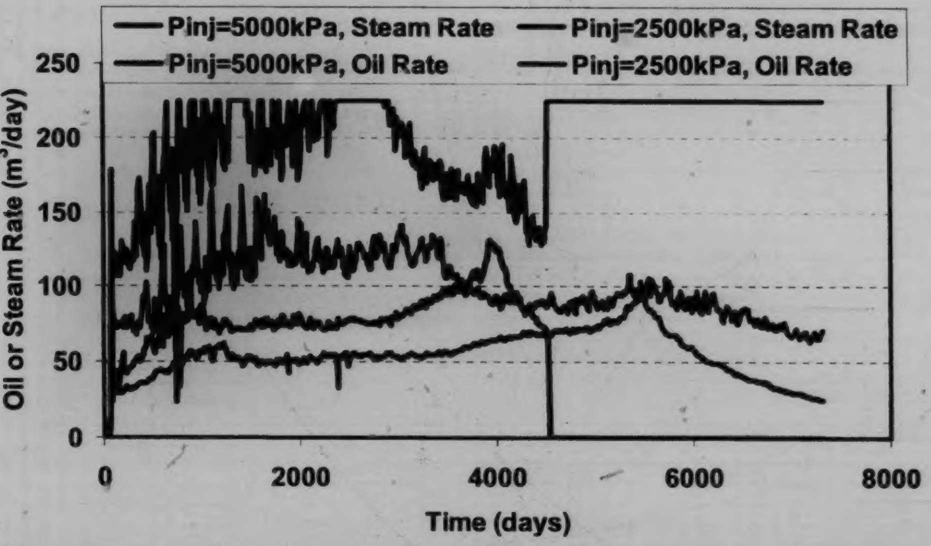

Figure 9-35. Oil rate and steam rate for injection pressures of 2500 kPa and 5000 kPa (Initial k_MS = 0.0001 md, mudstone failure occurs at time 4519 days for P_inj = 5000 days)

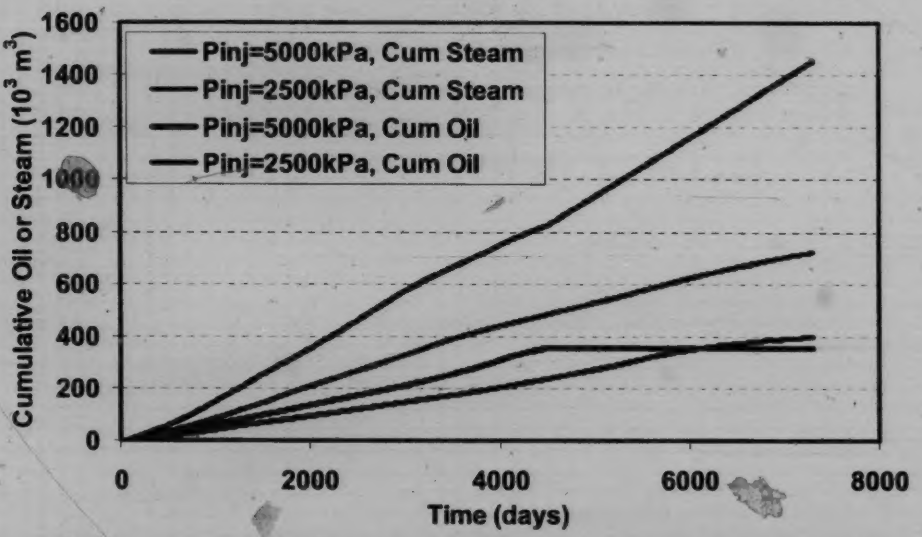

Figure 9-36. Cumulative oil production and steam injection for injection pressures of 2500 kPa and 5000 kPa (Initial k_MS = 0.0001 md, mudstone failure occurs at time 4519 days for P_inj = 5000 days)

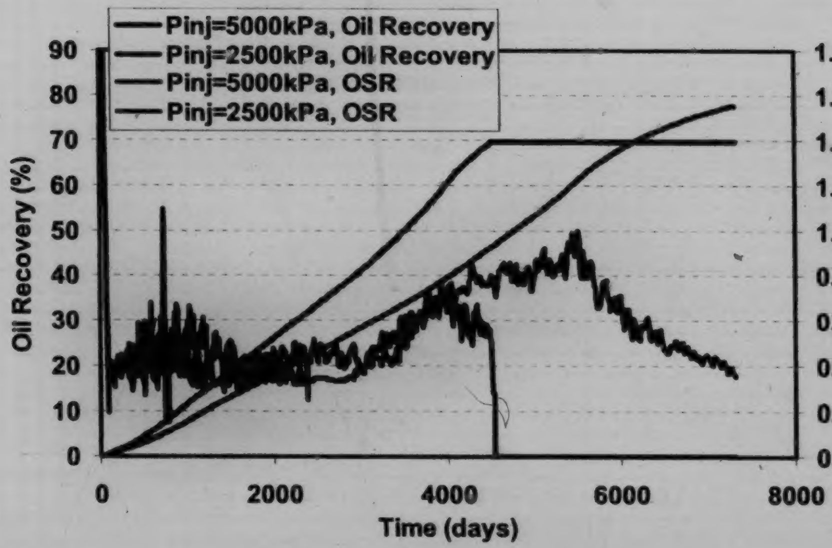

Figure 9-37. Oil recovery and OSR for injection pressures of 2500 kPa and 5000 kPa (Initial k_MS = 0.0001 md, mudstone failure occurs at time 4519 days for P_inj = 5000 days)

CHAPTER 10 CONCLUSIONS AND RECOMMENDATIONS

10.1 Summary

In this research program, the decoupled reservoir geomechanical simulation results showed that the SAGD process does induce reservoir parameter variations, particularly the absolute permeability of the oil sands material. Therefore, it is of great significance to conduct the coupled reservoir geomechanical simulation instead of the conventional reservoir simulation to provide realistic forecasts for commercial SAGD projects. In this study, the issues with the coupled reservoir geomechanical simulations of the SAGD process, including the geomechanical zones, reservoir processes and parameters affected by geomechanics, were investigated and clarified. The methodology of sequentially coupled reservoir geomechanical simulation technique was developed and tested successfully. In addition, because the major geomechanical behaviors during the SAGD process involve the isotropic unloading process and the shearing process, the effects of these two geomechanical behaviors on oil sands permeability were investigated separately based on laboratory testing results. A representative geomechanical model of the oil sands material was obtained based on 26 numerical experiments, which match laboratory results under various testing conditions. Finally, the methodology of the coupled reservoir geomechanical simulation technique was verified with the UTF Phase A project and also applied to the SAGD operation with the gas-over-bitumen geometry. The systematic and comprehensive academic study associated with both reservoir engineering and reservoir geomechanics has successfully quantified the effect of geomechanical behavior on the SAGD process.

10.2 Conclusions

10.2.1 Decoupled Reservoir Geomechanical Simulations

- The evolution of zones of shear induced volume changes is sensitive to the initial stress state and injection pressure.

- The magnitude of shear stress developed at the top of the reservoir depends on the relative size of the steam chamber to the reservoir dimensions.

- The interrelationship between pore pressure (reduction in effective stress) and temperature (increase in total stress) is complex.

- For injection pressures close to the initial mean effective confining stress within the reservoir, significant zones of shear failure can occur, which correspond to regions of enhanced absolute permeability.

- Decoupled reservoir geomechanical simulations do induce variations of reservoir parameters including pore volume and absolute permeability

10.2.2 Reservoir Geomechanical Zones and Reservoir Processes/Parameters Affected by Geomechanics

- The complex interaction of pore pressure and temperature throughout the reservoir result in varying degrees of reservoir geomechanical interactions. The primary geomechanical influence on SAGD recovery is associated with the volume change of the sand matrix in response to effective stress changes induced by steam injection pressures and temperatures.

- In the SAGD process, the reservoir can be divided into three geomechanical zones, i.e., drained zone, partially drained zone, and undrained zone, based on certain oil viscosity ranges.

- Owing to thermal stress and pore pressure changes in response to SAGD, isotropic unloading and shear dilation occur with varying degrees in different geomechanical zones. Gas evolution mainly takes place in the undrained zone as a result of dilative shear. With the expansion of the steam chamber, the three geomechanical zones propagate simultaneously, and the geomechanical phenomena occurring previously in an undrained zone will eventually play a role when this zone becomes drained.

- Reservoir parameters and processes, such as compressibility, porosity (pore volume), absolute permeability, relative permeability, saturations, capillary pressure, enthalpy transmissibility, gas evolution, and thermal expansion effects, are all affected by bulk volume changes. Variations of these parameters due to geomechanical effect are clearly shown based on related test results, calculation, and simulation studies.

10.2.3 Methodology of Sequentially Coupled Reservoir Geomechanical Simulation

- The methodology of sequentially coupled reservoir geomechanical simulation is developed, which is based on the reservoir simulator, EXOTHERM, and the geomechanical simulator, FLAC.

- The simulation procedure is controlled by Windows automation software, AutoMate. It can smoothly and successfully link the two simulators. The coupling modules were written with Visual Basic. This coupled simulation procedure is flexible and easy to use.

- The sequentially coupled reservoir geomechanical simulation procedure was tested by comparing the simulation results with that of the conventional reservoir simulation.

- The application cases show that the geomechanical behavior occurring in the SAGD operations does affect SAGD production performances. The geomechanical effects on the SAGD production are dependent on the steam injection pressure. Higher injection pressure induces significant changes of reservoir porosity and permeability.

- For relatively lower initial reservoir permeability, the difference is more obvious between the coupled reservoir geomechanical simulation and the conventional reservoir simulation.

10.2.4 Permeability Variations due to Reservoir Geomechanical Behaviors in SAGD Operations

- Isotropic stress and shear stress changes are two major geomechanical processes during the SAGD operations. The former occurs within the high pore pressure front and the latter predominantly around the interface between the drained zone and the partially drained zone.

- The shearing process induces more significant improvements on absolute permeability and effective permeability to water compared to the isotropic unloading process. Particularly, after shear failure, oil sands permeability increases dramatically.

- Tortike's equation is applicable for the isotropic unloading process if the initial absolute permeability is greater than 1 μm^2. Otherwise, it may induce significant errors. Tortike's equation is not appropriate to calculate the modified absolute permeability due to the shearing process.

- The absolute permeability of vertical specimens increases more significantly than that of the horizontal specimens for the same volumetric strain. This may result from the significant decrease of tortuosity for vertical specimens.

- Geomechanics induced absolute permeability and effective permeability to water can be determined based on Equation (6-7) with different C_{n1} values for geomechanical cases.

$$Ln \frac{k}{k_0} = C_{n_1}\ \varepsilon_v \tag{6-7}$$

- Water relative permeability increases due to the isotropic unloading and shearing processes. The shearing process produces more significant improvement, particularly after shear failure.

10.2.5 Geomechanical Model of Oil Sands

- A great number of lab testing results from Oldakowski (1994), Samieh and Wong (1997), and Touhidi-Baghini (1998) show that oil sands material reflects a strain softening stress strain behavior.

- Totally 26 numerical experiments were conducted, which matched the laboratory tests with the same testing conditions as in the laboratory, including the stress paths.

- Based on these numerical experiments, a comprehensive geomechanical model, the strain softening Mohr-Coulomb model, of oil sands material was established. The proposed strain softening model parameters, such as the modulus of elasticity, peak and post-peak friction angles, and peak and post peak dilation angles, can be applied in the coupled reservoir geomechanical simulations of the SAGD process. These parameters are expressed as the following equations

$$E = 950 P_a (\sigma_3' / P_a)^{0.5} \quad (7\text{-}2)$$

$$\phi_p' = 55 - 14.93 \log(\sigma_3' / P_a) \quad (7\text{-}3)$$

$$\psi_p' = 25.8 - 12.05 \log(\sigma_3' / P_a) \quad (7\text{-}4)$$

$$\phi_r' = 55.9 - 2.03 \gamma_p \quad (7\text{-}5)$$

$$\psi_r' = 27.3 - 1.5 \gamma_p \quad (7\text{-}6)$$

- It should be noted that this geomechanical model of oil sands was obtained based on the lab tests with shallow oil sands samples and lower confining stress conditions. Application of the model should take this limitation into consideration.

10.2.6 Verification of the Coupled Reservoir Geomechanical Simulation Methodology with UTF Phase A Project

- The coupled reservoir geomechanical simulation technique was applied to history match the field production performance of the UTF Phase A Project.

- Reservoir pressure and temperature distributions based on the coupled simulation are similar to those obtained from the field measurements.

- The vertical and horizontal strains in the geotechnical cross section were not fully matched. This difference may be induced by complex reservoir properties and also the limitation of the 2D simulation. Within the geotechnical cross-section, the steam chamber development based on the coupled reservoir geomechanical simulation is different from that in the field.

- The horizontal displacements obtained from the coupled simulation are larger than the field measurements. In addition to the different steam chamber development modes, the effects of thermal expansion coefficient and the modulus of elasticity were studied. The thermal expansion coefficient affects the simulation results more significantly than the modulus of elasticity.

- The simulated surface heave and vertical displacement at the reservoir top based on the coupled simulation are a little larger than the field measurements.

10.2.7 Application of the Coupled Reservoir Geomechanical Simulation Methodology in SAGD with Gas over Bitumen Geometry

- Mudstone permeability plays a very important role in the SAGD operations based on the gas-over-bitumen geometries described in this study. If the mudstone permeability is too large, the injected steam will flow into the top thief water zone without any difficulty. However, if the mudstone permeability is too low, shear failure or even tensile failure during the SAGD process may occur and damage the integrity of the mudstone layer. This geomechanical behavior can aggravate the SAGD production performance. Therefore, an ideal gas-over-bitumen SAGD geometry with a mudstone layer between the bitumen and gas pool should have a mudstone permeability that not only prevents significant steam loss to the top thief water zone but also avoids large pore pressure generation in the mudstone layer.

- Shear or tensile failure is possible under high steam injection pressures. For the same mudstone permeability, low steam injection pressure may not induce failure inside the mudstone layer, but high steam injection pressure may cause failure and worsen the SAGD production performance. Optimization of the steam injection pressure for a SAGD project should account for this complex behavior of the mudstone.

- Conventional reservoir simulations cannot characterize the tensile failure and shear failure behaviour during the SAGD process. However, coupled reservoir geomechanical simulation techniques can provide valuable and in certain cases, critical input to the optimization and design of a SAGD project.

10.3 Recommendations

- In general, oil sands reservoirs are heterogeneous and anisotropic. The effect of reservoir heterogeneity and anisotropy on the three reservoir geomechanical zones, drained, partially drained, and undrained zones, needs to be studied, which clearly define the geomechanical behaviors occurring inside the reservoirs with SAGD operations.

- When designing a commercial SAGD project, the coupled reservoir geomechanical simulation technique is more appropriate for the prediction of the SAGD production performance.

- It is of great importance to develop the 3D reservoir geomechanical simulation methodology when the pressure drop along the wellbore is significant during the SAGD process.

- The variation of absolute permeability due to isotropic unloading and shearing at higher temperatures needs to be studied. Moreover, the impact of temperature on effective permeability to water is also an issue of further research.

- The variation of relative permeability to oil due to the isotropic unloading and shearing needs to be investigated as a function of temperature.

- In situ permeability of mudstone layer is critical for a gas-over-bitumen SAGD project. It is of great significance to measure this value. In addition, mudstone permeability variation due to shear failure and tensile failure based on certain operation conditions is also an important issue and lab testing related to this issue is recommended.

- The investigation of in situ stress distribution is required before conducting the coupled reservoir geomechanical simulations. Permeability variations for both reservoir and mudstone layer during the SAGD process are dependent upon the in situ stress conditions.

REFERENCE

Adhikary, D.P., 1991. Laboratory Investigation of Effects of Stress Changes on Hydraulic Conductivity of Reconstituted Oil Sands. M.Eng. Report, Department of Civil Engineering, University of Alberta, 99p.

Agar, J.R., 1984. Geotechnical Behavior of Oil Sands at Elevated Temperatures and Pressures. Ph.D. dissertation, Department of Civil Engineering, University of Alberta, 906p.

Alberta Energy and Utilities Board, 2006. Statistical Series 2006-44 Active Oil Sands Schemes, Quarterly Statistics, March.

Alberta Energy and Utilities Board, 2003a. General Bulletin GB 2003-28, Bitumen Conservation Requirements Athabasca Wabiskaw-McMurray. 34p

Alberta Energy and Utilities Board, 2003b. Report-A, Athabasca Wabiskaw-McMurray Regional Geological Study. 195p.

Alberta Energy and Utilities Board, 2002. Statistical Series 2002-98, Alberta's Reserves 2001 and Supply/Demand Outlook 2002-2011, 130p.

AOSTRA, 1990. AOSTRA: A 15-Year Portfolio of Achievement. Alberta Oil Sands Technology and Research Authority, 174p.

Alberta Energy and Utilities Board, 2000. Gulf Canada Resources Limited, Request for the Shut-In of Associated Gas Surmont Area. 160p.

Bachu, S. and Haug K., 2002. Effects of Gas Production on Pressure in the Upper McMurray Water Sands Overlying Bitumen Reservoirs in the Athabasca Area of Alberta. CIPC 2002-039, Petroleum Society's Canadian International Petroleum Conference, Calgary, Alberta, Canada, June 11 – 13, 16p.

Beattie, C.I., Boberg, T.C., and McNab, G.S., 1991. Reservoir Simulation of Cyclic Steam Stimulation in the Cold Lake Oil Sands. SPE 18752, SPE Reservoir Engineering, Vol. 6, No.2, pp. 200-206.

Biot, M.A., 1941. General Theory of Three-Dimensional Consolidation. Journal of Applied Physics, Vol. 12, pp. 144-164.

Borst, R., Methods for Calculating Shale Permeability. unsolicited SPE 11768.

Butler, R.M., Jiang, Q., and Yee, C.-T., 2001. Steam and Gas Push (SAGP) –4: Recent Theoretical Developments and Laboratory Results Using Layered Models. Journal of Canadian Petroleum Technology, Vol. 40, No. 1, pp. 54-61.

Butler, R.M., 2001. Some Recent Developments in SAGD. Journal of Canadian Petroleum Technology, Vol. 40, No. 1, pp. 18-22.

Butler, R.M., Jiang, Q., and Yee, C.-T., 2000. Steam and Gas Push (SAGP) –3; Recent Theoretical Developments and Laboratory Results. Journal of Canadian Petroleum Technology, Vol. 39, No. 8, pp. 51-60.

Butler, R.M., 1999. The Steam and Gas Push (SAGP). Journal of Canadian Petroleum Technology, Vol. 38, No. 3, pp. 54-61.

Butler, R.M., 1997. Thermal Recovery of Oil and Bitumen. Calgary, Alberta, Canada, 528p.

Butler, R.M., 1994. Steam Assisted Gravity Drainage: Concept, Development, Performance and Future. Journal of Canadian Petroleum Technology, Vol.33, No.2, pp. 44-50.

Butler, R.M., and Mokrys, I.J., 1991. A New Process (VAPEX) for Recovering Heavy Oils Using Hot Water and Hydrocarbon Vapor. Journal of Canadian Petroleum Technology, Vol.30, No.1, pp 97-106.

Butler, R.M., 1987. Rise of Interfering Steam Chambers. Journal of Canadian Petroleum Technology, Vol. 26, No. 3, pp. 70-75.

Butler, R.M., 1986. The Expansion of Tar Sands During Thermal Recovery. Journal of Canadian Petroleum Technology, September-October, pp. 51-56.

Butler, R.M., McNab, G.S., and Lo, H.Y., 1981. Theoretical Studies on the Gravity Drainage of Heavy Oil during In-Situ Steam Teating. Canadian Journal of Chemical Engineering, Vol. 59, August, pp. 455-460.

Butler, R.M. and Stephens, D.J., 1981. The Gravity Drainage of Steam Heated Heavy Oil to Parallel Horizontal Wells. Journal of Canadian Petroleum Technology, April-June, pp.90-96.

Butler, R.M., Method for Continuously Producing Viscous Hydrocarbons by Gravity Drainage while Injecting Heated Fluids. UK Pat. Appl. GB 2,053,328 (1980), also US 4, 344,485 (1982), and Canada 1,130,201 (1982).

Chalaturnyk, R.J. and Li, P., 2001. When Is It Important to Consider Geomechanics in SAGD Operations? Paper 2001-46, Petroleum Society's Canadian International Petroleum Conference, Calgary, Alberta, Canada, June 12-14, 22p. Also, Journal of Canadian Petroleum Technology, Vol. 43, No. 4, pp. 53-61, 2004.

Chalaturnyk, R.J. and Scott, J.D., 1997. Geomechanical Response of Heavy Oil Reservoirs to the Steam Assited Gravit Drainage Process. SPE 37569, SPE International Thermal Operations & Heavy Oil Symposium, Bakersfield, California, U.S.A., February 10-12, 15p.

Chalaturnyk, R.J., 1996. Geomechanics of SAGD in Heavy Oil reservoirs. Ph.D dissertation, Department of Civil Engineering, University of Alberta, 576p.

Chalaturnyk, R.J. and Scott, J.D., 1992. Evaluation of Reservoir Properties from Geomechanical Tests. Journal of Canadian Petroleum Technology, Vol. 31, No. 5, pp. 31-41.

Chen, H.Y., Teufel, L.W., and Lee, R.L., 1995. Coupled Fluid Flow and Geomechanics in Reservoir Study – I. Theory and Governing Equations. SPE 30752, SPE Annual Technical Conference and Exhibition, Dallas, U.S.A., October 22-25, 13p.

Chilingarian, G.V., and Yen, T.F., 1978. Bitumens, Asphalts and Tar Sands. Elsevier Scientific Publishing Company.

Chin, L.Y. and Thomas, L.K., 1999. Fully Coupled Analysis of Improved Oil Recovery by Reservoir Compaction. SPE 56753, SPE Annual Technical Conference and Exhibition, Houston, Texas, U.S.A., October 3-6, 10p.

Chin, L.Y., Raghavan, R., and Thomas, L.K., 1998. Fully Coupled Geomechanics and Fluid Flow Analysis of Wells with Stress Dependent Permeability. SPE 48857, SPE International Conference and Exhibition, Beijing, China, November 2-6,16 p.

Collins, R.E., 1976. Flow of Fluids through Porous Materials; The Petroleum Publishing Company, Tulsa, U.S.A.

Dullien, F.A.L., 1979. "Porous Media – Fluid Transport and Pore Structure", Academic Press.

Dusseault, M., 2001. Petroleum Geomechanics. Norbert R. Morgenstern Symposium Celebrating 40 years of Teaching and Research Excellence, Telus Centre, University of Alberta, Edmonton, Alberta, Canada, April 26 – 27, 40p.

Dusseault, M., 1999. Petroleum Geomechanics: Excursions into coupled behavior. Journal of Canadian Petroleum Technology, Vol. 38, No. 12, pp. 10-14.

Dusseault, M.B. and Morgenstern, N.R., 1978. Shear Strength of Athabasca Oil Sands. Canadian Geotechnical Journal, Vol. 15, pp. 216-238.

Dusseault, M.B. and Morgenstern, N.R., 1979. Locked Sands. Q. Jl. Engen Geol., Vol. 12, pp.117-131.

Dusseault, M.B, 1977. The Geotechnical Characteristics of the Athabasca Oil Sands. Ph.D. dissertation, Department of Civil Engineering, University of Alberta, 653 p.

Edmunds, N.R. and Suggett, J.C., 1995. Design of a Commercial SAGD Heavy Oil Project. SPE 30277, International Heavy Oil Symposium, Calgary, Alberta, Canada, June 19-21, 7p.

Edmunds, N.R. and Gittins, S.D., 1991. Effective Steam Assisted Gravity Drainage to Long Horizontal Well Pairs. Paper 1991-65, CIM/AOSTRA Technical Conference, Banff, Alberta, Canada, Vol. 2, 13p.

Edmunds, N.R., Kovalsky, J.A., Gittens, S.D., and Pennacchioli, E.D., 1991. Review of the Phase A Steam-Assisted Gravity Drainage Test: An Underground Test Facility. SPE 21529, International Thermal Operations Symposium, Bakersfield, California, U.S.A., February 7-8, 10p.

Elliott, K.T. and Kovscek, A.R., 2001. A Numerical Analysis of the Single-Well Steam Assisted Gravity Drainage (SW-SAGD) Process. SUPRI TR – 124, Topical Report, U.S. Department of Energy, 36p.

Elliott, K.T. and Kovscek, A.R., 1999. Simulation of Early-Time Response of Single-Well Steam Assisted Gravity Drainage (SW-SAGD). SPE 54618, SPE Western Regional Meeting, Anchorage, Alaska, May 26-28, 12p.

Falk, K., Nzekwu, B., Karpuk, B., and Pelensky, P., 1996. Concentric CT for Single-Well Steam-Assisted Gravity Drainage. World Oil, July, pp. 85-95.

Farouq Ali, S.M. and Meldau, R.F., 1979. Current Steamflooding Technology. Journal of Petroleum Technology, October, pp. 1332-1342.

Fung, L.S.-K., Buchanan, L., and Wan, R.G., 1994. Coupled Geomechanical-Thermal Simulation for Deforming Heavy-Oil Reservoirs. Journal of Canadian Petroleum Technology, Vol. 33, No. 4, pp.22-28.

Gittins, S.D., Edmunds, N.R., and Mukherjee, N.J., 1992. Numerical Simulation of the Steam Assisted Gravity Drainage Process at the Underground Test Facility. IEA Collaborative Project on Enhanced Oil Recovery Workshop and Symposium, the Banff Springs Hotel and Conference Centre, Banff, Alberta, Canada, September 27-30.

Graton, L.C. and Fraser, H.J., 1935. Systematic Packing of Spheres-with Particular Relation to Porosity and Permeability. Journal of Geology, Vol. 43, No. 8, Part I, November-December, pp. 785-909.

Gutierrez, M. and Lewis, R.W., 1998. The Role of Geomechanics in Reservoir Simulation. SPE 47392, SPE/ISRM Eurock '98, Trondhelm, Norway, July 8-10, 10p.

Hart, R.D. and St. John, C.M., 1981. A Fully Coupled Thermal-Hydraulic-Mechanical Model for Non-Linear Geologic Systems. Proceedings 22nd US Symposium on Rock Mechanics, Cambridge, pp. 90-96.

Itasca Consulting Group, Inc., 2000. FLAC (Fast Lagrangian Analysis of Continua) Version 4.0 User's Guide.

Ito, Y. and Suzuki, S., 1996. Numerical Simulation of the SAGD Process in the Hangingstone Oil Sands Reservoir. Paper 96-57, 47th Annual Technical Meeting of Petroleum Society of CIM, Calgary, Alberta, Canada, 14 p.

Ito, Y., 1984. The Introduction of the Microchanneling Phenomenon to Cyclic Steam Stimulation and Its Application to the Numerical Simulator (Sand Deformation Concept). SPE Journal, August, pp. 417-429.

Ingram, G.M. and Urai, J.L., 1999. Top-seal Leakage through Faults and Fractures: the Role of Mudrock Properties. Aplin, A.C., Fleet, A.J. & Macquaker, J.H.S. (eds) Muds and Mudstones: Physical and Fluid Flow Properties. Geological Society, London, Special Publications, 158, pp. 125-135.

Iyoho, A.W., 1978. Selecting Enhanced Oil Recovery Processes. World Oil, November, pp. 61-64.

Jiang, Q., Butler, R.M., and Yee, C.-T., 2000. The Steam and Gas Push (SAGP) – 2: Mechanism Analysis and Physical Model Testing. Journal of Canadian Petroleum Technology, Vol. 39, No. 4, pp.52-61.

Khan, M. and Teufel, L.W., 2000. Determining the Effect of Geological and Geomechanical Parameters on Reservoir Stress Path through Numerical Simulations. SPE 63261, SPE Annual Technical Conference, Dallas, 11 p.

Kisman, K.E. and Yeung, K.C., 1995. Numerical Study of the SAGD Process in Burnt Lake Oil Sands Lease. SPE 30276, International Heavy Oil Symposium, Calgary, Alberta, Canada, 12p.

Komery, D.P., Luhning, R.W., and O'Rourke, J.C., 1995. Towards Commercialization of UTF Project Using Surface Drilled Horizontal SAGD Wells. Paper 1995-60, the 46th Annual Technical Meeting of the Petroleum Society of CIM, Banff, Alberta, Canada, May 14-17, 15p.

Kosar, K.M., 1989. Geotechnical Properties of Oil Sands and Related Strata. Ph.D. dissertation, Department of Civil Engineering, University of Alberta, 795 p.

Laing, J.M., Scott, J.D., Stokes, A.W., Suggett, J.C., and Wood, D.F., 1988. Geotechnical Instrumentation of the AOSTRA Mine-Assisted Underground Steaming Trial. Paper 112, Fourth UNITAR/UNDP Conference on Heavy Crude and Tar Sands, Edmonton, Alberta, Canada, August 7-12, pp. 112-1 to 112-18.

Law, D., Nasr, T.N. and Good, W., 2000. Field-scale Numerical Simulation of SAGD Process with Top-water Thief Zone. SPE 65522, SPE/Petroleum Society of CIM International Conference on Horizontal Well Technology, Calgary, Alberta, Canada, November 6-8, 11p.

Leverett M.C., 1941. Capillary Behavior in Porous Media; Trans., AIME, Vol. 142, pp. 152-169.

Lewis, R.W. and Sukirman, Y., 1993. Finite Element Modeling of Three-Phase Flow in Deforming Saturated Oil Reservoirs. International Journal for Numerical and Analytical Methods in Geomechanics, Vol. 17, No. 8, pp.577-598.

Li, P., Chalaturnyk, R.J., 2004. Permeability Variations Associated with Shearing and Isotropic Unloading during the SAGD Process. Paper 2004-240, Petroleum Society's Canadian International Petroleum Conference, Calgary, Alberta, Canada, June 8 – 10, 20p. Also, Journal of Canadian Petroleum Technology, Vol. 45, No. 1, 2006, pp.54-61.

Li, P. and Chalaturnyk, R.J., 2003. Discussion of "SAGD and Geomechanics"; Journal of Canadian Petroleum Technology, Vol. 42, No. 9, pp. 37-39.

Li, P., Chalaturnyk, R.J., and Tan, T.B., 2003. Coupled Reservoir Geomechanical Simulations for the SAGD Process. Paper 2003-083, Petroleum Society's Canadian International Petroleum Conference, Calgary, Alberta, Canada, June 10 – 12, 15p. Also, Journal of Canadian Petroleum Technology, Vol. 45, No. 1, 2006, pp.33-40.

Li, P., Chalaturnyk, R.J., and Yue, Q., and Zhao, H, 2002. A Simplified Methodology on Selection, Operation, and Optimum Design of Steam Drive Reservoirs. CIPC 2002-131, Petroleum Society's Canadian International Petroleum Conference, Calgary, Alberta, Canada, June 11 – 13, 15p. Also, Journal of Canadian Petroleum Technology, Vol. 44, No. 2, 2005, pp.33-41.

Li, P., Chalaturnyk, R.J., and Polikar, M., 2002. Issues with Reservoir Geomechanical Simulations of the SAGD Process. Paper 2002-130, Petroleum Society's Canadian International Petroleum Conference, Calgary, Alberta, Canada, June 11 – 13, 16p. Also, Journal of Canadian Petroleum Technology, Vol. 43, No. 5, 2004, pp. 30-40.

Li, P., Chalaturnyk, R.J., and Yue, Q., 2001. The Effect of Reservoir Fluid Pressure on Steam Drive of Heavy Oil Reservoirs. CIPC 2001-22, Petroleum Society's Canadian International Petroleum Conference, Calgary, Alberta, Canada, June 12–14, 17p.

Magara, K., Porosity-Permeability Relationship of Shales. unsolicited SPE 2430.

Mattax, C.C. and Dalton, R.L., 1990. Reservoir Simulation; Society of Petroleum Engineers, Richardson, TX, U.S.A, 173p.

McCormack, M., Fitzgibbon, J., and Horbachewski, N., 1997. Review of Single-Well SAGD Field Operating Experience. Canadian Petroleum Society Publication, No. 97-191.

Mori, A. and Tamura, M., 1986. Effects of Dilatancy on Permeability in Sands Stabilized by Chemical Grout; Soils and Foundations. Japanese Soc. of Soil Mech. And Foundation Engineering, Vol. 27, No. 1, pp. 96-104.

Oldakowski, K., 1994. Absolute Permeability of Oil Sands. M.Sc. Thesis, Department of Civil Engineering, University of Alberta, 234p.

Osorio, J.G., Chen, H.Y., and Teufel, L.W., 1999. Numerical Simulation of the Impact of Flow-Induced Geomechanical Response on the Productivity of Stress-Sensitive Reservoirs. SPE 51929, SPE Reservoir Simulation Symposium, Houston, Texas, U.S.A., February 14-17, 15p.

Panda, M.N. and Lake, L.W., 1994. Estimation of Single-Phase Permeability from Parameters of Particle-Size Distribution. AAPG Bulletin, Vol. 78, No. 7, pp. 1028-1039, 1994.

Petroleum Production Handbook, 1962. Society of Petroleum Engineers of AIME, Dallas, Texas, Frick Thomas C., Ed.

Plewes, H.D., 1987. Undrained Strength of Athabasca Oil Sands. M.Sc. Thesis, University of Alberta, 428 p.

Polikar, M., Cyr, T.J., and Coates, R.M., 2000. Fast-SAGD: Half the Wells and 30% Less Steam. SPE 65509, SPE/Petroleum Society of CIM International Conference on Horizontal Well Technology, Calgary, Alberta, Canada, November 6-8, 6p.

Pooladi-Darvish, M. and Mattar, L., 2002. SAGD Operations in the Presence of Overlying Gas Cap and Water Layer – Effect of Shale Layers. Journal of Canadian Petroleum Technology, Vol. 41, No. 6, pp. 40-51.

Rottenfusser, B.A., Alwast, N.K., Kidston, C.R., and Cotterill, D.K., 1989. Geology of UTF Phase A. Alberta Research Council Report submitted to AOSTRA, 36p. + Maps.

Rottenfusser, B.A., Alwast, N.K., Kidston, C.R., and Cotterill, D.K., 1989. Appendix F: Geology of UTF Phase A. Alberta Research Council Report submitted to AOSTRA.

Rutqvist, J., Wu, Y.-S., Tsang, C.-F., and Bodvarsson, G., 2002. A Modeling Approach for the Analysis of Coupled Multiphase Fluid Flow, Heat Transfer and Deformation in Fractured Porous Rock. International Journal of Rock Mechanics and Mining Science, Vol. 39, pp. 429-442.

Samieh, A.M. and Wong, R.C.K., 1997. Deformation of Athabasca Oil Sand at Low Effective Stresses under Varying Boundary Conditions. Canadian Geotechnical Journal, Vol. 34, pp.985-990.

Sanyal, S.K., Marsden, Jr. S.S., and Ramey, Jr. H.J., 1974. Effect of Temperature on Petrophysical Properties of Reservoir Rocks. SPE 4898, Annual Fall Meeting of the Society of Petroleum Engineers of AIME, Houston, Texas, October 6-9, pp.19.

Sawhney, G.S., Liebe, H., and Butler, R.M., 1995. Vertical Injection Wells for SAGD: A Practical Option or Not? Journal of Canadian Petroleum Technology, Vol. 34, No. 1, pp.47-54.

Scheidegger, A.E., 1974. The Physics of Flow through Porous Media; Third edition, University of Toronto Press.

Scott, J.D., Proskin, S.A., and Adhikary, D., 1991. The Relationship between Absolute Permeability and Stress State for Heavy Oil Sand. Eastern Oil Shale Symposium, Lexington, Kentucky, USA, November 14, 10p.

Scott, J.D., Adhikary, D., and Proskin, S.A., 1991. Volume and Permeability Changes Associated with Steam Stimulation in an Oil Sands Reservoir. Paper 1991-63, Petroleum Society of CIM/AOSTRA Technical Conference, Banff, Alberta, Canada, April 21-24, 14p.

Settari, A., Walters, D.A., and Behie, G.A., 2001. Use of Coupled Reservoir and Geomechanical Modeling for Integrated Reservoir Analysis and Management. Journal of Canadian Petroleum Technology, Vol. 40, No. 12, pp. 55-61.

Settari, A. and Walters, D.A., 1999. Advances in Coupled Geomechanical and Reservoir Modeling with Applications to Reservoir Compaction. SPE 51927, SPE Reservoir Simulation Symposium, Houston, Texas, U.S.A., February 14-17, 13p.

Settari, A. and Mourits, F.M., A., 1995. Coupled Reservoir and Geomechanical Simulation System. SPE 50939, SPE Reservoir Simulation Symposium, San Antonio, Texas, U.S.A., February 12-15. Also, SPE Journal, September 1998, pp.219-226.

Settari, A., 1989. Physics and Modelling of Thermal Flow and Soil Mechanics in Unconsolidated Porous Media. SPE 18420, Proceedings Symposium on Reservoir Simulation, Houston, USA, pp. 155-168.

Sheng, J., 1997. Foamy Oil Flow in Porous Media. Ph.D. dissertation, Department of Civil Engineering, University of Alberta.

Singhal, A.K., Das, S.K., Leggitt, S.M., Kasraie, M., and Ito, Y., 1996. Screening of Reservoirs for Exploitation by Application of Steam Assisted Gravity Drainage/Vapour Processes. SPE 37144, International Conference on Horizontal Well Technology, Calgary, Alberta, Canada, November 18-20, 10p.

Siu, Nghiem, L.X., Gittins, S.D., Nzekwu, B.I., and Redford, 1991. Modeling Steam Assisted Gravity Drainage in the UTF Project. SPE 22895, Annual Technical Conference and Exhibition of the Society of Petroleum Engineers, Dallas, TX, USA, October 6-9, 10p.

Soeder, D.J., 1986. Porosity and Permeability of Eastern Devonian Gas Shale. SPE 15213, Unconventional Gas Symposium, Louisville, KY, U.S.A., May 18-21.

Sukirman, Y. and Lewis, R.W., 1993. A Finite Element Solution of A Fully Coupled Implicit Formulation for Reservoir Simulation. International Journal for Numerical and Analytical Methods in Geomechanics, Vol.17, pp. 677-698.

Tortike, W.S. and Farouq Ali, S.M., 1993. Reservoir Simulation Integrated with Geomechanics. Journal of Canadian Petroleum Technology, Vol. 32, No. 5, pp. 28-37.

Tortike, W.S. and Farouq Ali, S.M., 1991. Prediction of Oil Sand Failure due to Steam-Induced Stresses. Journal of Canadian Petroleum Technology, Vol. 30, No. 1, pp.87-96.

Tortike, W.S., 1991. Numerical Simulation of Thermal Multiphase Fluid Flow in an Elastoplastic Deforming Oil Reservoir. Ph.D dissertation, School of Mining and Petroleum Engineering, Department of Civil and Environmental Engineering, University of Alberta.

Tortike, W.S. and Farouq Ali, S.M., 1987. A Framework for Multiphase Nonisothermal Fluid Flow in A Deforming Heavy Oil Reservoir. SPE 16030, SPE Symposium on Reservoir Simulation, San Antonio, U.S.A., 7p.

Touhidi-Baghini, A., 1998. Absolute Permeability of McMurray Formation Oil Sands at Low Confining Stresses. Ph.D dissertation, Department of Civil Engineering, University of Alberta, 339 p.

Vaziri, H., 1988. Coupled Fluid Flow and Stress Analysis of Oil Sands Subjected to Heating. Journal of Canadian Petroleum Technology, Vol. 27, No. 5, pp. 84-91.

Vaziri, H., 1986. Finite Element Analysis of Oil Sands Subjected to Thermal Effects. Paper 86-37-74, presented at 37th Annual Technical Meeting of CIM, Calgary, Alberta, Canada, 21p.

Wilson, L.A., Reed, R.L., Reed, D.W., Clay, R.R., and Harrison, N.H., 1963. Some Effects of Pressure on Forward and Reverse Combustion. SPE Journal, No. 3, pp.127-137.

Wong, R.C.K., 2000. Shear Deformation of Locked Sand in Triaxial Compression. Geotechnical Testing Journal, Vol. 23, No. 2, June, pp. 158-170.

Wong, R.C.K., 1998. Swelling and Softening Behavior of La Biche Shale. Canadian Geotechnical Journal, Vol. 35, pp. 206-221.

Wong, R.C.K., Barr, W.E., and Kry, P.R., 1993. Stress-Strain Response of Cold Lake Oil Sands. Canadian Geotechnical Journal, Vol. 30, No. 2, pp. 220-235.

Wong, R.C.K., Barr, W.E., To, N.M., and Paul, R., 1991. Laboratory Measurement of Effective Permeability to Water and Compressibility in Unconsolidated Athabasca Oil Sands Cores. The 44th Canadian Geotechnical Conference, Calgary, Alberta, Vol. 2, pp. 56-1 to 56-7.

Xia, T.X., Greaves, M., and Turta, A.T., 2003. Main Mechanism for Stability of THAI – "Toe-to-Heel Air Injection". CIPC 2003-030, Petroleum Society's Canadian International Petroleum Conference, Calgary, Alberta, Canada, June 10 – 12, 20p.

Zhang, C., 1994. Geomechanical Behaviour of Grand Rapids Formation Oil Sands. M.Sc. Thesis, University of Alberta, 250 p.

APPENDIX A

NUMERICAL EXPERIMENTS MATCHING LAB TESTING

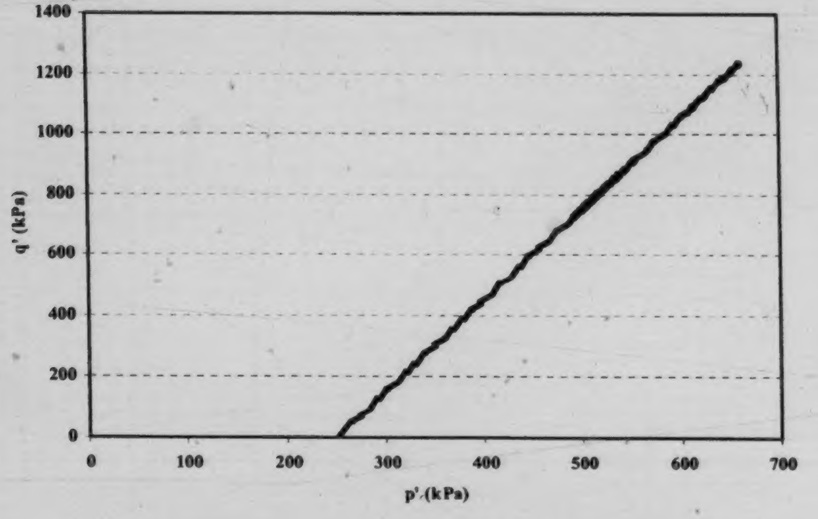

Figure A1 Deviatoric stress versus mean effective stress
Stress Path 1 (σ_3' = 250 kPa), Horizontal Core, T40

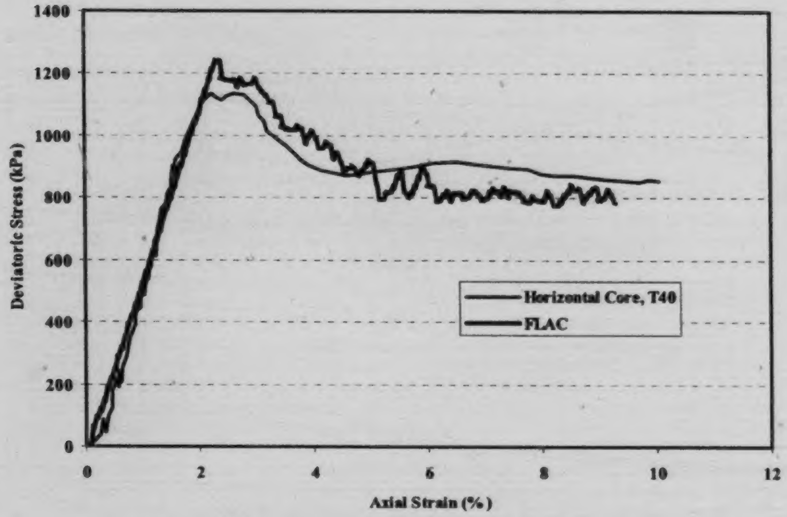

Figure A2 Deviatoric stress versus axial strain
Stress Path 1 (σ_3' = 250 kPa), Horizontal Core, T40

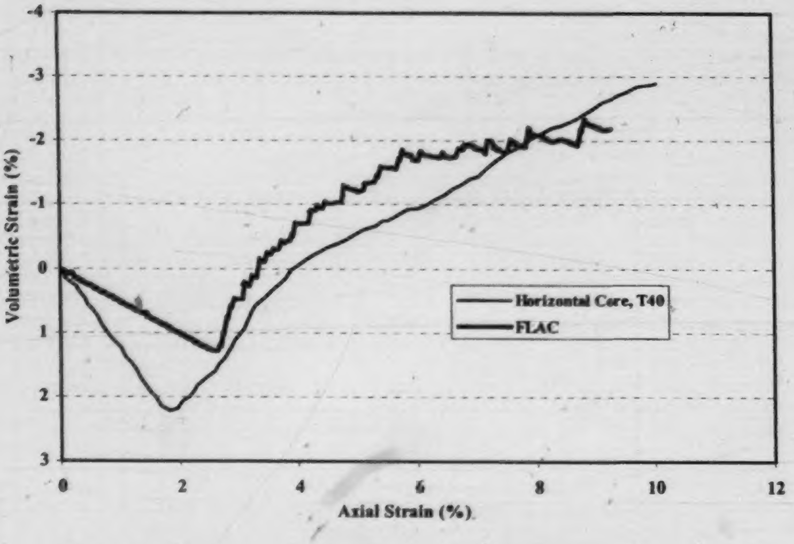

Figure A3 Volumetric strain versus axial strain
Stress Path 1 ($\sigma_3' = 250$ kPa), Horizontal Core, T40

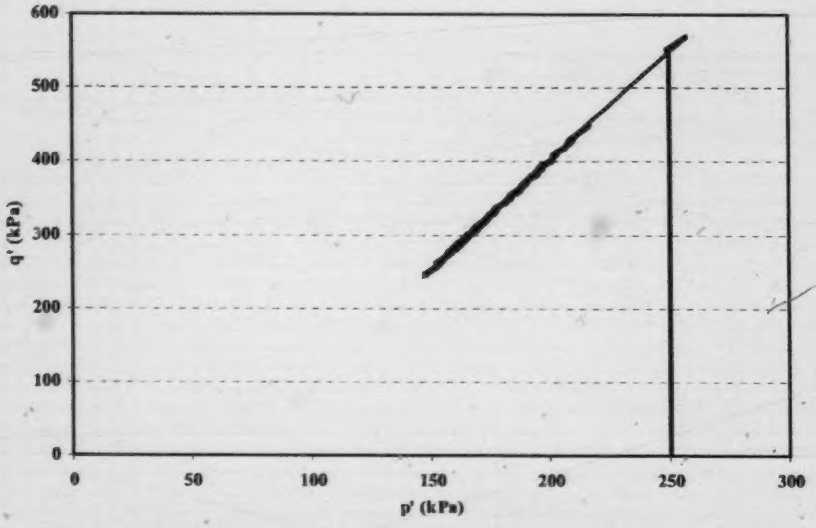

Figure A4 Deviatoric stress versus mean effective stress
Stress Path 2 (Initial $\sigma_3' = 250$ kPa), Horizontal Core, T41

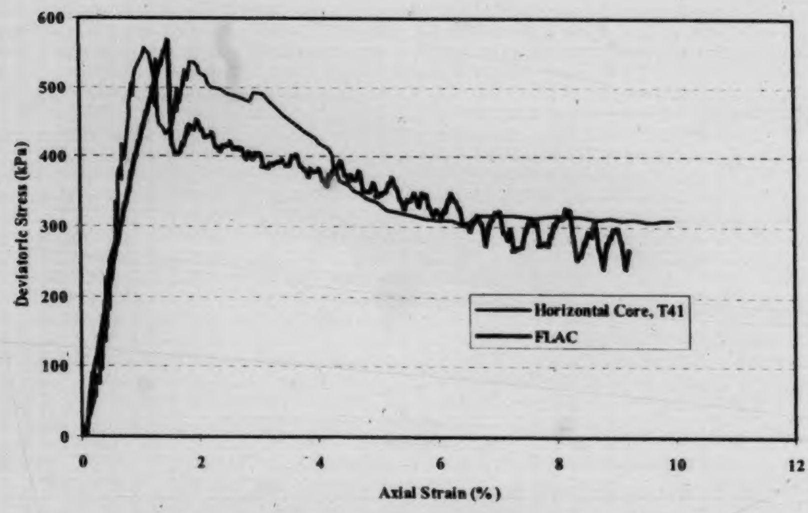

Figure A5 Deviatoric stress versus axial strain
Stress Path 2 (Initial σ_3' = 250 kPa), Horizontal Core, T41

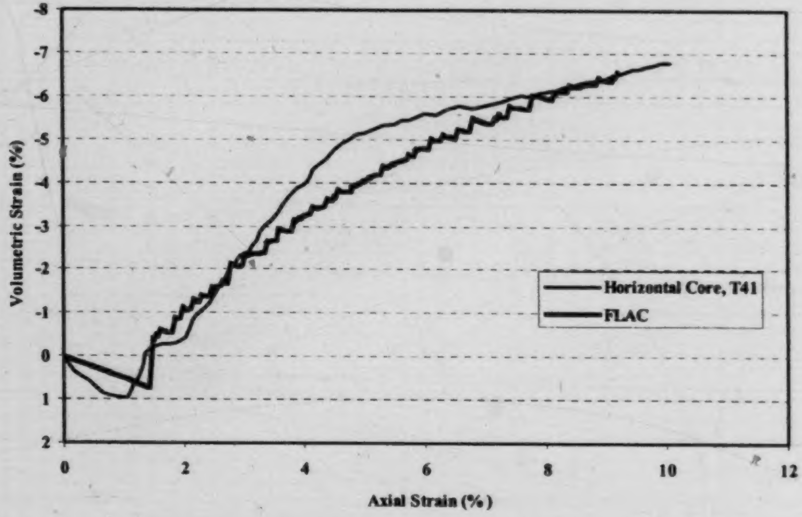

Figure A6 Volumetric strain versus axial strain
Stress Path 2 (Initial σ_3' = 250 kPa), Horizontal Core, T41

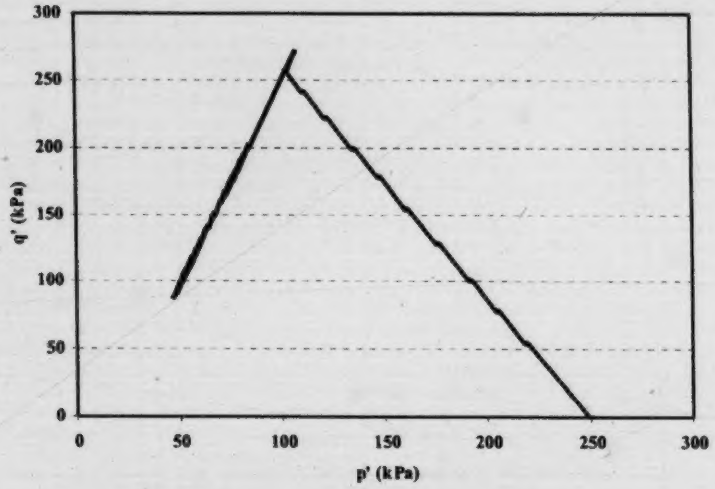

Figure A7 Deviatoric stress versus mean effective stress
Stress Path 3 (Initial $\sigma_3' = 250$ kPa), Horizontal Core, T42

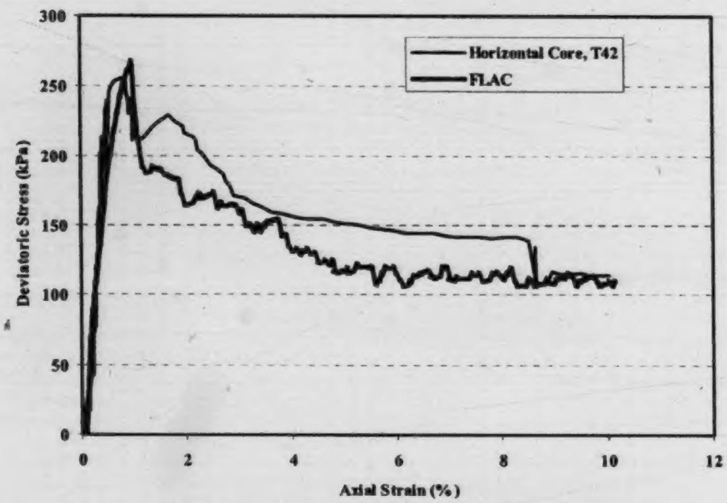

Figure A8 Deviatoric stress versus axial strain
Stress Path 3 (Initial $\sigma_3' = 250$ kPa), Horizontal Core, T42

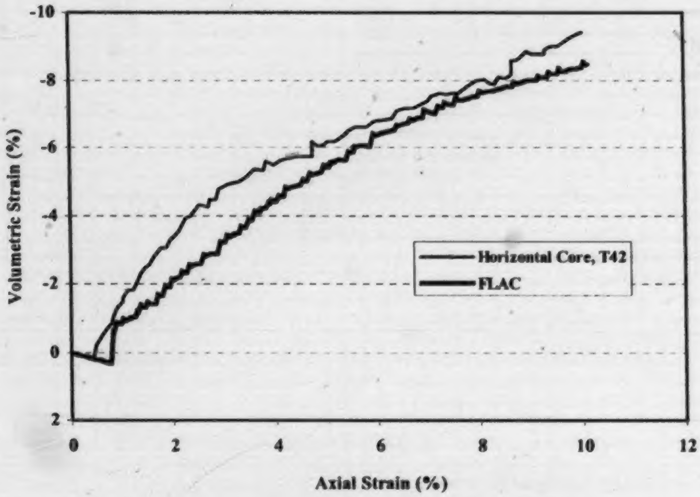

Figure A9 Volumetric strain versus axial strain
Stress Path 3 (Initial σ_3' = 250 kPa), Horizontal Core, T42

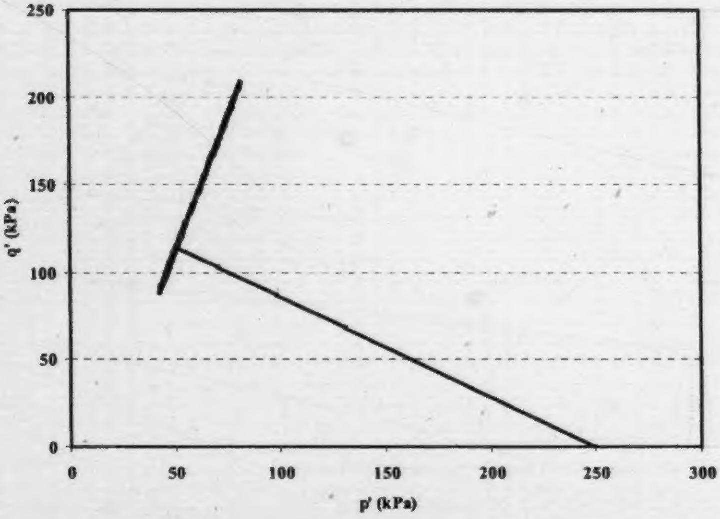

Figure A10 Deviatoric stress versus mean effective stress
Stress path 4 (Initial σ_3' = 250 kPa), Horizontal Core, T43

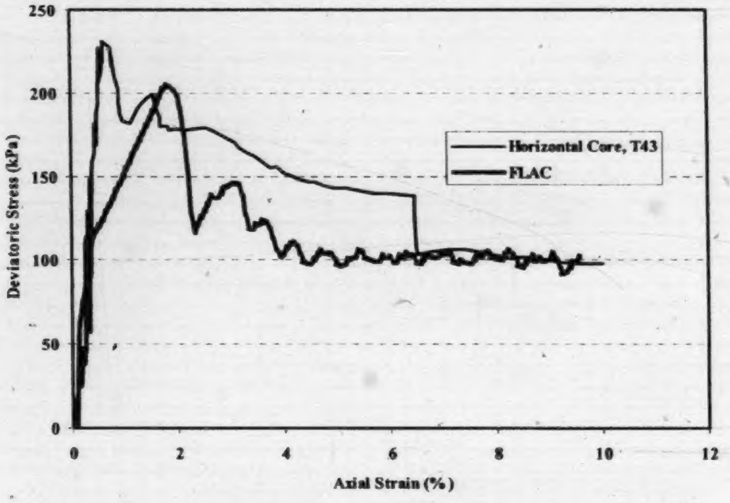

Figure A11 Deviatoric stress versus axial strain
Stress Path 4 (Initial σ_3' = 250 kPa), Horizontal Core, T43

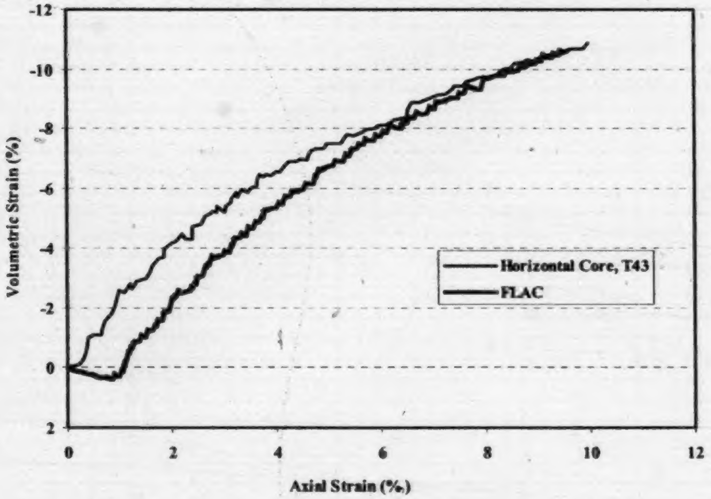

Figure A12 Volumetric strain versus axial strain
Stress Path 4 (Initial σ_3' = 250 kPa), Horizontal Core, T43

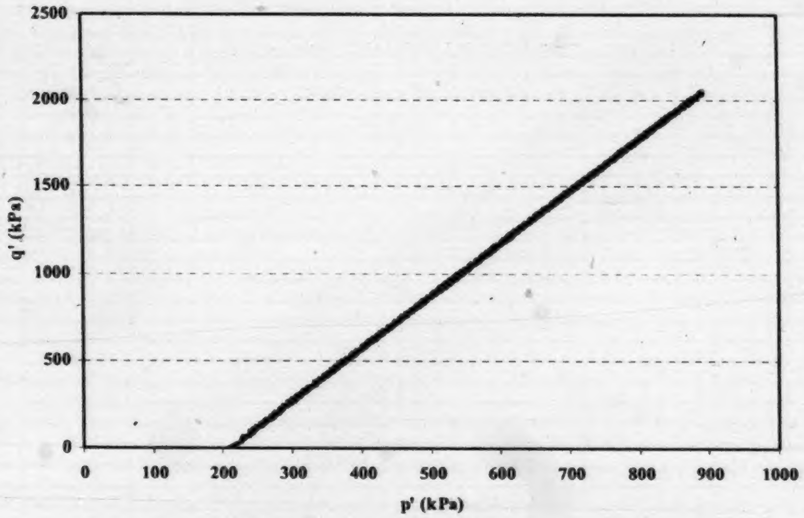

Figure A13 Deviatoric stress versus mean effective stress
Stress path 1 (σ_3' = 250 kPa), Vertical Core, T29

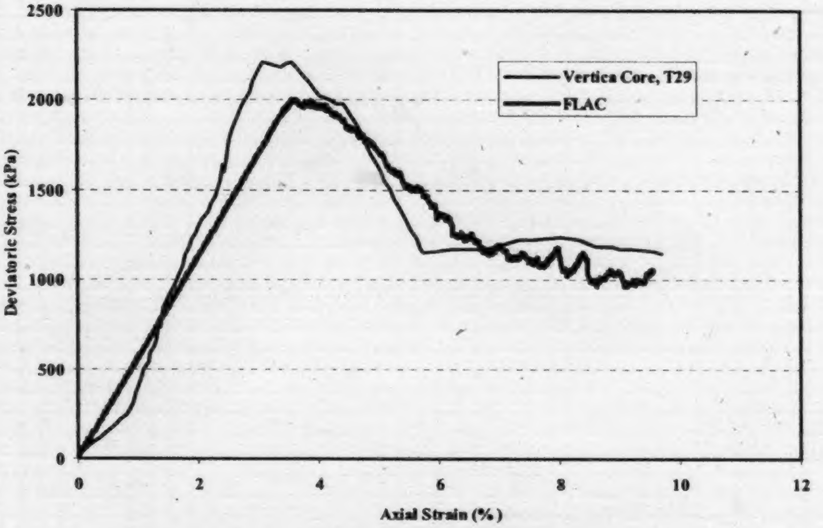

Figure A14 Deviatoric stress versus axial strain
Stress path 1 (σ_3' = 250 kPa), Vertical Core, T29

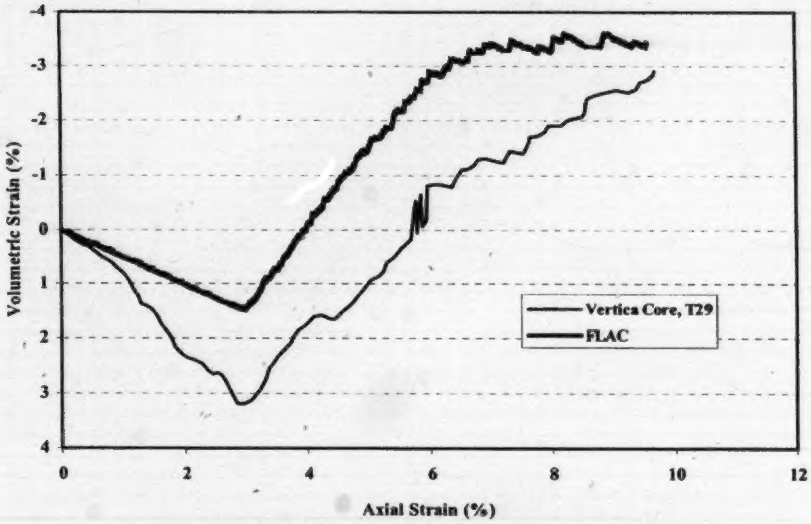

Figure A15 Volumetric strain versus axial strain
Stress path 1 ($\sigma_3' = 250$ kPa), Vertical Core, T29

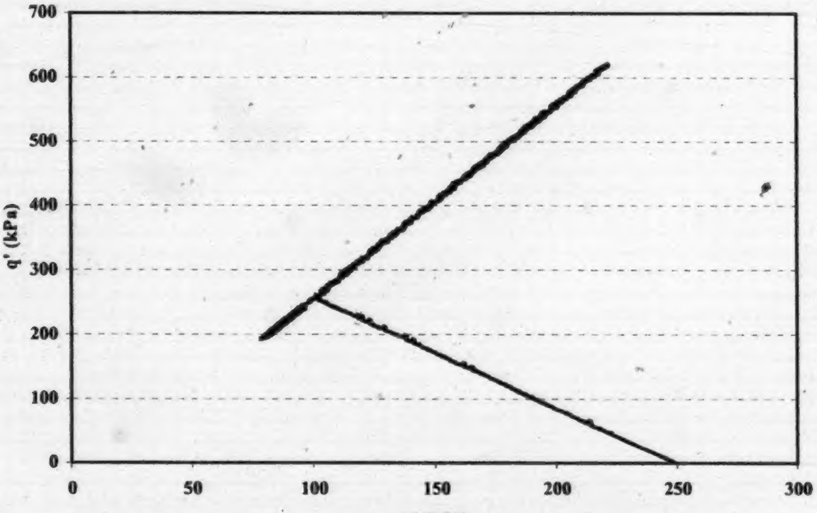

Figure A16 Deviatoric stress versus mean effective stress
Stress Path 3 (Initial $\sigma_3' = 250$ kPa), Vertical Core, T36

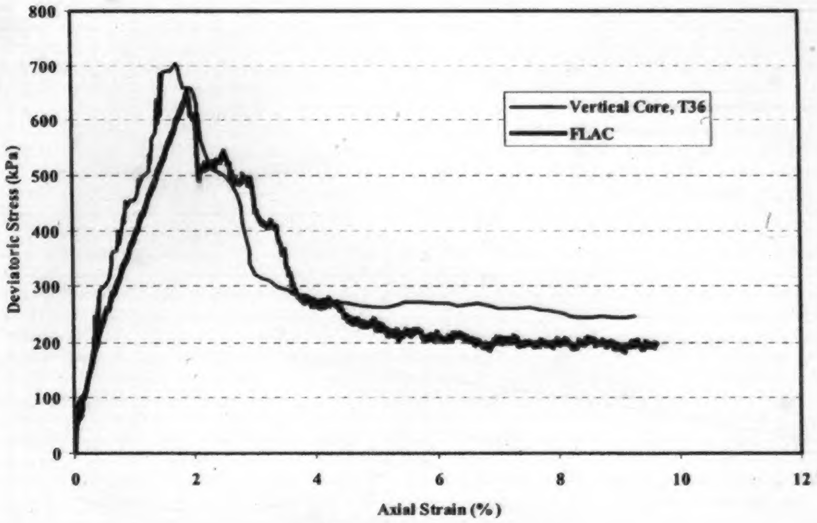

Figure A17 Deviatoric stress versus axial strain
Stress path 3 (Initial σ_3' = 250 kPa), Vertical Core, T36

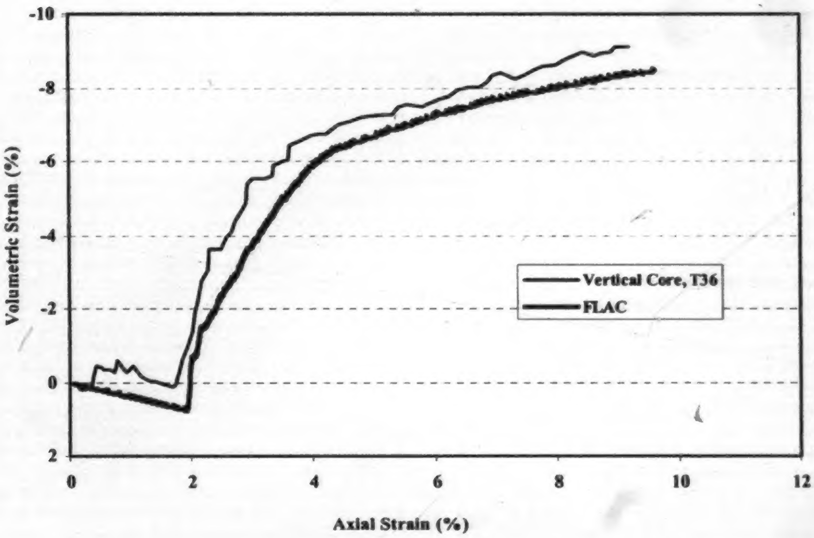

Figure A18 Volumetric strain versus axial strain
Stress path 3 (Initial σ_3' = 250 kPa), Vertical Core, T36

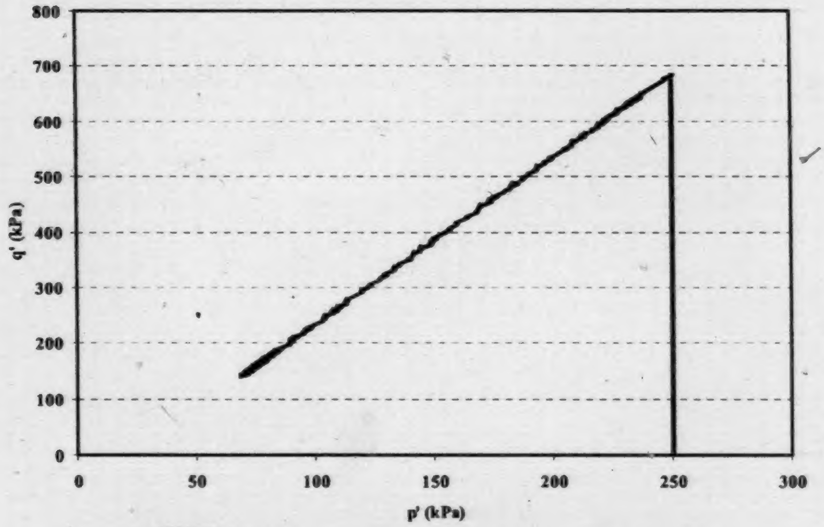

Figure A19 Deviatoric stress versus mean effective stress
Stress path 2 (Initial $\sigma_3' = 250$ kPa), Vertical Core, T38

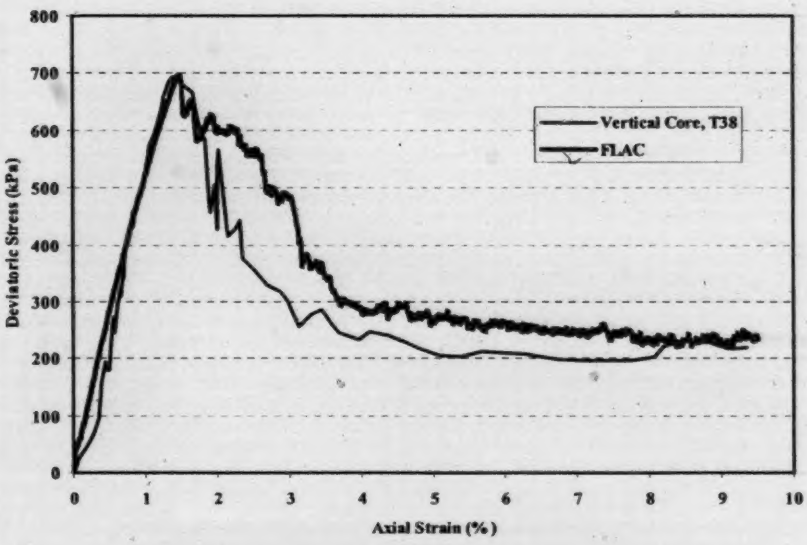

Figure A20 Deviatoric stress versus axial strain
Stress path 2 (Initial $\sigma_3' = 250$ kPa), Vertical Core, T38

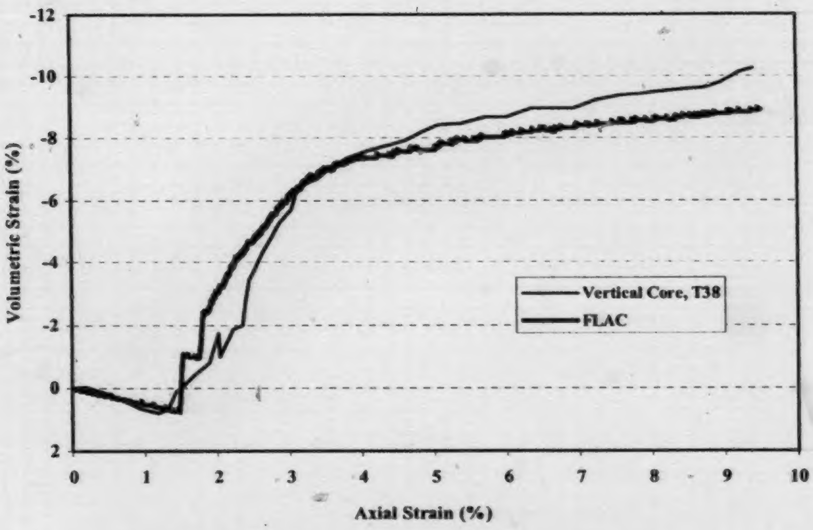

Figure A21 Volumetric strain versus axial strain
Stress path 2 (Initial $\sigma_3' = 250$ kPa), Vertical Core, T38

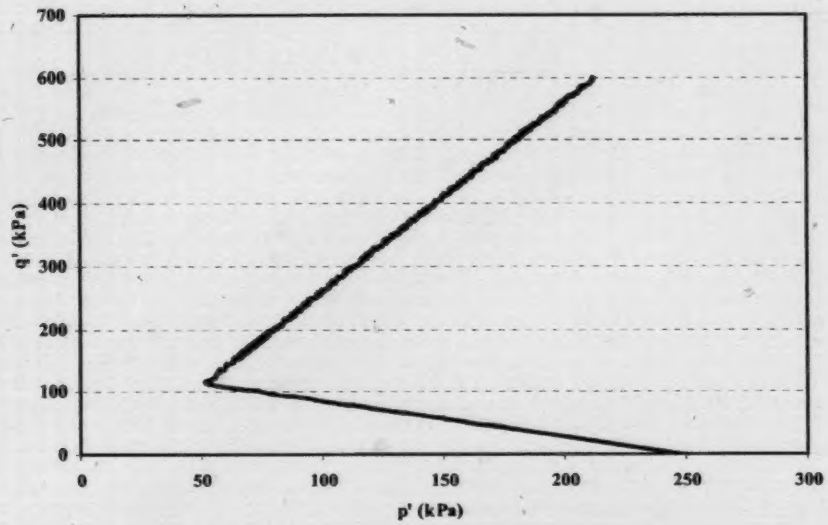

Figure A22 Deviatoric stress versus mean effective stress
Stress Path 4 (Initial $\sigma_3' = 250$ kPa), Vertical Core, T39

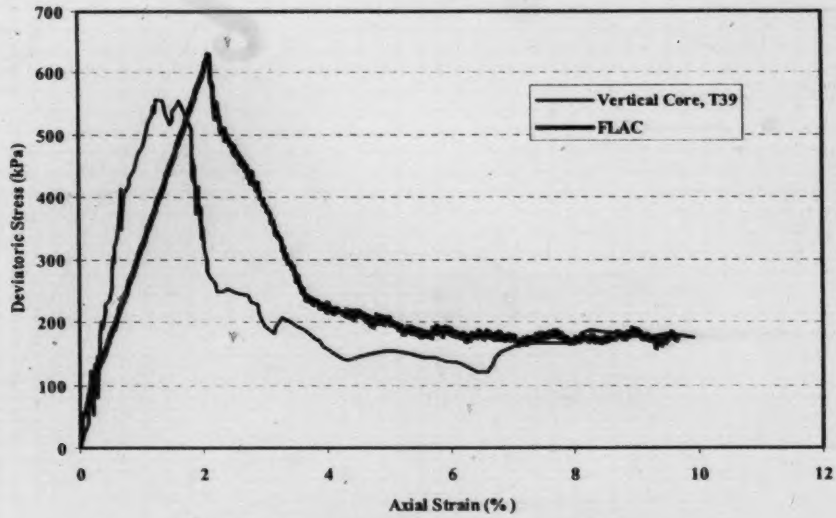

Figure A23 Deviatoric stress versus axial strain
Stress Path 4 (Initial σ_3' = 250 kPa), Vertical Core, T39

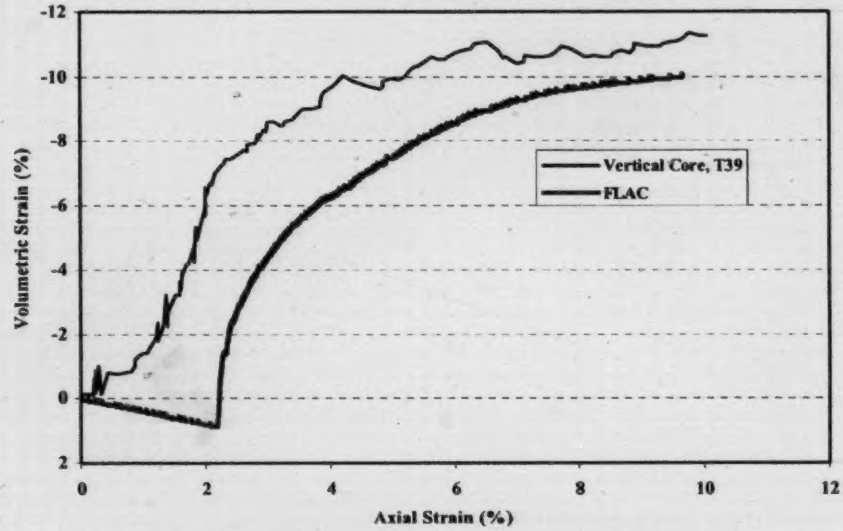

Figure A24 Volumetric strain versus axial strain
Stress Path 4 (Initial σ_3' = 250 kPa), Vertical Core, T39

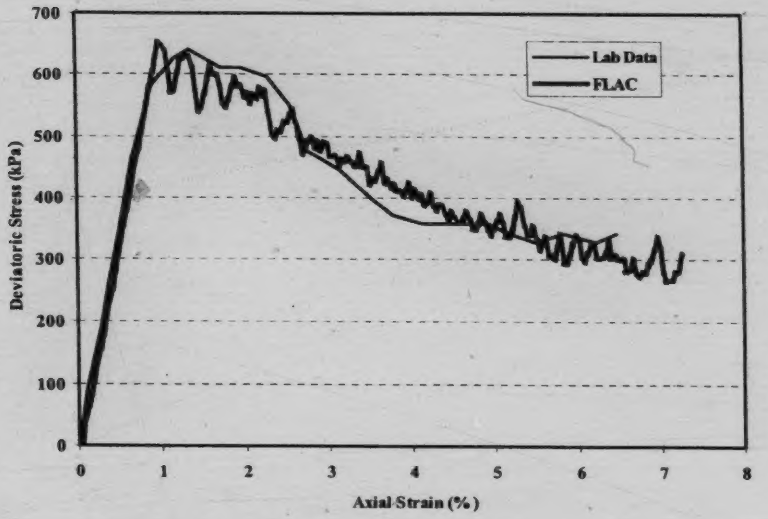

Figure A25 Deviatoric stress versus axial strain
($\sigma_3' = 50$ kPa)

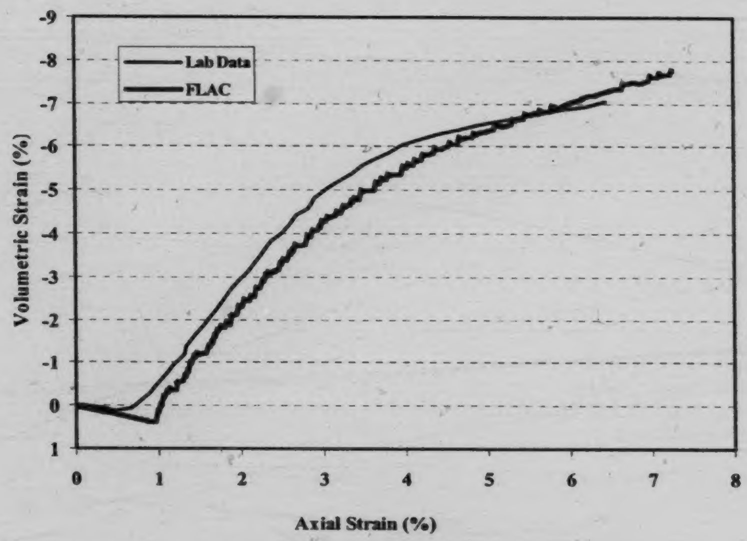

Figure A26 Volumetric strain versus axial strain
($\sigma_3' = 50$ kPa)

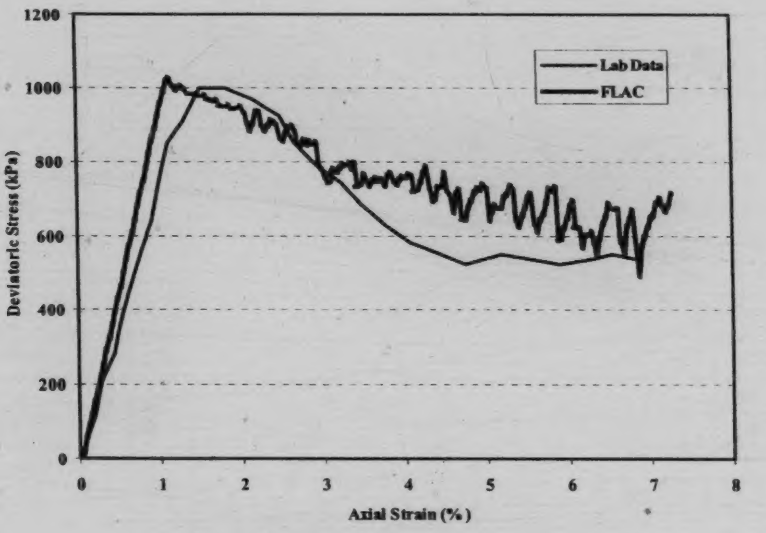

Figure A27 Deviatoric stress versus axial strain (σ3′ = 100 kPa)

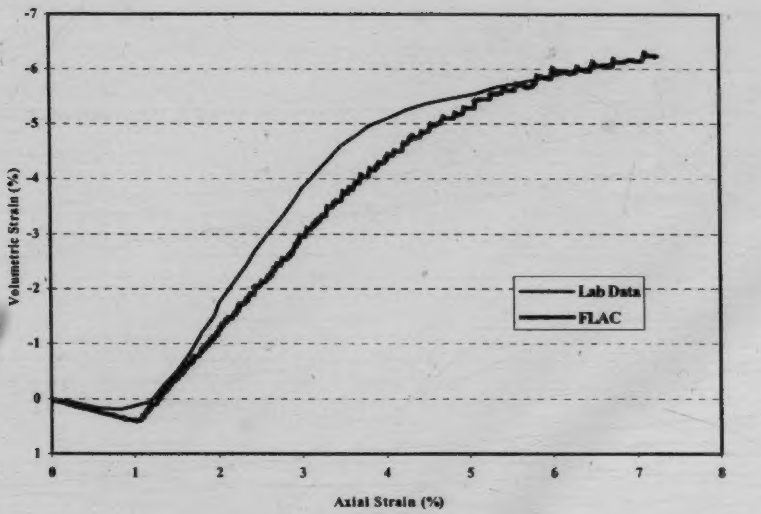

Figure A28 Volumetric strain versus axial strain (σ3′ = 100 kPa)

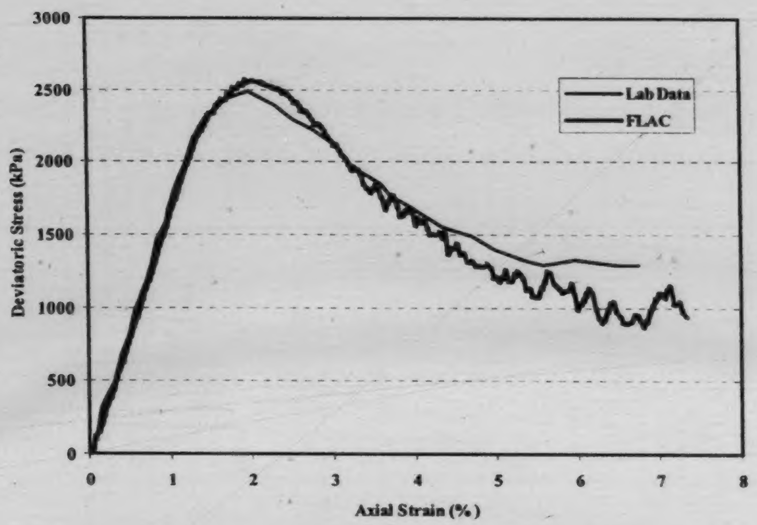

Figure A29 Deviatoric stress versus axial strain ($\sigma_3' = 300$ kPa)

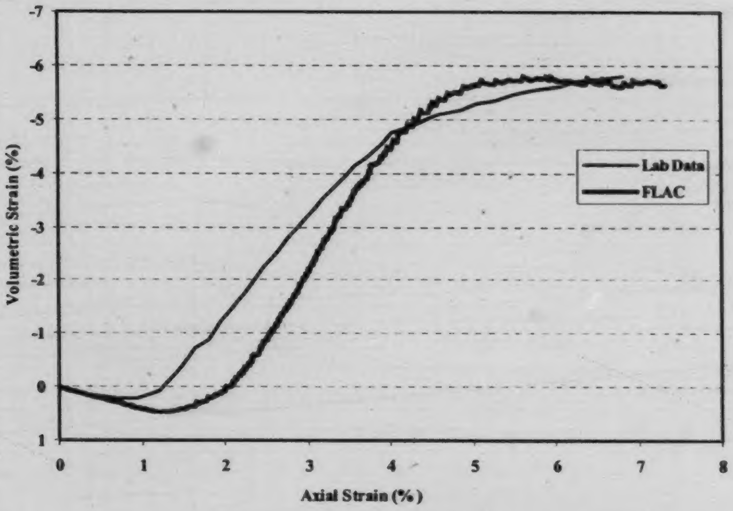

Figure A30 Volumetric strain versus axial strain ($\sigma_3' = 300$ kPa)

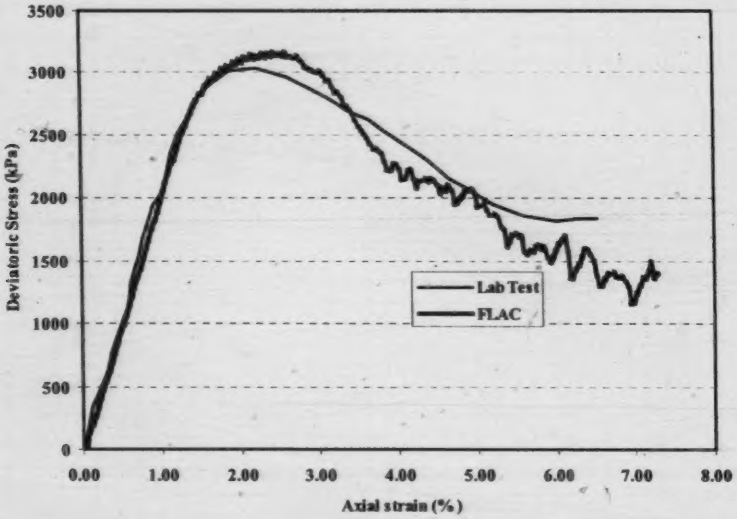

Figure A31 Deviatoric stress versus axial strain ($\sigma_3' = 450$ kPa)

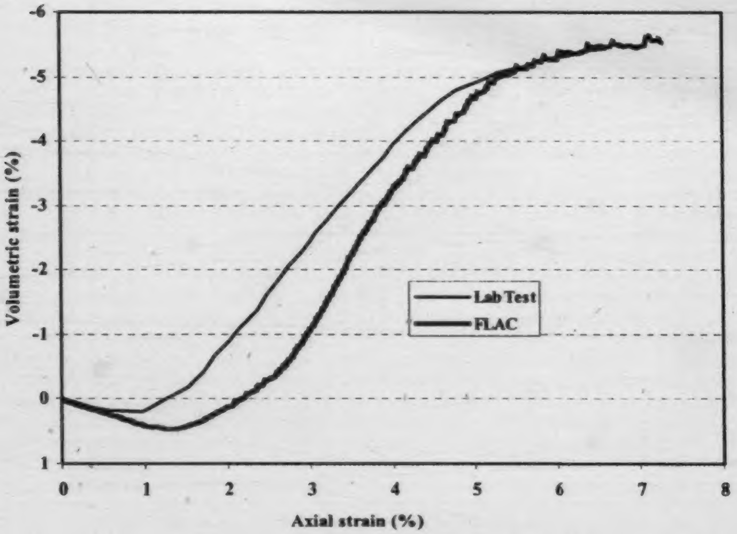

Figure A32 Volumetric strain versus axial strain ($\sigma_3' = 450$ kPa)

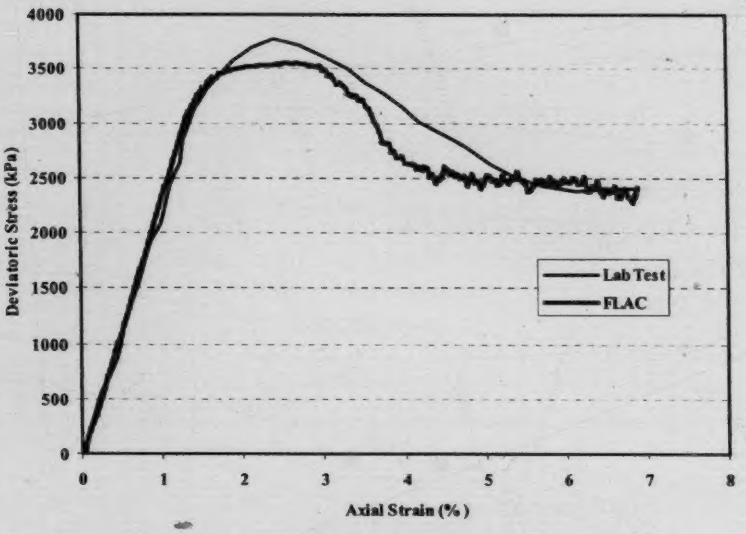

Figure A33 Deviatoric stress versus axial strain
($\sigma_3' = 600$ kPa)

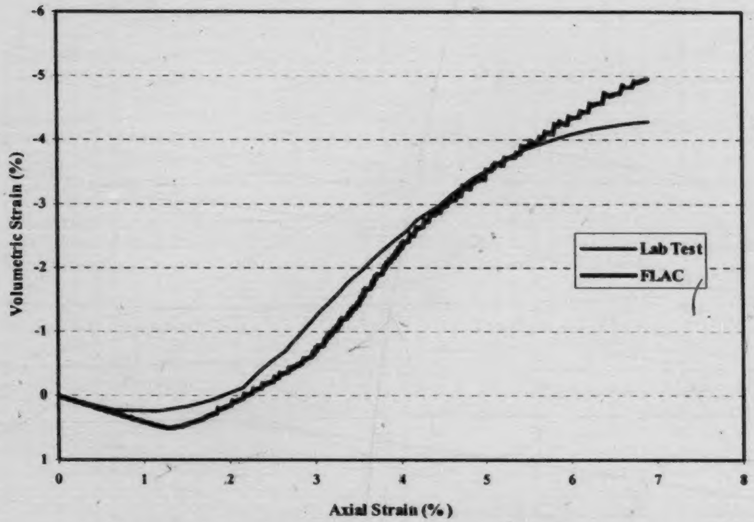

Figure A34 Volumetric strain versus axial strain
($\sigma_3' = 600$ kPa)

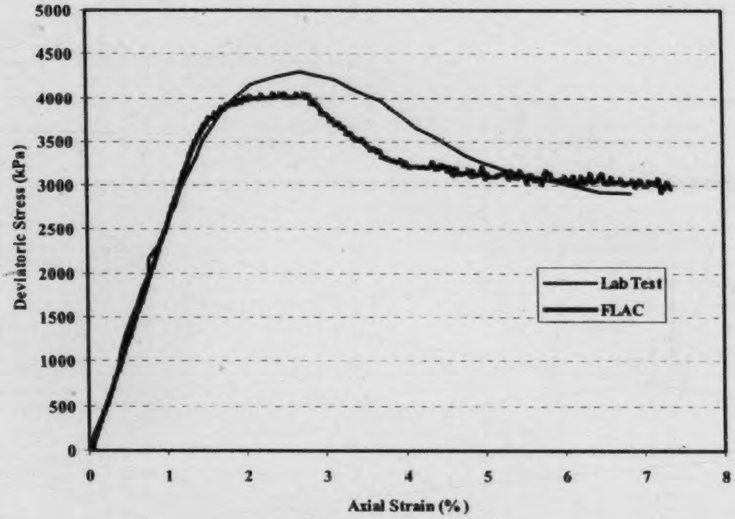

Figure A35 Deviatoric stress versus axial strain (σ_3' = 750 kPa)

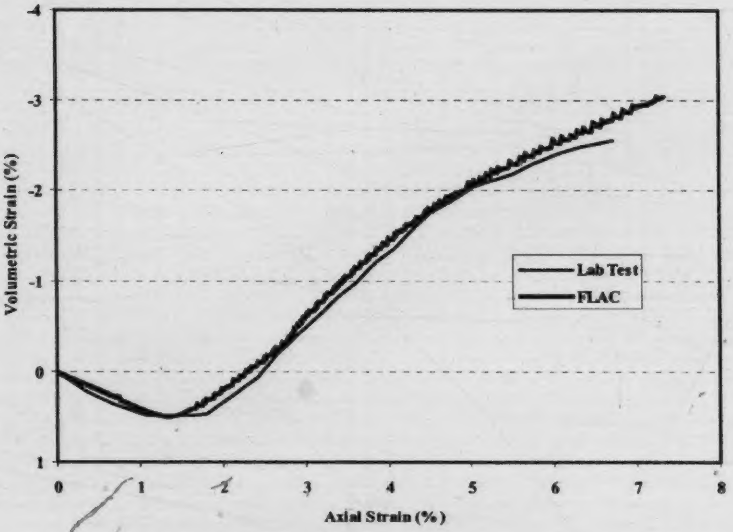

Figure A36 Volumetric strain versus axial strain (σ_3' = 750 kPa)

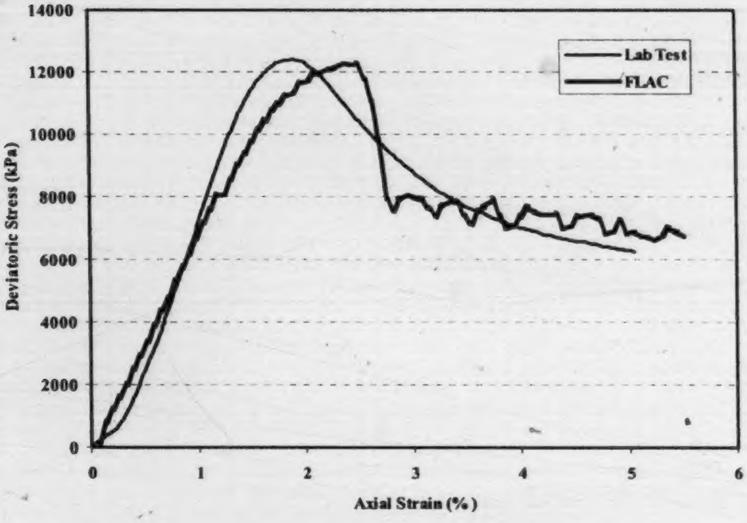

Figure A37 Deviatoric stress versus axial strain
Stress Path 1 (σ_3' = 1300 kPa), Specimen S3

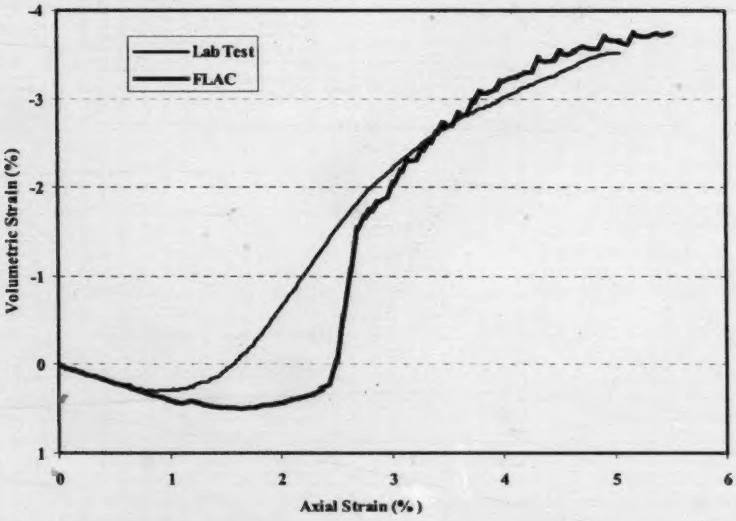

Figure A38 Volumetric strain versus axial strain
Stress Path 1 (σ_3' = 1300 kPa), Specimen S3

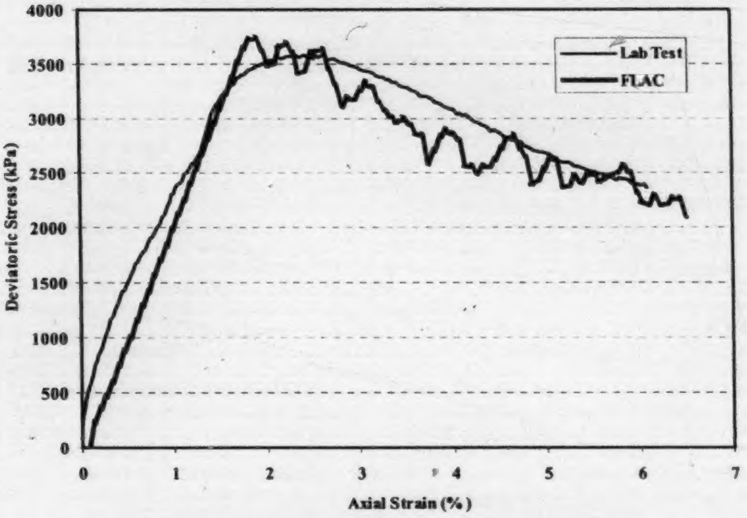

Figure A39 Deviatoric stress versus axial strain
Stress Path 1 (σ_3' = 480 kPa), Specimen S4

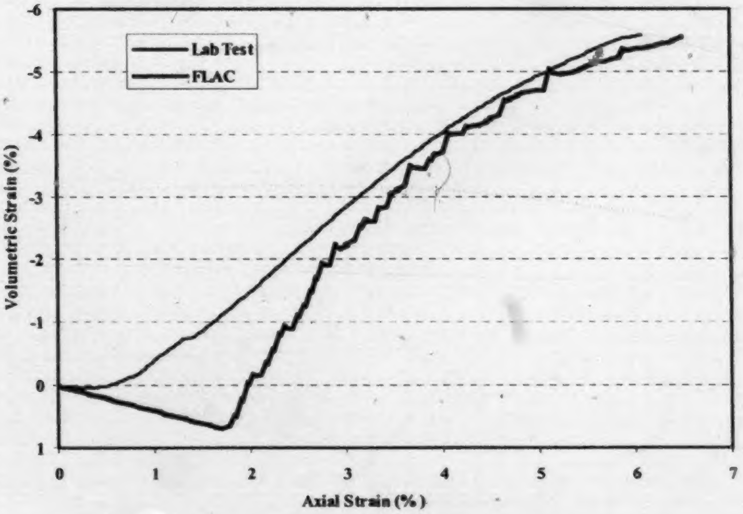

Figure A40 Volumetric strain versus axial strain
Stress Path 1 (σ_3' = 480 kPa), Specimen S4

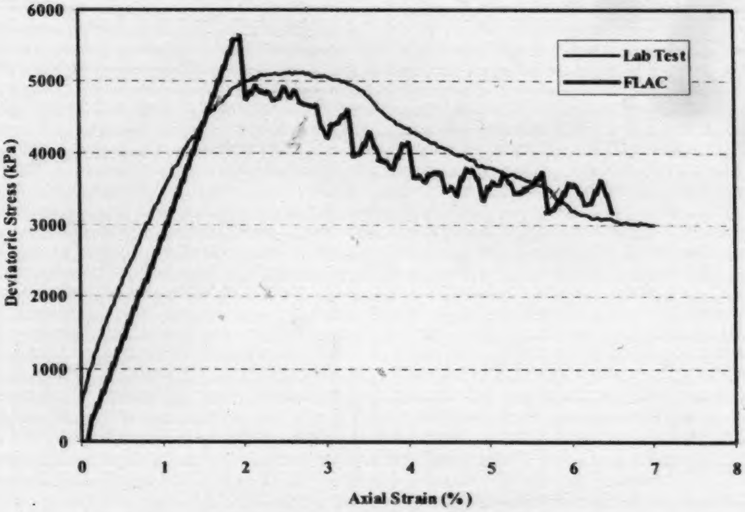

Figure A41 Deviatoric stress versus axial strain Stress Path 1 ($\sigma_3' = 970$ kPa), Specimen S5

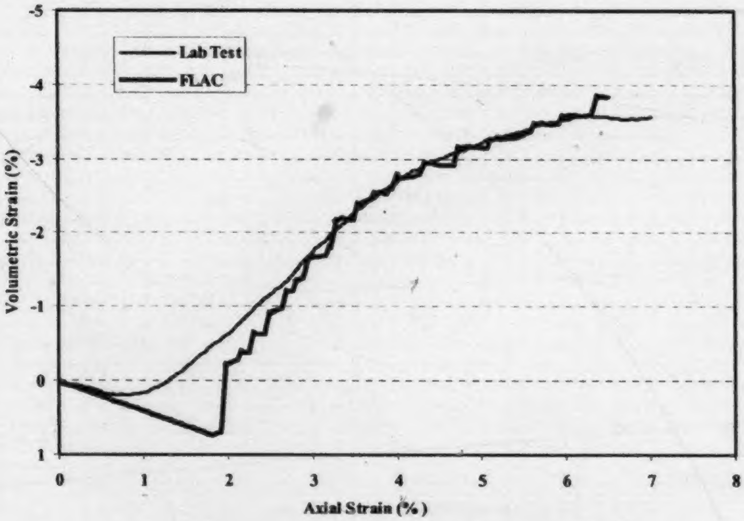

Figure A42 Volumetric strain versus axial strain Stress Path 1 ($\sigma_3' = 970$ kPa), Specimen S5

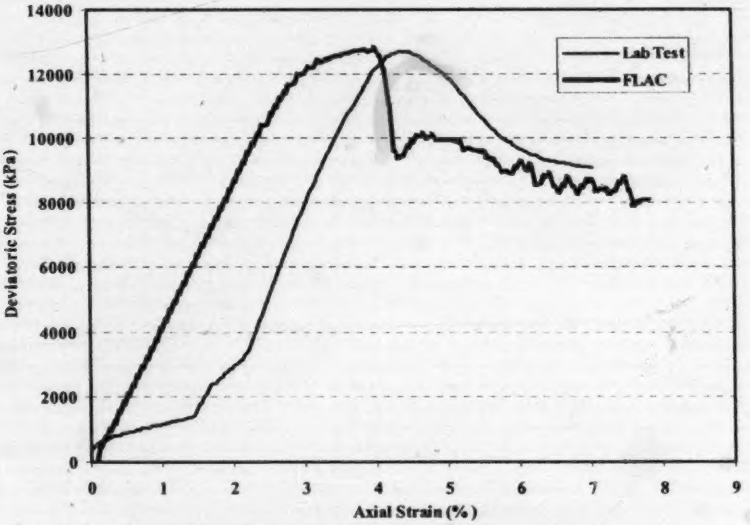

Figure A43 Deviatoric stress versus axial strain
Stress Path 1 ($\sigma_3' = 2030$ kPa), Specimen S6

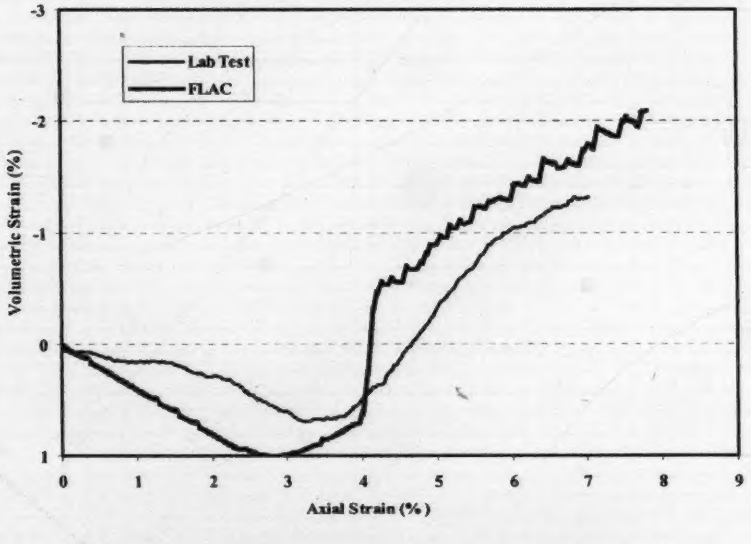

Figure A44 Volumetric strain versus axial strain
Stress Path 1 ($\sigma_3' = 2030$ kPa), Specimen S6

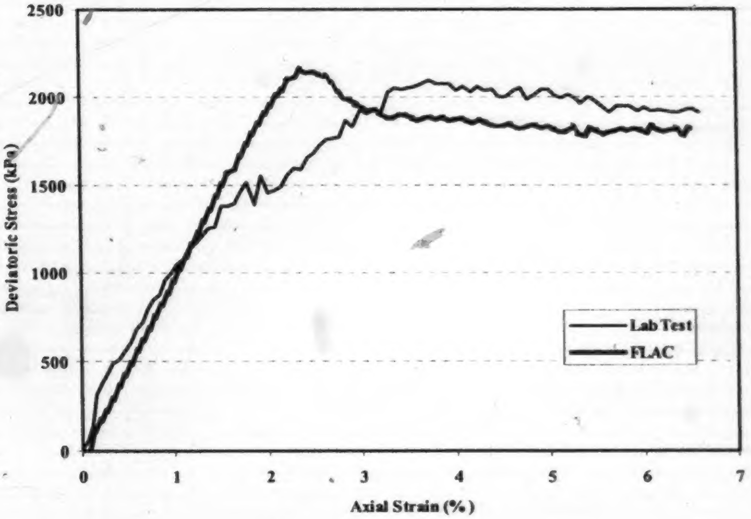

Figure A45 Deviatoric stress versus axial strain
Stress Path 1 ($\sigma_3' = 240$ kPa), Specimen S7

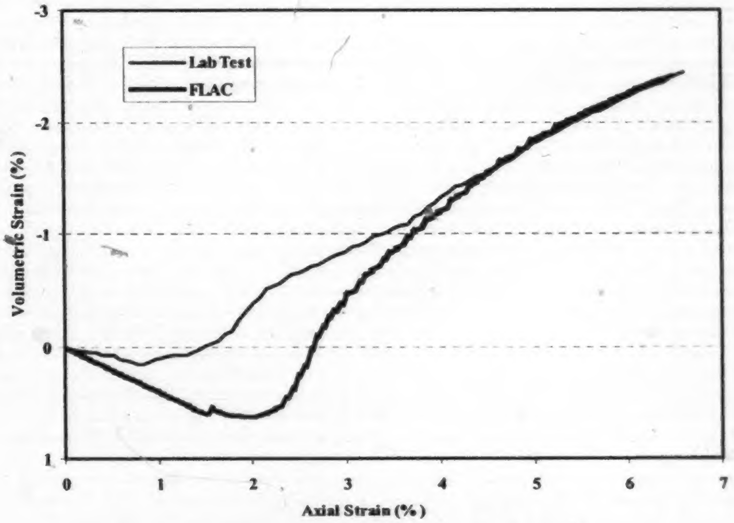

Figure A46 Volumetric strain versus axial strain
Stress Path 1 ($\sigma_3' = 240$ kPa), Specimen S7

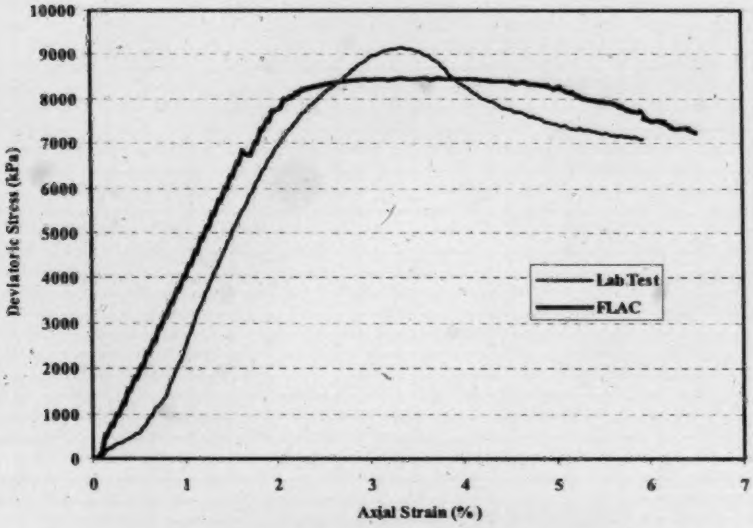

Figure A47 Deviatoric stress versus axial strain
Stress Path 1 (σ_3' = 1970 kPa), Specimen S8

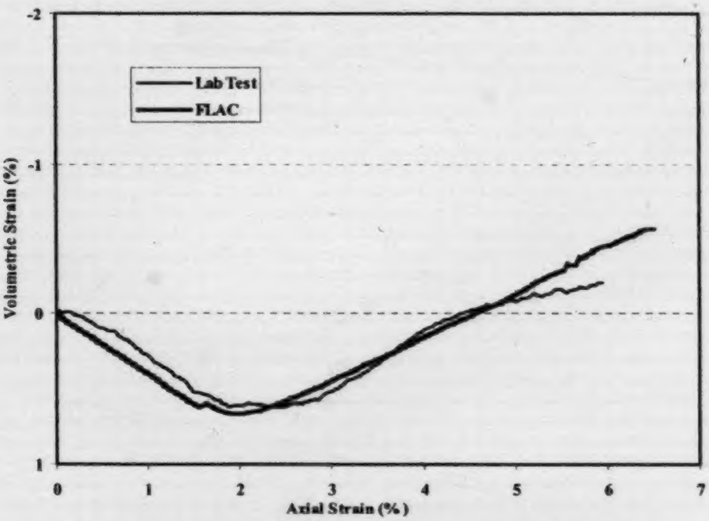

Figure A48 Volumetric strain versus axial strain
Stress Path 1 (σ_3' = 1970 kPa), Specimen S8

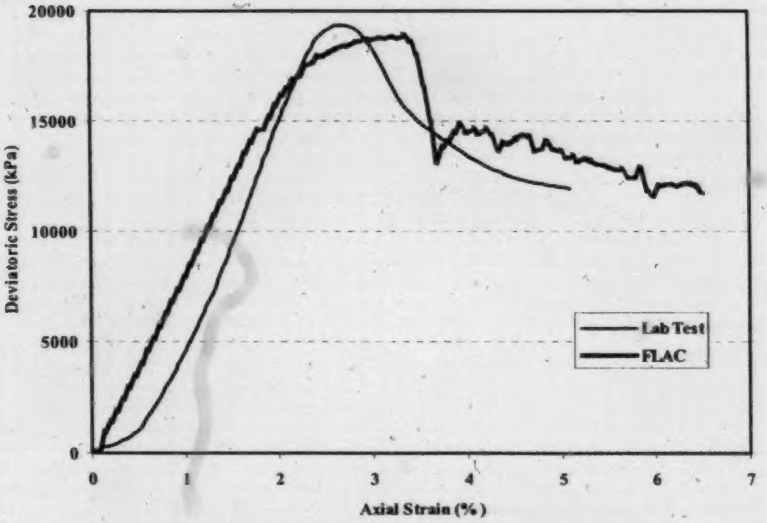

Figure A49 Deviatoric stress versus axial strain
Stress Path 1 (σ_3' = 2960 kPa), Specimen S10

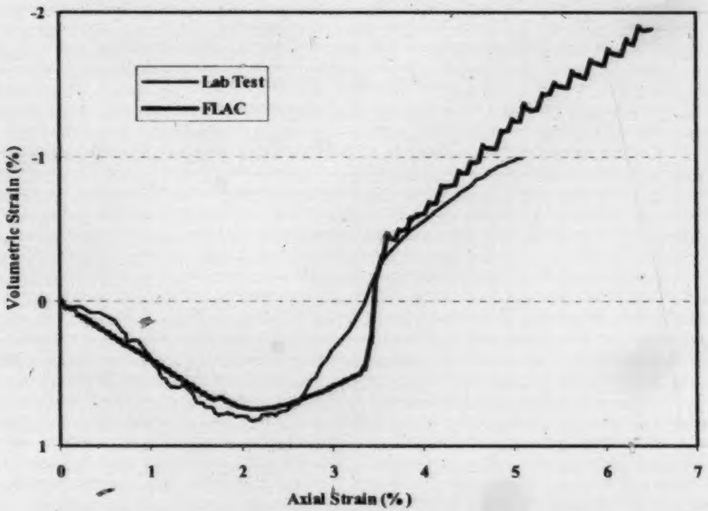

Figure A50 Volumetric strain versus axial strain
Stress Path 1 (σ_3' = 2960 kPa), Specimen S10

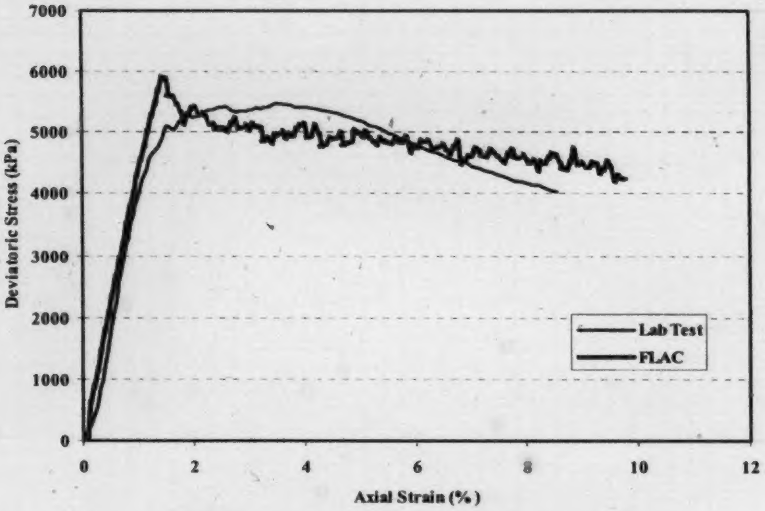

Figure A51 Deviatoric stress versus axial strain Stress Path 2 (Initial $\sigma_3' = 3000$ kPa), Specimen S19

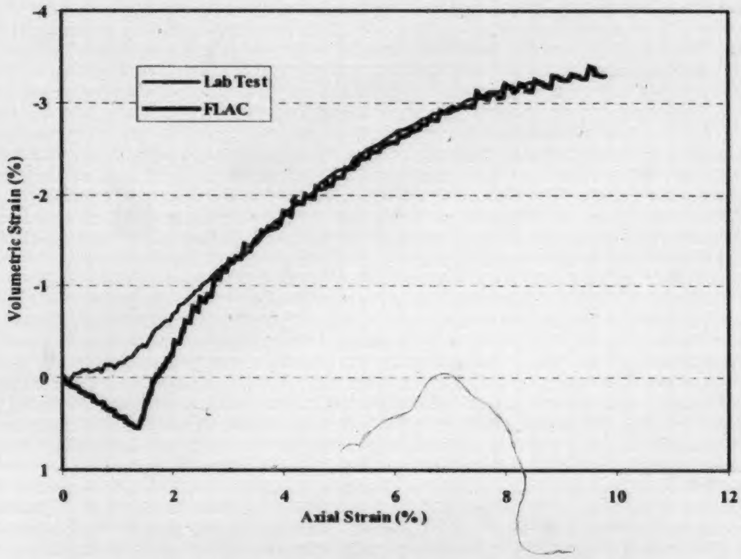

Figure A52 Volumetric strain versus axial strain Stress Path 2 (Initial $\sigma_3' = 3000$ kPa), Specimen S19

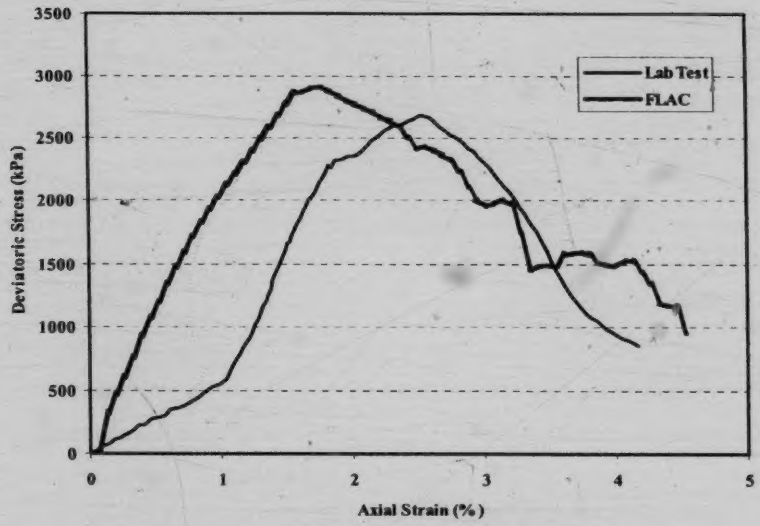

Figure A53 Deviatoric stress versus axial strain Stress Path 2 (Initial $\sigma_3' = 890$ kPa), Specimen S20

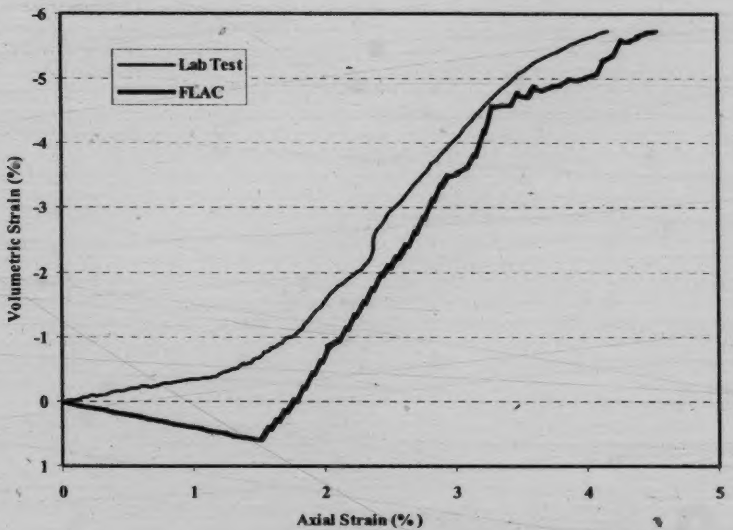

Figure A54 Volumetric strain versus axial strain Stress Path 2 (Initial $\sigma_3' = 890$ kPa), Specimen S20

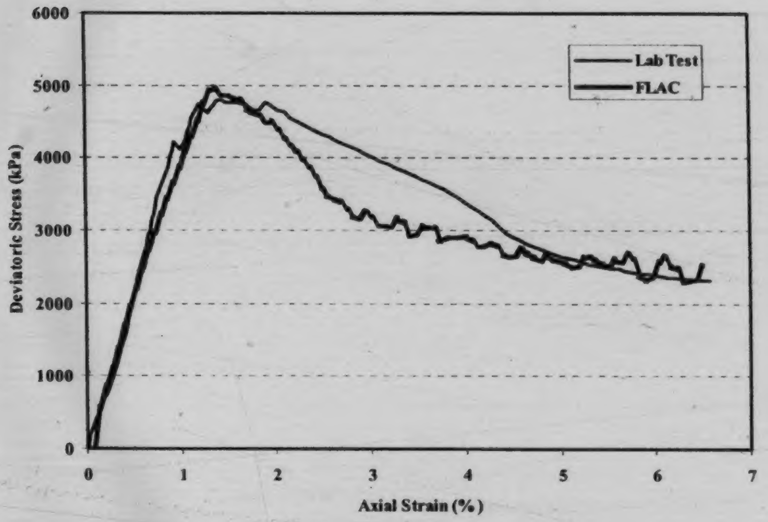

Figure A55 Deviatoric stress versus axial strain Stress Path 2 (Initial $\sigma_3' = 1950$ kPa), Specimen S21

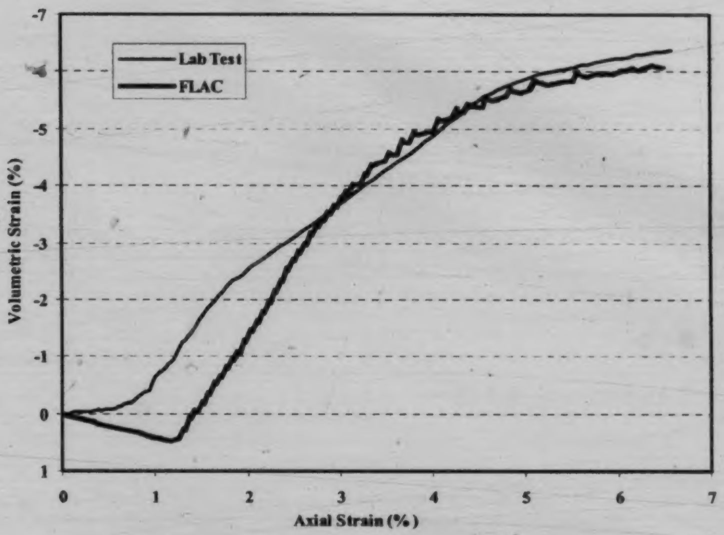

Figure A56 Volumetric strain versus axial strain Stress Path 2 (Initial $\sigma_3' = 1950$ kPa), Specimen S21

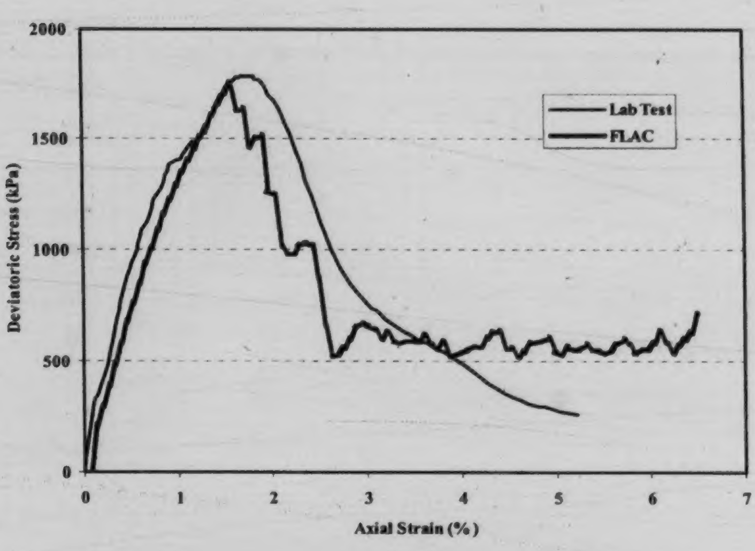

Figure A57 Deviatoric stress versus axial strain Stress Path 2 (Initial σ_3' = 570 kPa), Specimen S22

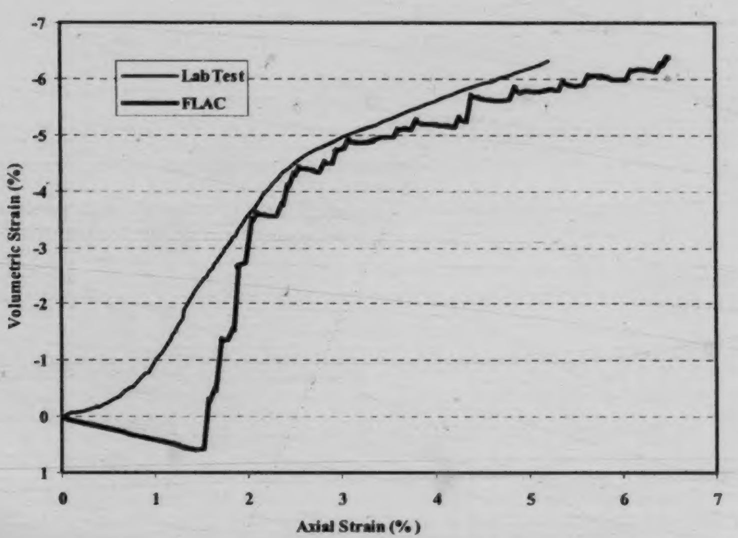

Figure A58 Volumetric strain versus axial strain Stress Path 2 (Initial σ_3' = 570 kPa), Specimen S22

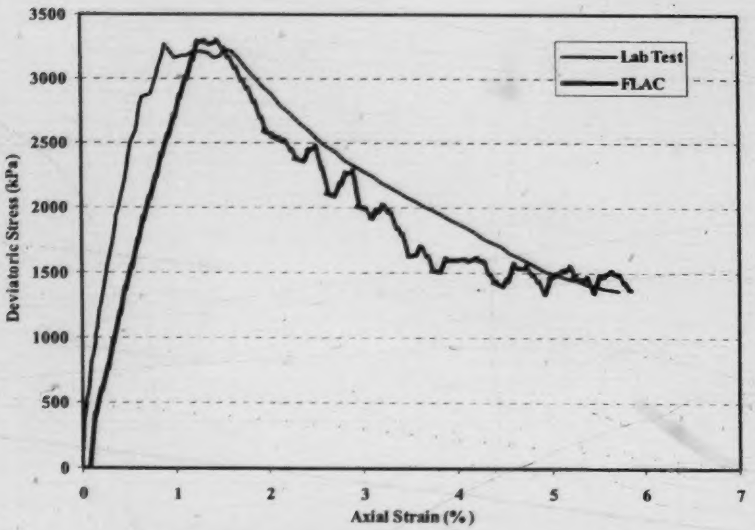

Figure A59 Deviatoric stress versus axial strain
Stress Path 2 (Initial $\sigma_3' = 1390$ kPa), Specimen S23

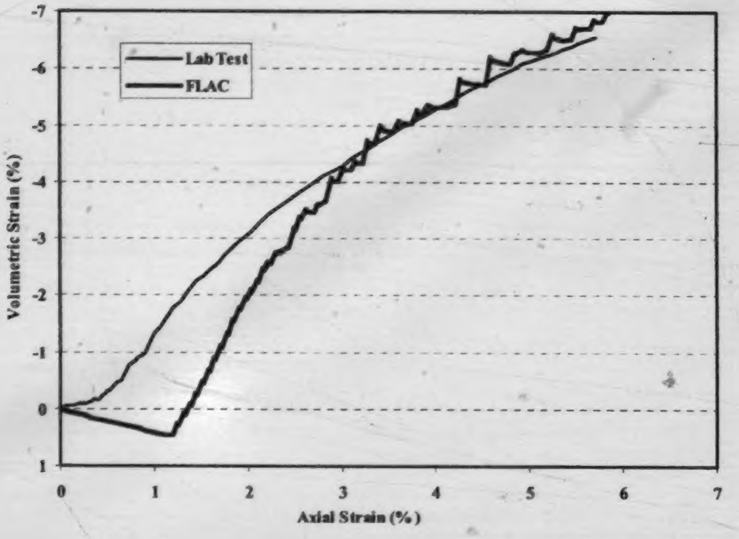

Figure A60 Volumetric strain versus axial strain
Stress Path 2 (Initial $\sigma_3' = 1390$ kPa), Specimen S23

APPENDIX B

UTF PHASE A HISTORY MATCH FIGURES

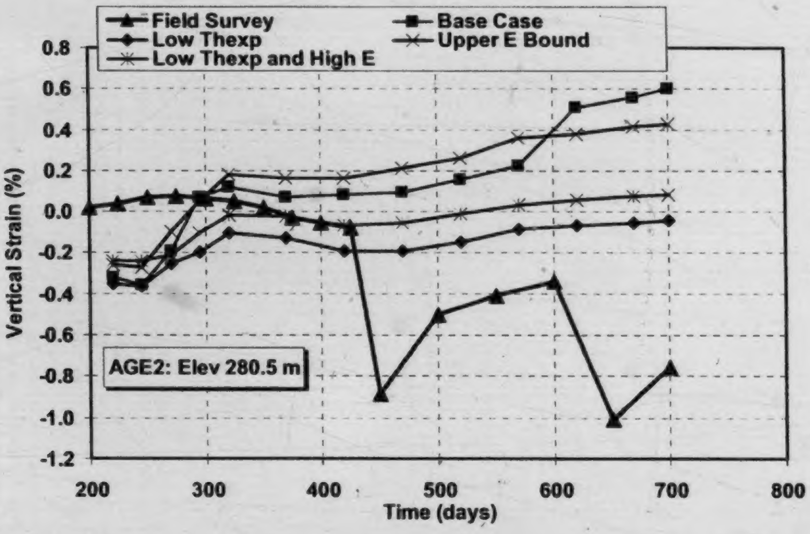

Figure B1 Comparison of simulated vertical strain and the field survey at elevation 280.5 in well AGE2

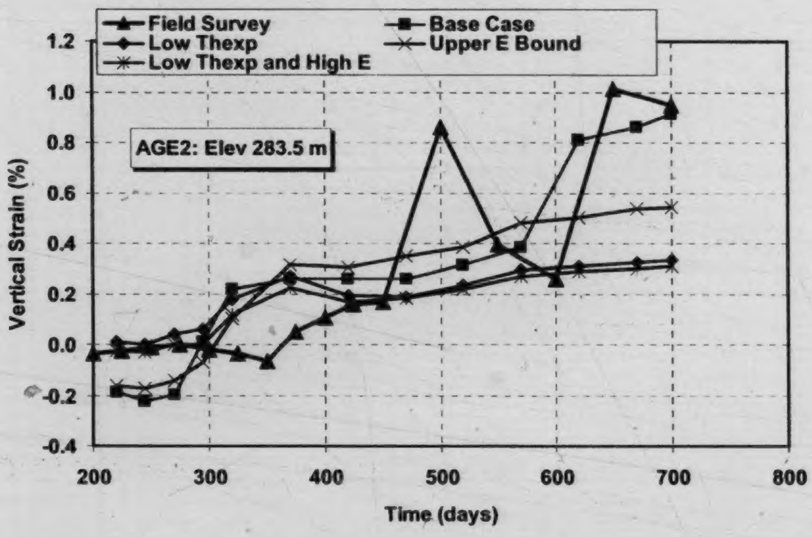

Figure B2 Comparison of simulated vertical strain and the field survey at elevation 283.5 in well AGE2

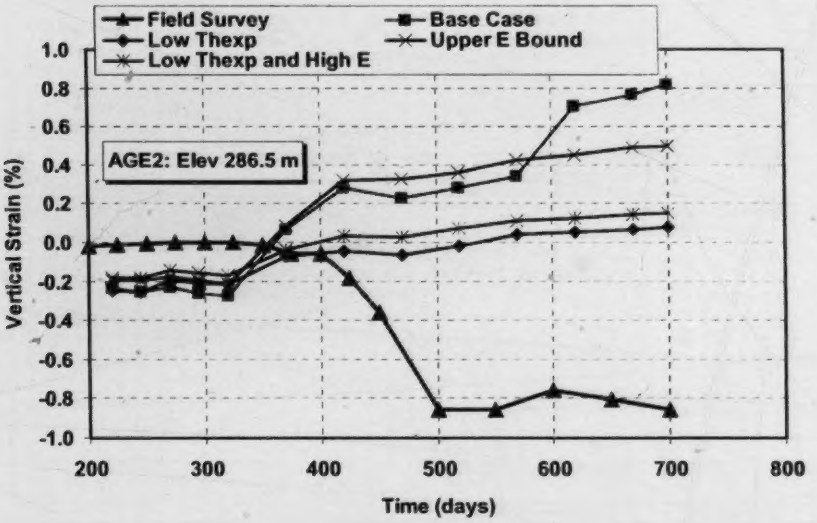

Figure B3 Comparison of simulated vertical strain and the field survey at elevation 286.5 in well AGE2

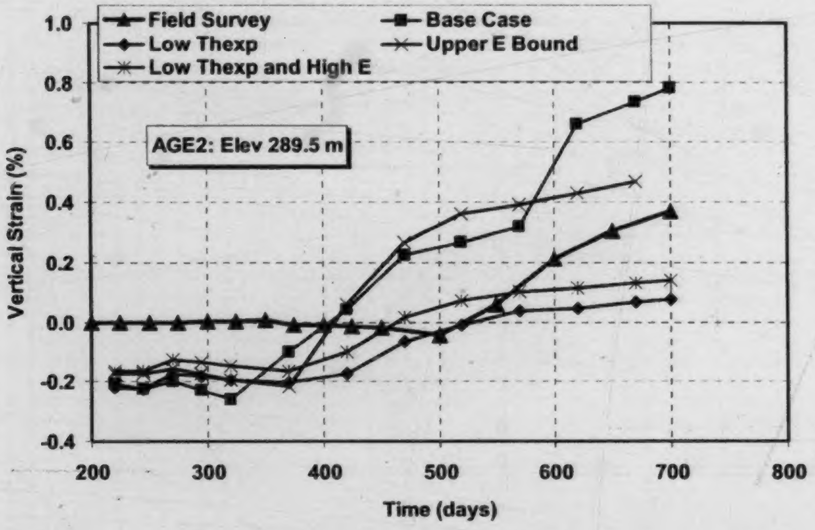

Figure B4 Comparison of simulated vertical strain and the field survey at elevation 289.5 in well AGE2

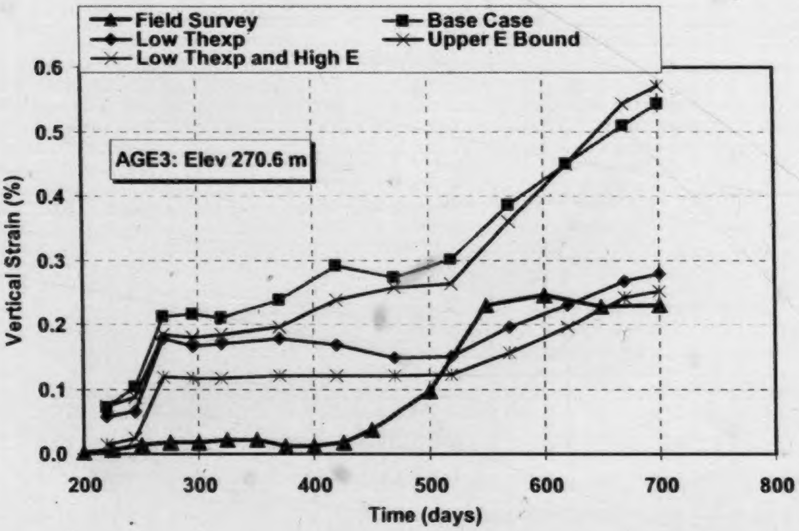

Figure B5 Comparison of simulated vertical strain and the field survey at elevation 270.6 in well AGE3

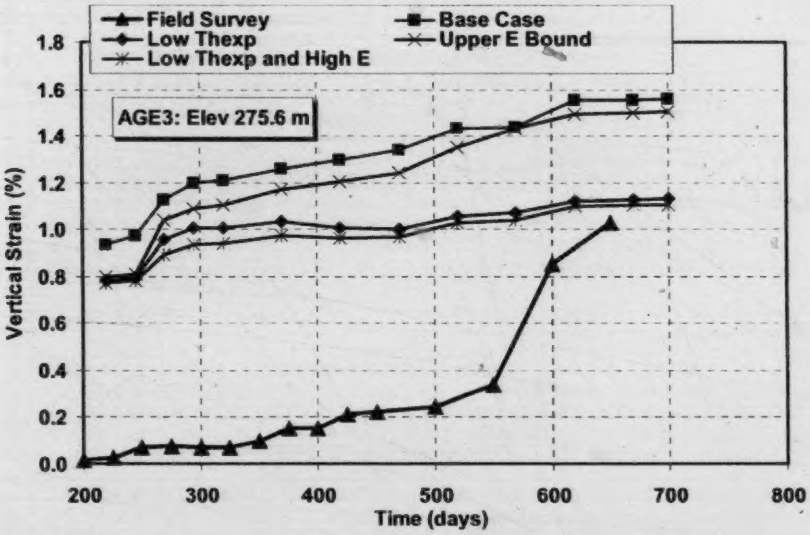

Figure B6 Comparison of simulated vertical strain and the field survey at elevation 275.6 in well AGE3

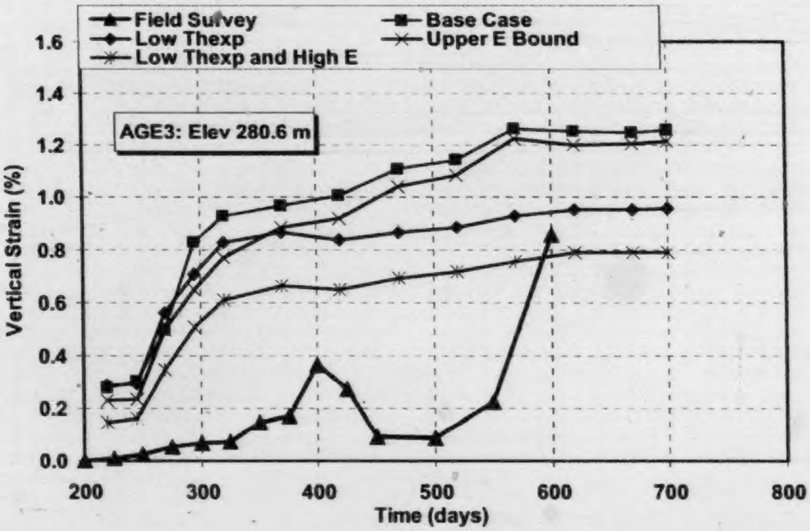

Figure B7 Comparison of simulated vertical strain and the field survey at elevation 280.6 in well AGE3

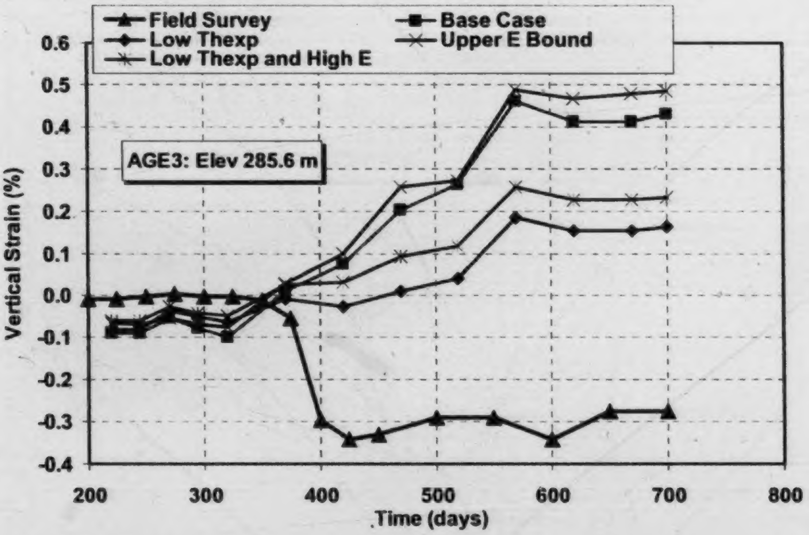

Figure B8 Comparison of simulated vertical strain and the field survey at elevation 285.6 in well AGE3

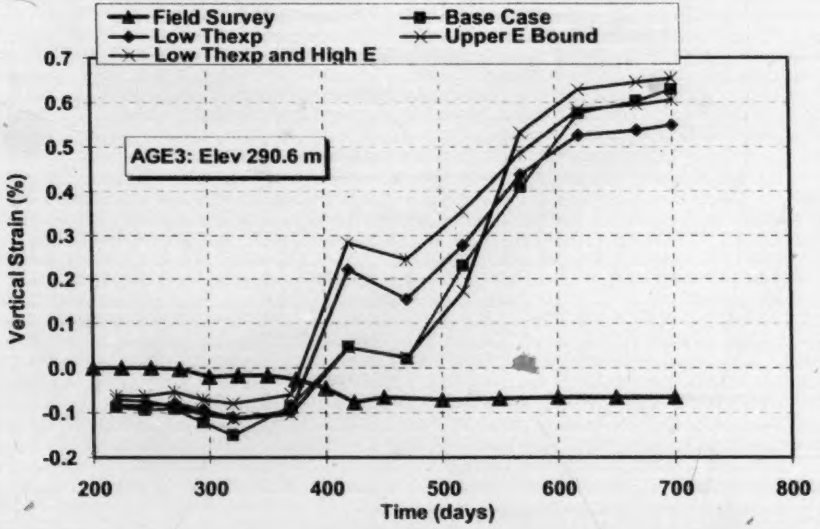

Figure B9 Comparison of simulated vertical strain and the field survey at elevation 290.6 in well AGE3

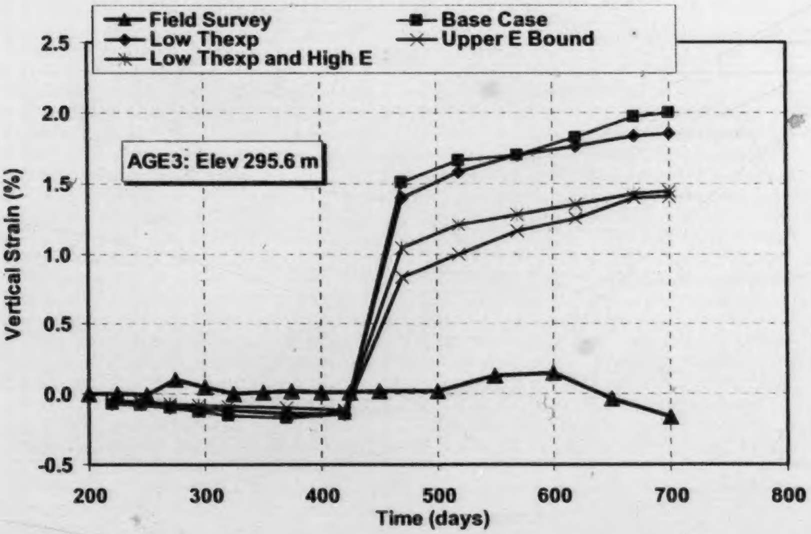

Figure B10 Comparison of simulated vertical strain and the field survey at elevation 295.6 in well AGE3

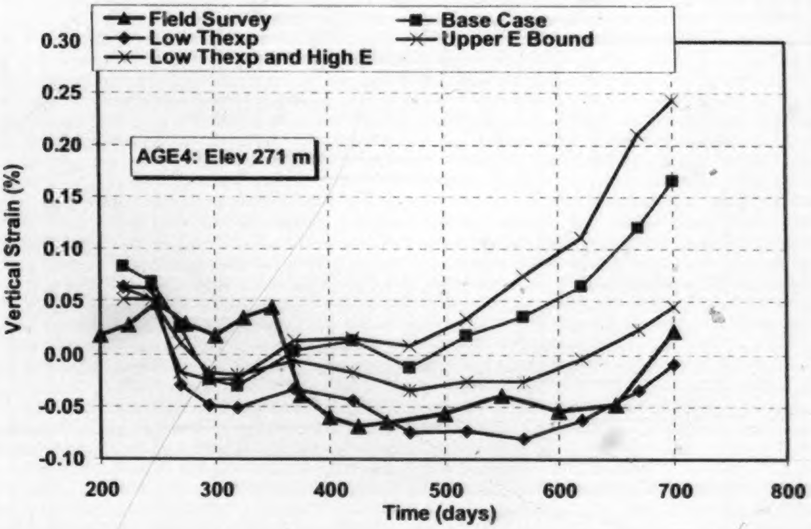

Figure B11 Comparison of simulated vertical strain and the field survey at elevation 271 in well AGE4

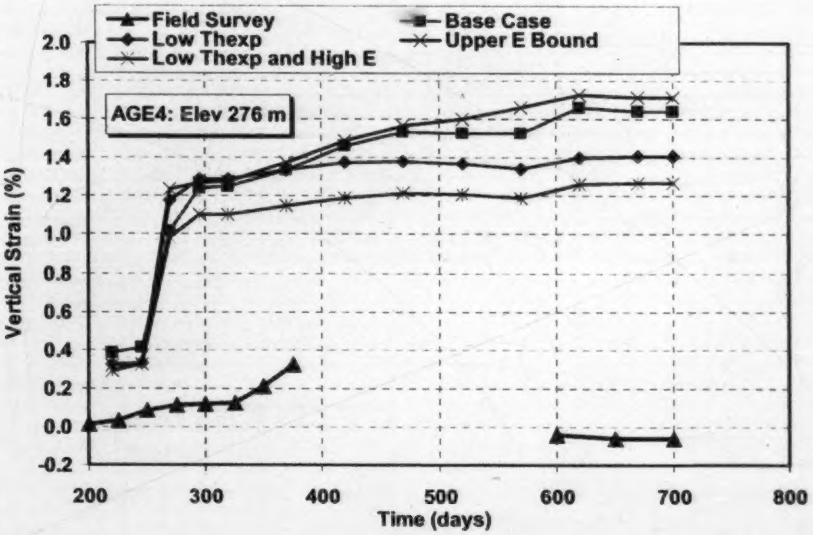

Figure B12 Comparison of simulated vertical strain and the field survey at elevation 276 in well AGE4

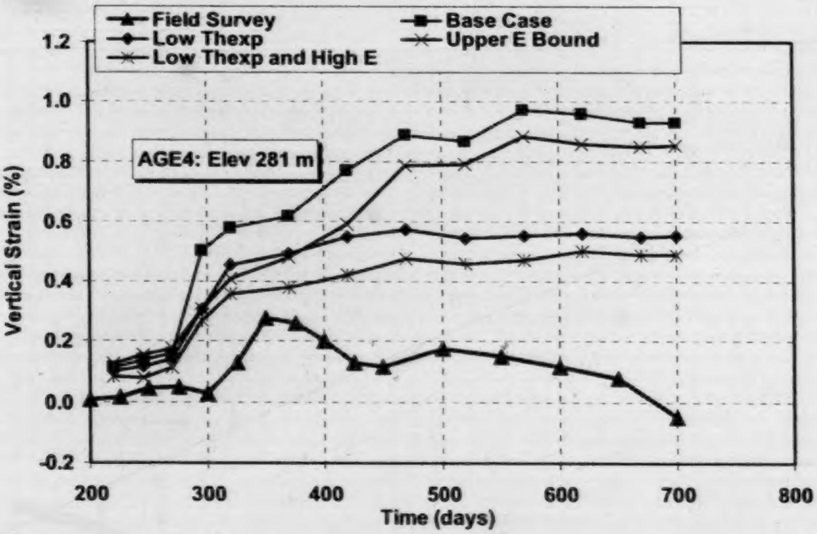

Figure B13 Comparison of simulated vertical strain and the field survey at elevation 281 in well AGE4

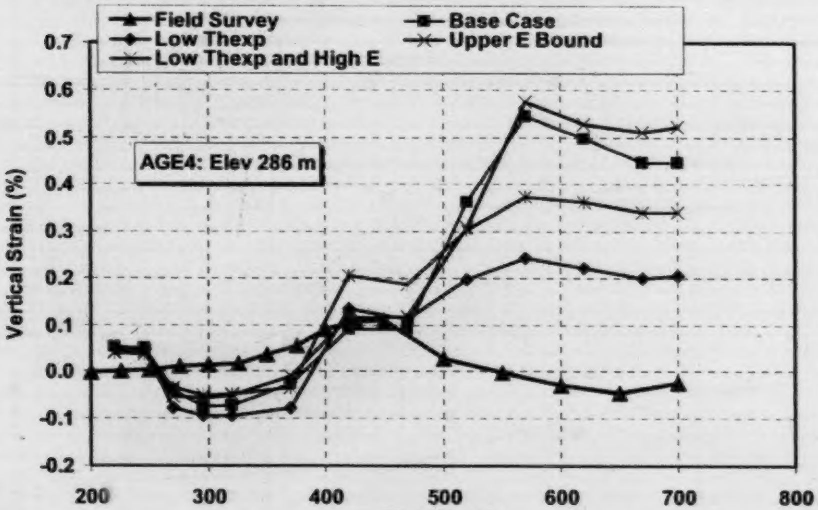

Figure B14 Comparison of simulated vertical strain and the field survey at elevation 286 in well AGE4

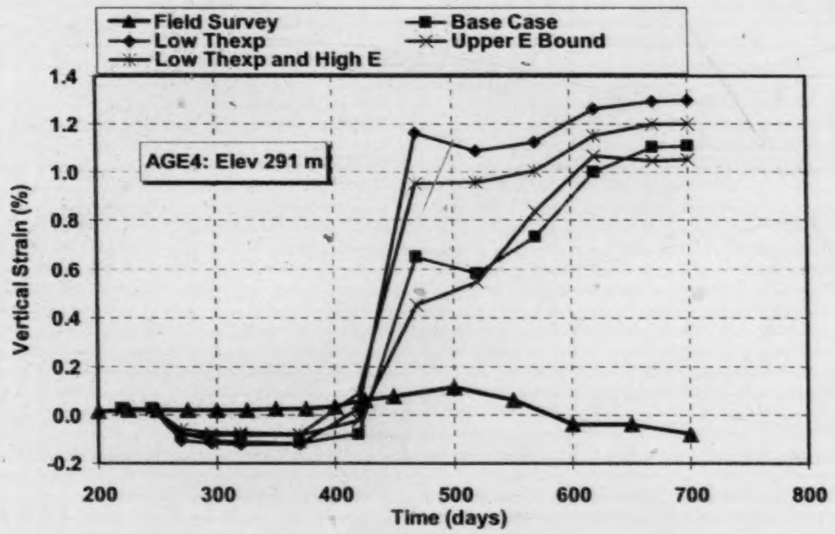

Figure B15 Comparison of simulated vertical strain and the field survey at elevation 291 in well AGE4

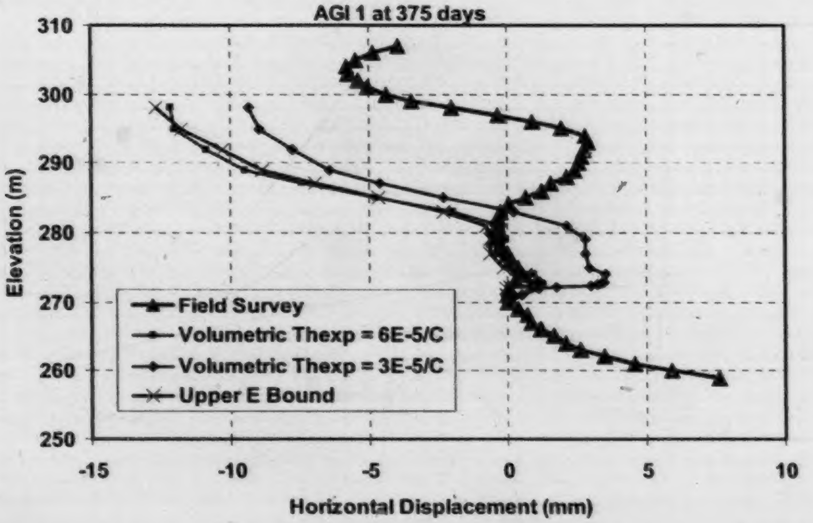

Figure B16 Comparison of simulated horizontal displacement and the field survey at 375 days in well AGI1

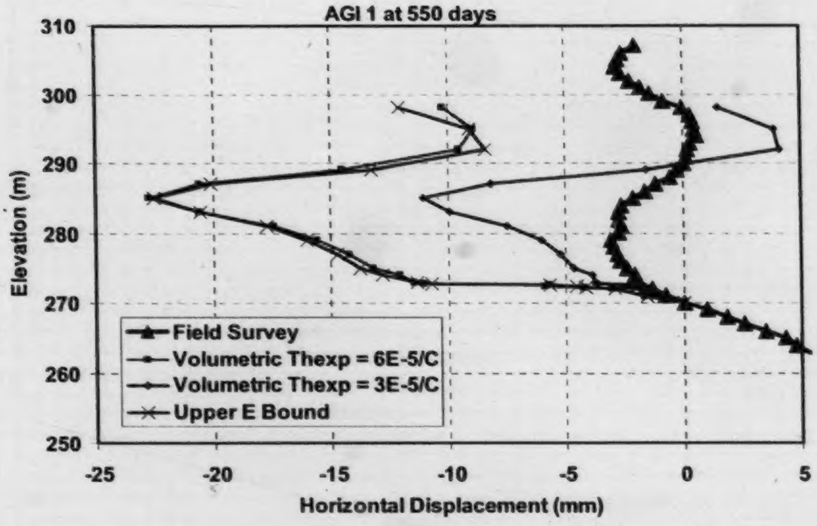

Figure B17 Comparison of simulated horizontal displacement and the field survey at 550 days in well AGI1

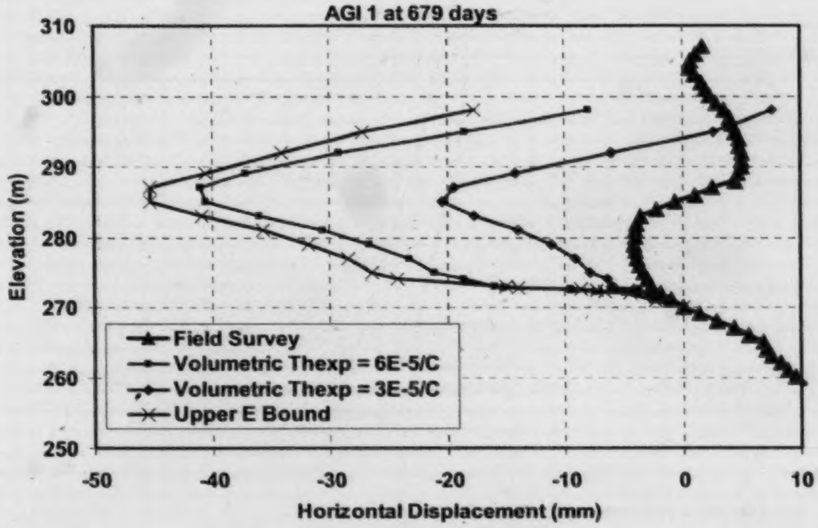

Figure B18 Comparison of simulated horizontal displacement and the field survey at 679 days in well AGI1

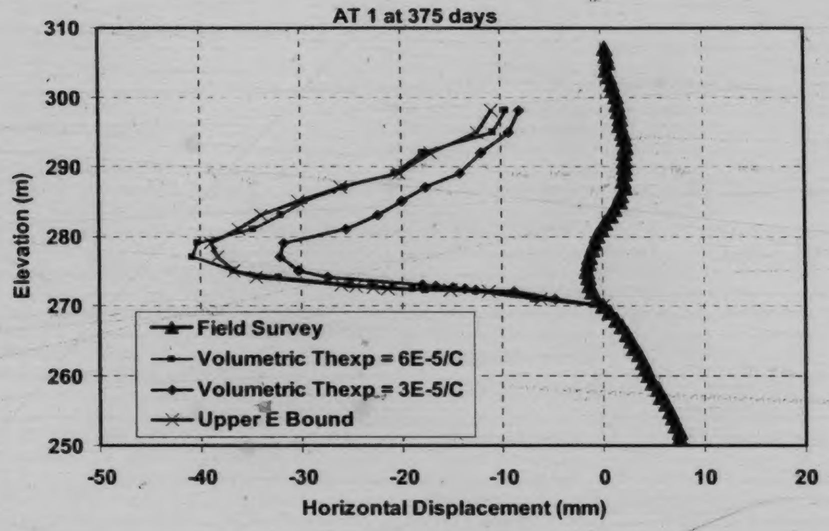

Figure B19 Comparison of simulated horizontal displacement and the field survey at 375 days in well AT1

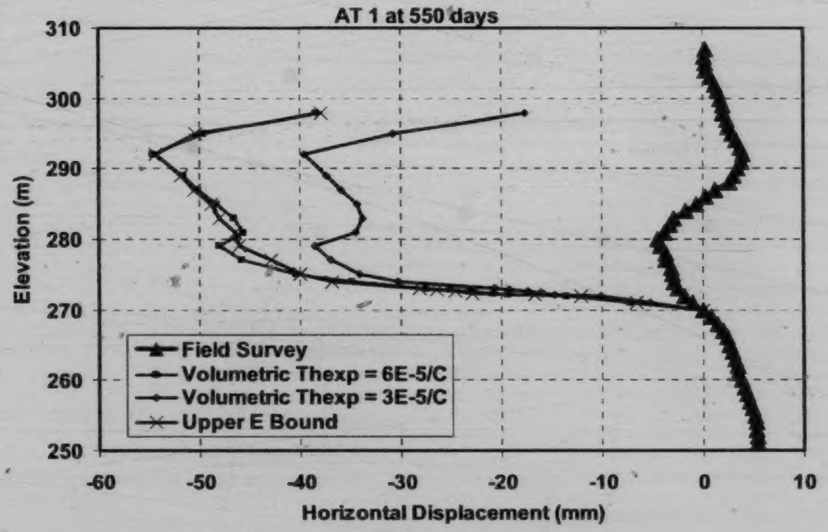

Figure B20 Comparison of simulated horizontal displacement and the field survey at 550 days in well AT1

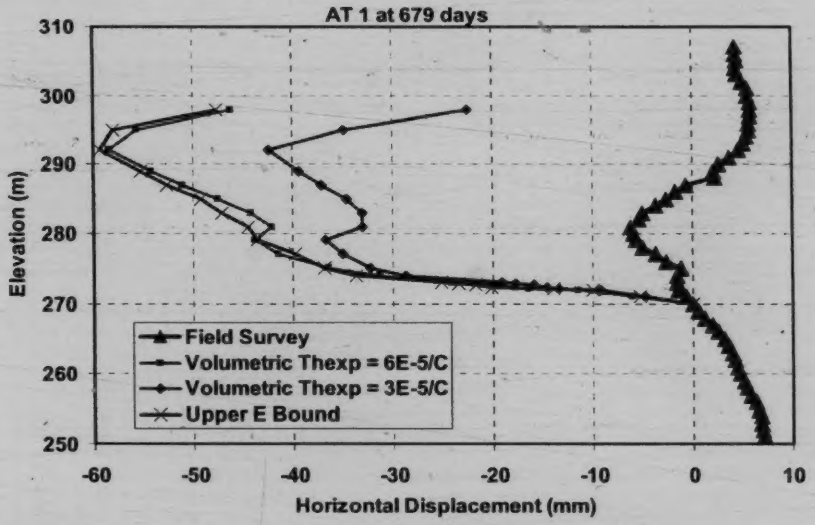

Figure B21 Comparison of simulated horizontal displacement and the field survey at 679 days in well AT1

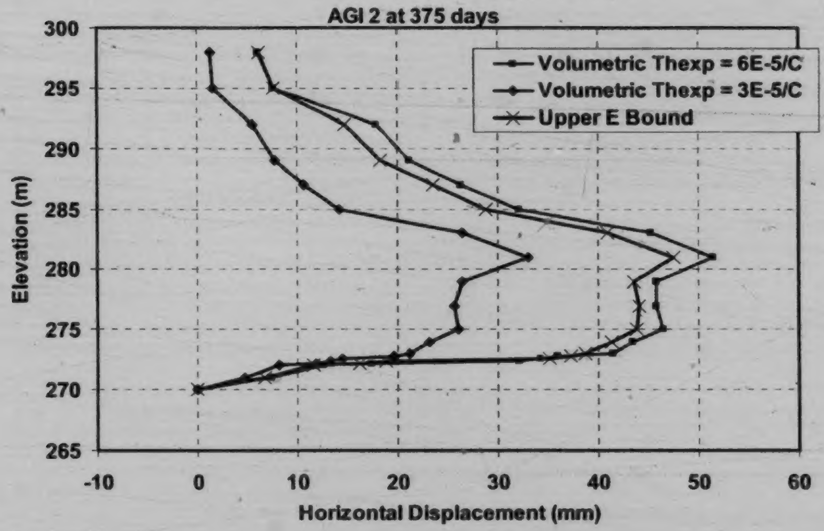

Figure B22 Comparison of simulated horizontal displacement and the field survey at 375 days in well AGI2 (field survey data not available)

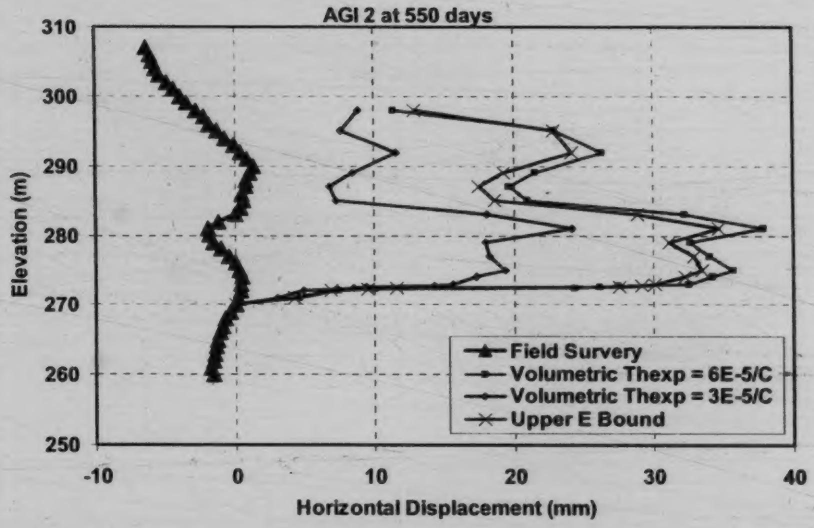

Figure B23 Comparison of simulated horizontal displacement and the field survey at 550 days in well AGI2

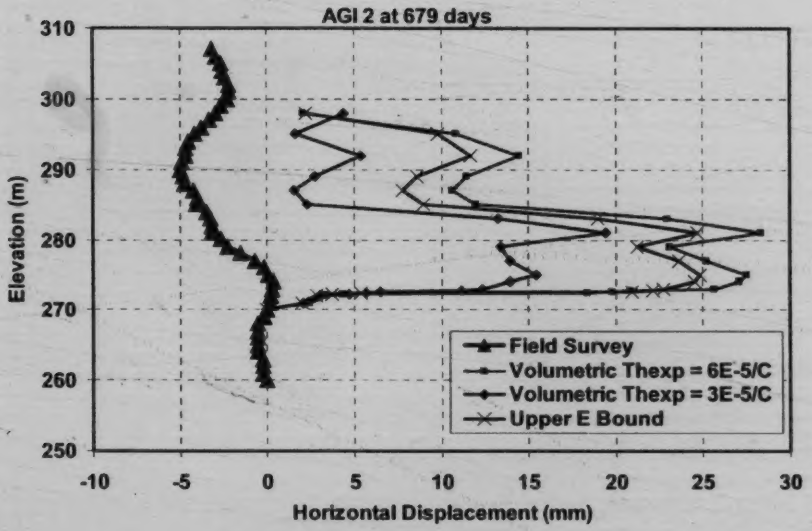

Figure B24 Comparison of simulated horizontal displacement and the field survey at 679 days in well AGI2

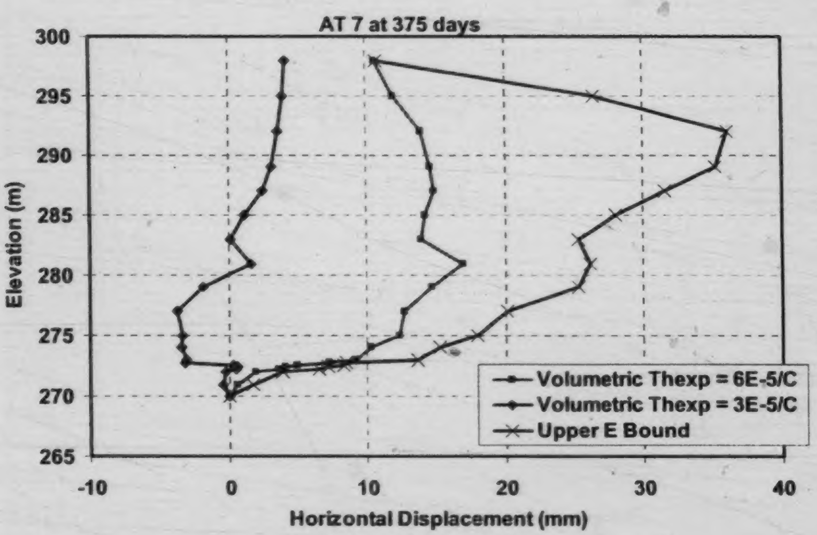

Figure B25 Comparison of simulated horizontal displacement and the field survey at 375 days in well AT7 (field survey data not available)

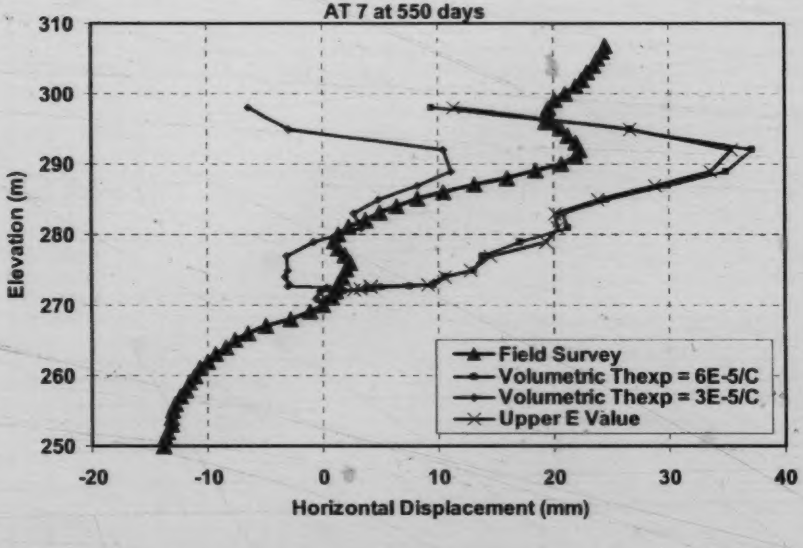

Figure B26 Comparison of simulated horizontal displacement and the field survey at 550 days in well AT7

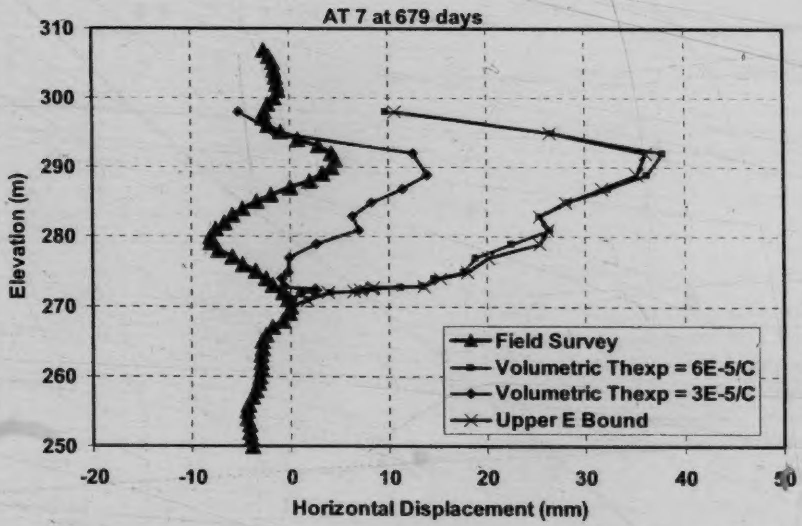

Figure B27 Comparison of simulated horizontal displacement and the field survey at 679 days in well AT7

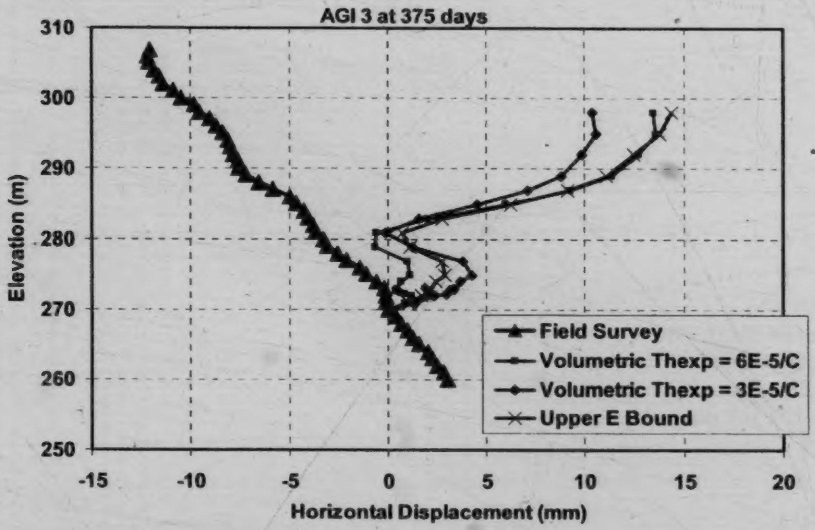

Figure B28 Comparison of simulated horizontal displacement and the field survey at 375 days in well AGI3

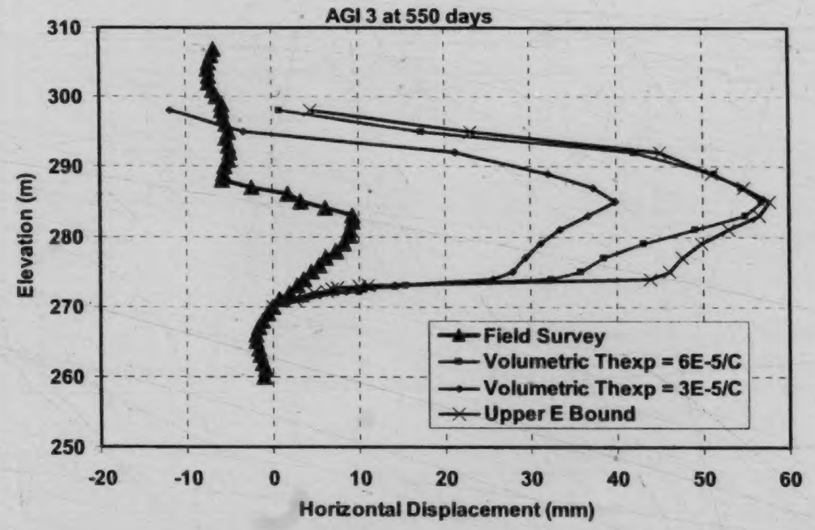

Figure B29 Comparison of simulated horizontal displacement and the field survey at 550 days in well AGI3

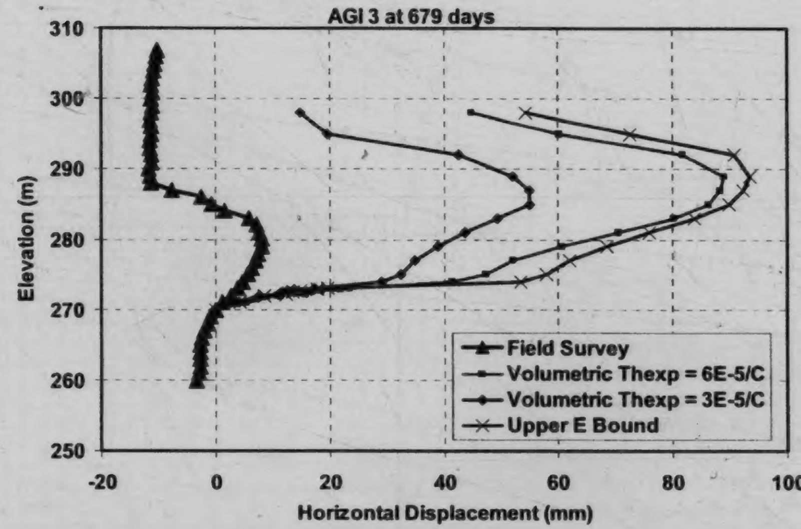

Figure B30 Comparison of simulated horizontal displacement and the field survey at 679 days in well AGI3